FILAMENT WINDING OF LONG TAPERED TUBES

BY

Vladimyr Ivan Burachynsky

A Thesis

Submitted to the Faculty of Graduate Studies

In Partial Fulfillment of the Requirement for the Degree of

DOCTOR OF PHILOSOPHY

Department of Civil and Geological Engineering

University of Manitoba

Winnipeg, Manitoba

THE UNIVERSITY OF MANITOBA

FACULTY OF GRADUATE STUDIES

*****

COPYRIGHT PERMISSION

FILAMENT WINDING OF LONG TAPERED TUBES

BY

Vladimyr Ivan Burachynsky

A Thesis/Practicum submitted to the Faculty of Graduate Studies of The University of Manitoba in partial fulfillment of the requirement of the degree

OF

DOCTOR OF PHILOSOPHY

ABSTRACT

This thesis presents a number of procedures and methods developed to fabricate tapered filament wound tubes intended to serve as electric utility poles. The two basic winding patterns, circumferential and geodesic are discussed in detail and mathematical models presented with subsequent illumination of critical properties as these patterns alter the material properties of the tubes. Models of the interaction of the two types of winding patterns are presented describing the non-linear variations of material properties. Techniques for the production of light weight composite mandrels with unequal dome apertures with integrated part extraction properties are described.

Experimental tubes were fabricated using a robotic filament winding machine and tested to failure. Full scale tubes were constructed using a variety of winding patterns and tested to determine the equivalent ANSI 05.1 Pole Standard. A second set of smaller poles were constructed to examine the behavior of jointed poles composed of two sections coupled with a variable length ferrule type joint.

A computer program is described to simulate the load performance behavior of both single and multiple section poles composed of both circumferential and geodesic winding patterns. The computer program contains subroutines to determine the thickness and wind angle drift at any arbitrary point along the length of the pole sections. Thus permitting the direct solution of the effective axial

stiffness at any point along the length of the structure using classical lamination theory principles. The incorporation of the Fundamental Bernoulli-Euler beam deflection equations, capable of modeling large deflections, into an iterative procedure within the program permits the solution of deflection under arbitrary loading. The analysis program is structured to permit the investigator to use inputs that are compatible with those required by the computer controlled filament winding machines. Computer modeling is compared to experimental results and demonstrates encouraging concurrence. A demonstration of the ability of a simplified computer program to determine the best method of upgrading a pole from one ANSI 05.1 class to a higher class is described. The work described is expected to result in the ability of fabricators to quickly determine the most appropriate laminate structure to meet specific performance criteria eliminating the trial and error process. The program also permits the solution of the design problem using inputs compatible with the computer controlled filament winding machine eliminating the need for translation to winding machine inputs.

ACKNOWLEDGMENTS

The experimental winding was carried out with the assistance of the staff of Faroex Ltd. of Gimli, Manitoba. Special thanks are due Mr. Mark Michaluk, P.Eng. Mr. Mark Wallace, C.T.E. and Mr. Aaron Lutz. Valuable technical assistance with the experimental testing program was provided by Mr. Dino Philopulos B.Sc. M.Sc. (E.I.T.) and Dr. Ningguang Xu Ph.D. . I would especially like to thank Dr. Dimos Polyzois my thesis advisor for his forbearance during the past years.

DEDICATION

The course of this project was marked by the deaths of my, father Roman Burachynsky, mother Franziska Burachynsky, uncle Dmitro Negrych and wife's father Stephen Srayko. Without their encouragement I would never have had the resolve to attempt such a challenge. My dear wife Valerie Burachynsky was my anchor through the years and absorbed much of the strain that otherwise would have ended my efforts when disillusion and despair seemed overwhelming. I have to admit that in some sense I have finished this work to prove that human beings are capable of much more than they assume and most obstacles in our lives are imaginary.

TABLE OF CONTENTS

LIST OF FIGURES

LIST OF TABLES

1 INTRODUCTION

The world wide standing inventory of timber suitable for the production of poles is not likely to increase in the foreseeable future. Lumber prices world wide show a steady trend upward as local supplies are depleted or protected for environmental reasons. The remaining stands of timber are sought after by developed and developing nations alike for many industries from pulp to housing.

The likelihood of lumber producers continuing to supply low cost pole logs to electric utilities while other markets are prepared to pay higher prices for large logs is questionable. In spite of the more obvious environmental concerns about chemically treated utility poles and the relatively short service life span, escalating market value for clear structural timber will ultimately make solid wood too valuable for use as utility poles.

Fiberglass reinforced polymers have been considered as potential replacement for wood poles, as have both steel and concrete. The choice of alternative materials does depend on local conditions with respect to cost, transportation and industrial capacity among other factors. FRP type poles are presently available from a number of suppliers and have received only limited acceptance by the North American utilities and may be regarded as very rarely utilized. Compliance with the pole classification system presently being used is not without some difficulty.

This project had as its primary focus, the production of poles suitable for use by electric power utilities. One of the utility's major criteria for use was classification of poles into distinct classes on the basis of load capacity.

In particular it was the goal of this project to determine the most feasible method of producing FRP poles, designing the production facility, implementing the selected technology and subsequently fabricating small scale and full scale test specimens. The technology was to be transferred to the industrial partner Faroex Ltd. The first part can be summarized quickly as Filament Winding. This phase of the project was simply reduced to consideration of economics. Since filament winding utilizes raw materials with the lowest cost per pound and one of the highest production rates; it inevitably places second to pultrusion which typically has a higher production rate in pounds of material per hour.

The design limitations of pultrusion limit parts to parallel fiber orientation collinear with the extrusion direction. Monolithic tapered structures were not feasible. This left filament winding as the only possible choice.

Knowing that a number of very low angle, axially oriented laminates as well as hoop or circumferential fibers were required to withstand bending and torsional loads, Filament Winding was clearly less restrictive than pultrusion. Additionally the choice of winding technology, robotic versus mechanical clearly favored the automated machines with the greater repertoire of wind patterns and higher speeds.

The second stage of setting up the production facility was facilitated by the industrial partner, FAROEX, and the machine supplier, McClean Anderson.

The third phase of the project, implementation, saw the beginning of serious difficulties. The determination of wind paths for tapered mandrels was not straightforward. Though software was supplied by McClean Anderson that purported to be sufficient to the task, it was found to be very limited in value.

What had not been considered is the task of designing mandrels. Early on it was thought that once pole geometry was determined that the same would be used for the mandrel, since the pole was thought to simply be over wrapped. The interrelationships between wind paths, machine motion and mandrel geometry proved to be extremely complex and difficult to organize in a practical fashion with the tools available.

The first hurdle was finding a method to reverse the filament path direction over a mandrel without altering the direction of rotation. The second issue was to prevent the fiber from sliding off the mandrel during rotation. Solutions to both issues were developed independently after solutions from other industries proved deficient.

The third issue was the removal of the part from the mandrel subsequent to curing. Development of the self-extracting mandrel technology was a major development. Fourth was determination of the optimal resin viscosity to provide fiber wet out. Fifth was the need for a reduction in friction between part and mandrel surface requiring a serious examination of release agents and removal forces. The problems were resolved progressively and

finally considered solved. As work on small scale poles progressed we learned that not all wind patterns are equal.

The greatest hurdle of all was a phenomenon we termed premature turnaround. Geodesic wind paths proved to be the best candidate for low angle axial winding with the greatest stability. However they are subject to a phenomenon called premature path reversal. Long tapered tubes appeared to be impossible to wind. The problem was investigated and as a result, a number of major innovations were developed. The major portion of the thesis deals with this area of concern. Finally the issue of tube wall thickness control was resolved and it was possible to actually determine the thickness for tapered tubes prior to fabrication by controlling roving parameters of TEX and band width, during the design phase.

Ultimately, over 20+ large poles were fabricated in an experimental production environment providing further data on the economics of the production methodology.

The pole static load test program was designed originally to deliver information on the structural properties of the various wind angle patterns and laminate stacking sequences to the design group. However the project terminated prior to a second production run being implemented. Further work on theory and design issues continued in spite of this set back. The experimental testing proved satisfactory and efforts were focused on developing mathematical tools to reduce the enormous complexity of the design process which was found to be highly sensitive to pole geometry.

A set of small scale poles were fabricated using some of the solutions and incorporating what we believe are innovative intrinsic ferrule joints.At this point we were capable of designing mandrels, extraction systems, laminate sequences, laminate thickness, roving line properties and joints. In addition we now had the capability to examine the preliminary structural properties of a pole i.e. bending stiffness as well as provide a data base for finite element analysis and robotic axes position coordinate tables during the design stage.

Dozens of wind path configurations could now be evaluated very quickly and the best candidates selected. The algorithms later detailed, promise to streamline the design of filament wound structures and eliminate the costly trial and error learning curve for structural optimization.

Literature on filament winding principals is not widely available, and outside of industry restricted documents, is extremely fragmented. While much work is published regarding analysis of filament wound structures, in general it is restricted to constant diameter tubes and mechanically wound tubes. Both of these can be regarded as special cases of filament winding, as will be discussed later in depth. These papers do not typically concern themselves with the details of the fabrication methods.

The thesis is organized in a manner that does not reflect the original project sequence of events. In general the rationalized order of the thesis was imposed retrospectively, in order to clarify the concepts in the reader's mind and establish a hierarchy of concepts.

1.1 HISTORICAL BACKGROUND

An excellent, though short review of filament winding technology and the industry can be found in the ``Filament Winding: Composite Structure Fabrication" by Peters, et. al. (1991). It is the author's position that, though the earliest examples of fibre glass manufacturing date to the time of the pharaohs around 1370 B.C., the modern industry begins in 1945.

It was at that time that George Lubin and W. Greenburg at Bassons Industries agreed to manufacture springless suspension systems for General Motors. No mention of the success of the project was forthcoming however. Lubin and Greenburg had during the war years produced lightweight plastic hoops for the Manhattan Nuclear Project on a conventional lathe while with Bassons Industries. The same rings eventually became the Naval Ordinance Laboratory (NOL) standard for short beam and tensile ring testing (Peters, et al 1991).

In 1946. R.E. Young was instrumental in developing a prototype filament wound rocket motor case. A year later, with assistance of M.W. Kellog, Young completed the design for the world's first filament winding machine, expressly for the production of rocket motor cases. This early version was of necessity a mechanical winder, but it was the beginning of a new industry (Peters, et al 1991). Subsequently, R.E. Young had left his former employer to start his own company, secure in having just filed for and received US patent protection. Subsequently, Young licensed his technology to other manufacturers and ultimately sold his interest to the Hercules Powder Corporation (Peters, et al ,1991).

Many companies aggressively pursued the technology during the 1960's such as Thiokol, Hercules, Brunswick, Aerojet Hitco and the Douglas Aircraft Company. The only publicly available paper found, directly relating to filament winding theory, during the 60's was by R.F. Hartung (1963) on planar wound pressure vessels. It was in this paper where the ideas for netting analysis were presented in an open forum. However design engineers at Douglas Aircraft were actively engaged in similar research.

A preliminary report by John Hofeditz for the 18th annual Meeting of the Reinforced Plastics Division of the Society of the Plastics Industry titled "Structural Design Considerations for Fiberglass Pressure Vessels" shows just how active Douglas Aircraft was at the time. Six internal technical reports were listed in that paper for the period April, 1961 to March 1962. Two of the papers listed were in preparatory stages and identified as "To be published".

The team of researchers at Douglas Aircraft at that time were L.B. Greszchuk, W.L. Read, H. Chao, and C. Wills. The primary focus of the reports was the stresses at the dome cylinder interface region of rocket motor cases. A similar pattern of activity can readily be assumed for the other companies involved, unfortunately no evidence has been found. As Peters, et al 1991 indicates there was a lot of money being made available to cover development costs, by the US Air Force.

This period coincides with the Cold War and within a short period of time both the Minuteman Missile system and the Polaris Missile system were in production incorporating filament wound rocket motor cases. The world watched in horror as the tension between the Soviets and Americans was reaching extravagant heights.

Lightweight rocket motor cases and nuclear weapons were proving to destabilize global politics. The involvement even extended to Canada with its own nuclear missile crisis under Prime Minister Diefenbaker and only grew worse as the years progressed. Filament wound rocket motor cases were making it easier and easier for the nuclear powers to reach each other with bigger and bigger payloads.

In 1961 another development occurred that made the future of the world ever more frightening. Continuous graphite filament begins production in that year, produced from low cost Rayon, polyacrylinitrile (PAN) polymer filament. The new development promised higher performance than anything previously available and higher payloads for smaller, lighter, and cheaper rockets (Peters, et al 1991).

The early decades of the industry are characterized by a lack of public literature, in part due to the ongoing Cold War issues but also due to commercial interests. As Peters, et al (1991) point out, the history of filament winding is a history of patents. The list of patents demonstrates an industry dominated by few and very large corporations during the 70's and 80's. The literature for the period is also very sparse.

During the late 80's and early 90's a new development is seen. The Europeans are beginning to publish papers notably on Computer controlled filament winding machine technology. One paper appears to foreshadow a coming trend in European industry.

In 1982, J.P. Denost published "New design concepts for Filament wound pressure vessel with unequal polar openings." He was working under the *Societe Nationale Industrielle Aerospatiale Division Systemes Balistiques*

et Spatiaux Etablissement d"Aquitaine S.N.I.A.S., at the time. The paper was released to AIAA for publication but it was never confirmed if it was made public. One fact stands out; the research deals with many of the same issues previously discussed by Hofeditz (1962) at Douglas Aircraft.

One quickly assumes that the French are now in the development stages of their own rocketry programs, but they are forced to relearn all that the Americans have never openly published. Not a single reference is made to previous research in the entire paper. France had only recently entered the nuclear race with testing in French Polynesia. Europe and especially France were in a heightened state of tension, as yearly they witnessed the unprecedented escalation in the arms race.

Nuclear weapons were being deployed throughout NATO occupied Europe and matched enthusiastically by the Warsaw Pact countries. The Denost paper would suggest that the French were also looking at delivery systems. In hind sight the speculation is confirmed since historically, the French were chaffing under NATO restrictions and DeGaulle made no effort to disguise his intentions to steer a separate course from the Americans. Later developments would prove the success of this initiative with the launching of unmanned rockets from Kourou in French Guiana and the later creation of the European Space Agency and the Aerospatialle Consortium.

The ESA was equivalent to NASA in many ways and included many of the European counterparts to the American Corporations that dominated the industry in the West. By the early 90's it was clear that the Europeans were behind the development of an advanced composites industry. If this impetus was due to anxiety over the escapades of the superpowers or to the

debilitating effects of the world's first oil embargo, it is open for interpretation.

BRITEURAM and other research funding were supporting both English and Belgian research programs, notably at the University of Nottingham and K.U. Leuven, to develop composite technology. These programs were successful in their own ways.

A group from Nottingham broke away to commercialize software for computer controlled filament winders under the name of CADFIL. Another group supported by BRITEURAM at Leuven is closely linked with the only other commercial robotic control software in Europe, CADWIND. Remarkably the same pattern of development characterizes the European experience as it did in the US, three decades later.

The history of the industry is a history of patents, military and corporate interests. The Europeans have taken to publicizing their research much more actively than the Americans, at various proceedings, however little is revealed about the internal algorithms and numerical methods. In fact many of the papers are a restatement of basic equations from earlier papers with the dramatic presentations of the capability of their new technology developments. One is lead to believe that the Leuven group is also on the road to patenting a recent development called CAWAR, as is the tradition for the industry.

In spite of these shortcomings the Europeans have demonstrated tremendous innovation in adapting modern technology. Filament Winding may require a name change as it appears to rapidly becoming a robotic fibre placement system with integrated design capabilities and even structural analysis. Winding in the traditional sense may no longer be essential for many

of the unusual geometries being considered. Examples of curved panels and multiple axis T-Joints are being produced regularly. Object inclusion and avoidance is now being considered by the Leuven group. This would lead to a resolution of the many problems associated with joining and coupling components of mixed materials. Further cost savings would result by having the robotics manipulate sub assemblies and incorporate them into the finished product.

Another innovation of the Europeans is the use of multiple axes-robotic manipulator arms that apparently have dropped considerably in price as the market for machine tools expanded greatly.

New technology was unveiled by an American firm, Entec of Salt Lake City Utah, October 2000 at the Las Vegas, Composite Fabricators Association annual conference and trade show. The new design, called a gantry system, is based on the robotic manipulator operating inside a very large suspended frame. This permits the floor area to be occupied by unusual geometries.

The arm is now capable of manipulating a variety of fibre types and fabrics. Significantly, its primary use will be machining composites. This machine is the beginning of a new revolution in fabrication technology. Ultimately the robotic arm will machine moulds and mandrels, place fibre and inserts at the appropriate locations and finally inspect the entire structure for defects before finish trimming and painting. The vision is of a complete robotic composites manufacturing station in a closed container with complete freedom to utilize chemicals not legal in the presence of human beings.

In recent years the Japanese have become active in building rockets and a number of papers have been published independently and in

collaboration with Americans (Gramoll, Namiki and Onoda, 1990). Modelling and structural analysis of the composite laminates dominates the concerns.

Two companies in the USA have commercial software developed to run on machines that they have produced. MacClean Anderson of Wausau Wisconsin and Composite Machines of Salt Lake Utah both has proprietary products. Composite Machines has recently been absorbed by Entec. The software was at the time specific to the machines and motion control boards that controlled the robotics.

The early versions encapsulated basic routines typically used by the most common customers. Those routines were highly oriented toward constant diameter dome shapes used by the pressure vessel industry. MacClean Anderson was also able to supply routines for primitive winding of tubes using algorithms that blended circumferential winding with a small slip factor to provide path reversal. (Later in this paper this is referred to as non-linear winding or dog-bone winding). There was a small software package for helical winding made available that served to help us choose to purchase their machine at the beginning of our research. Unfortunately the early versions were plagued by a design problem related to extremely low wind angle routines where the carriage motion is very great relative to mandrel rotation.

Another serious limitation was that the original programs did not handle tapered mandrels with dome ends very well. Some of these issues are being resolved by faster signal processing, typical of Digital Signal Processing based motion controllers, and finer resolution on motor encoders. Computer controlled filament winders are now capable of position resolution of a few

thousands of an inch, .005", and a few specialty machines below .001" precision.

The continued growth of the industry since the collapse of the Soviet Union and the demilitarization of the globe may be due to the ground transportation and recreation industries. During the 90's many patents were being registered for sporting equipment such as golf clubs and tennis racquets. New demands from the off shore drilling industry as well as the energy delivery sector require replacement of steel pipe and large tubes, with chemical and high pressure resistant composite products.

Filament winding clearly has significant contributions for the civil engineering community, and can make major inroads into the infrastructure renewal problem facing North America. The only provision required is that engineers begin to familiarize themselves with the nature of the process. Filament winding is not exclusively a pressure vessel production process. It should not be regarded as a simplified fibre placement technology that initially reflected the limitations of the 50's and 60's. Now that the computer era is in full stride the evidence from Europe suggests that winding cylinders is simply a special case of fibre placement technology.

1.2 SCOPE

The design of long tapered filament wound tubes is a rather complex issue based on a number of theoretical and practical issues that require detailed treatment. The introduction to the text, Chapter 1, of the thesis describes the history and basics of filament winding.

The theoretical aspects of the basic circumferential winding pattern are discussed in Chapter 2.0. Many concepts are introduced in this chapter that

are also fundamental to Geodesic winding, which is discussed in Chapter 3.0. Since there are fundamental differences in the mathematical formulations of each type of wind pattern, these result in significant differences for the structural modelling procedures based on the laminates composed of the two wind patterns. These differences also require different approaches to robotic programming.

The chapters detailing the Circumferential and Geodesic wind patterns each progress through the respective mathematical foundations and describes how these features affect the programming of robotic equipment. The mathematics of the wind patterns is rarely discussed in any detail in the literature and the parametric equations which form the platform of this thesis, have never before been presented. While the Circumferential wind pattern is based on the Circular Helix equation, it has never been presented in full detail. The parametric equations discussed are technically not those of the true Circular Helix, which by definition is of constant diameter, but may be loosely referred to as tapered circular helices

. The method of determining the wind angle for circumferential winding, using tangent vectors is described. The parametric form of Geodesic equation for tapered tubes is presented with its derivations for the first time. The numerical and iterative methods used in Chapter 3.0 are also a first, in a rather limited body of literature.

The author does not presume that such equations have completely escaped the notice of the scientific community but rather that they have never been publicly detailed within the scope of the filament winding industry. As recently as 1999, the U.S. Patents office has awarded patent rights (US

Patent Number 5,935,704 Aug.10 1999) on a filament winding concept that provided only vague descriptions of the turn around provisions and no mathematical description of winding patterns. The term geodesic winding never appears in the patent, only references to helical, hoop and axial patterns. Such references only serve to further obscure critical differences in the wind paths.

The peculiar features of each wind pattern are described in Chapter 4.0 and methods of controlling the thickness, wind angle drift and subsequent consequences to the material properties are discussed in Chapter 5.0, with examples of numerical solutions.

Chapter 6.0 is devoted to the issue of tooling. The mandrel design and construction details are presented, as is the algorithm for designing a geodesic dome end for stable winding direction reversal. The basic algorithm has been described previously for use with pressure vessels; however this is first presentation for use with tapered structures requiring unequal dome geometries for small and large ends. The absence of these practical considerations would leave the tapered tube designer with a strictly academic design, without the ability to fabricate the required structures. A short section on self-extracting mandrels permits the removal of poles from these new mandrels.

Chapters 2.0 through 6.0 take the reader from mathematical fundamentals through to practical design tools which include all the required algorithms and tooling concepts required to construct filament wound, tapered tubes.

Since the thesis topic is the design and fabrication of filament wound tubes, it is proper to describe the salient features of the technology and theory which affect the manner in which the designer of such tubes will be obliged to operate. It would be difficult, if not impossible, to describe the design process without discussion of the reasons why the design proceeds in a specific manner.

In Chapter 7.0, the analytical processes are detailed by which the pole performance can be modelled. Knowing how the winding patterns behave from the earlier chapters, the reader is taken through the process of modelling variable thickness and variable material properties to determine the deflection and stresses in the composite tubes.

The model is based on iterative solutions of the fundamental Bernoulli-Euler Beam Deflection equations, modified to handle variable material properties, and the basic equation for stress. This modelling method permits the analysis of poles for ranges of properties such as thickness and stiffness.

The Chapter 7.0 hypothetical poles also corroborate the variable material property issue through modeling and verify the variable thickness issue. An example of the use of the Classical lamination theory to determine the material property, Effective Axial Modulus, is detailed.

In Chapter 8.0, coupon fabrication and testing results are discussed. This section presents details of the fabrication methods and of material properties of test coupons from testing data. The experimental program for single segment poles is examined using two distinctly different sets of large scale poles. Modeling pole deflection using the solutions for the Bernoulli-Euler equations of curvature is evaluated by comparison to experimental data.

The modelling permits the examination of variable Young's moduli, and thickness along the length of the pole.

In Chapter 9.0, jointed poles are examined for load versus deflection behaviour. The computer programs used in Chapter 8.0 for deflection modeling curves are modified to perform analysis for two segments of a jointed pole each with different material properties. Chapter 9.0 concludes the experimental component of the thesis.

In Chapter 10.0 the design problem is resolved. In preceding chapters the techniques of analysis are sufficient to rationalize any existing pole structure. To facilitate the designing of a new pole to meet a specific load capacity and deflection limit a new approach is required. This chapter describes how the various analysis tools are linked within a single program to permit the designer to engineer a laminate structure to meet performance criteria based on load and deflection limits. The concepts of Chapter 10.0 permit a designer to quickly evaluate a pole design, for load capacity at a deflection limit, in terms of thickness for axial and circumferential lamina as well as winding angles. Actual winding machine input variables have as yet not been directly incorporated into the code.

While it is recommended that the material properties be determined prior to analysis and design of poles, this was not possible for this project. Typically many unstated assumptions from traditional isotropic materials fabrication were subtly embedded in the original project design and were often identified only after problems were encountered. As an example the initial project concept was totally unaware of the variable material properties issue. Though some appreciation of the thickness issue was self evident from

geometry of the tapered mandrels, no anticipation of the complexity of wind angle drift effects was possible in the early stages, as they were unknown.

Part of the problem was no doubt the limited literature, which was further biased toward pressure vessels and constant diameter structures that do not possess variable property characteristics encountered with the tapered structures.

The theoretical issues of winding must be explored prior to discussion on the practical engineering problems of path reversal, and path stability. These issues must be incorporated into the design of the mandrel which is often treated as if it were trivial problem, but from experience we now recognize the mandrel to be the most critical issue requiring resolution before production can proceed.

Unfortunately the mandrel issues and tube issues tend to be avoided in academic discussions but are inextricably related from a design perspective. Failure to recognize this relationship has serious repercussions, making it virtually impossible to fabricate poles or any other structures. Mandrels and their design features are discussed in limited detail in Chapter 6.0.

It is one of the purposes of this thesis to impress the reader with the complexity of the design issue. Before one can fabricate any structure the wind path types must be validated as feasible with respect to the proposed geometry. This may only be possible using numerical methods. The mandrel must be capable of supporting the production piece and permit easy removal. The mandrel must provide a means for wind paths to reverse direction, due to the continuous nature of filament roving. One method is required for Geodesic winding and another distinct method for Circumferential winding. The winding

machine has no means to interpret wind path equations, feasible or otherwise rather the robotics rely on fibre tow end position data, which is calculated from the derivatives of the fibre path. The robot interprets the payout eye position data tables of Cartesian coordinates. As such it would be insufficient to describe the wind path without the methods of developing the machine motion data required to drive the production process. It is also required to examine the feasibility of the machine motion in order to avoid contact of the pay out eye with the mandrel and other fixed points.

Once feasible paths have been determined the product thickness must be determined from modelling studies. The thickness is set as a unique, one dimensional, variable for a pole in the design process, but no such input variable is possible in the robotics, and rather it must be implemented in the program of the robot by controlling the variables, of number of fibre tows and circuits within the pattern. If a designer wishes to control thickness, it must be possible for him to implement such a desire in a feasible manner. The thesis assumes that the designer is not interested in theoretical structures and as such requires a somewhat more involved discussion.

It should be pointed out to the reader that at the time of writing, the author has used this material in six distinctly different projects. Three of these auxiliary projects have been of a, limited, commercial nature. As such all have been tested for feasibility in production. Two distinctly different winding machines have at this time used various components of the algorithms and while much refinement is still required the principles have all been tested.

It is hoped that the reader will realize that it was the author's intent to integrate the entire performance design process with the programming and production processes.

Many of the algorithms at present are not linked and as such there are many points in the process requiring knowledgeable input to go from one algorithm to another.

1.3 BASIC PRINCIPLES OF FILAMENT WINDING

The basic concept of filament winding is to cover a surface with a continuous strand of fibre. Wrapping a rope around a shaft such that the fibre or rope path never crosses itself yet totally closes the shaft surface is an elementary example (Figure 1.1). If the rope were impregnated with a polymer resin, then in effect the rope will be stabilized in this configuration producing a tube with inside diameter determined by the shaft outside diameter and wall thickness determined by the rope cross-sectional diameter

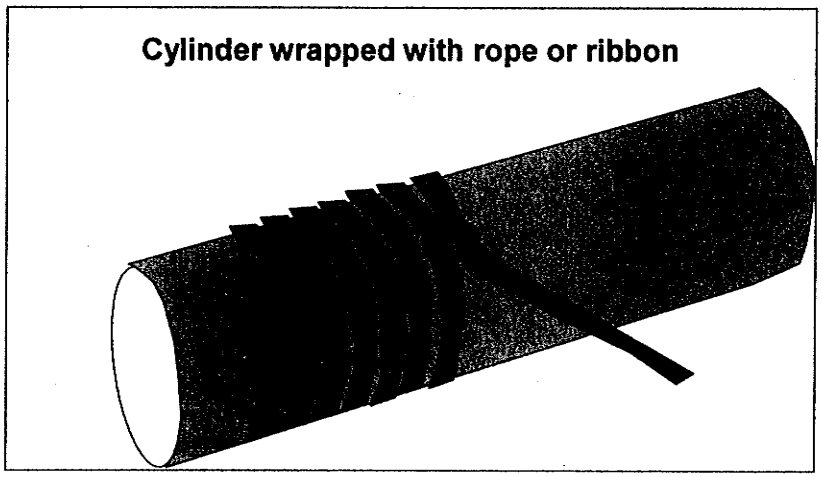

Figure 1.1: Simple Filament Winding

Industrial filament winding is indeed more complex than just described. The principal reason is that the circumferential winding as just described is structurally undesirable for many applications. Ideally structural fibres are placed in line with principal loads. The most desirable angle for tube winding might be somewhat lower than 90 ° with respect to the shaft, or mandrel meridian (the line connecting pole to pole over the surface).

The fibre can in effect be pulled at any angle between 0 ° and 90 ° between the poles if tension is applied to the fibre. The path that the fibre takes is referred to as the geodesic, at any point the angle that the fibre tangent makes with the meridian is,

$$\sin^{-1}\left(\frac{C}{r}\right), \qquad \textbf{(Eq.1.1)}$$

where r is radius and C is the Constant of Clairaut, unique to the wind path. In this configuration the fibre is stable on the surface and will not slip (Figure 1.2).

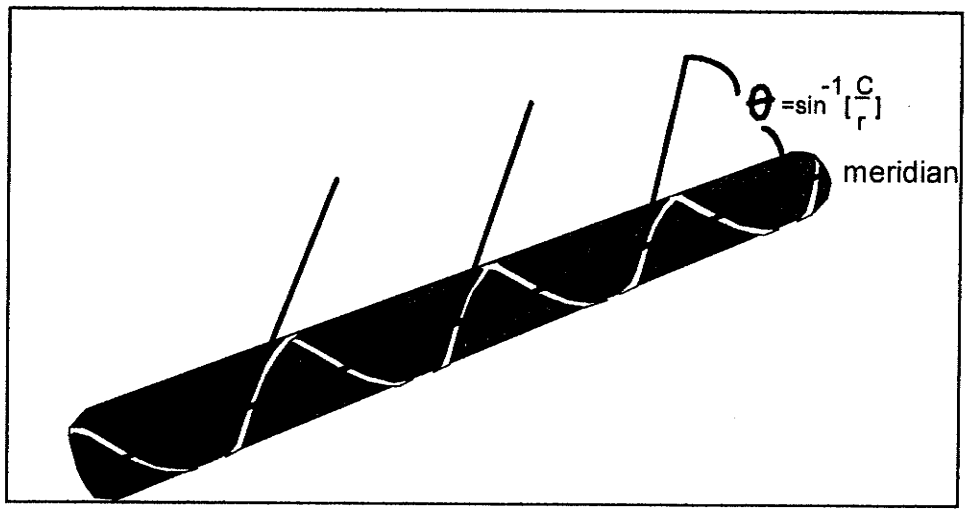

Figure 1.2: Stable winding using Clairaut's Constant

Knowing then the stable fibre path at a desired angle relative to the meridian, one can begin to think of covering the entire surface of the cylinder. At 0 ° ,

$$\#\_of\_circuits = circumference/(Band\_Width) \quad \text{(Eq.1.2)}$$

At other angles than 0^0 , the effective Band Width must be taken into consideration, so that,

$$\#\_of\_circuits = circumference\_/(BandWidth/\sin(90-\theta)) \quad \text{(Eq.1.3)}$$

Since a circuit is composed of a forward and reverse direction, there are effectively two distinct paths to each circuit.

Typically once the fibre traverses the length of the mandrel on the forward path it must be returned to the start position, without stopping the mandrel rotation, this is the return circuit and it is simply the inverse of the initial path. The point of inflection or path reversal occurs at a radius equal to Clairaut's Constant. This yields a positive and negative angle with the meridian. This is a single circuit. Rotation of the cylindrical coordinates as previously described will close the surface; however the result is not a single layer but two distinct layers that are interwoven. The complexity of the interweaving is a function of the circuit increment angle. A wide variety of patterns result in spite of the simplicity of the basic single circuit path.

The subtle problem not described previously is, "What prevents the fibre from simply being unwound on the return stroke of the circuit?" Many techniques are presently utilized but simply put if the fibre passes around the support shaft or the end of the mandrel some variable number of degrees it

will be stable on the return path. Otherwise it will simply slip and destroy any potential closure.

Problems become complex quickly when mandrels are not strictly constant diameter cylinders. Problems become more serious when one considers not simply the mathematics of the path but include the physical envelope of the machinery. Typically the payout eye maintains the roving at a vector tangent to the fibre path and mandrel surface under tension (Figure 1.3). The lower the winding angle the more difficult it becomes to maintain clearance between the mandrel and payout eye (the tangent is closer to the surface).

Once a stable fibre path has been determined, the path is discretized and the tangent vectors determined to find the position of the payout eye in space relative to the mandrel surface. Translation of these positions to a motion control program can be a daunting task once performed manually, now with computers.

The building of a structure may require repetition of the same program or many others based on a variety of angles to optimize structural and material performance.

Modern proprietary software can often be used with the simpler geometries encountered during the construction of cylinders, making the task of programming machine motion quite straight forward. However if more complex structures are desired, considerable investment is required in programming minute details of machine motion to avoid collisions , derive smooth and continuous motions and avoid fibre slippage. Compounding the issue further is the fact that as the part is being wound, the surface is no

longer the same as the original mandrel. This requires that fibre paths be altered slightly for expanding base dimensions.

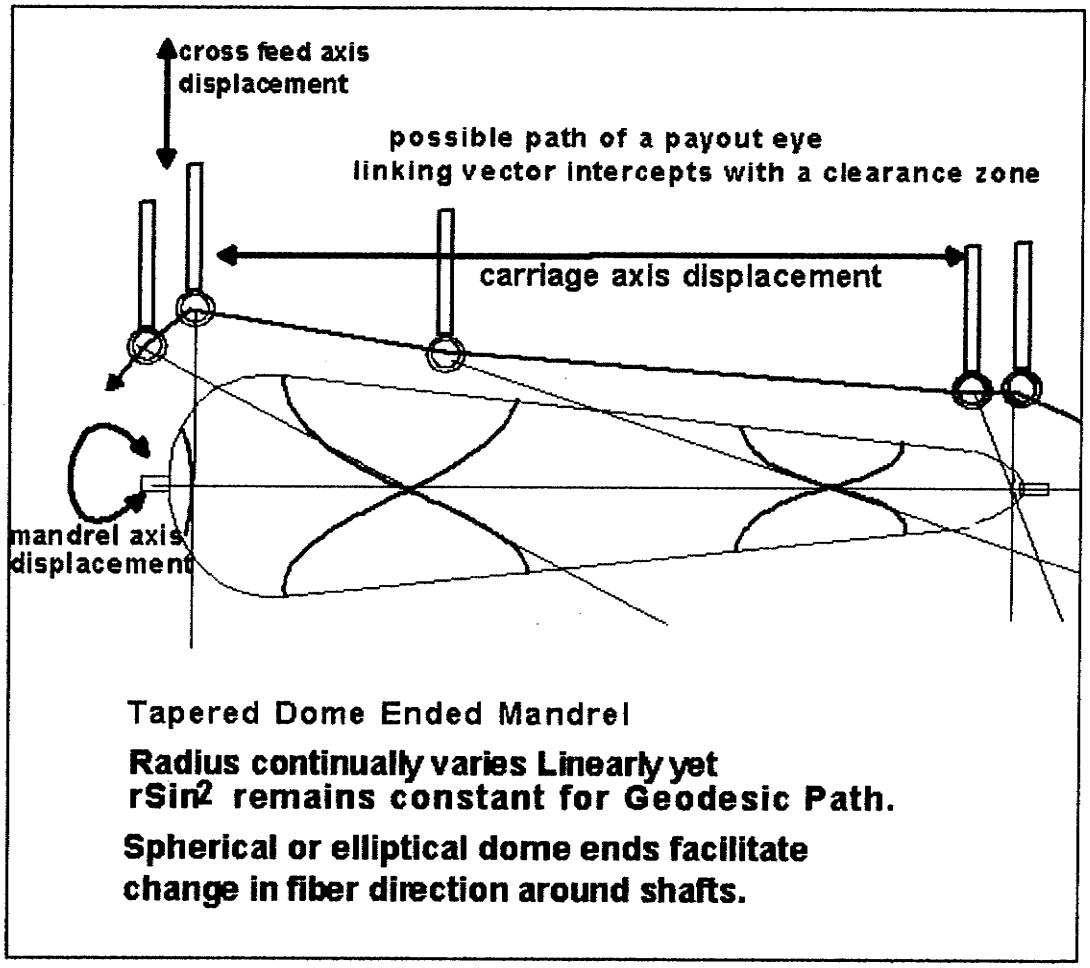

Figure 1.3 Winding Machine Basics

High speed computer controlled filament winding machines are capable of producing composite structures inexpensively and quickly without sacrificing precision or quality. At low angle winds material can be deployed over the mould or mandrel surface at rates of 100 lbs per hour and at high angle winds as much as 400lbs per hour (Peters, et.al,1991). Speeds vary greatly depending on fibre type and resin wet out systems. Often unrelated factors control the speed of deployment. In some complex systems the roving

is passing through restriction eyelets at such high speeds that sizing can begin to char and fuse due to the heat of friction. In open resin bath impregnation systems, resin viscosity if too low can cause sloshing during high accelerations. Further resin can be physically pulled out of the resin bath by the exiting fibre. Nevertheless, large structures are regularly made in minutes and hours by winding versus days and weeks by more conventional techniques. The materials are primary bulk commodities having the lowest production costs.

A typical filament winder is a large lathe like machine. A mandrel is rotated as if it were a work piece, a payout eye analogous to a tool support is mounted on a cross feed arm and that on a carriage. This allows the payout eye to be positioned at some distance from the mandrel, deploying resin impregnated fibre over a surface of a mandrel, as precisely as cutting threads into a piece of round stock. A typical three axes winder has a mandrel axis, carriage axis and a cross feed axis. More complex machines may have additional axes for payout eye rotation, yaw and elevation. The more complex the mandrel surface geometry the more control over fibre placement that is required.

Fibre is characterized by type i.e. glass, Kevlar, Carbon, weight or TEX grams of a roving strand per 1,000 metres of length. A fibre band width is a function of the number of roving strands being deployed and the TEX of the fibre. Typically a five line band of 1,110 TEX glass roving will have a band width dry of .5 inches. Wet-out this is reduced to an average of .38" . Band width is subject to inconsistencies in the manufactured product. Glass fibre is typically supplied in 50lb bales of continuous roving. The bales can either be

mounted on the carriage aligned with the resin impregnation bath or separately in a stationary or mobile bale rack. Access to bales is required for replacement during winding and repair of broken lines. Carriages travelling at or near 250 feet per minute can develop severe problems accelerating large weights of fibre, so often the choice is made not to transport bales. Resin is loaded into baths in batches, the size determined by required open time or the size of the part. Rarely is the resin continuously supplied to the moving resin bath. Between the resin bath and the mandrel are numerous control structures to strip excess resin, guide fibres, and basically control the band width of the multiple rovings.

Fibre deployment can be measured in many ways but one important method is the line speed which is a function of mandrel circumference and rotation rate. For instance a 24" diameter mandrel rotating at 250 rpm would be pulling fibre through a resin bath at 1570 feet per minute.

Typically a pultrusion machine is pulling fibre at 36" per minute (pers. Comm. Ralph Daigneault , Faroex Ltd.). Such high rates are not normally desirable since fibre may break, burn and fail to wet out properly. Choosing the correct resin viscosity can allow for faster rates. Other limitations may also be encountered such as roving vibration, throwing resin into the air much like a dog shaking itself dry.

1.4 WIND PATH TYPES

Three basic types of winding patterns are typically discussed in context with industrial winding. The pressure vessel industry typically utilizes the Geodesic wind paths primarily for stability and the ability to get low wind

angles (Figure 1.4) Since the industry typically uses mandrels with constant diameter , symmetric dome ended mandrels are employed (Figure 1.2 and 1.4).

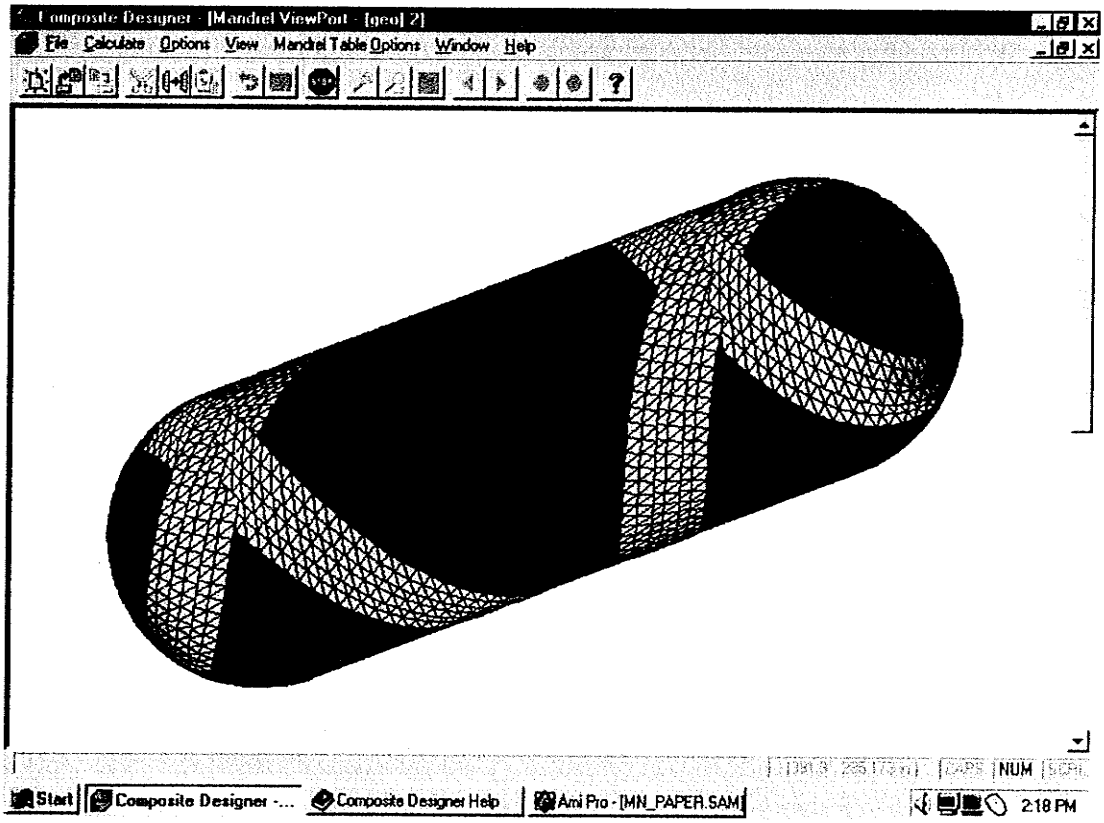

Figure 1.4: Geodesic Winding of Pressure Vessel, Dome Ended

Planar winding is often discussed in relation to rocket motor cases. This form of winding is described as having the lowest possible wind angles. The path is described as following the intersection of a plane with the surface of the mandrel. The plane is oriented to intercept the opposite sides of the polar openings of a dome . The wind angle is determined as:

$$\tan\theta = \frac{Polar\_Radius}{(Length/2)} \qquad \text{(Eq.1.4)}$$

where the Polar radius is the radius of the aperture of the dome of the mandrel and the length is that of the barrel portion of the mandrel.

The literature often describes techniques to provide ideal geometries for the domes of such mandrels and is typically geodesic in nature. Further the netting analysis methods used in conjunction with such planar analysis assumes path stability identical with geodesic winding methods. As such it may be better to classify planar winding as the extreme limit of geodesic winding on a particular mandrel. This form of winding was not employed during the course of the study. The greatest limitation of this winding method is the low surface normal force directed at the mandrel surface (Figure 1.5). The lack of force permits extremely long wind paths to be affected by gravity and centripetal forces, counteracting any natural stability.

Conventional geodesic paths which pass through several degrees of mandrel rotation can exploit the mandrel surface curvature for higher surface normal forces and thus are significantly more stable.

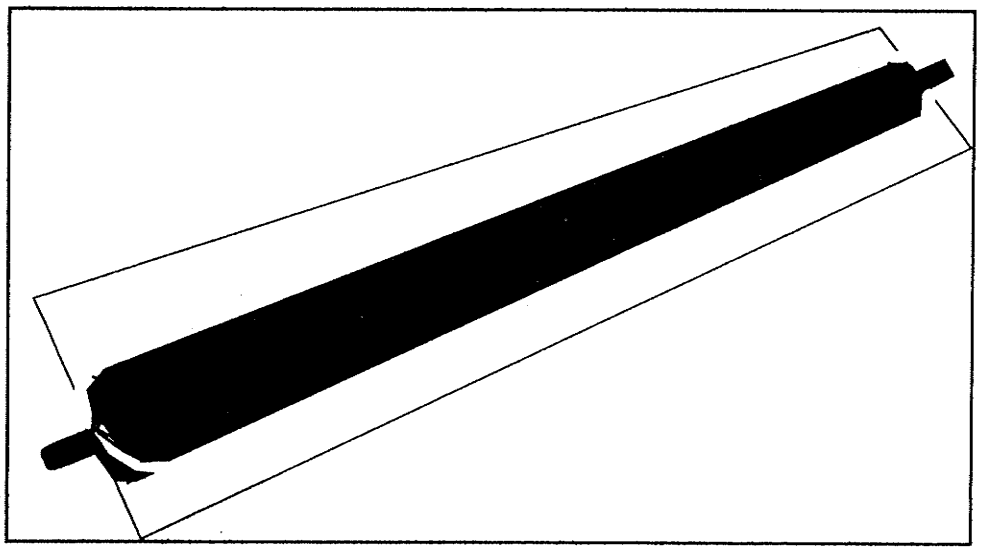

Figure 1.5: Planar Winding

Circumferential Winding is fundamental to the pressure vessel industry since this winding provides hoop fibres for resisting internal pressures (Figure 1.1). This pattern may also be employed to provide layers of particular thickness for use as protection against chemical corrosion. Other uses include confinement of underlying layers and protection against external damage. In principle it appears to be the simplest of all winding patterns. It is easily modelled on constant diameter mandrels with equations based on the circular helix, and requires the simplest of all turn around provisions. The technique is so widely used that it is often thought of first when winding is discussed. It is the commonest technique used industrially, most often in spooling materials from the packaging industry.

The last of the more common forms of winding appears to be the non-linear winding method (Figure 1.6) . This is a particularly complex form of winding though relatively easy to implement with numerically controlled winders.

In fundamental terms it starts out as a circumferential wind pattern. After some predetermined period it begins drifting to a lower wind angle, progresses at that value for some distance then drifts back up to a true circumferential wind. This marks the end of the first part of a stroke. During the period of time at the end of a stroke the mandrel rotates a small amount to set the pattern advance and the reverse stroke begins. The point of the dwell phase is to permit the low angle portions of the wind path to be placed next to each other permitting closure after repetition of the correct number of strokes.

The central region of the wound structure can have relatively uniform

material properties but the slip or drift zones will have significant build up of thickness and highly variable wind angles. The chief recommendation for this form of winding is the simple mandrel requirements. No turn around provisions is required and often this form of winding is used for over wrapping of a primary structure. Unfortunately if the central portion of the wind is the primary focus, this method entails the use of very long mandrels with tremendous waste material.

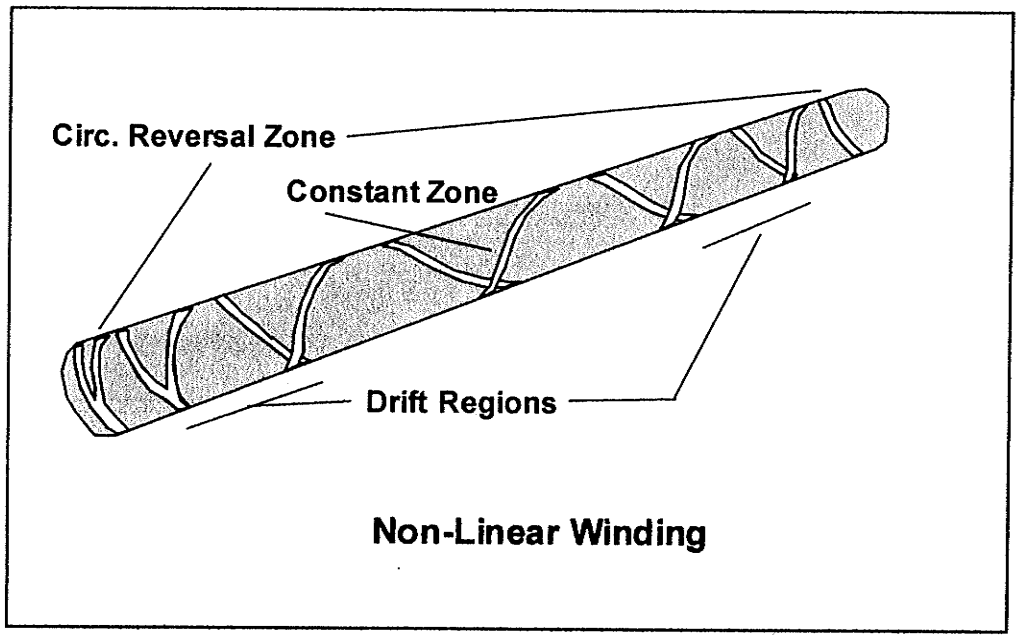

Figure 1.6: Non-linear Winding

2 WINDING THEORY

2.1 WIND PATH SOLVERS AND MACHINE MOTION

A Beta version of software developed by R.Anderson of McClean Anderson called, ***Composite Designer*** and a machine motion generation program called ***OmniWind*** were used during the initial stagesof the project. The first program was used extensively during the preliminary stages of the project and prior to the installation of the machinery. The software performed as intended, which was to provide a machine operator with a simple method of solving the wind paths over basic mandrel surfaces and to provide motion control programs for the robotics. No fault was ever detected at its intended tasks.

However, the original software was only intended to handle dome ended turn around for constant diameter mandrels. It was not designed to use geodesic paths over manually input tapered mandrels. Non-linear slip winding was assumed to take precedence, and over ride user input. The software was not designed to provide Cartesian coordinates for solved paths, but rather to output relative motion velocity tables for each of the three axes. Furthermore it was not designed to provide, user accessible Cartesian coordinates for the machine axes. It was, thus not possible to relate wind paths either to structural properties nor to thickness of the laminate. The software had many built in defaults based on typical industry requirements and the fact that output was directly coupled to a machine specific motion control card, left the designer with little control.

As a consequence, it was decided to develop parallel programs to illuminate the parameters required for full understanding of the selected wind paths. The software developed for the project used the same input parameters as that supplied by McClean Anderson. During the course of the mandrel design phase, portions of the in house code were used to solve for dome geometry and support shafts and these values were input into the McClean Anderson program.

In effect this new code matured from completely parallel to becoming the primary input and output. Subsequent to the large pole program, the in house software began to be used extensively to determine the basic thickness and material parameters for other projects and provide the basic FEM data. Once this phase was accomplished the values would again be used as input to the proprietary software which would convert the information to machine motion programs. Since the motion control system was integrated with the McClean Anderson software, no method of decoupling their design software from the ***OmniWind***, motion controls was attempted. Rather the in house developed algorithms were used to generate input parameters for use by the original software, and determine the feasible design parameters for construction of the mandrels and end domes.

2.2 CICUMFERENTIAL WIND PATHS

The circumferential wind path or hoop winding is a very commonly used wind path type. It is an easily implemented wind path for the purposes of compaction and surface protection. In some cases, the resin system can be adapted to meet certain specific chemical resistance requirements and initial

layers of circumferential winding will be laid down to provide a barrier of guaranteed thickness. Subsequently, structural helical fibers can be overlaid using the same or different resin systems. Typically a product's internal and external surfaces are circumferentially wound.

Circumferential winding, appears to get little mention in the literature. Gramoll (1993) notes that the treatment of hoop winding as 90^0 to the axis is not valid. He implies that many analysis projects simply assume that all hoop winding is orthogonal. This assumption may have its roots in classical mechanics where this is the case. In practice, the term circumferential winding is a poor one, leading to misinterpretation. It would be better served by examination of its fundamental mathematics.

The basic equation, in parametric form, for all circumferential wind paths, denoted as space curve, Γ, is

$$\Gamma = R\cos t, R\sin t, bt \qquad \textbf{(Eq.2.1)}$$

For a constant radius, R, Equation 2.1 is the classical Circular Helix, where the z-term, ***bt***, is in radians such that 2π equals one revolution. The b term sets the height of the path, and t the number of revolutions over that distance. Setting *bt* equal to the height of the tube, and knowing the number of revolutions desired, one can readily find the value of the b parameter. Unfortunately the designer does not normally consider the wind path in terms of revolutions but rather as a function of the winding angle, θ. To set the winding angle one might simply consider the band advance per revolution. Using, a crude approximation where the wind angle,

$$\theta = \sin^{-1}(L_f/BA.) \qquad \textbf{(Eq.2.2)}$$

With L_f being the length of the inclined path for one revolution and B.A. being the *Band Advance* required for closure of the path. However, the actual winding angle is that described by the meridian or generatrix of the mandrel and the tangent to the space curve, Γ at a given point.

2.3 DETERMINATION OF ACTUAL CIRCUMFERENTIAL WIND ANGLE FOR TAPERED MANDRELS

A slightly more complex method of finding the winding angle, θ, is to find the first derivative of the path .Typically the majority of industrial filament winders use mandrels of constant diameter. In the case of linear tapered mandrels the value of R is defined by a linear equation of the form,

$$R = mz + B \qquad \textbf{(Eq. 2.3)}$$

Where m, is the slope or $\tan\alpha$, α being the Cone angle. The B term is simply the starting radius generally assumed to be the base of the cone, implying that m is typically negative. Therefore the space curve over a tapered mandrel becomes,

$$\Gamma = (mbt + B)\cos t, (mbt + B)\sin t, bt \qquad \textbf{(Eq.2.4)}$$

Converting Equation 2.4, the parametric form, to that of the vector form of a parametric equation, results in

$$r_t = (mbt + B)\cos t\,\mathbf{i} + (mbt + B)\sin t\,\mathbf{j} + bt\,\mathbf{k} \qquad \textbf{(Eq.2.5)}$$

Where r_t is the vector radius from the origin to any point along the path.

The path tangent, r_t' is now presented in vector form as the first derivative of the radius vector with respect to the rotation parameter, *t*, as

$$r_t' = [(mb\cos t) - (mbt + B)\sin t]\mathbf{i} + [(mb\sin t) + (mbt + B)\cos t]\mathbf{j} + b\mathbf{k} \qquad \textbf{(Eq.2.6)}$$

This vector can be regarded as coincident with the unit Tangent vector.

The point, $P_{(t)}$, corresponding to a particular value of t then, in parametric form is,

$$P_{(t)} = ([((mbt) + B)\cos t], [((mbt) + B)\sin t], [bt]) \quad \textbf{(Eq.2.7)}$$

It is now possible to apply the Cosine Law to find the actual winding angle between the tangent and the meridian through point, P.

The tangent line can be put into parametric form as,

$$x = [(mb\cos t) - (mbt + B)\sin t]T + [(mbt + B)\cos t] \quad \textbf{(Eq.2.8)}$$

$$y = [(mb\sin t) + (mbt + B)\cos t]T + [(mbt + B)\sin t], \quad \textbf{(Eq.2.9)}$$

$$z = bt + bT \quad \textbf{(Eq.2.10)}$$

With the T parameter being introduced to facilitate plotting. In order to plot this line as a vector using a program such as **Maple V,** T is set to have a range of value from 0 to 1.

Having determined the parametric equation of the tangent line at a point, it remains to determine the parametric equation of the meridian line through the same point. The following form may be used to divide up the entire tapered mandrel surface into a ruled pattern of meridians.

$$x = (mbt + B)\cos\left(\frac{n}{n_{\max}} \times 2\pi\right) \quad \textbf{(Eq. 2.11)}$$

$$y = (mbt + B)\sin\left(\frac{n}{n_{\max}} \times 2\pi\right) \quad \textbf{(Eq. 2.12)}$$

$$z = bt \quad \textbf{(Eq. 2.13)}$$

Where, $n_{\max}$ is the total number of meridians desired and n is 1 to $n_{\max}$. Alternatively, for a meridian through a specific point, the angle in x and y

terms is set to correspond to the value of t, at the specific location. It should be noted that t is in radians and it is simply the angular rotation of the path.

To determine the actual winding angle, θ , the angle between the vectors of the meridian and the tangent to the wind path , the Cosine law is used. By taking Equations 2.11, 2.12, and 2.13 and adding to it the point on the meridian, one finds the tangent vector end point. For the dot product we require parametric vector notation for the two actual line segments. Thus, the tangent vector notation required is that of Eq.2.6 which is then solved explicitly for the point on the meridian, and is in the form of a unit vector, with the subscript indicating the tangent vector components

$$r_t' = \langle x_t \mathbf{i} + y_t \mathbf{j} + z_t \mathbf{k} \rangle \qquad \textbf{(Eq. 2.14)}$$

Introducing the scalar parameter t_v =0 to 1 or any arbitrary value , which will be shown later to represent the physical quantity known as the tow length, the correct vector form of the tangent to the wind path at point P corresponding to t revolutions is obtained as follows,

$$a = < x_t t_v + P_1,\ y_t t_v + P_2,\ z_t t_v + P_3 > \qquad \textbf{(Eq. 2.15)}$$

The point P is composed of three terms P_1, P_2 and P_3 corresponding to the parametric terms given in Eq. 2.7. In a similar fashion the unit vector form of the meridian (*with components denoted by the subscript m*) through the same point is determined, so that

$$b = < x_m t_v + P_1, y_m t_v + P_2, z_m t_v + P_3 > . \qquad \textbf{(Eq. 2.16)}$$

Accordingly the Cosine of the wind angle, θ, which is the vector dot product of the meridian and tangents is divided by the product of the absolute lengths of the two vectors,

$$\cos\theta = \frac{a \bullet b}{|a||b|} \qquad \text{(Eq. 2.17)}$$

The actual winding angle at any given point can now be determined. Later, this process can be applied equally well to Geodesic winding to derive the wind angles or to determine the appropriate tow length, the scalar parameter t_v, at each point along the path. It should be pointed out that the end point of the tow length also defines the position of the pay out eye of the filament winding machine. The filament winding machine does not rely directly on any of the wind path coordinates.

The actual inputs to motion control are the parameters relevant to the principal axes, rotation, and carriage advance and cross feed position (Figure 1.4). The last two parameters are determined by mapping the tangent end point against mandrel rotation. The process may seem cumbersome, but the entire wind path solution is used simply to determine the motion parameters required by the filament winder.

In determining the best wind path, it is important to consider the concept of fiber slip. A fiber wrapped about a cylinder is not always stable. Under the influence of tension one can readily see a loosely wound filament would slide to a more stable position. Technically, a circumferential wind path, based on the circular helix equation, on a constant diameter cylinder, will be stable under the influence of tangential tension. The tension applied to the filament at the wind path tangent vector end point results in a force, normal to the surface and directed into the surface. This vector is perpendicular to the tangent vector and lies in the osculating plane defined by the tangent and the derivative of the tangent with respect to parameter t On a constant diameter mandrel, the path normal, N, and the vector normal to the surface, $\mathbf{n_s}$, are

coincident. If, however, the two vectors emanating from the path point, P, are not identical but rather divergent then a new vector, **b**, the geodesic curvature vector is created. This is the cross product vector of the path normal and the normal to the surface, N **x** $\mathbf{n_s}$ and it represents the physical slip force affecting the fiber. The stability of the fiber can be imagined to be determined by the frictional forces between the fiber and mandrel and the magnitude of the slip force.

The path Normal with respect to t, is found by treating the first derivative of the parametric equation of the circumferential wind path as the velocity vector V,

$$r'(t) = v\mathrm{T}(t) = V \qquad \textbf{(Eq.2.18)}$$

where T(t) is the unit Tangent vector

$$\mathrm{T}(t) = \frac{1}{|r'(t)|} \times |r'(t)| = \mathrm{T}(s) \qquad \textbf{(Eq.2.19)}$$

$$v = \sqrt{V \bullet V} = \sqrt{\left(\frac{dx}{dt}\right)^2 + \left(\frac{dy}{dt}\right)^2 + \left(\frac{dz}{dt}\right)^2} = \frac{ds}{dt} \qquad \textbf{(Eq.2.20)}$$

and v is typically interpreted as the speed or the change of arc length with respect to time. However, the parameter t in our case is rotation. The principal unit normal vector, N(t) is found by differentiating T with respect to t and normalizing the vector length to one.

$$\mathrm{N}(t) = \frac{1}{|\mathrm{T}'(t)|}\mathrm{T}'(t) \qquad \textbf{(Eq. 2.21)}$$

According to D.J. Struik (1988), the plane determined by the perpendicular vectors T and N is called the osculating plane. The osculating circle is defined as the circle passing through three consecutive points, intersecting the

Tangent at point, P, along the curve. The circle lies within the osculating plane, the centre then lies along the principal normal at a distance R from P. Quoting Struik (1988),"*Though R=k $^{-1}$ may be positive or negative, the vector Rn is independent of the sense of n, having the sense of the curvature vector. Its end point is also called the centre of curvature" (n is defined as the principal normal)*

It is also possible to evaluate the principal unit Normal using the arc length, s as the parameter.

The binormal, B is defined as the cross product of the Tangent and the Normal, $\mathbf{B} = \mathbf{N} \times \mathbf{T}$

Thus,

$$\mathrm{N} \times \mathrm{T} = \begin{bmatrix} \mathrm{i} & \mathrm{j} & \mathrm{k} \\ \mathrm{N}_1 & \mathrm{N}_2 & \mathrm{N}_3 \\ \mathrm{T}_1 & \mathrm{T}_2 & \mathrm{T}_3 \end{bmatrix}$$

with the determinant being,

$$(\mathbf{N}_2\mathbf{T}_3 - \mathbf{N}_3\mathbf{T}_2)\mathrm{i} + (\mathbf{N}_3\mathbf{T}_1 - \mathbf{N}_1\mathbf{T}_3)\mathrm{j} + (\mathbf{N}_1\mathbf{T}_2 - \mathbf{N}_2\mathbf{T}_1)\mathrm{k} = \mathbf{B} \qquad \textbf{(Eq. 2.22)}$$

The binormal can be set up to have the correct orientation. This may require reversing the direction of the inward pointing unit normal so it is pointing outward. The vector form of the Binormal,

$$\mathbf{B} = \langle \mathrm{i}t_v + P_1,\ \mathrm{j}t_v + P_2,\ \mathrm{k}t_v + P_3 \rangle \qquad \textbf{(Eq.2.23)}$$

defines the vector endpoint for purposes of graphical plotting.

The term, t_v, is used to set the effective band width, or magnitude of the vector. The vectors **T, N, and** B make up the trihedral of a space curve at a point.

The moving trihedral of various circumferential wind paths can be seen in Figure 2.1 to 2.4. The lifting of the Binormal can be seen in Figures 2.3 as the path approaches the small end of a long tapered mandrel. Note also that the effective wind angle has changed significantly and the band can be seen to overlap significantly. Such conditions are problematic and create some difficulty in modeling for FEM analysis. Typically these problems can be avoided or their effects lessened by reducing the band width, which effectively raises the wind angle and brings the binormal closer to the mandrel surface. In Figures 2.2 and 2.3 a 3.5" band width is compared to a 7.0" band width.

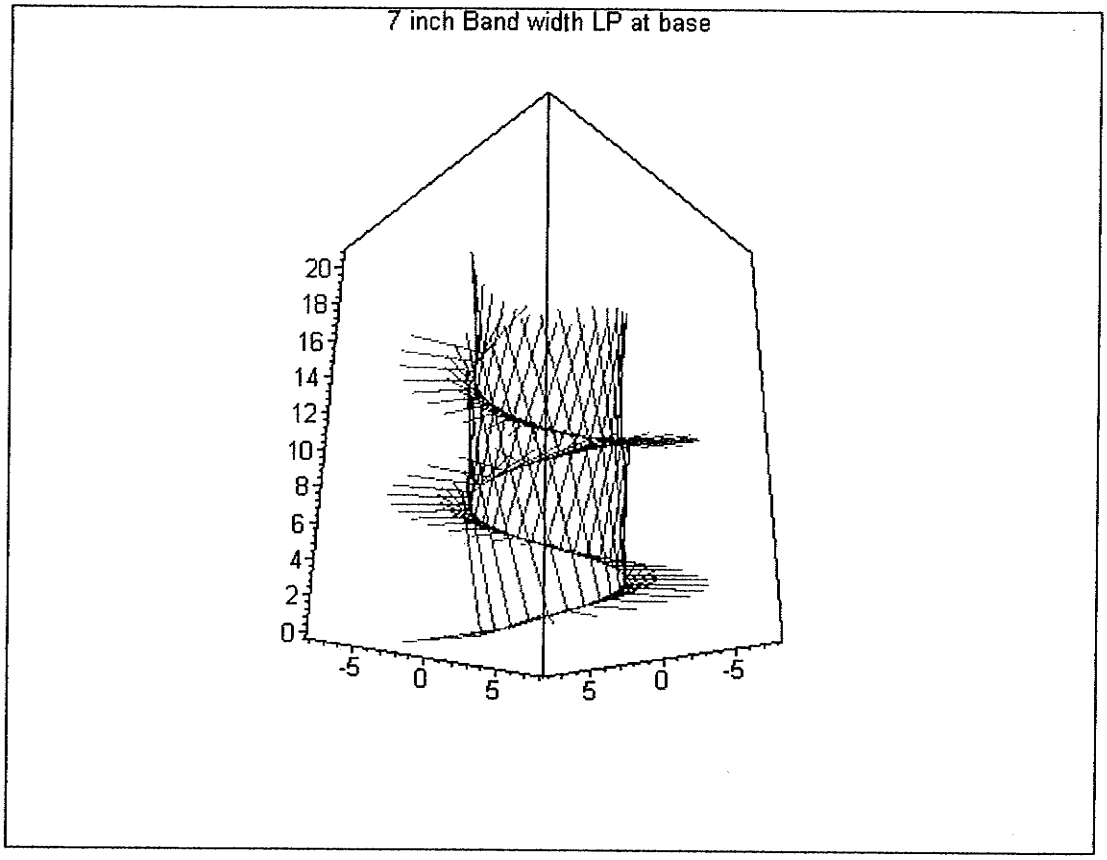

Figure 2.1: Circumferential Wind Path, 7" Band width on the Long Pole Mandrel

The 7" band requires half the number of mandrel rotations as the 3.5". 53.145 versus 106.3 revs., for the mandrel presented. The carriage velocity is equally affected in direct correspondence if the mandrel angular velocity is treated as the independent variable. 7" advance per revolution for 7" band and compared to 3.5" advance per revolution for the 3.5" band. Alterations to these velocities will result in different wind paths that either result in a gap, (if the mandrel rotates too fast) or in an overlap (if the mandrel rotates too slow). To vary the carriage speed as it begins motion or comes to the end of a stroke, one must also reduce the mandrel angular velocity, in order to maintain correct placement. To reverse direction the carriage velocity must be brought to zero,

thereby creating overlap for a short distance depending on the degree of coupling with mandrel rotation. The carriage rate must be kept fixed. A very slight change in advance rate results in detectable gapping of the bands, as shown in Figure 2.6.

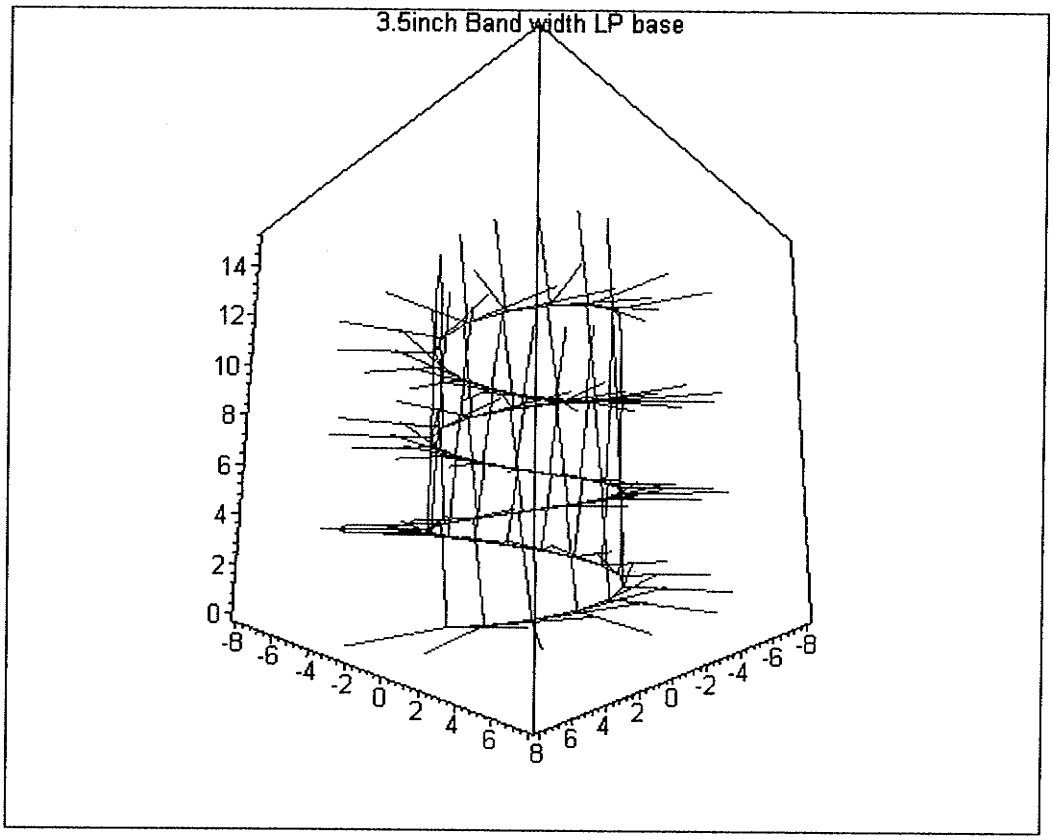

Figure 2.2: Circumferential Wind Path, 3.5" Band Width on the Long Pole Mandrel

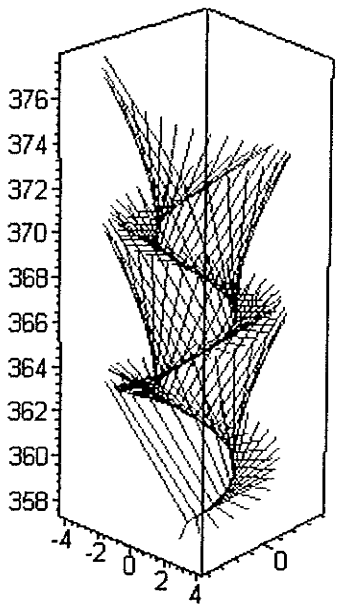

Figure 2.3: Circumferential Wind Path, .7" Band width on the Long Pole Mandrel, showing Overlap and Lifting of the Binormal Vector

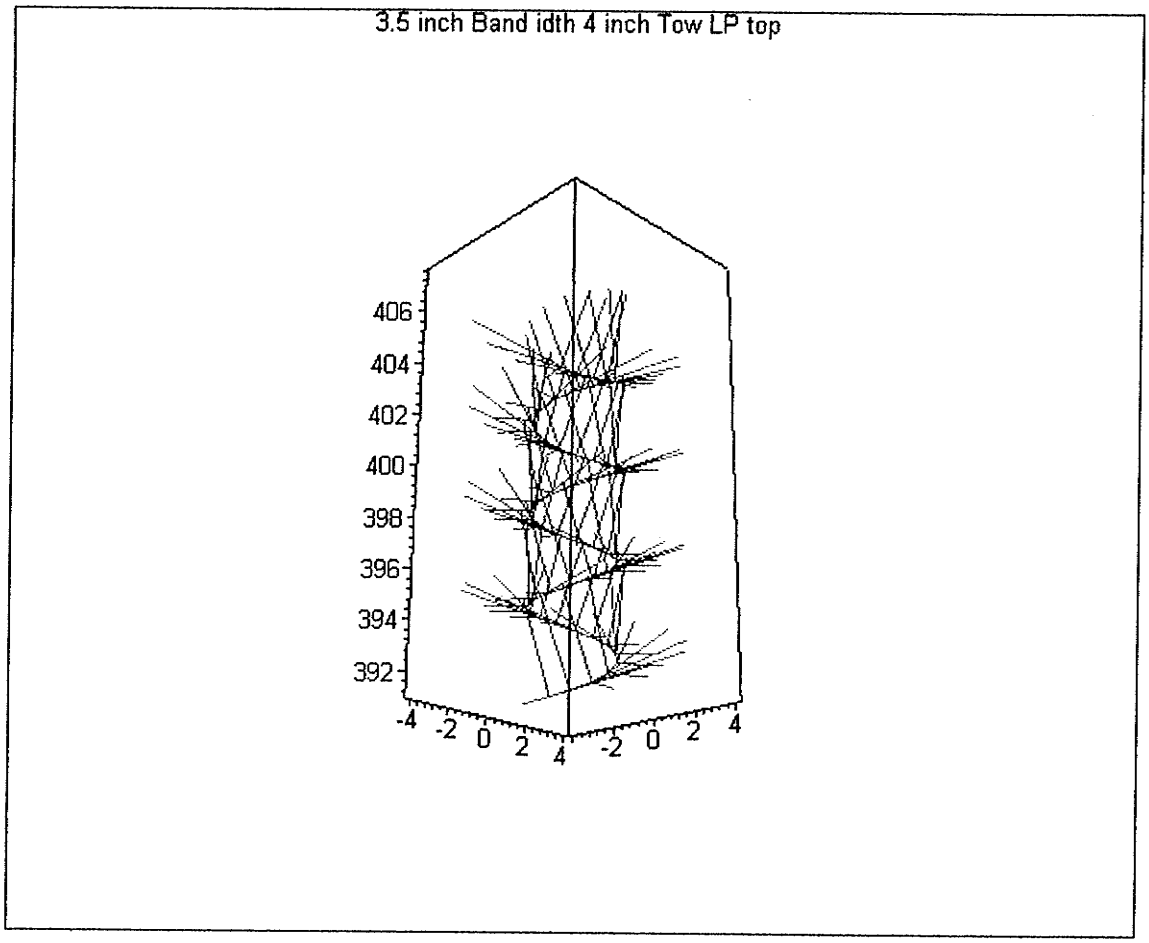

Figure 2.4: Circumferential Winding, 3.5" Bandwidth and no Gapping

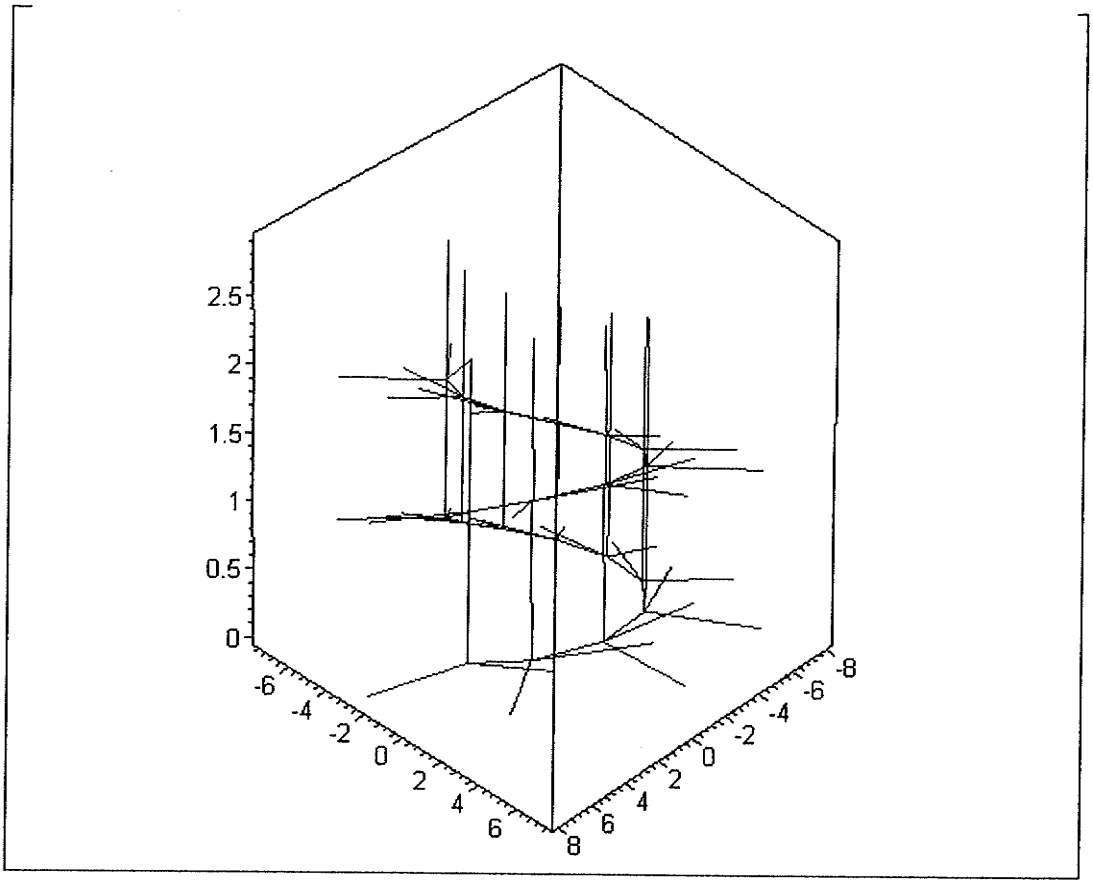

Figure 2.5: Circumferential Path @88.72^0 with no Gapping

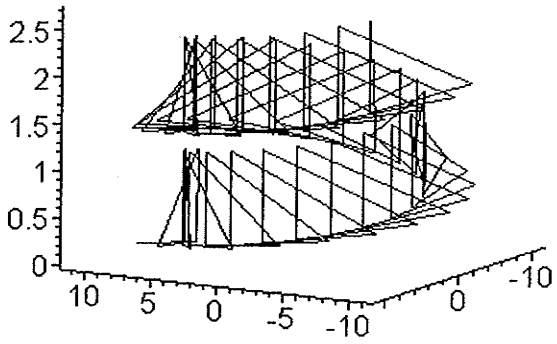

Figure 2.6 Circumferential Path @88.63^0 with Gapping

In Figure 2.7, the angle between the vectors **n** and $\mathbf{n_s}$, ψ, is used to define the slip ratio as

$$k = |\tan\psi| \qquad \textbf{(Eq. 2.24)}$$

When k =0, perfect stability of the filament is guaranteed and as such is the defining characteristic of geodesic space curves.

The second derivative of the circumferential wind path in vector form,

$$r''_{(t)} = \left[-2mb\sin t - (mbt + B)\cos t\right]\mathbf{i} + \left[2mb\cos t - (mbt + B)\sin t\right]\mathbf{j} + [0]\mathbf{k}$$

(Eq. 2.25)

Clearly the z component is now a constant zero value. This then demonstrates that the vector normal to the circumferential wind path is intrinsically unable to line up with the surface normal vector n_S. The surface

Normal n_s is simply the perpendicular to the meridian or generatrix of the conical surface of revolution and readily determined.

Then by simple methods one can deduce that the slip factor k will inevitably be equal to α the cone angle.

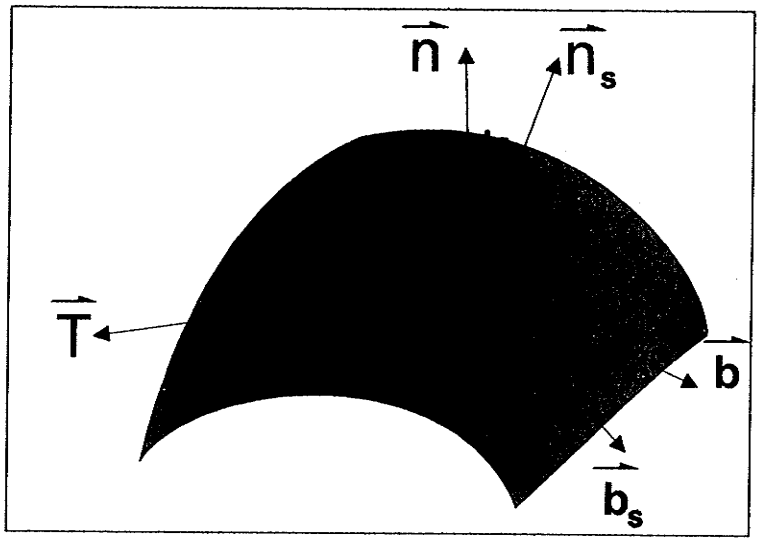

Figure 2.7The Moving Mandrel Trihedral of Path Vectors

The principal normal, N(t) to the curve is not coincident with the surface normal, n_s (normal to the meridian). The dot product of the two normals, the slip vector magnitude, clearly is not zero, and therefore is not capable of maintaining position under the influence of tension for circumferential winding on tapers. However in practice a friction component exists that permits some stability even with non zero slip factors.

Using the basic equations presented here, a simple spread sheet was developed which was used to iterate through a tapered mandrel in step wise increments, to determine the actual wind angles. The purpose of this exercise was to determine whether or not the wind angle was constant and furthermore to understand the nature of the laminate thickness properties.

The nature of the circumferential wind path on a given mandrel and the consequences of manipulating the wind angle were examined in Figure 2.1 to Figure 2.3. The rotation parameter is manipulated and the wind angle is determined and presented as feed back. (*The term **Mandrel LP** is used in many of the examples presented in this study and is the short form for a 31' (372") long Light Pole mandrel, tapered from an 8" diameter down to a 3.5" diameter.*). The meridian, and the tangent vector coordinates are plotted as space curves point by point, using the mathematics program, MAPLE V. In Figure 2.5, the 1" band is inferred by the equal length vertical Binormal vector lines and no gap is detectable at 88.72^0. In Figure 2.6 gaps between the 1" band are just barely visible at 88.63^0 indicating incomplete coverage of the mandrel. This graphical representation permits the designer to modify the wind angle to close the gap.

One present short coming of the process as employed here is that the iterative routine and the graphical routines are in separate programs and require a slightly complex procedure to fully integrate. Ideally the algorithms for path solution and graphics would be simultaneously viewed.

In order to obtain hoop windings as near to 90^0 as possible the band width will have to be minimized. Unfortunately this will increase the winding time required to complete a layer. In cases where very large width tows are to be employed the physical limitations of the payout system may be such to limit the tow width to a smaller size.

In such a case it is possible to establish a second or multiple start position system composed of smaller tows, that collectively yields a double

sized band width. A demonstration of the double headed winding technique is presented in Figure 2.8. This technique is implemented by using two versions of the basic Equation 2.1, with start points separated by 180^0 or π radians.

The sine and cosine terms in the Equation 2.1 would be kept in the same order so that both wind paths progress in the same direction. To close such a system of paths, the gap would be set to the other line dimension of tow band width. The two bands do not need be equal in width.

Now it appears from the previous discussion that we only consider the value of circumferential winding in terms of hoop direction. It is by no means limited to high angle winding. Examples of low wind angle circumferential and geodesic wind paths are presented simultaneously in Figure 2.9 . In Figure 2.10 the path tangents and normals are presented for the circumferential windpath with the Blue line representing the wind path. The solution method is based on Eq.2.4 as an input to MapleV for plotting of the basic function. The rotation parameter, t, which describes the number of revolutions that the path traverses over the length of the mandrel, is set very low so that a very low wind angle is described.

The Red line in Figure 2.9 represents a geodesic path, plotted and superimposed over a Blue circumferential path on the same tapered mandrel. The geodesic path is produced using an iterative method described in the following chapter. The circumferential path was manipulated to fit as close as possible to the geodesic. Both paths start at the same point on the mandrel and ultimately intersect at some distance down along the taper. In the next chapter a comparison of the two curves is given in more detail. The purpose of this demonstration is to show that while the circumferential path is not

optimally located, it nevertheless can be forced to be very similar to the geodesic for a large portion of the path. It appears enticing to consider such a path augmented by multiple heads to affect closure.

The advantage of the circumferential wind path over the geodesic wind path would be greater control of the laminate thickness. The problem of band overlap however will require the use of an appropriate strategy. Unfortunately, the geodesic laminates are subject to extreme variations in material properties and thicknesses, as will be discussed in a subsequent chapter. However, the limitation of slippage as a function of the taper will limit the suitability of such circumferential winding techniques to very low taper ratios.

The double-headed, circumferential winding technique was physically implemented in another project (Elliot, 2000 *pers. comm*) and found to work quite well. Careful attention to coordination of mandrel rotation and carriage advance were required. One source of concern was the payout eye position relative to the path tangent. While the wind path is calculated as a line over a surface, the fiber tow is definitely a three-dimensional problem. The payout eye roller bar requires angular rotation to remain perpendicular to the fiber tow and in the plane of the tow band. As the curvature increased at the small end of the mandrel, the wind angle drifted to slightly lower values and the tow tends to slide sideways within the payout eye. This sliding tendency can cause fiber damage and result in reduced material properties or even worse, in a broken tow or jammed winder. The binormal vector can be used to determine the appropriate payout eye rotations, and used as input for motion control programming. Note that such motion control is not presently available

on 3-axis winders, and this would represent fourth and fifth axis (comparable to pitch and yaw control).

The actual stand-off distance for the payout eye is arbitrarily chosen to clear the mandrel surface. For winding on tapered mandrels, one of three options is chosen. In the first case the payout eye is positioned to clear the maximum diameter of the cylinder and remains at a fixed distance, (y= constant), from the axis of rotation, in the y-z plane where x=0. This method is not discussed here, since it does not readily permit direction reversal. It is apparent that the tangent vector corresponding to the free length of the fiber tow must be continually updated as the wind angle changes. This requires the solution of the scalar parameter, t_v, discussed earlier and presented in Equation 2.15. In the second case the Tow length from the mandrel surface is maintained at a constant distance, t_v therefore remains fixed. However the cross-feed axis must be continually updated. The payout eye must however remain in the y-z plane where x=0. The third method is to maintain a fixed stand off distance that insures that the payout eye maintain a fixed distance from the surface of the mandrel. Such a method permits positioning the payout eye very close to the surface without risk of collision.

In Figure 2.10, the tangent vector, shown in Red, is maintained at a constant length and it is clear that as the path, shown in Blue, approaches the small end of the mandrel, the terminal point of the tangent vector is getting closer to the central axis. This is of concern since it implies that there is a risk of collision between the payout eye and mandrel surface.

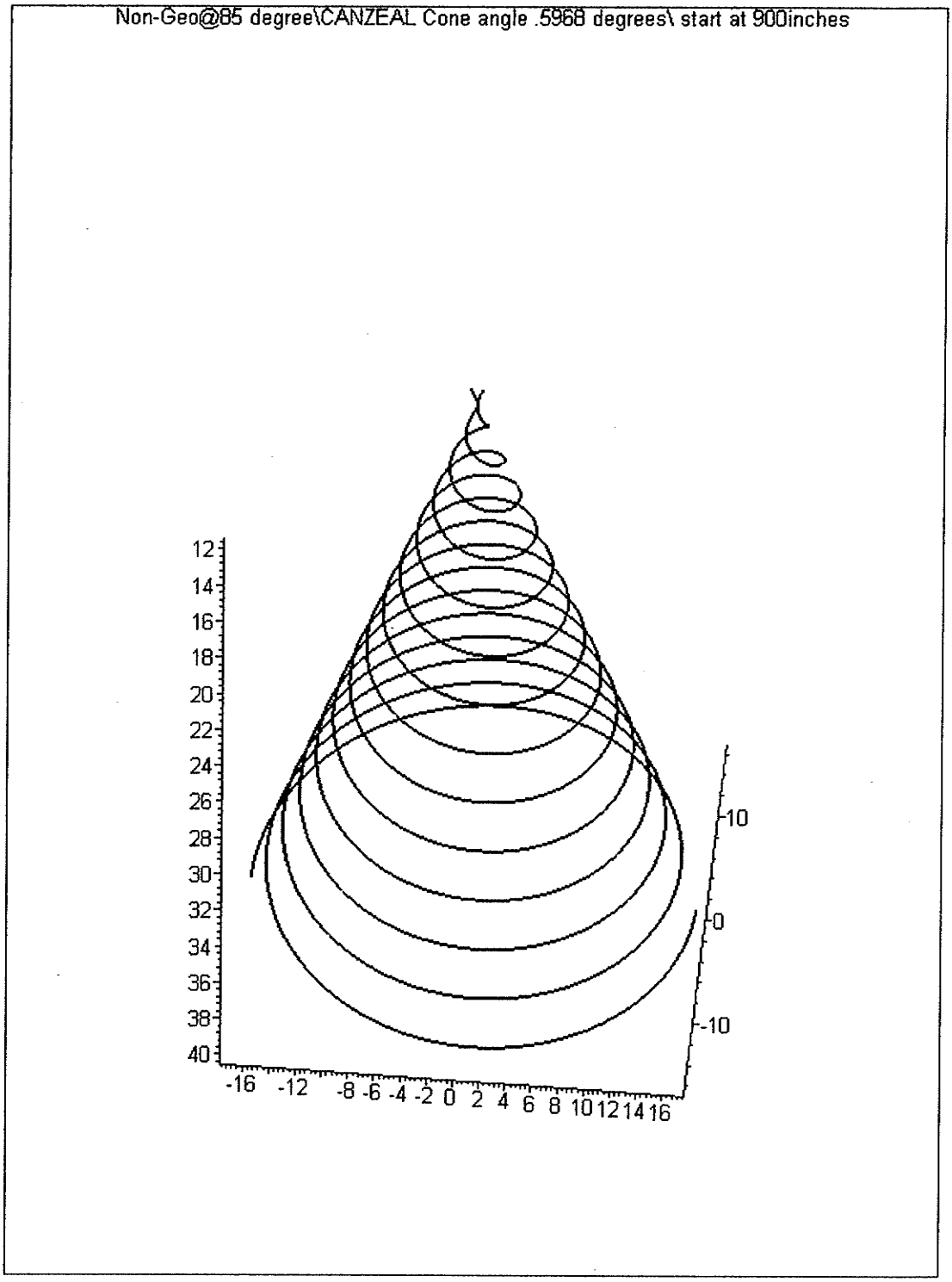

Figure 2.8: Double Headed Circumferential Low Angle Winding

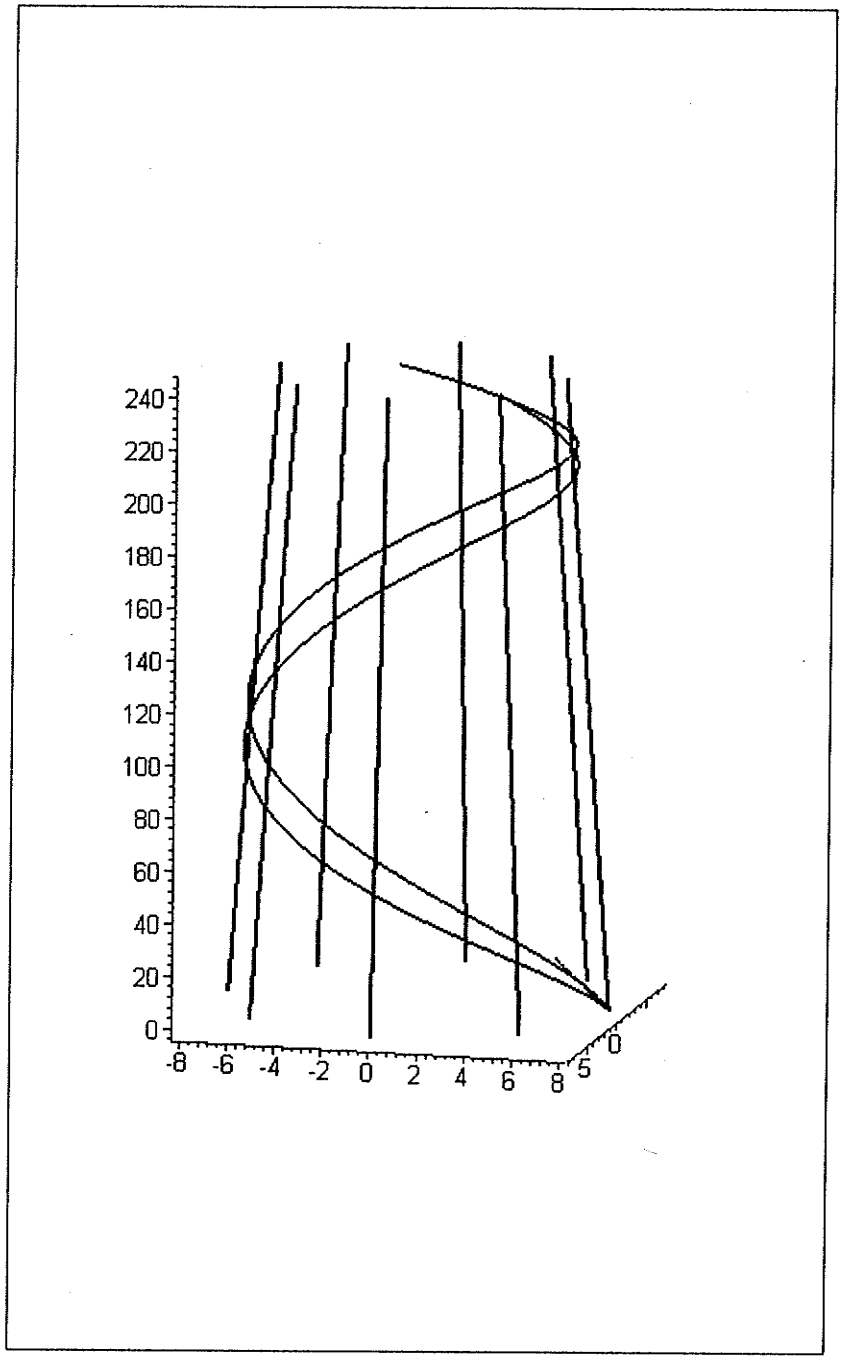

Figure 2.9: Low Angle Circumferential Wind Path (Blue), Fitted to a Low Angle Geodesic Path (Red)

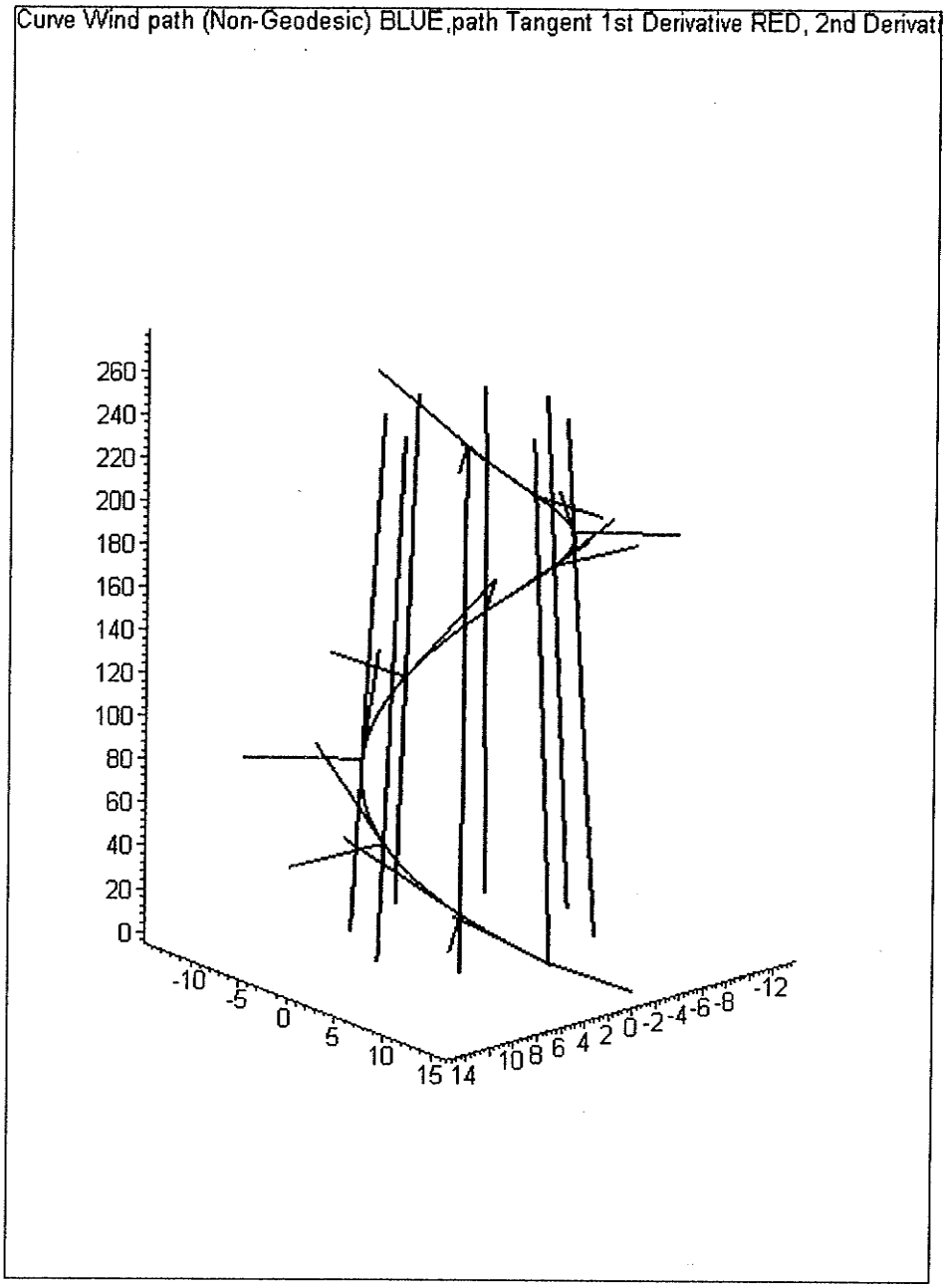

Figure 2.10: Circumferential Path (Blue) with Tangent (Red) and Tangent Normal (Green) Vectors

2.4 MACHINE MOTION: PAYOUT EYE POSITION CONTROL

The first step in preparing to wind a path over a mandrel is to convert the wind path coordinates into a set of procedures that can be used by a filament winding machine.

The wind path coordinates are based on a mandrel local coordinate system. As discussed earlier, using such a coordinate system implies that the tangent vectors representing the free tow length are to be rotated about the z-axis. In reality, the mandrel rotates and the carriage and payout eye or eyes are fixed in the y-z mid-plane where x=0. The cross-feed arm moves in or out in the positive y-axis and never ventures inside the mandrel radius, for obvious reasons.

Since the winding machine has these restrictions, the wind path must be converted to machine coordinates. Examples of this procedure, and resulting consequences are discussed in the following section. In these examples the right-handed 3-dimensional Cartesian coordinate system is used. For these purposes it is most convenient to have the observer looking along the z-axis which increases away from the observer. The positive x-axis is directed upwards and the y-axis increases positively toward the right of the observer. The conventional right hand coordinate system is tilted over so that the y-z plane is now horizontal. The basic equation of the circumferential wind path as presented will result in a clockwise progression of the wind path as it advances up and away from the observer.

The mandrel is assumed to be rotating in a counter-clockwise direction, when viewed from the base, which in this case is a negative rotation. It is also required to determine the coordinates of the terminal end of the tangent vectors. The payout eye location is derived from the tangent vector end point coordinates. The absolute distance of the vector end point, from the axis of rotation, becomes the y coordinate of the payout eye, since the payout eye is fixed in the y-z plane where x is zero. The z-coordinate of the payout eye is

identical to the end point of the tangent vector. The tangent vector rotation is then considered to be in the opposite direction of the mandrel rotation. These assumptions are made to permit the use of standard vector matrix rotation techniques to find the location of the payout eye.

With a known tangent vector of required length, the base and the terminal coordinates can be rotated to bring the tow or tangent vector into the correct position. Let A be the point at the base of the tangent vector on the surface of the mandrel and B the point on the terminal end (where the payout eye is expected to be found), thus the points A and B can be represented as,

$$A = < a_1, a_2, a_{3>} \_and\_ B = < b_1, b_2, b_3 > \qquad \textbf{(Eq. 2.26)}$$

where a1, a2 and a3 are the Cartesian values in the x,y,and z directions respectively and similarly for the point B.

The angle of rotation, θ, required to bring the tangent vector end point into position to represent the tow and payout eye then is simply the angle between the terminal end of the tangent and the x=0 yz plane such that ,

$$\theta = \sin^{-1}\left[\frac{b_1}{\sqrt{b_1^2+b_2^2}}\right] \qquad \textbf{(Eq. 2.27)}$$

The Transformation matrix, $\mathbf{T}$, is of the conventional form so that the transformed point A , A^T , which is the point where the payout eye must be positioned, can now be determined

$$\mathbf{A^T = TA} = \begin{bmatrix} \cos\theta & -\sin\theta & 0 \\ \sin\theta & \cos\theta & 0 \\ 0 & 0 & 1 \end{bmatrix} \begin{bmatrix} a_1 \\ a_2 \\ a_3 \end{bmatrix} = \begin{bmatrix} a_1\cos\theta - a_2\sin\theta + 0 \\ a_1\sin\theta + a_2\cos\theta + 0 \\ 0a_1 + 0a_2 + 1a_3 \end{bmatrix} \qquad \textbf{(Eq. 2.28)}$$

and

$$\mathbf{B}^{T} = \mathbf{TB} = \begin{bmatrix} \cos\theta & -\sin\theta & 0 \\ \sin\theta & \cos\theta & 0 \\ 0 & 0 & 1 \end{bmatrix} \begin{bmatrix} b_1 \\ b_2 \\ b_3 \end{bmatrix} = \begin{bmatrix} b_1\cos\theta - b_2\sin\theta + 0 \\ b_1\sin\theta - b_2\cos\theta + 0 \\ 0b_1 + 0b_2 + 1b_3 \end{bmatrix} \quad \text{(Eq. 2.29)}$$

Note that the z axis is not transformed since this is the axis of rotation.

Since this coordinate transformation is required for each calculated tangent vector, it is convenient to establish the procedure as a subroutine type algorithm. In the case where a number of variations on band width or tow length are to be investigated, the transformation subroutine was actually incorporated into the same spread sheet as the one that generated the wind paths and various vectors. In Figure 2.11 and Figure 2.12 and Figure 2.15s 2.15 to 2.17, the wind paths for the LP mandrel are presented. In Figure 2.11 and Figure 2.12 the classical mandrel coordinate representation is given with the addition of the free fiber tow positions and the payout eye locations for Figure 2.15 to Figure 2.17. In Figure 2.17, a 3.5" bandwidth is used, and in Figure 2.15, a 7" band width is displayed. Examination of these plots shows that the payout eye start positions will shift, as will the stand off distances when using constant tow length. In the case of tapered mandrels the small end angle drift can actually bring a stand off clearance dangerously close to the mandrel surface. Figure 2.13 and Figure 2.14 show the plotted values of band overlap on the same LP mandrel for two options in Band Width.

2.5 MACHINE MOTION: CONSTANT STAND OFF DISTANCE

Should the mandrel geometry indicate the need for a constant stand off distance, a slightly different procedure is employed to determine the actual Tow length required at each interval. Assuming the mandrel is tapered, then a

constant stand off distance requires the payout eye to follow a path parallel to the mandrel surface in the x=0 plane. At any position along z for the path point the radius as a function of z and the standoff distance must be determined. Also required is the wind angle at the point where the tangent leaves the surface. The tangent length, Tl , for a constant stand off distance, SO , is then,

$$Tl_{(t)} = \frac{\sin(90-\psi)*\sqrt{(r_{(t)}+SO)^2-(x_{(t)}^2+y_{(t)}^2)}}{\sin(180-(90-\theta_{(t)})-(90-\psi))} \qquad \text{(Eq. 2.30)}$$

Where

$\psi = \tan^{-1}[m]$ the slope of the mandrel, which will be constant for the taper.

$\theta_{(t)} =$ the wind angle at point t which is the vector cross product of the meridian and tangent vectors at point t.

$r_{(t)} = m * bt + B$ the radius defining function previously described and

$x_{(t)} and\, y_{(t)}$ are the solutions of the parametric circular helix (Equation 2.1).

Having established the value of ***Tl*** the end point needs yet to be determined and having solved for the unit Tangent vector at point t , < i,j,k.> then the end point is ,

$$\langle \mathbf{i}Tl + P_1, \mathbf{j}Tl + P_2, \mathbf{k}Tl + P_3 \rangle \qquad \text{(Eq.2.31)}$$

However the Tangent vector must be transformed by a matrix rotation as was previously detailed in section 2.3 , in order to position the terminal end of the fiber tow in the x=0 plane where the payout eye is located. Clearly these steps are best handled by a subroutine within the wind path solver.

This exercise was presented to demonstrate the difficulties in making changes to wind angle or band width without due consideration of the pay out

eye position changes. In addition this exercise points out the difficulty that is associated with a simple parametric equation being translated to the real world problem of positioning a payout eye to produce the specific wind path. In order to integrate design and production it is often required that some complex translation routines be employed. These procedures are ideally suited to encapsulation within computer routines which would become transparent leaving a designer to concentrate on the more important load performance issues.

2.6 DIRECTION REVERSAL

Direction reversal requires a short period at the end of the stroke for the carriage to reverse direction and line up with the terminal end of the wind path. This short procedure provides a short true 90 degree wind zone usually of less than 360 degrees of rotation. The carriage then moves to a new start position for the reverse stroke. Note that the reverse stroke requires the governing parametric equation to be reversed in x and y resulting in a clockwise negative helix. Keeping the carriage velocity identical will result in the mirror image wind path superimposed over the forward layer. This typically results in a positive and negative angle ply, very near to 90^0, but definitely not constant over the length of the mandrel, as was seen previously. There is absolutely no interweaving of the layers possible.

2.7 SUMMARY ON CIRCUMFERETIAL WINDING

The circumferential winding process presented here was based on the fundamental equation of the circular helix (Eq. 2.1) and as such manifests the following properties,

a) The pitch of the fiber path is constant, the angle with respect to the meridian is not, for linear tapered mandrels the winding angle must decrease as it progresses down to the smaller end. In the strictest sense wind angle constancy is not possible using a circular helix based wind pattern on a tapered mandrel.

b) The bands overlap as the angle decreases and the diameter decreases. The amount of overlap is a function of the starting bandwidth. The narrower the bandwidth the slower the rate of wind angle decrease and the smaller the overlap problem.

c) A circumferential winding pattern is of constant thickness everywhere except in areas where overlap occurs. Controlling overlap then makes it possible to guarantee that circumferential winding is of constant thickness.

d) It should also be pointed out that the wind angle may be regarded as nearly constant if the bandwidth is small enough. For the rest of the thesis the assumption is made that the circumferential wind paths are of constant angle since all poles will have very small tapers and the sections being produced have been purposfully limited in length.

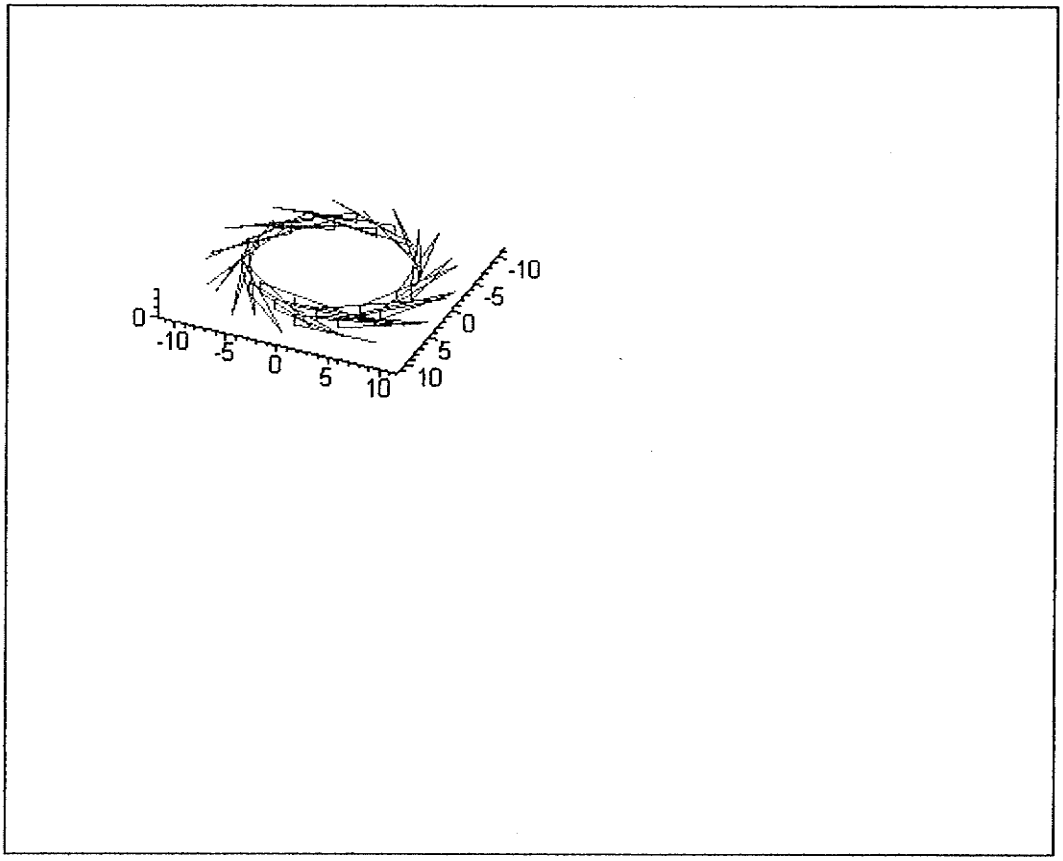

Figure 2.11: 8" Tow Length

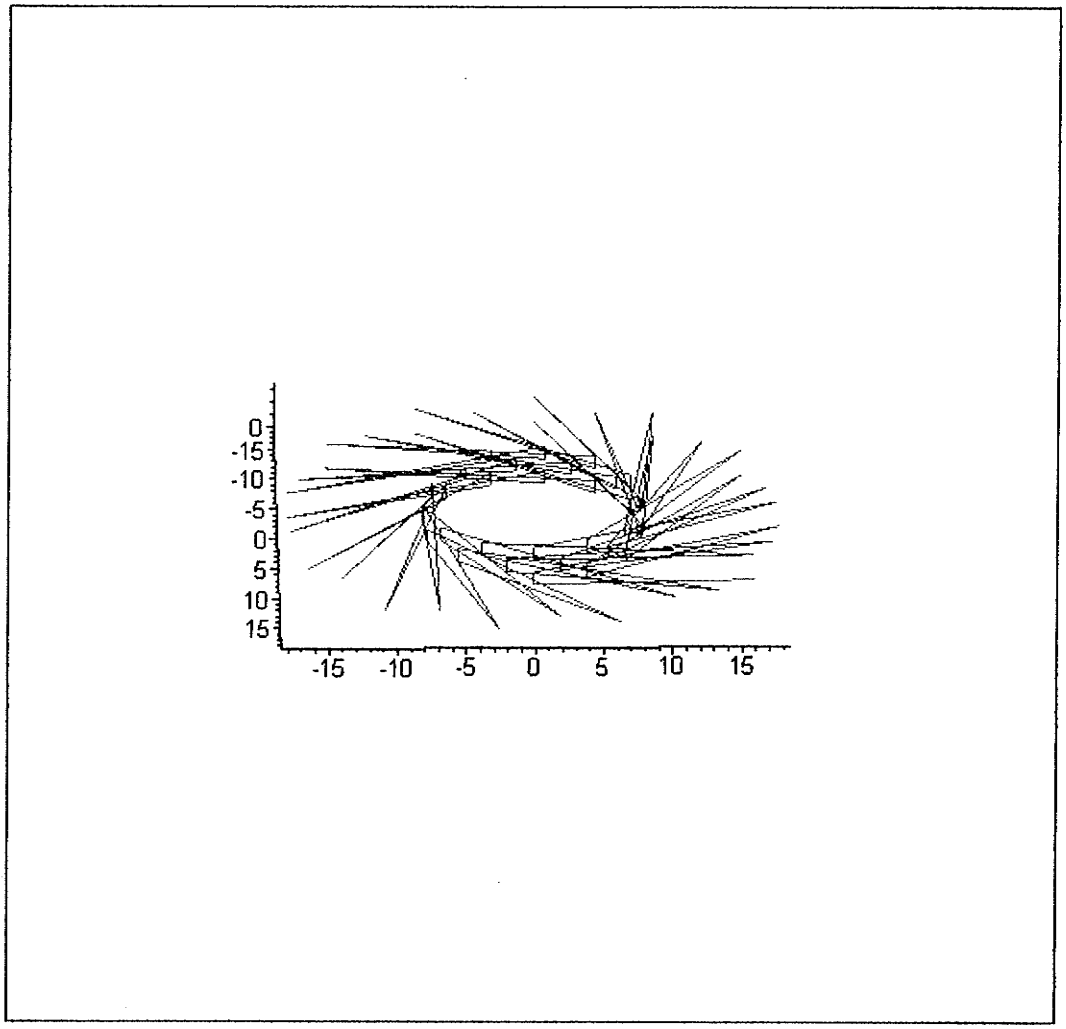

Figure 2.12: 16" Tow Length

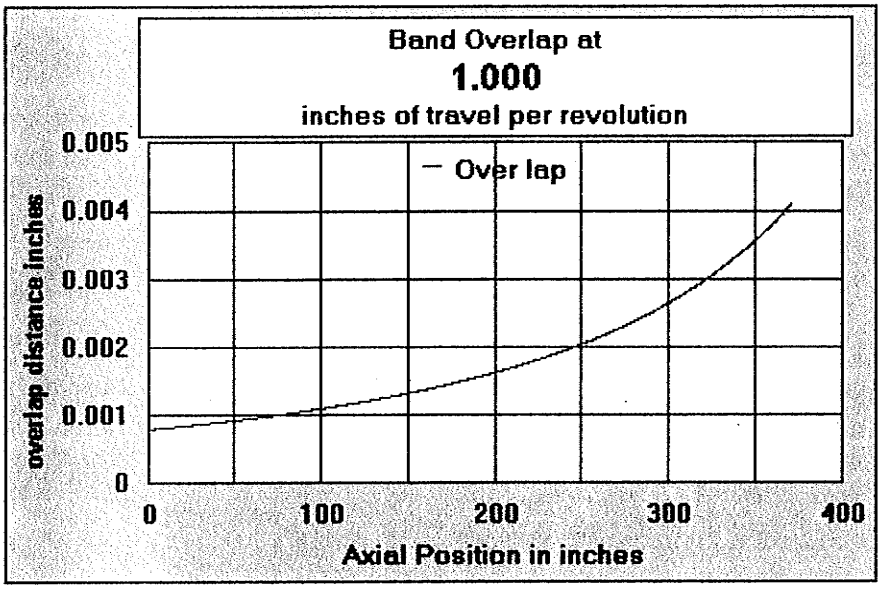

Figure 2.13: Band Overlap for a 1" Band width

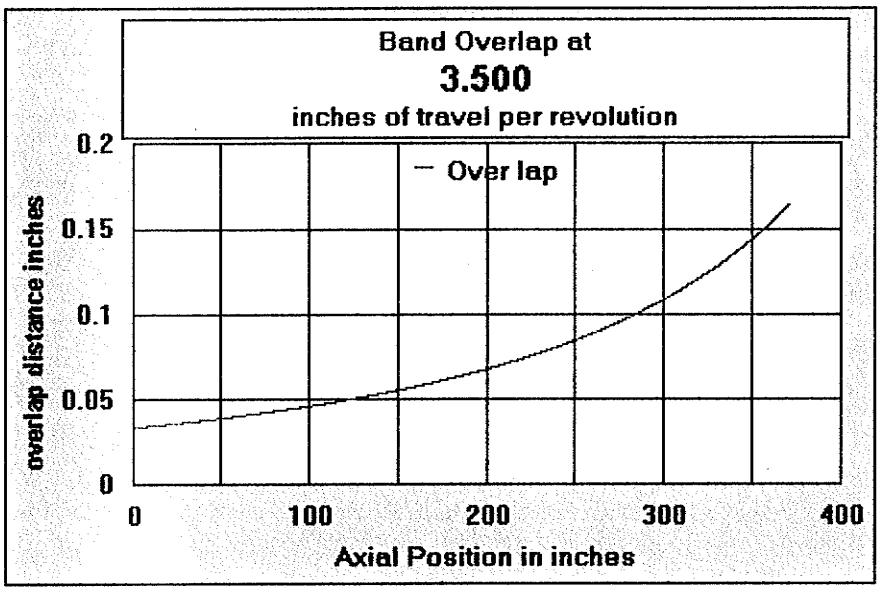

Figure 2.14: Band Overlap for a 3.5" Band Width on LP Mandrel

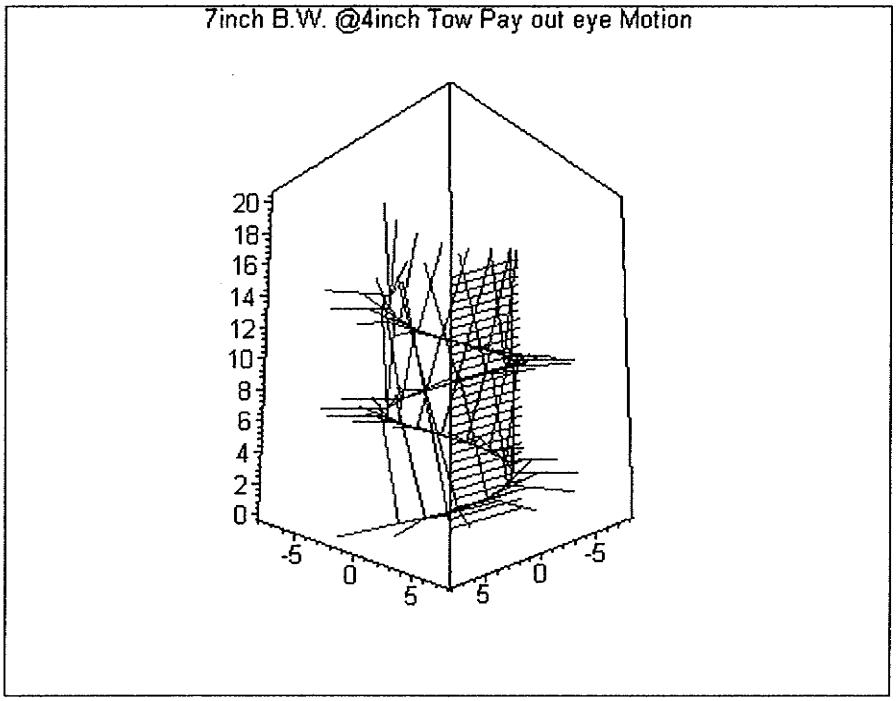

Figure 2.15: 7" Band Width on Mandrel LP showing the Payout Eye Motion Plane for a 4" Tow Length

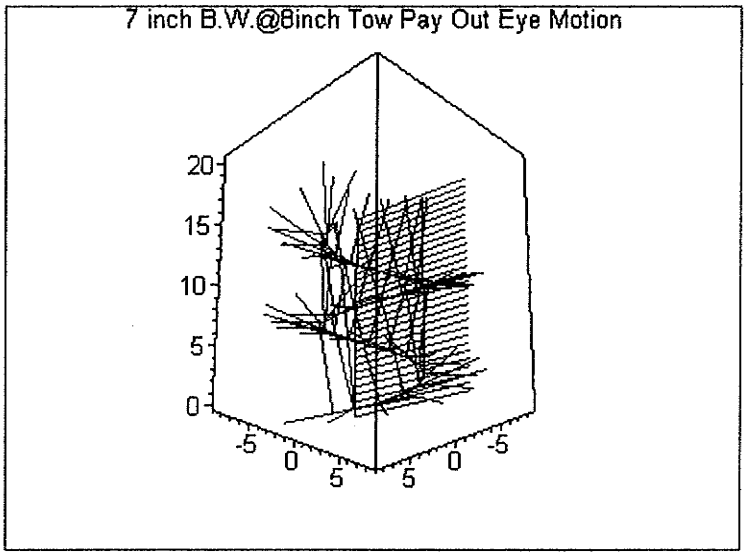

Figure 2.16: 7" Band Width on Machine LP showing the Payout Eye Motion Plane for a 4" Tow Length

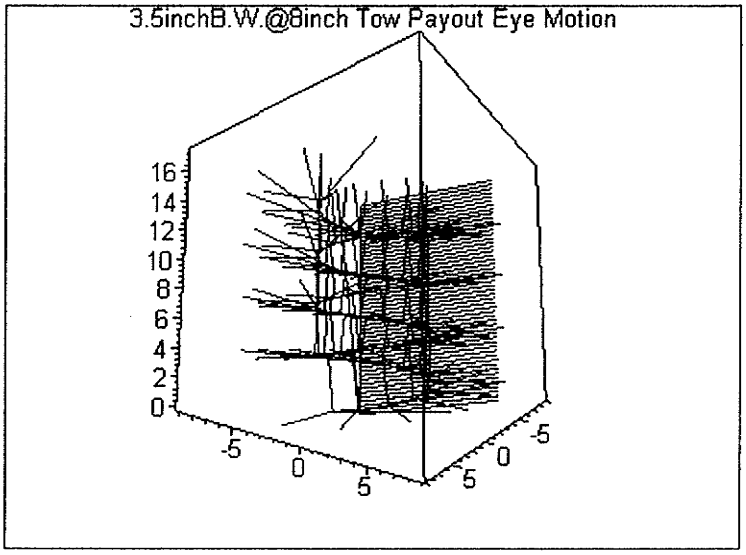

Figure 2.17: 3.5" Band Width on Mandrel LP showing the Payout Eye Motion Plane for an 8" Tow Length

3 GEODESIC WINDING

3.1 GEODESIC WINDING PATHS

The geodesic path has been variously defined; as the shortest distance between two points on a surface, the path over a surface whose geodesic curvature is equal to zero, the stable path with slippage reduced to zero. Specifically for axisymmetric surfaces the definition includes the theorem of Clairaut that states the geodesic path is that which crosses every meridian at an angle such that the product of the radius and the sine of the angle is equal to a Constant value. In filament winding all these factors play a role in one form or another. That fact must be stated that for any given surface of revolution there are an infinite number of geodesic paths possible at any given angle. There are an infinite number of Constant's of Clairaut. Yet the paths are hardly straight forward to determine.

In the special case of the circular helix, (Equation 2.1), where by definition the radius is a constant, all helices are geodesic. As explained in Chapter 2, the cross product of the surface normal vector $\mathbf{n}_S$ and path normal vector N, determine the geodesic curvature vector $\mathbf{b}_S$. As such, it was fundamentally impossible for the two vectors to be collinear on tapered mandrels as was determined from the second derivative. However, in the special case of zero slope, this is true. Therefore the geodesic curvature resolves itself to be zero. As is also clear, when a 3D surface of a cylinder is developed into a 2D mapping, all helices are found to be straight lines that are

also parallel. One of the requirements of Classical Lamination Theory is that fibers are both straight and parrallel.

There is no special reason to exclude non-constant surfaces of revolution from having Geodesic paths. Of particular interest is that such paths exist on any smoothly continuous function surfaces, as will be demonstrated later in this chapter.

The greatest advantage of using the Geodesic (Helical) paths is the variety and stability offered the designer. The first obvious shortcoming is the defining of the Cartesian coordinates.

In the following section a simple closed form solution for the determination of geodesic wind paths over generalized tapered mandrels is presented along with its derivation. This solution provides the Cartesian coordinates of the wind path of interest as well as the winding angle at any point along the length of the mandrel, as well as in terms of the machine motion.

In a paper by Hofeditz (undated) a concept of graphically using a 2-dimensional mapping of a geodesic path over a very short distance was presented. Taking this concept a step further, it was found that it would lend itself to detailed numerical mapping of the geodesic path in 2-D which evolved into a simple closed form solution for tapered mandrels using geodesic paths.

Furthermore, knowing the specific wind angle and axial location, a method of calculating the laminate thickness and elastic modulus at that location , is presented, in the following Chapters. This method is very simple; however it is limited to linearly tapered surfaces of revolution. More complex

shapes may be approximated by sections of different cones as reported by Maheswaran(1998).

Software requirements are minimal, a simple spread sheet and a mathematics application such as MapleV (1997), as was used here, for three dimensional viewing of the wind path should suffice. Values calculated for thickness and elastic moduli can be further exported for use in Finite Element Analysis software.

3.2 CLOSED FORM SOLUTIONS (Derivation of a Closed Form Expression for Geodesic Wind Paths over Generalized Tapered Mandrels)

Two methods are presented here by which a geodesic path, over a tapered surface of revolution is mapped onto a 2D surface representing the 3D surface, providing simple methods for determining the parametric equations of geodesic space curves.

Method A does not incorporate the Constant of Clairaut. As such the assumption is that the 2D mapping of a straight line over the surface of a 3D tapered cylinder is in fact a geodesic line. In our approach knowledge of the existence of Clairaut's Constant is not required. It is shown that this model method can be used to subsequently derive the Constant of Clairaut.

The closed form solution method will permit the carriage advance to be solved directly from the mandrel rotation and basic mandrel geometries. This in theory permits a wind path to be generated on the "fly" so to speak. That is no path coordinates need be stored prior to winding. Knowing only the basic

geometry of the tapered cylinder and a desired wind angle, a closed form solution for the 3D-geodesic space curve is generated.

Method B takes advantage of the Constant of Clairaut and provides a very compact algorithm to find the 3D Cartesian coordinates for a geodesic space curve. As such it is presented in the belief that this method may be used for surfaces problematic for the previous method, such as hybrid surfaces derived from multiple primitive solids.

3.2.1 Method A

The equation of a tapered cylinder, where the radius, R, is a function of the axial position, in the generalized form is,

$R = mz + B$ for the frustrum of the cone, **(Eq. 3.1)**

where m is the slope and B is the starting radius at $z = 0$.

Alternatively the cone can be represented in terms of the angle of taper and axial position with the expression,

$R = z\tan\alpha + B$ **(Eq.3.2)**

The major difference between Eq. 3.1 and 3.2 is that in the former the radius increases or decreases with respect to z depending on the sign of slope, while the later assumes that the radius and z are positively correlated. The difficulty is not mathematical but rather interpretive since this paper is attempting to preserve a view point reflective of the filament winder, Eq. 3.2 implies that the zero axial position is beyond the limits of the physical envelope of the winding machine.

To avoid confusing z position with mandrel position, the height of the cone will be represented by L. L is also the start point for the geodesic wind

path on the cone. The base of the mandrel is positioned to align with the base of the cone. However, when solving for a geodesic wind path the start point, L can be set at any position along the barrel of the mandrel.

The 2D-mapping of the tapered cylinder is set up in Cartesian coordinates, with the major 2D-radius, of the great circle, R_{gc}, see Figure 3.1

$$Rgc = \frac{z}{\cos\alpha} \qquad \text{(Eq.3.3)}$$

R_{gc} is aligned with the base meridian of the 3-D coordinate system of the cone. This results in the 2D map laying in the tangent plane of the cone's surface meridian. The two coordinate systems are further aligned by having the z axis of the 3d model intercept the origin of the 2D- map. The cone angle α is simply

$$\alpha = \tan^{-1}(m) \qquad \text{(Eq.3.4)}$$

The arc length at radius *Rgc* in 2D between revolutions of the mandrel is equal to the 3D butt circumference, which can be found using the cone base position, Z_B along the axis

$$2\pi(z_B \times \tan\alpha) \qquad \text{(Eq.3.5)}$$

Therefore, the arc angle in 2D at the base (denoted by the superscript 0), the Z_B term referring to the base,

$$\psi_{2D}^{0} = \frac{2\pi(z_B \times \tan\alpha)}{2\pi(\frac{z_B}{\cos\alpha})} \qquad \text{(Eq.3.6)}$$

Eq.3.6 is just a fraction of a complete gyration of the mandrel about the 2D origin. So the right hand side should be multiplied by 360^0 for the actual angle in degrees.

So then $$\psi_{2D}^{0} = \sin\alpha \times 360^{o} \qquad \text{(Eq. 3.7)}$$

One complete revolution of the mandrel corresponds to the angular increment, ψ_{2D}^{0}. A direct correspondence between the 2D angular increment and the 3D-mandrel rotation is therefore,

$$\psi_{3D} = \frac{\psi_{2D}^{i}}{\psi_{2D}^{0}} \qquad \textbf{(Eq. 3.8)}$$

Or $\psi_{3D} = \psi_{2D}^{i} \times \zeta$

where ζ is simply a correspondence factor equal to $\frac{1}{\sin\alpha}$ **(Eq. 3.9)**

$$\psi_{3D} = \psi_{2D}^{i} \times \frac{1}{\sin\alpha} \qquad \textbf{(Eq. 3.10)}$$

The 2D projection of the 3D geodesic path is superimposed upon the 2D map such that it represents a straight line (Figure 3.1), where

$$y = -(x)\tan\theta_0 + R_{gc}\tan\theta_0 \qquad \textbf{(Eq. 3.11)}$$

The lower case terms *y* and *x* denoting coordinates on the 2D map. θ_0 is the arbitrarily chosen wind angle at the start point , in this case at the base of the cone (start position *L*), where

$$y = 0 \text{ and } x = R_{gc} = \left(\frac{L}{\cos\alpha}\right). \qquad \textbf{(Eq. 3.12)}$$

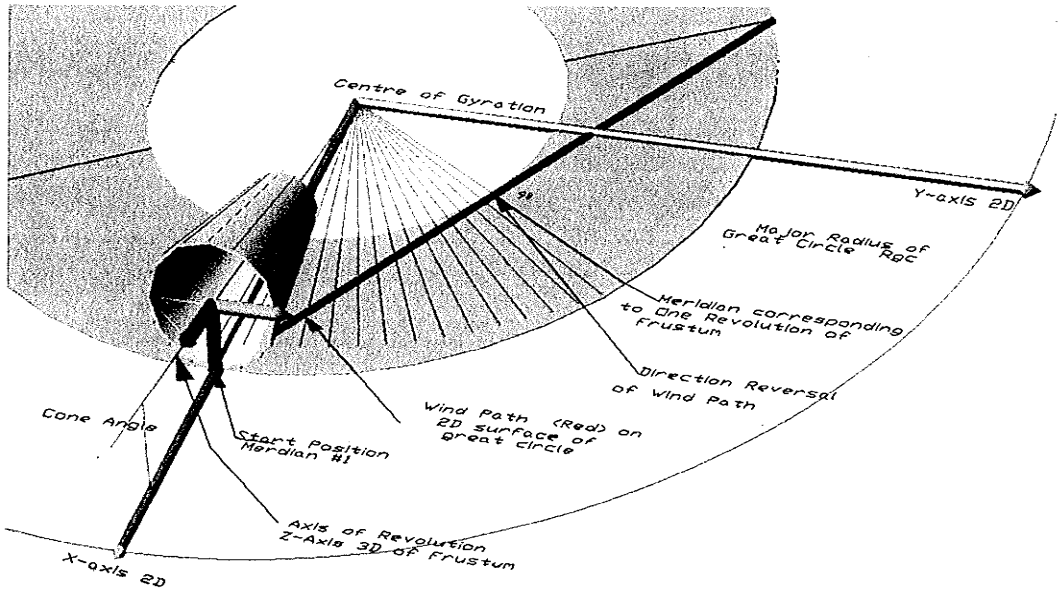

Figure 3.1: 2D-Mapping of 3D-Cone showing Geodesic Projection

The assumption here is that since the geodesic curve can be defined as a shortest distance between points on a surface then the same surface in 2D would show the geodesic path to be a straight line.

Note that the 2D x axis lies directly beneath a meridian of the cone (Figure 3.1). The wind angle is defined as the angle between the tangent to the wind path and the meridian of the surface at a given point. This then implies that the tangents to the wind path crossing the particular meridian all lie within the 2D plane. Thus if the 2D plane is aligned with the mandrel meridian then the 2D and 3D wind path projections of the start point will have identical wind angles, in fact they will be indistinguishable, since they are superimposed.

There are two methods by which one can solve for the coordinates of the geodesic line over the surface of the mandrel. In the first method it is

possible to get an expression in parametric form of the geodesic with the independent variable chosen to be mandrel angular rotation. In the second method the carriage advance is chosen as the independent variable.

The first derivative, the tangent to the path is required to determine the exact position of the payout eye in order to maintain a clearance of the mandrel surface. The principal normal of the path, **n**, along with the surface normal vector, $\mathbf{n_s}$, is required to assess the slippage forces at any given point along the path, as was discussed in the previous chapter on circumferential winding. Maheswaran (1998) points out that helical winding techniques, referred to as non-geodesic, are in fact only variants of the geodesic winding, which have non-zero slippage vectors. The values for slippage are increased slightly to permit a deviation from geodesic paths to negotiate surface obstacles.

The mandrel rotation increment ψ_{3D} is used to determine the x and y coordinates of the geodesic line on the 2D-surface. While these points are of limited interest, the x distance is required to determine the path advance along the Z axis of the Mandrel Coordinate system. In order to clarify the use of two distinct coordinate systems in the following discussion lower case x,and y will refer to the 2D system, and upper case X,Y,Z will refer to the 3D mandrel coordinate system.

To determine x then, one must solve for the intercept point of the Geodesic line in 2D with the rotation angle in 2D, ψ_{2D}^{i}, so that x now becomes

$$x = \frac{\left(\frac{L}{\cos\alpha}\right)\tan\theta}{\tan\left(\sum\psi_{2D}^{i}\right)+\tan\theta} \qquad \text{(Eq. 3.13)}$$

and without the 2D reference,

$$x = \frac{\left(\frac{L}{\cos\alpha}\right)\tan\theta}{\tan\left(\psi_{3D}\times\sin\alpha\right)+\tan\theta} \qquad \text{(Eq. 3.14)}$$

Note that the denominator in **Eq 3.13 and 3.14** is the angle the wind path makes with the meridian of the mandrel, and is simply the original wind angle supplemented with the rotation increment.

Now the value of Z along the mandrel axis is ,

$$Z = x\left[\frac{\cos\alpha}{\cos\psi_{2D}^{i}}\right] \qquad \text{(Eq.3.15)}$$

or in terms of mandrel rotation

$$Z = x\left[\frac{\cos\alpha}{\cos\left(\psi_{3D}\sin\alpha\right)}\right] \qquad \text{(Eq. 3.16)}$$

The 2D y coordinate can be found by substituting x **(Eq. 3.14)** into

$$y = R_{gc}\tan\theta_0 - x\tan\theta_0 \qquad \text{(Eq. 3.17)}$$

$$y = R_{gc}\tan\theta_0 - \left(\frac{\left(\frac{L}{\cos\alpha}\right)\tan\theta}{\tan(\psi_{3D}\sin\alpha)+\tan\theta}\right)\tan\theta_0 \qquad \text{(Eq. 3.18)}$$

At this point the X, Y, and Z-coordinates in 3D-Cartesian space, can be determined using the following equations,

$$X = (Z\tan\alpha)\sin\psi_{3D} \qquad \text{(Eq. 3.19)}$$

$$Y = (Z\tan\alpha)\cos\psi_{3D} \qquad \text{(Eq. 3.20)}$$

$$Z = x\left(\frac{\cos\alpha}{\cos(\psi_{3D}\sin\alpha)}\right) \qquad \text{(Eq. 3.21)}$$

The only term including the original start wind angle and position is,x, Eq.3.14, which has no reference to the 2D plane.

The previous equations can also be used to set the cross feed displacement, which is simply the change in radius. The cross feed position then is the original standoff distance incremented by the value, Δr from Eq.3.1.

The preceding triplet of equations, Eq. 3.19-3.21, can now be used to represent the parametric equations of a geodesic wind path over a generalized tapered cylinder, where again, both the wind angle and radius are functions of the mandrel rotation. Rotation is now the independent variable. The entire parametric system can be manipulated around the known mandrel constants and the desired wind angle at some arbitrary point.

It needs only to be demonstrated that the Constant of Clairaut can be expressed in terms of the mandrel constants (geometric properties of the cone) and the arbitrary choice of wind angle and the start point.

The constant of Clairaut can now be presented as,

$$C = R\sin\theta \qquad \text{(Eq. 3.22)}$$

The wind angle θ was previously defined as the angle between the tangent to the geodesic wind path and the meridian at any point on the surface. In 2D, $\theta\emptyset$ is the angle between the geodesic line equation and the vector $\langle x,y \rangle$ at point (x,y) such that ,

$$\theta = \psi^{i}_{2D} + \theta_0 \qquad \text{(Eq. 3.23)}$$

(Recall that θ_0 was defined earlier as the arbitrary start angle at base)

In 3D , then θ is defined as,

$$\theta = \left(\psi^{i}_{3D}\sin\alpha\right) + \theta_0 \qquad \text{(Eq. 3.24)}$$

Substituting Eq. 3.3 and Eq. 3.23 into Eq. 3.1, yields the Constant of Clairaut entirely in terms of the single basic geometrical property of the cone, namely the cone angle, and an arbitrary choice of wind angle, θ_0 and the arbitrary choice of start position L, which is incorporated into the Z term, see Eq. 3.15.

$$C = \left[Z\tan\alpha\right]\sin\left[\left(\psi^{i}_{3D}\sin\alpha\right) + \theta_0\right], \qquad \text{(Eq. 3.25)}$$

It is clear that for a constant diameter cylinder the cone angle goes to zero, and the radius function becomes a constant value, resulting in the classical presentation of Clairaut's Theorem Eq.3.22.

To demonstrate the generality of the equations, they were input into Maple V, mathematical software. Plots of various manipulations of wind angle are illustrated in Figure 3.2 to Figure 3.5. The salient point of these figures is that wind angles are not constant and drift upward as the radius decreases. The characteristic of drifting angles results in the condition of premature turn around, which will be discussed in more detail in a following section. The turn around characteristic of the geodesic wind paths prevents tapered mandrels of long length from being completely covered with higher starting wind angles. This condition forces the designer to utilize wind patterns with extremely low wind angles which, as previously mentioned, are not easily implemented on most winding machines

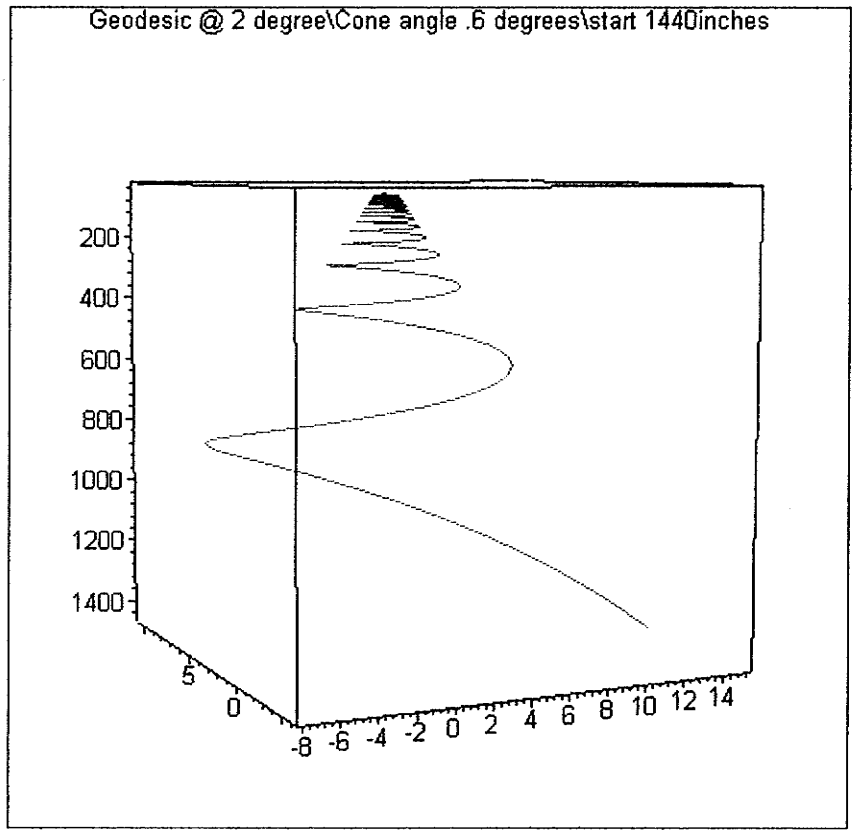

Figure 3.2: Geodesic Wind Path at 2 Degrees on Tapered Mandrel with Cone Angle Equal to 0.6 Degrees. Start Position at 1440 inches, Travelling toward Small End

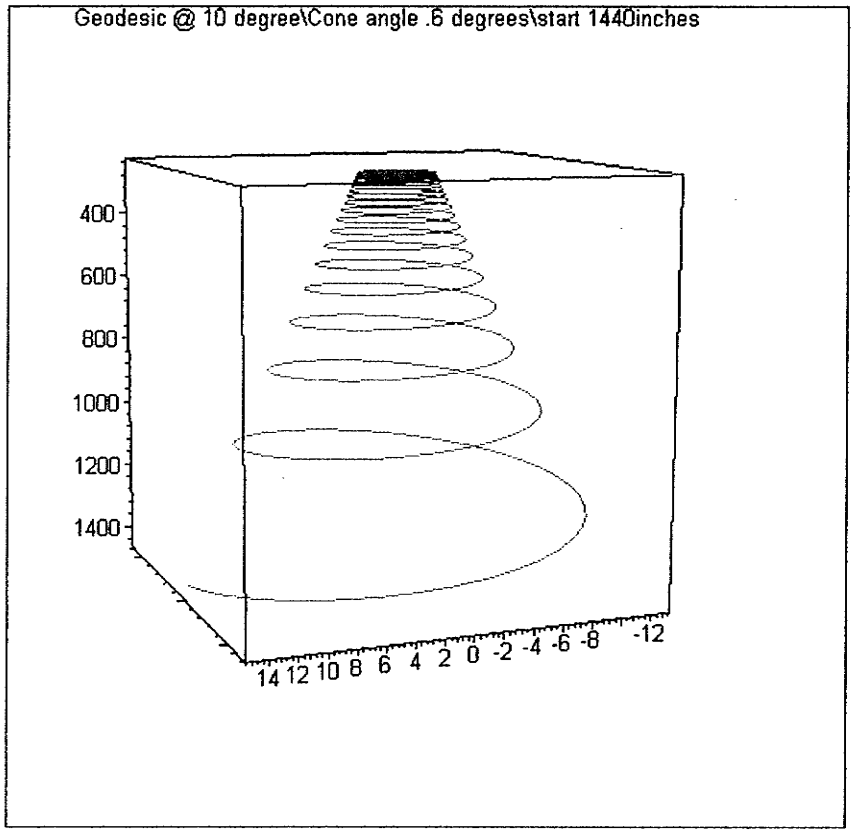

Figure 3.3: Geodesic Wind Path at 10^0 on Tapered Mandrel with Cone Angle equal to 0.6^0. Start Position at 1440", Travelling toward Small End

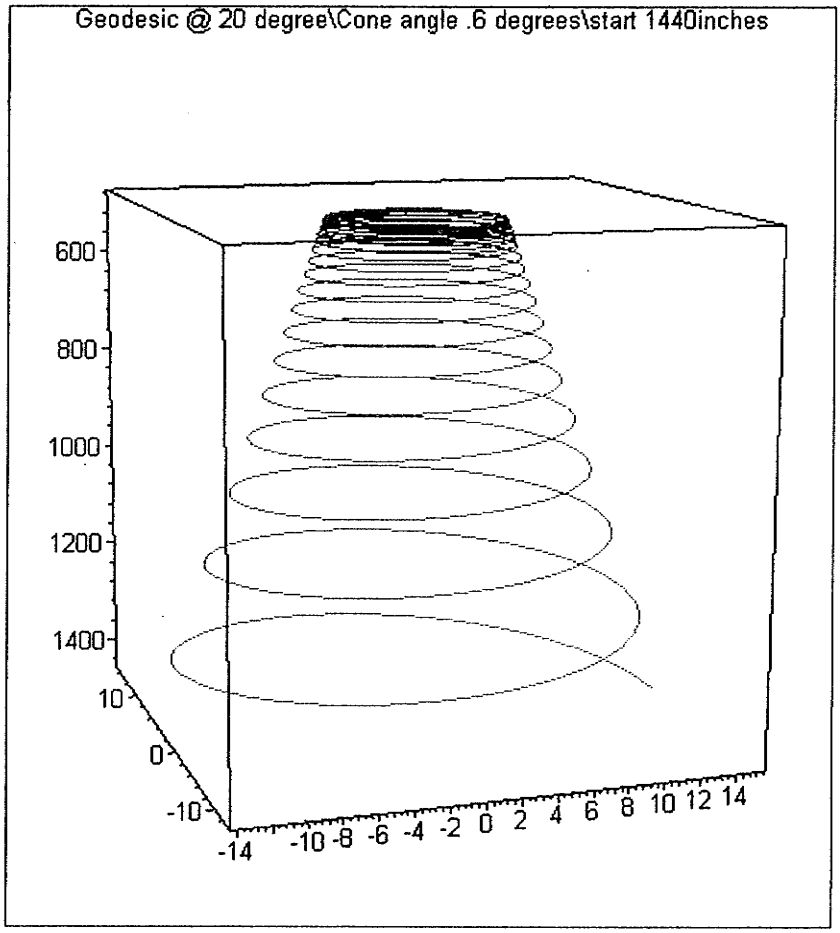

Figure 3.4: Geodesic Wind Path at 20^0 on Tapered Mandrel with Cone Angle equal to 0.6^0. Start Position at 1440", Travelling toward Small End.

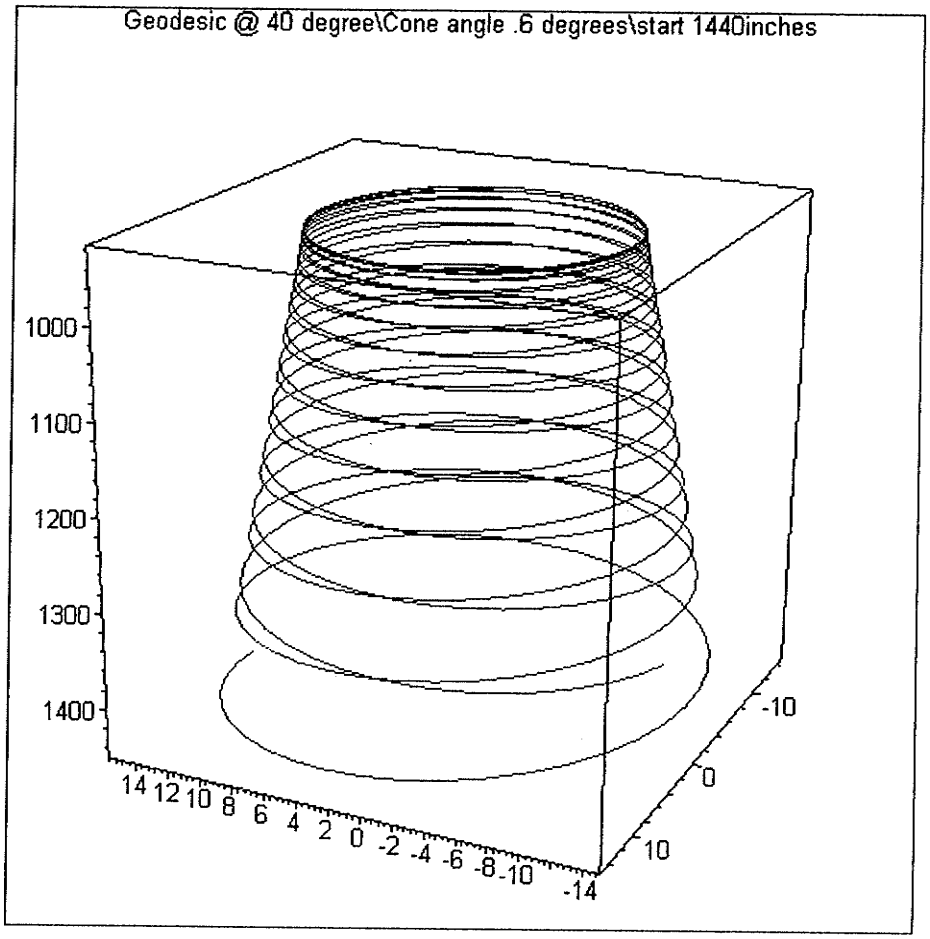

Figure 3.5: Geodesic Wind Path at 40^0 on Tapered Mandrel with Cone Angle equal to 0.6^0. Start Position at 1440", travelling toward Small End. Path Reversal clearly Evident

Figure 3.2 to Figure 3.5 demonstrate the nature of the turnaround condition and its sensitivity to cone angle, and starting angle. It can be seen that moving a start location for a given wind angle to another point along a mandrel, changes the value of Clairaut's constant, and is the same as changing the angle at the original point (Figure 3.2). So if one wanted to maintain a very low wind angle at the top of a tapered mast, a much lower wind angle is required at the base. Such low wind angles are not very practical since extremely small support shafts would then be required. Dome geometry is discussed in Chapter 6.0, section 6.3.

The derivatives of the parametric equations of the geodesic space curve were determined using Maple V. In Figure 3.6 the space curve of tangent end points (Red) is plotted over the space curve of the geodesic wind path (Blue). The length of the tangent vectors was set arbitrarily. The mandrel in this example is a full cone with slope .6 (cone angle $.54^0$) and length 960" using a $10.^0$ wind path. In Figure 3.7, the individual Tangent vectors (Red) are plotted between the two space curves. Now that the tangent vector can be determined for the geodesic using the explicit form, a very compact solver can be constructed that provides information suitable for machine motion programming.

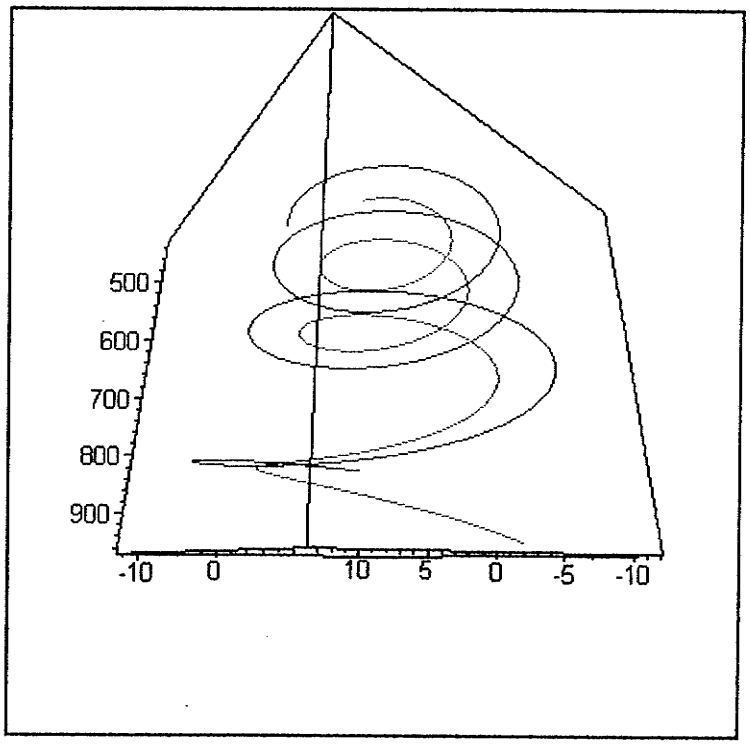

Figure 3.6: Tangent end point Path (Red) and Wind Path (Blue) Spacecurve for 10^0. Geodesic Wind Angle. Base View

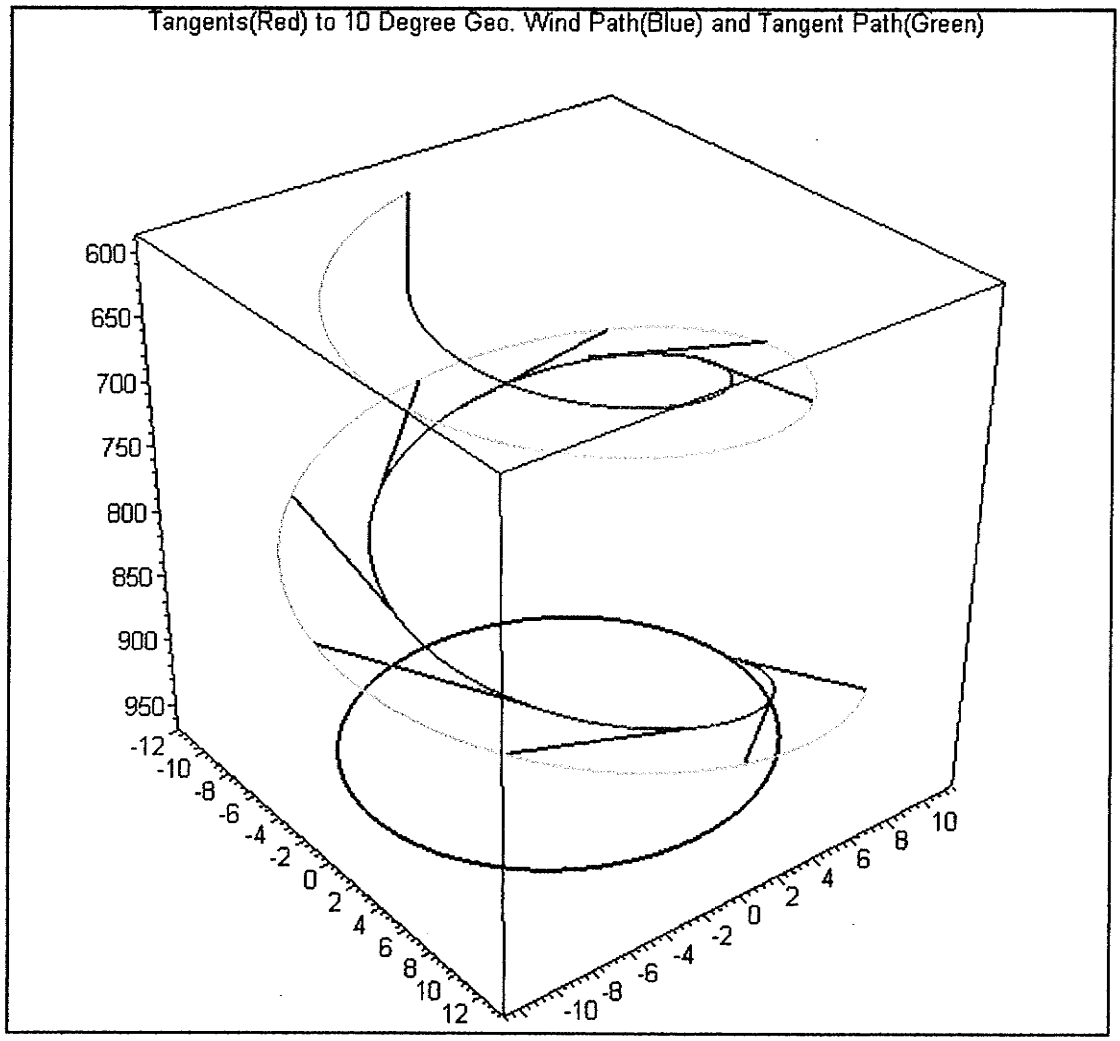

Figure 3.7: Tangent Vector (Red) and End Point (Green) to 10^0 Geodesic Wind Path (Blue) on Tapered Mandrel

3.2.2 Method B

The wind angle at each new point is expressed in terms of Clairaut's Constant and the new mandrel radius. The major difference being that now the carriage advance is used as the independent variable unlike previous method where mandrel rotation is the independent variable. This method is suitable for determining geodesic wind paths over dome ends or complex

surfaces of rotation. The wind angle at any axial position, i, is defined as,

$$\theta_i = \sin^{-1}\left[\frac{C}{r_i}\right] \qquad \text{(Eq. 3.26)}$$

Where C is the constant of Clairaut, θi the angle between the wind path and the meridian of the tapered cylinder, at radius $r i$. Note the basic geometry of the mandrel can again be represented with the linear equation,

$$r_i = (z_i \tan\alpha) \qquad \text{(Eq. 3.27)}$$

$$\theta_i = \sin^{-1}\left[\frac{C}{(z_i \tan\alpha)}\right] \quad \text{or} \quad \theta_i = \psi_{2D}^{i} + \theta_0 \qquad \text{(Eq. 3.28)}$$

Using geometry to find the position along the 2D meridian up from the base of the mandrel corresponding to an increment along the 3D Z axis of the mandrel

$$H = [Rgc - \frac{\Delta z}{\cos\alpha}]$$

$$x_{2D} = H\cos\psi_{2D} \quad \text{or} \quad x_{2D} = [Rgc - \frac{\Delta z}{\cos\alpha}]\cos[\theta_i - \theta_0] \qquad \text{(Eq. 3.29)}$$

$$y_{2D} = H\sin\psi_{2D} \quad \textbf{or} \quad y_{2D} = [Rgc - \frac{\Delta z}{\cos\alpha}]\sin[\theta_i - \theta_0] \qquad \text{(Eq.3.30)}$$

Now it is possible to show that the Constant of Clairaut represents a simple relationship in the 2D map, such that,

$$C_{2D} = \left[Rgc - \frac{\Delta z}{\cos\alpha}\right]\sin\left[\psi_{2D}^{i} + \theta_0\right] \qquad \text{(Eq. 3.31)}$$

It is clear that when the total angular increment reaches 90^0 that an indeterminacy is reached equivalent to the turn around radius. However, that very radius of turn around is now a simple function of the radius of the Great Circle (2d map), Figure 3.1, and cone geometry. For the case of a tapered mandrel at least, one can begin to see the physical interpretations of what

Clairaut's Constant represents. Since as was shown earlier, ψ^{i}_{2D}, is the initial starting angle of the 3D cone surface developed into 2D, which is also ,

$$\psi^{0}_{2D} = \sin\alpha \times 360^{o} \qquad \text{(Eq. 3.32)}$$

3.3 Iterative Solver

A simple method of calculating a geodesic path over a tapered axisymmetric surface is presented in this section. The significance of this method is it's adaptability to a variety of axisymmetric surfaces, including surfaces for which no radius defining function is available. As well the procedure can be readily adapted to surfaces composed of multiple functions. The procedures were incorporated into a simple Lotus 123 spread sheet and proved to be quite effective.

The path begins at a known arbitrary start point with a winding angle determined arbitrarily. This set of conditions then would define the constant of Clairaut for all points where the wind path crosses a meridian.

The iterative solver is set up quite differently from the 2D-3D mapping discussed previously, see Figure (3.9). The wind path, through the start point defined as p1, is projected in the direction of the point p2. The distance along the axis direction, Z, is incremented by a fixed step size, Δz,

Since radius is a function of Z, the taper can be defined by

$$r = mZ + B \qquad \text{(Eq. 3.33)}$$

The new radius is simply

$$r_1 = m\Delta Z + B \qquad \text{(Eq. 3.34)}$$

At this point we know displacements for, two of the three axes of motion, carriage motion ΔZ , and cross-feed motion

$$\Delta r = (r_i - r_{i+1}) . \qquad \textbf{(Eq.3.35)}$$

and remaining to be determined is the amount of mandrel rotation, ψ_i ,such that ,

$$\psi_i = 2\sin^{-1}\left(\frac{\Delta Z \tan\theta^{temp}}{2r_i}\right) \qquad \textbf{(Eq.3.36)}$$

and the new angle between the wind path and meridian is

$$\theta' = \sin^{-1}\left(\frac{C}{r_1}\right) \quad where \quad C = r_0 \sin\theta_0 \qquad \textbf{(Eq. 3.37)}$$

The value of the wind angle at the surface point can now be determined such that

$$\theta = \cos^{-1}\left[\frac{p1a2 \bullet p1p2}{|p1a2| \times |p1p2|}\right] \qquad \textbf{(Eq. 3.38)}$$

from which the Constant of Clairaut can be set if not known initially. The absolute magnitudes of the line segments can be found from

$$|p1a2| = \sqrt{\Delta r^2 + \Delta Z^2} \qquad \textbf{(Eq. 3.39)}$$

and $|a2p2| = \Delta Z \tan\theta^{temp}$ **(Eq.3.40)**

If the initial temporary value θ^{temp} is set at some arbitrarily close value to the desired wind angle, the calculations for mandrel rotation, ψ are simplified. The actual arc length of **a2p2** following the surface is slightly longer at , $(r_0 - \Delta r)\psi_i$

$$|p1p2| = p2 - p1 = \langle r_0 - (r_1 \sin\psi), -r_1 \cos\psi, \Delta Z \rangle \qquad \textbf{(Eq. 3.41)}$$

$$\psi_i = 2\sin^{-1}\left(\frac{\Delta Z \tan\theta_i}{2r_i}\right) \qquad \textbf{(Eq. 3.42)}$$

$$X = r_1 \sin\psi \ , Y = r_1 \cos\psi \ , Z = \sum \Delta z \qquad \textbf{(Eq. 3.43)}$$

$$C = r_0 \sin\theta_0 \qquad \textbf{(Eq. 3.44)}$$

$$\theta_i = \sin^{-1}\left(\frac{C}{r_i}\right) \qquad \textbf{(Eq. 3.45)}$$

The summation of individual angular rotation increments is updated with each increment ΔZ.

The numerical solution was checked at each of the Δz increments where a new value of the wind angle was determined. The value of Clairaut's constant at the new position was checked against the value of C at the start position. The test mandrel was 240" long tapered from 8" radius to 6" radius such that

$$r = -\frac{1}{120}z + 8 \ . \qquad \textbf{(Eq. 3.46)}$$

The value of Δz was set at 0.5", the value of the wind angle θ^{temp} at position zero was 10^0 . As such the value of Clairaut's Constant was determined to be 1.38654. The actual starting wind angle at the mandrel surface is set as 9.9860^0. After iteration to a length of 240" , the value of C had drifted to 1.3858 or an accuracy of .9995%. A comparison of the closed form solution and the iterative method is presented in Figure 3.8. The blue closed form solution was solved for a total of 500 points in MapleV and appears slightly polygonalized. At a higher resolution the two curves appear indistinguishable and are not presented.

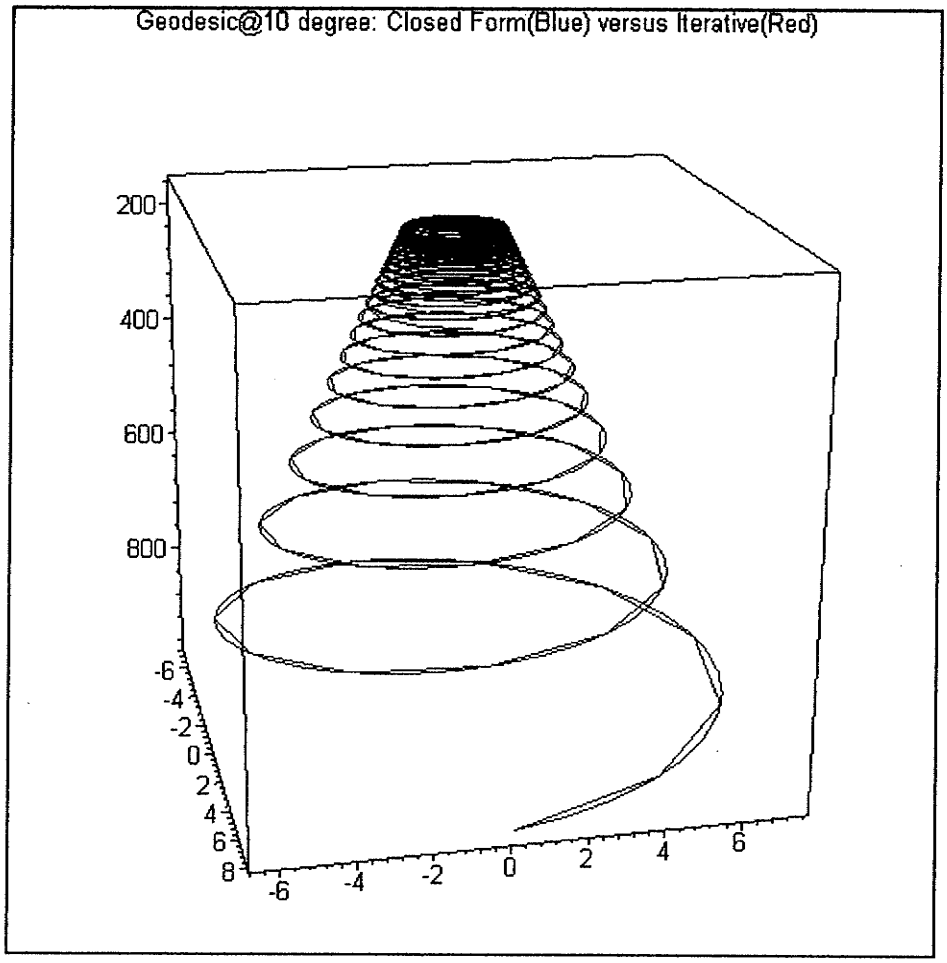

Figure 3.8: 10^0 Geodesic Path Solutions, Closed-form (Blue) Iterative Solution (Red)

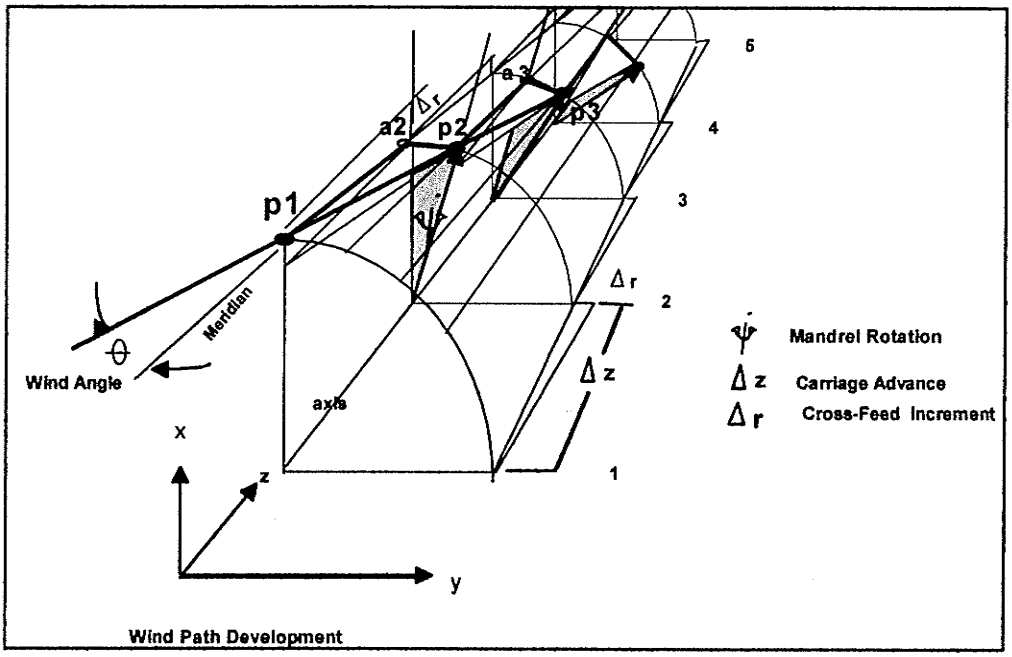

Figure 3.9: Notation Used to Develop Iterative Solutions for Geodesic Wind Path on Arbitrarily Tapered Mandrels

3.4 Machine Motion

The values for position displacement along a geodesic space curve are however insufficient for the functioning of a filament winder. As the solution stands, it is sufficient only to trace the geodesic path over the surface, point by point, as if a pen were placed at the start position tracing the intended path. To affect the proper placement of a filament we require knowledge of the tangent at a given point along the wind path. Since the arc lengths between points are slightly longer than the vector paths, which lie below the actual surface except at the ends, tracing the vector between any two adjacent points along the path is a simple approximation of the tangent to the mid point. Following along the **P1P2** vector (see Fig.3.9) one must clear the surface of the mandrel permitting the payout eye to stand off the mandrel and the

filament thickness. Since we have a method of determining the Cartesian coordinates of the points along the wind path,

$$X_i = r_i \sin\psi_i, \quad Y_i = r_i \cos\psi_i, Z_i = \sum \Delta Z_i \qquad \text{(Eq. 3.47)}$$

A position for the payout eye can be determined with reasonable accuracy.

What is required is to determine a point along the vector , which represents the position of the filament tow, where the radius is greater than the mandrel radius by the arbitrary stand off distance SO. (See Circumferential Wind Path Chapter 2)

$$[mZ_i + b] + SO = \sqrt{X_i^2 + Y_i^2} \qquad \text{(Eq. 3.48)}$$

Note in the above example the values of X and Y are based on the carriage position not the actual wind path. The start position of the payout eye can be determined by extending the tangent from the start position of the filament path. All subsequent displacements of the coordinates of the wind path are applied to the start coordinates of the payout eye.

The techniques for determining the payout eye coordinates are identical to those employed for circumferential winding. Maintaining the tangent points is again possible by rotating the mandrel in reverse to the wind path direction. This still holds true during the reverse or return stroke portion of the wind path. The fact that the paths are mirror images is due to the turnaround effect prior to return.

As mentioned earlier there is a requirement that the continuity of the fiber not be interrupted during the winding procedure. We must work with a

fiber tow of continuous length until the tube is completed. This condition requires that the path reverse itself twice in the length of the mandrel. After a completed circuit, forward and reverse, the path is advanced by an arbitrary angle. Failure to do so will result in each circuit traversing the previous circuit, and therefore closure of the structure is impossible.

The fact that a singularity is reached when the wind angle approaches 90^0 is the basis for control of path direction. Similarly the circumferential wind paths were reversed, however in that instance the deviation in wind angle is very slight. Geodesics wound at low wind angles can not be drifted into 90 degrees as easily as are the circumferential wind paths.

Knowing that the path reverses at a given radius from the Great Circle we must introduce into the mandrel a transition to this lesser radius. Each transition results in one direction reversal. The solution was to use dome ends attached to the mandrel cylinder body. Each of the two dome geometries was made contiguous with the respective position on the mandrel body. The radii could be quickly reduced in a very compact distance without depending on slip. The solution used in this project was to adapt dome technology for controlled geodesic turnarounds.

It is also required to have repeated circuits with appropriate pattern advance after each circuit to complete coverage of a structure. Pattern advance or lag permits the next circuit to be positioned at a desirable location to effect ultimate closure. To accomplish this effect the large dome is arbitrarily chosen as the location of the pattern shifting. At the end of each

circuit the carriage remains fixed in position as the mandrel rotates the appropriate angle prior to the next circuit. This angular increment without carriage travel is referred to as Dwell. Two regions of reversal, one at each end of the mandrel, are therefore required in order to complete a circuit and begin the next.

Using a method introduced by Hofeditz (1962), it is possible to determine the geometry of a stable surface for geodesic winding around a dome ended mandrel. The method was originally proposed for the design of dome ends for pressure vessels, with constant diameter cylinders. The intrinsic assumptions being that there are equal polar opening diameters for both ends and therefore equal dome geometries. However for this study some liberties have been taken with those earlier assumptions, even with maintaining equal polar apertures (*as a direct consequence of having equal diameter support shafts*) the dome geometries for a tapered cylinder are clearly not equal.

The original method is based on netting analysis, balancing the surface forces in the fiber under the influence of a surface normal acting pressure such that the fiber is stabilized by having no slipping forces. The assumption being that in our case with tapered cylinders the stable positions over the dome are identical for a given wind path and identical barrel/ dome diameters. One can see that the dome geometry is a function of the wind angle at the start of a dome or end of a cylinder barrel. A review of this procedure is also given by Peters et. al. ,(1991). Full details are given in section 6.3 .

In this section a simple method of finding the geodesic wind path over a tapered barrel was presented. In view of the previously mentioned limitations due to fiber continuity and the need for two distinct turn around sites there is a further need to plot the geodesic path it travels over the dome and then in the reverse direction.

A computer program based on the previously discussed algorithms was created in a Lotus123 spreadsheet and made to accept input of radii according to the method described by Hofeditz (1962) for dome ends (Chapter 6.3) which was originally a type of manually produced 2D graphic. In simple terms the geometry of the tapered barrel was described by a linear equation where the radius at any point along the Z axis was simply, $r = mZ + b$.The algorithm is set up with an arbitrarily small incremental distance and run between Z=0 and Z= length of the barrel.

The geometry of the domes was determined using a different coordinate system distinct from the barrel, with radius versus X coordinates (discussed in detail in Chapter 6.3). By aligning the X axis with the Z we can get new radius points versus Z+X axial distance. The "Step and Shoot" method is now capable of calculating rotation and carriage advance for the path as it approaches the polar aperture. At the singularity, when the wind angle goes to 90^0, the table of radius values is simply reversed, last in first out order until the next dome interface is encountered and new dome geometry is input as previously.

However, as the path approaches the last singularity one is required to consider the input of a dwell zone to insure proper placement of the subsequent circuit. A simple approach is to solve for the single path as described rotate the mandrel by the calculated dwell amount and reset the mandrel coordinates to the new position as zero position. Now the original coordinates can be reused with no sophisticated recalculations. Obviously a complex geometry that is no longer radially symmetric will require multiple path storage capabilities and larger memory. As such the next example using this technique is limited to a single circuit path.

3.4.1 Example of wind path development

An example (see Figs.3.10) of a low wind angle Geodesic path is presented to demonstrate the development of a wind path using the numerical methods based on the previously discussed equations. The mandrel for this example is a 240" long tapered cylinder, with a butt diameter of 16" and a top diameter of 12". The slope is -1/120 with the large end serving as the start position.

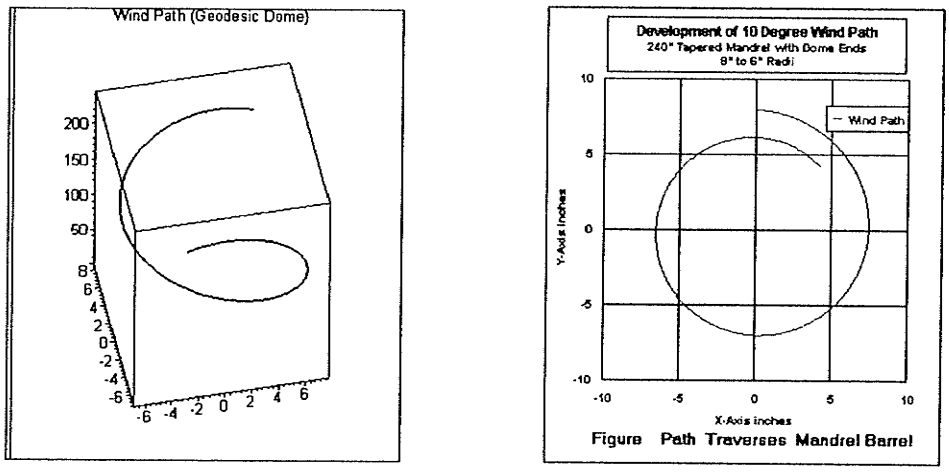

Figure 3.10: Development of 10^0 Wind Path: Path Traverses Mandrel Barrel

Start position is arbitrarily chosen to be on the large end, and for this example the start position is X=0", Y=8" Z= 0". Looking up the Z axis the path appears to be progressing in a clockwise direction consistent with mandrel rotation in a counter clockwise direction. The mandrel is equipped with a dome ended turn around at both ends (*the method for determining exact dome geometry is described in Chapter 6.3*). The domes are by nature unequal in dimension but having equal dome apertures. In Figure 3.10 the path reaches the end of the tapered mandrel barrel and then transitions to the surface of the small dome, Figure 3.11 . The path reaches the maximum height of the dome at a radius equal to the dome aperture seen in the right hand side Top View of Fig. 3.11. At this position the path is now at 90^0 to the meridian. The path may then continue down the opposite side of the dome with 0^0 of dwell , as in Figure 3.12,

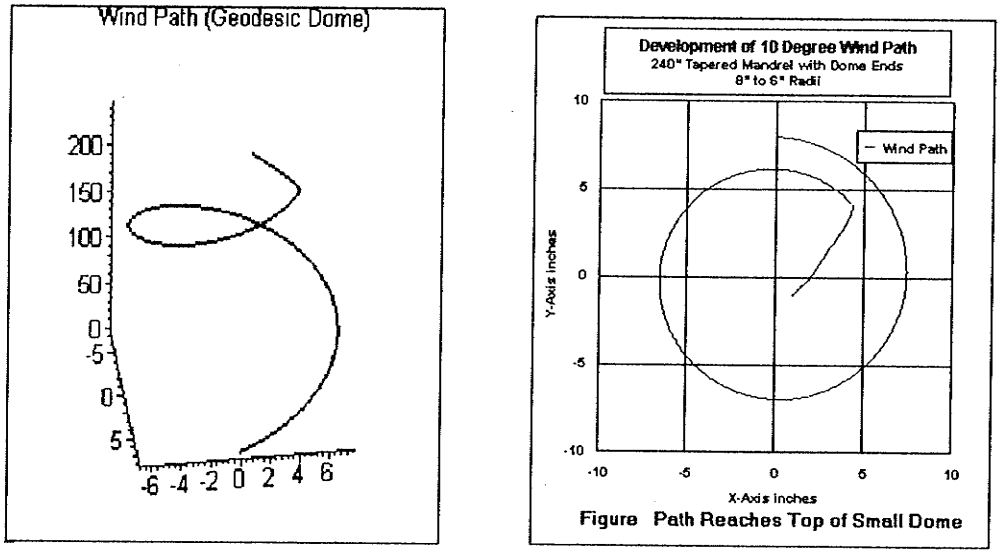

Figure 3.11: Development of 10^0 Wind Path: Path Reaches Top of Small Dome

or it may simply be permitted to rotate for a variable dwell period. As the path descends the dome in reverse direction the mandrel continues to rotate in the same direction. It should be noted that the relationship between mandrel rotation and carriage advance is now highly nonlinear. In Figure 3.12 the path approaches the mandrel barrel. The iterative solver had used radius inputs for the dome solution based on radii input from the dome geometry subroutine discussed in detail later.

Upon completion of the dome solutions a new radius defining function based on mandrel geometry is used. This function is simply the inverse of that used for the first portion of the wind path. In Figures 3.13 and 3.14, the path ascends the mandrel and the large dome. It reaches the point of reversal at exactly the same radius as per the small dome. This position is typically used for primary input of dwell values. As can be seen in Figure 3.15 , adjustment of the dwell angle can be used to set the position of the next circuit start position.

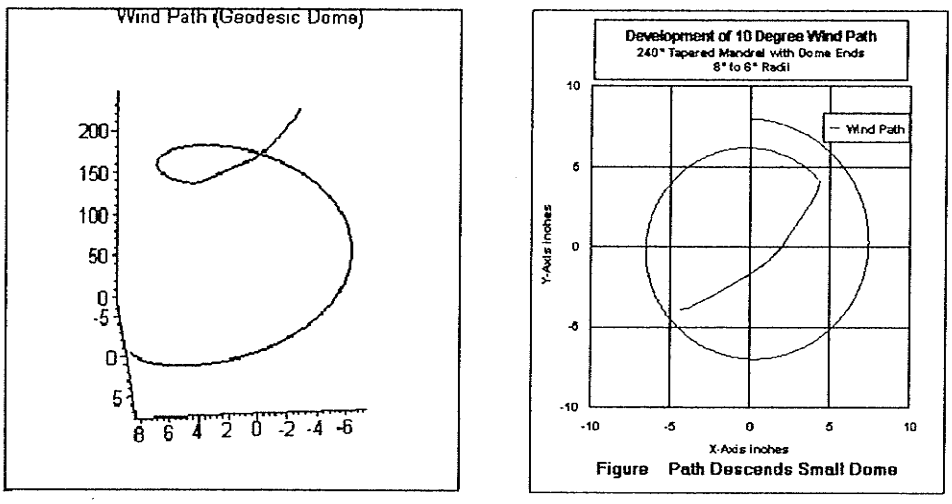

Figure 3.12 Development of 10 degree wind path: Path descends small dome

The computer algorithms were set up in a LOTUS 123 spread sheet, and generated a table of Cartesian coordinates for points along the path. The coordinate table is restructured to facilitate input to MAPLE V. The coordinates are used to generate the space curve that permits dynamic rotation and visualization, Figures 3.13-3.15 .

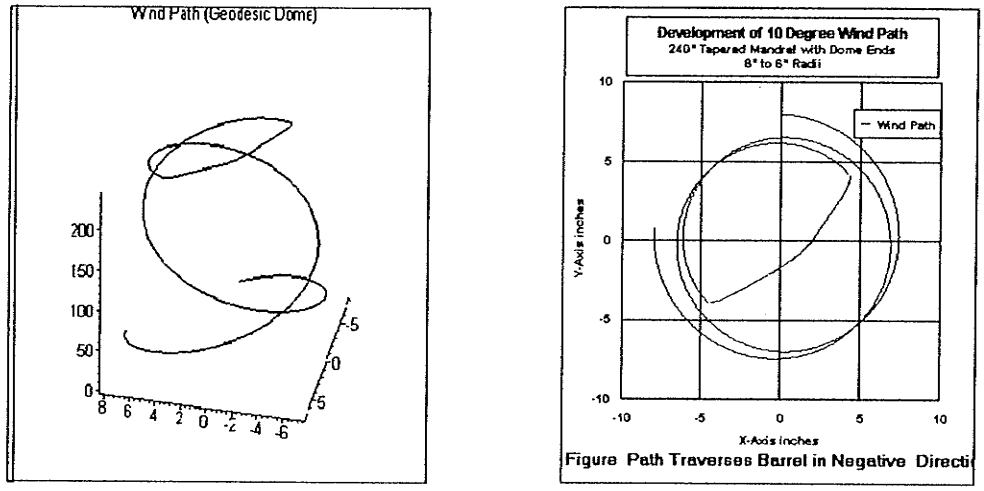

Figure 3.13: Development of 10 degree wind path: Path traverses barrel in negative direction

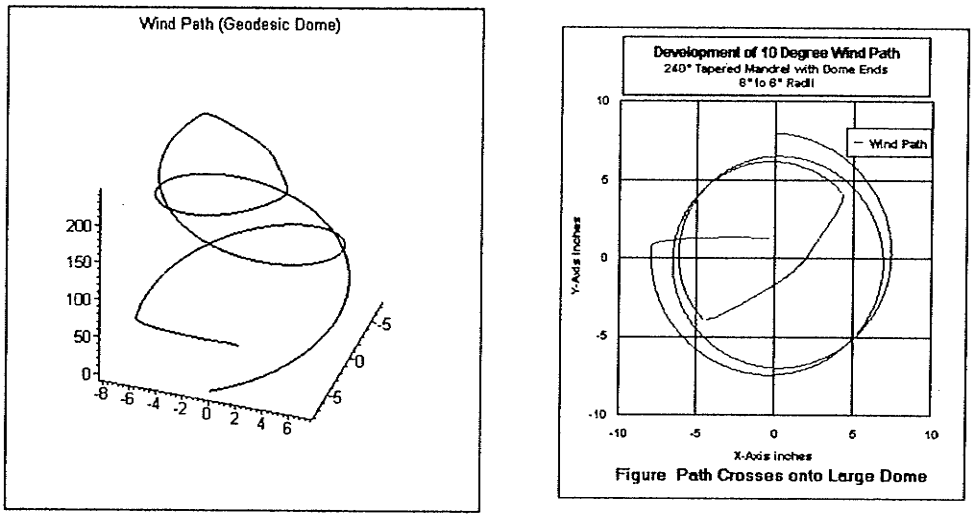

Figure 3.14: Development of 10 degree wind path: Path crosses onto large dome

In the above example the iterative solver was used to determine a geodesic path over a complex surface composed of a linear function and an iterative near spherical surface with no obvious closed form solution.

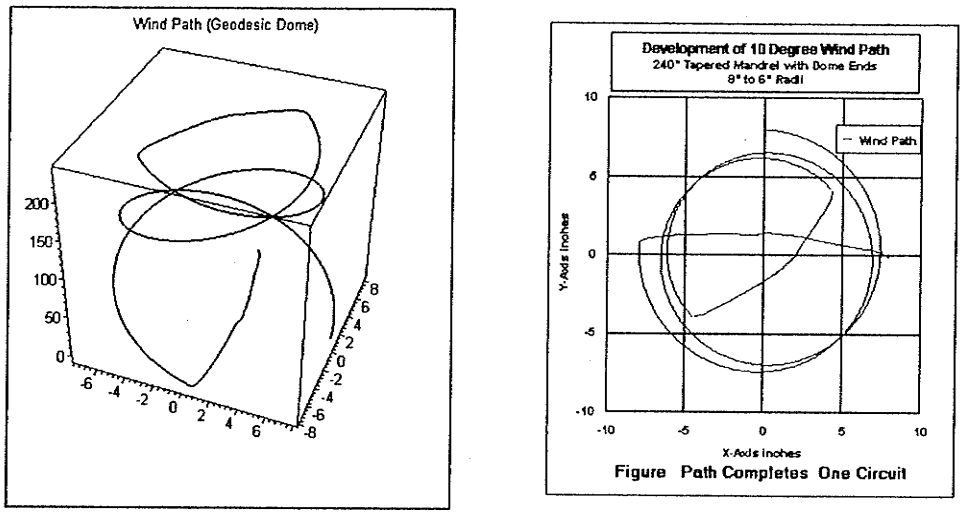

Figure 3.15: Development of 10 degree wind path: Path completes one circuit

4 WIND PATH EFFECTS ON MATERIAL PROPERTIES

4.1 THICKNESS VARIATION

Calculation of the thickness of filament wound laminate layers for tapered poles is presented in this chapter.

Design parameters for finite element analysis of composite structures require the input of material properties and geometry. The classical laminate theory may be used in one form or another to determine laminate properties from a stack of individual lamina each with known material properties.

Essential to using Classical Lamination theory is knowledge of the stacking sequence, fiber orientation for each lamina, thickness and material properties. Any given composite structure is therefore designed by controlling lamina properties and general sequencing of lamina to produce the desired laminate.

Unfortunately, the filament winding process does not produce lamina in the manner assumed by most casual observers of the art. The filament winder is not by definition a lamina winder. The consequence of the winding process is a set of nearly parallel fiber paths oriented in a manner that produces a layer composed of forward and reverse running fibers. It is a layer of interwoven fibers oriented at a positive and negative wind path. The two angles can be thought of as an angle of incidence and an angle of reflection. The Turn Around zone, be it pins or domes, acts as the reflection zone.

Since a filament winding machine does not generate layers directly, the operator or machine programmer must work with the fiber tow and the machine robotics to generate the closed surface. If the product designer requires a laminate of a specific thickness and fiber angle, the production engineer can not directly convert a strand of fiber into a cylinder of given thickness. The wind angle is directly implementable since it describes a relationship between mandrel rotation and carriage advance. The problem becomes even more complex in tapered tubes where the same amount of material is placed over a decreasing diameter and the wind angle changes towards the smaller end.

Thickness is not so easily conceived. Thickness is a fixed metric, normal to a surface. The key issue confronting the process engineer is how to find a fixed thickness measure for a bundle of fibre that appears almost liquid in cross section.

The first problem is how to define the dimensions of a fiber tow. As supplied by the manufacturer we have a tow weight, a specified length of fibre has a given weight. The TEX system specifies the weight of 1,000 metres of fiber. 1,100 TEX is a fiber tow that weighs 1.1 Kg at 1 kilometre. Tow weights may be supplemented by an end count that defines the number of fibers per tow. This does not however give one any further information as to the thickness of the tow nor does the production engineer have any method of calculating laminate thickness.

To solve the problem of finding the thickness metric, first we asked what measure can we in fact derive that approaches the thickness measure. We used the cross sectional area of the fiber tow as used by the filament

winder to develop a procedure to determine thickness of a laminate. Confinement of the fibers into a cylinder produces a circular cross section. Knowing the circumference of the tow, it is straight forward to determine the cross sectional area. Since most Filament winding operators prefer running specific numbers of lines of given TEX, the cross sectional area of the tow is easily determined. The wind path programmer can incorporate this basic information into the machine control processes and insure with a high degree of accuracy that a given winding program generates a layer of specified thickness.

4.2 CALCULATING THE THICKNESS OF FILAMENT WOUND LAMINATE

Knowing the mandrel geometry, and having a fixed cross sectional area, the addition of the total fiber area to the base area yields a composite area that is assumed to be completely concentric with the base section

An additional consideration was the lack of thickness control over the length of a tube. Wall thicknesses are a function of the mandrel radius and wind angle. For tapered tubes of constant wind angle, θ the wall cross sectional area is constant and thickness is simply a function of radius at any given axial position. However the typical non-linear wind angle is not constant and as such the thickness varies with θ. While the band width and thickness remain constant the effective band width increases so that

$$Eff.Band. = \frac{BandWidth}{\cos\theta} \quad \text{(Eq.4.1)}$$

The consequence is thickness build up faster than one would expect on the basis of taper ratio alone. On some parts the waste material volume was found to approach that of the functional material.

An equation for lamina thickness as a function of wind angle and axial location was developed as part of the project and is presented below.

$$t_{(z,\theta)} = \left[2 \times \left[\frac{L^2}{4\pi} \times \frac{1}{BW_e}\right] \times \left[\frac{r_o}{r_z} \times \frac{\cos\theta_o}{\cos\theta_z}\right]\right]$$

(Eq.4.2)

Where L is the circumference of the roving bundle as measured by tying a string about the bundle. BW_e is the effective Band Width of the roving tow. The radii at the zero position is denoted with the zero subscript as is the starting wind angle at the zero position. Both the unknown radius and wind angle, θ can be determined from the basic radius defining function and therefore the wind angle can be found knowing Clairaut's equation (Eq.3.22)

Since the filament winder must produce a positive angle layer at the same time as the negative angle, the factor 2 precedes all other terms of Eq.4.2. The second term establishes a cross sectional area for the fiber tow. The parameter BW_e is set by the operator as the Band width of the tow in the normal direction. Setting this value arbitrarily provides the wind path solver with a means to calculate the correct number of circuits required to close the surface at the start point.

The point at which closure is determined should be ordinarily the greatest radius so that all other axial positions are also closed. The last term is composed of two variables, the first checks for changes in radius and the

second for the drift in the wind angle, making appropriate adjustments to the laminate thickness at each axial position. This algorithm was attached to the "Step and Shoot" wind path solver as a subroutine. The use of the thickness equation requires that the cross sectional area of a single line of given TEX be known. The operator then sets the number of lines he wishes to use in the tow, and the expected Band Width (Figure 4.1). As the wind angle is determined for each point along the tube so is the laminate thickness.

Variation in thickness values for given mandrels have been presented for tapered mandrels previously. While the absolute values are of no consequence the relative changes can be alarming. These variations in thickness due to mandrel geometry also affect the material properties. These issues are linked and later explored in greater detail.

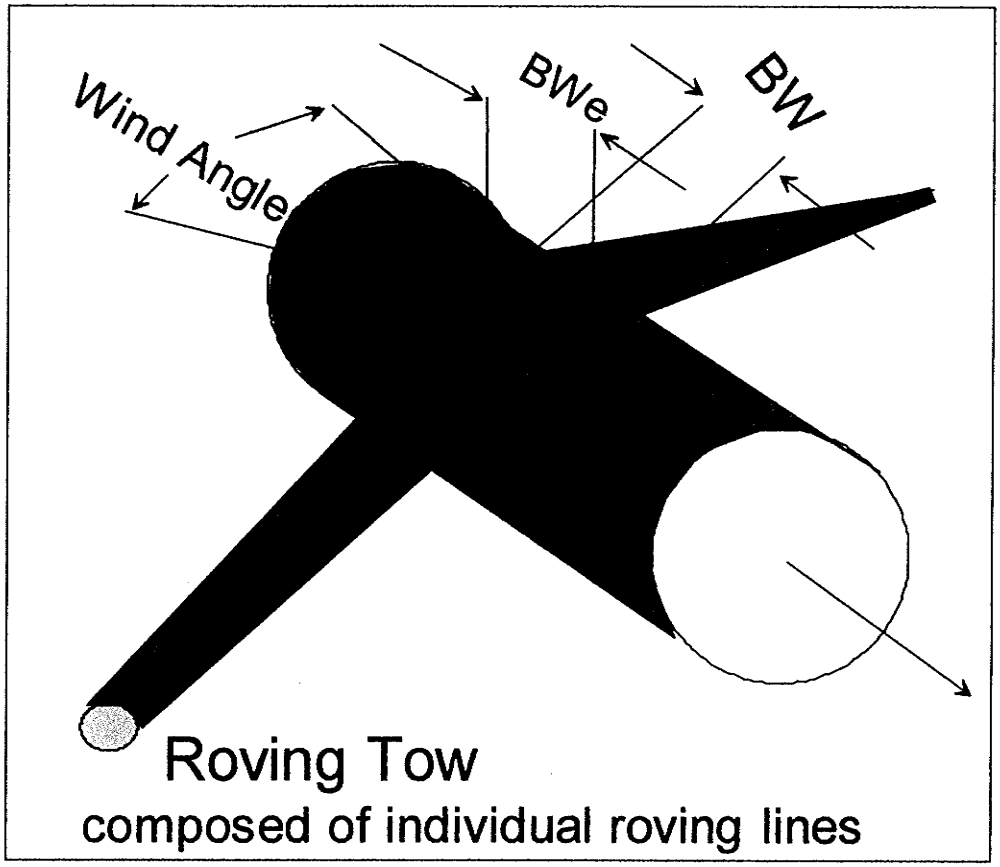

Figure 4.1: Roving Tow with Effective Band Width at various Wind angles

4.3 VARIATION OF MATERIAL PROPERTIES FOR GEODESIC WINDING

Knowing the basic unidirectional material properties for a given fiber and matrix of a composite, E_1, E_2, G_{12}, ν_{12}, ν_{21}, one can begin to calculate the transformed lamina longitudinal modulus using the classical lamination theory (Peters , et al . 1991, Daniel and Ishai, 1993, Tsai,1992).

The effective Laminate axial modulus is a somewhat more meaningful value for designing structures. However to derive this value, the bidirectional nature of the filament winding process is treated as a biaxial laminate, with + and - angle plies corresponding to the winding angle at each axial location.

The thickness of the laminate, h is divided by 2 to get a value for lamina thickness, t_k and the reference plane is taken to be the midplane. Here k, is set to 2, because we are concerned with single filament winding layers of variable angle and thickness.

The determination of effective axial modulus of an Angle Ply laminate according to Daniel and Ishai (1993) can be greatly simplified in this special case and is defined as follows,

$$\overline{E}_x = \frac{1}{h}\left[A_{xx} - \frac{A_{xy}^2}{A_{yy}}\right] \qquad \text{(Eq.4.3)}$$

Where

$$Axx = \sum_{k=1}^{n} (Qxx)^k t_k = h\, Qxx \qquad \text{(Eq.4.4)}$$

$$Axy = \sum_{k=1}^{n} (Qxy)^k t_k = h\, Qxy \qquad \text{(Eq.4.5)}$$

$$Ayy = \sum_{k=1}^{n} (Qyy)^k t_k = h\, Qyy \qquad \text{(Eq.4.6)}$$

Where the value t_k is the lamina thickness h is the laminate thickness and Q_{xx}, Q_{xy} *and* Q_{yy} are the transformed lamina stiffnesses at the desired wind angle, θ.

The basic stress strain relationship for a thin unidirectional lamina under a state of plane stress, along the principal material axes is given to be,

$$\begin{bmatrix} \sigma_1 \\ \sigma_2 \\ \tau_6 \end{bmatrix} = \begin{bmatrix} Q_{11} & Q_{12} & 0 \\ Q_{12} & Q_{22} & 0 \\ 0 & 0 & Q_{66} \end{bmatrix} \begin{bmatrix} \epsilon_1 \\ \epsilon_2 \\ \gamma_6 \end{bmatrix} \qquad \text{(Eq.4.7)}$$

Where the four independent reduced stiffnesses are given as,

$$Q_{11} = \frac{E_1}{1-\nu_{12}\nu_{21}} \quad \text{(Eq.4.8)}$$

$$Q_{22} = \frac{E_2}{1-\nu_{12}\nu_{21}} \quad \text{(Eq.4.9)}$$

$$Q_{12} = \frac{\nu_{21}E_1}{1-\nu_{12}\nu_{21}} = \frac{\nu_{12}E_2}{1-\nu_{12}\nu_{21}} \quad \text{(Eq.4.10)}$$

$$Q_{66} = G_{12} \quad \text{(Eq.4.11)}$$

The transformed reduced stiffnesses for a lamina loaded along an arbitrary x and y axes, in our case the winding angle, are determined using the matrix transformation,

$$\begin{bmatrix} Qxx & Qxy & 2Qxs \\ Qxy & Qyy & 2Qys \\ Qsx & Qsy & 2Qss \end{bmatrix} = [T^{-1}] \begin{bmatrix} Q_{11} & Q_{12} & 0 \\ Q_{12} & Q_{22} & 0 \\ 0 & 0 & 2Q_{66} \end{bmatrix} [T] \quad \text{(Eq.4.12)}$$

Where

$$[T] = \begin{bmatrix} m^2 & n^2 & 2mn \\ n^2 & m^2 & -2mn \\ -mn & mn & m^2-n^2 \end{bmatrix} \quad \text{(Eq.4.13)}$$

And

$$[T^{-1}] = \begin{bmatrix} m^2 & n^2 & -2mn \\ n^2 & m^2 & 2mn \\ mn & -mn & m^2-n^2 \end{bmatrix} \quad \text{(Eq.4.14)}$$

And with the ***m*** and ***n*** terms $m = \cos\theta$ and $n = \sin\theta$

Input of the specific values for the material constants, the general values for the mandrel geometries, and the roving parameters permit solving for the lamina and laminate properties. Using this technique, one can examine the effects of slight alterations to the mandrel geometry and / or wind angle on the tube structural properties. For the examples being demonstrated in this Chapter, the material properties of a typical Unidirectional E-Glass / Epoxy composite are used. The values are taken from Daniel and Ishai (1993) and given as follows,

$E_1 = 39GPa$, $E_2 = 8.6GPa$, $G_{12} = 3.8GPa$, $\upsilon_{12} = 0.28$, and $\upsilon_{21} = .06$.

Ideally the material properties should be determined directly from specimens fabricated from the proposed fiber and resin system, using a process that models the winding system under consideration. It has been noted that significant losses in material properties from the theoretical values often accompany the winding process (Peters et. al. 1991). These losses are referred to as translation losses and have been attributed to damage to fiber during the deployment processes where contact with stripper eyelets and a guide roller is required. While some of these losses may be avoided with better design and tooling, in general there will always be some losses from fibers simply contacting other fibers during the winding process.

In the experimental section of this thesis a procedure is detailed for establishing material values from the actual experimental materials that reflects the production methodologies. Substitution of the experimentally determined material constants for theoretical values is readily implemented in the iterative solver for wind paths.

In the quest for optimal configuration of tubes, it was noted that significant losses of stiffness and unwanted thickness deviations were experienced when adjusting a laminate wind pattern from 5 to 10 degrees (Figures 4.2 to 4.4). Such adjustments may be required to facilitate ease of winding. However, such compromises can affect the structural performance of parts.

Due to the problem of premature turn around, there is a limit to the length of winding possible on tapered mandrels. As a consequence, practical winding angles that cover the required axial distance are limited to lower angles. Winding at 30 degrees demonstrates this point (see Figures 4.2 to 4.4). As the wind path approaches the smaller radii, the angle increases quickly and may approach the limit of 90 degrees before covering the length. In Figure 4.2, one can see the increase in tube wall thickness is dramatic and clearly non-linear.

The iterative solver, presented earlier was modified to make the additional calculations at each solution point. In the preliminary analysis, the wind angle at every point is taken as the ply orientation of a symmetric angle ply. The thickness based on the effective wind angle and radius is determined and used to establish the ply thickness which must be doubled for the + and - angle plies (see previous section). The constitutive matrix is then determined for the point and the effective axial Young's Modulus determined. The axial distance can be used as well to determine the axial bending stiffness (Figure 4.4). Note that the iterative solver never needs to complete all the circuits of the part intended to be produced and relies on the property of radial symmetry. The value of the computer to perform these point-by-point

calculations is clearly demonstrated especially when multiple wind paths are being compared for evaluation. (*At this point in the thesis it should be pointed out that the algorithms are simple and discreet making it possible to conduct all preliminary analysis of theoretical poles with only the use of Lotus 123 spreadsheets.*)

Using the wind angles 5^0, 10^0 20^0 30^0 40^0 and 50^0, the effects of premature turn around are shown for the higher wind angles in Figures 4.2 to 4.4. In the case of the higher wind angles, the effective winding angles approach the 90^0 much sooner than may be desirable and the thickness values increase dramatically (Figure 4.2). The effects of premature turn around can be seen in every one of the three Figures 4.2-4.4 as dramatic inflection of the angle specific plots. Not shown for brevity is the sensitivity of the curves to slight changes in mandrel geometry. The differences for effective axial modulus values between the base and tip regions are plotted in Figure 4.3 and summarized in Table 4.1. The bending stiffnesses for each of the winding patterns is plotted in Figure 4.4

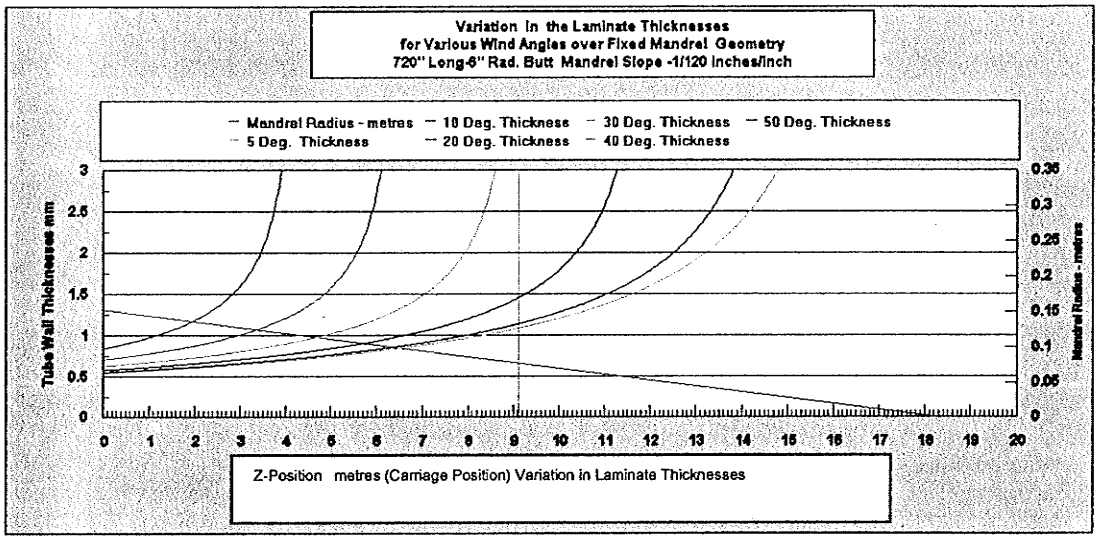

Figure 4.2 Variation in Thickness for various Wind Angles

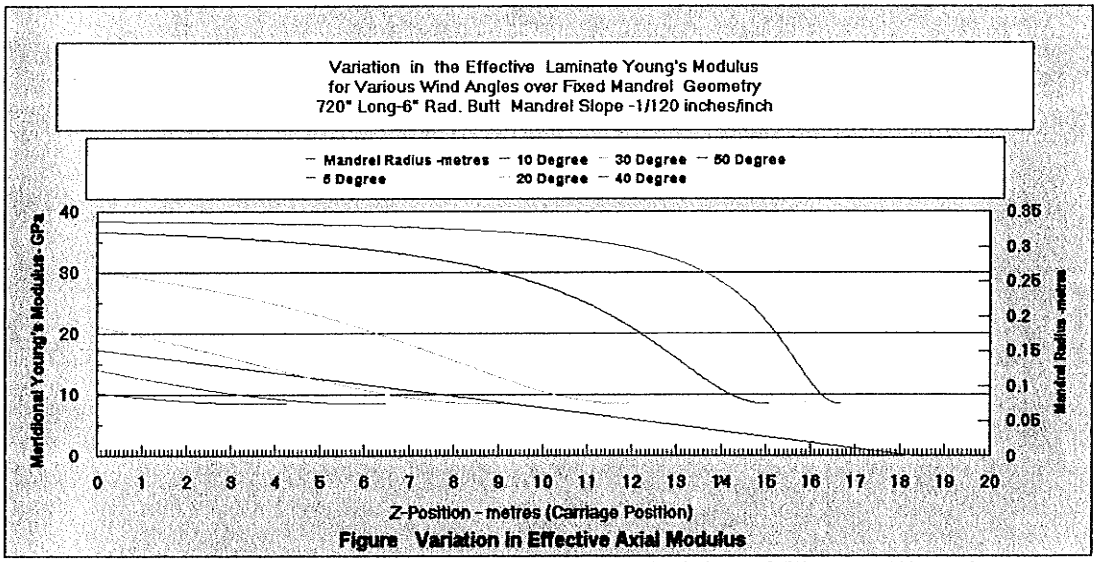

Figure 4.3 Variations in Effective Longitudinal Modulus of Filament Wound

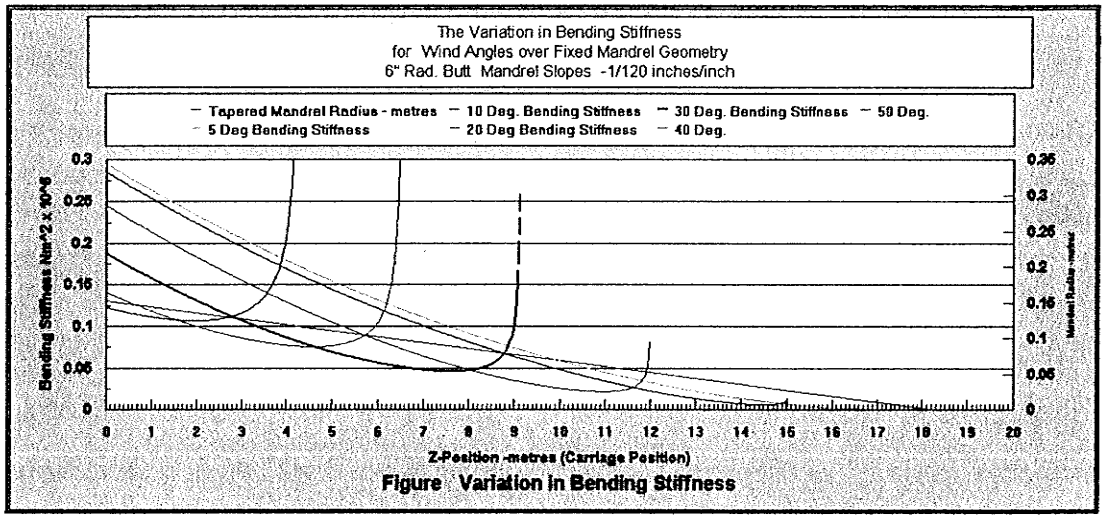

Figure 4.4 Variation in Bending Stiffness

Table 4.1: Comparison thickness and moduli for various winding angles on the same mandrel

Base Thickness	Base E_x (GPa)	Starting Wind Angle	Tip Thickness	Tip Axial Modulus(GPa)
.00054 m	38.42	5	.00109 m	36.69
.000547 m	36.73	10	.001144 m	29.83
.000573 m	30.09	20	.001466 m	12.56
.000622 m	21.23	30	.0138 m	8.59
.000703 m	14.09	40* TA@13.05m	.014 m	8.59
.000838 m	10.31	50*TA@ 8.53 m	.0168 m	8.59

*TA, Turn Around , location noted where failure of complete mandrel coverage occurs.

All configurations in Table 4.1 use the same Band Width, 10 lines of 2,200 TEX E-Glass with a measured Circumference of 0.365 in. The unidirectional Young's Modulus E_x for this material is taken also to be 39 GPa. The mandrel geometry and filament tow values were taken from the actual

values developed to produce the experimental poles used in the Ph.D. thesis of S. Ibrahim (2000).

In the case of a 10^0 wind path over the designated mandrel of 720", a loss of 23% of the original starting modulus is noted. This loss is also accompanied by a substantial increase in tube thickness of over 100% relative to the base thickness. The loss in effective stiffness resulting from increasing the wind angle must be countered by increasing the laminate thickness. Such solutions result in ever heavier poles and consequently poles become ever more costly. Clearly poles built ignoring the premature turnaround issue are unlikely to perform satisfactorily, and clearly a solution to this problem is required.

5 THE JOINTED POLE

5.1 JOINTED POLE CONCEPT

Knowing the difficulties associated with long tapered tubes required for use as electric power transmission and distribution poles, some fundamental changes to the design were adopted to mitigate the consequences. In short, it was decided to begin focusing on the feasibility of using jointed components to assemble a much larger pole.

The basic concept is shown graphically in Figure 5.1 showing the relationships between barrel dimensions and joint length (*J.L.*). However physical constraints and economics play a significant role in determining the minimum acceptable length. In this study, a 20' length for the segments was selected in order to utilize conventional trucking capacity and minimize the number of additional mandrels to be constructed. Much larger mandrels would have required larger support shafts and thus polar apertures which in turn would have forced the use of higher less efficient wind angles.

Other issues related to utility poles that had to be considered included crane capacity, building length and internal working space. The removal of a pole from a mandrel requires that the floor space be able to accommodate the doubling of the actual part. As the part is removed from the mandrel along the length, the inner mandrel length is added to the part length and complete separation occurs at only twice the length when the mandrel is fully exposed.

5.2 SOLUTION TO VARIABLE MATERIAL PROPERTIES

The concept of a jointed pole was justified by assembling an analysis of the individual pole segments, each shown with its own start position, in Figure 5.2.The axial stiffness degrades rapidly with increasing length. For a single segment pole the stiffness is reduced from 37 GPa to less than 8 GPa in total over a 600 inch length (Green Line). If the 600" pole is assembled from 5 lengths each of 120" then the total loss of stiffness is reduced by only 8 GPa (Brown Line).The jointed pole concept demonstrates the stabilizing effect on pole stiffness. However, the tip region remains vulnerable to serious degradation.

The experimental component of the project examines the nature of joint development lengths and thicknesses. The joint design as presented requires a modified region of the mandrel that permits the integration of the joint into the tube winding process eliminating the requirement for both separate production process and complex assembly procedure. Further details on the integration of the joint region with the mandrel are given in the next section.

In Figure 5.3 a superposition of three winding programs is shown. All the segments start at the same wind angle and laminate thickness. To achieve this goal, the actual circuit number for each segment is set for full coverage at its respective base. Figure 5.3 also demonstrates the utility of the previously discussed algorithms when encoded into MapleV software. In Figure 5.4 the jointed pole thickness is compared to that of

single poles. Clearly a substantial control of thickness as well as stiffness variation becomes possible. Further the material usage and cost decline for the smaller segments and the centre of gravity is forced toward the base.

Figure 5.1: Jointed Pole Schematic

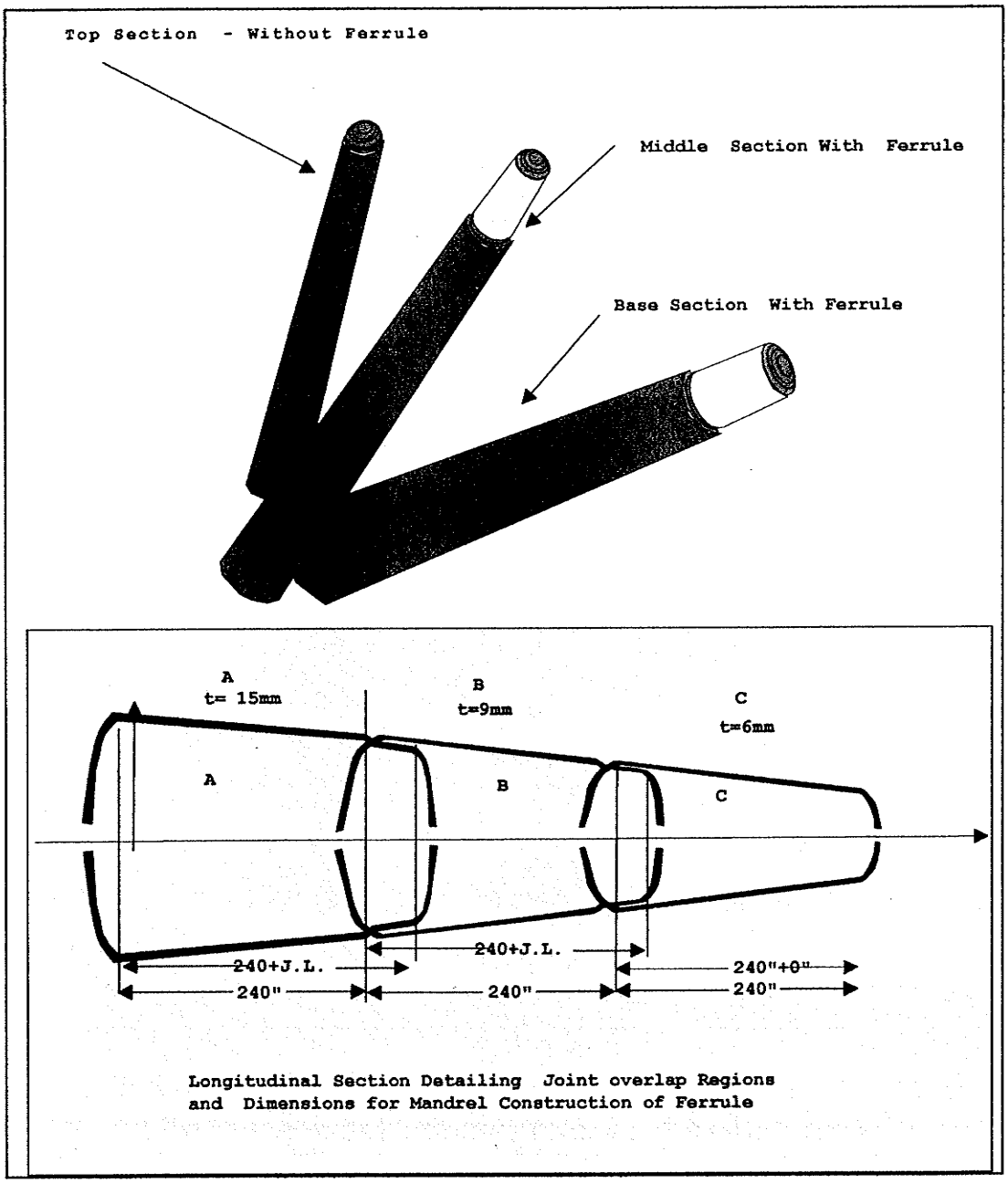

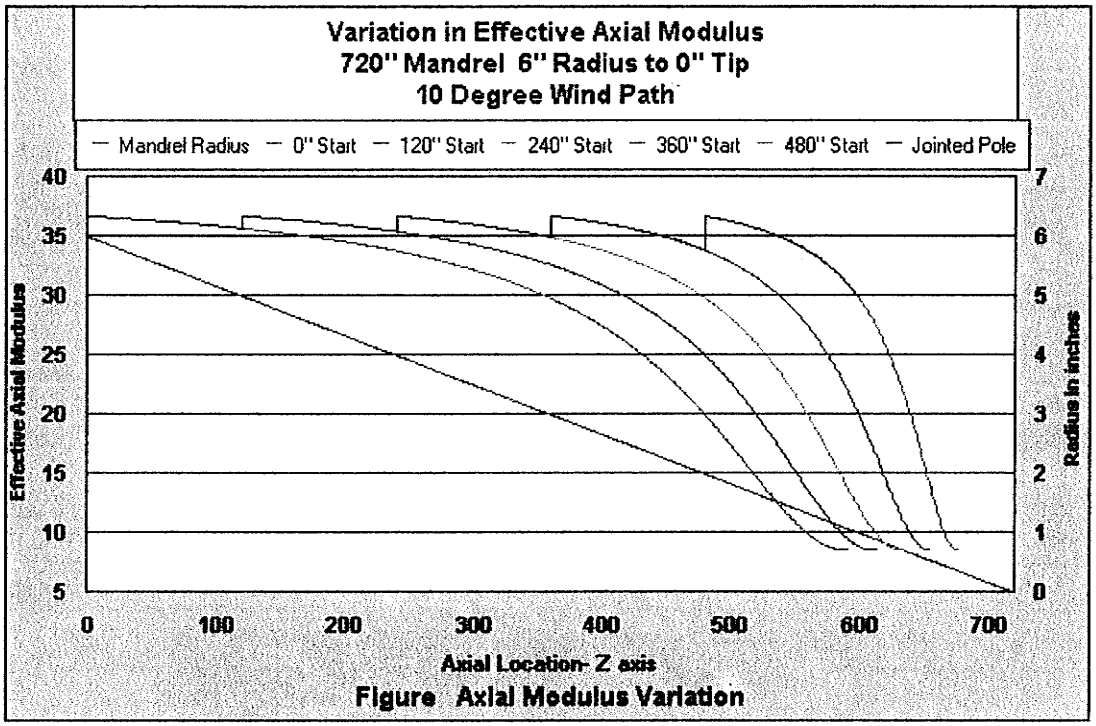

Figure 5.2: Jointed Pole compared to Single Segment Pole – Axial Modulus

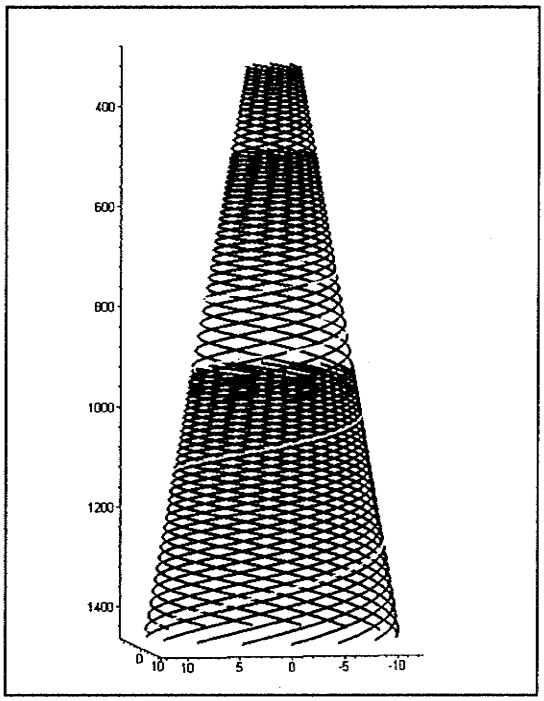

Figure 5.3: Superposition of 10^0 Geodesic wind Path

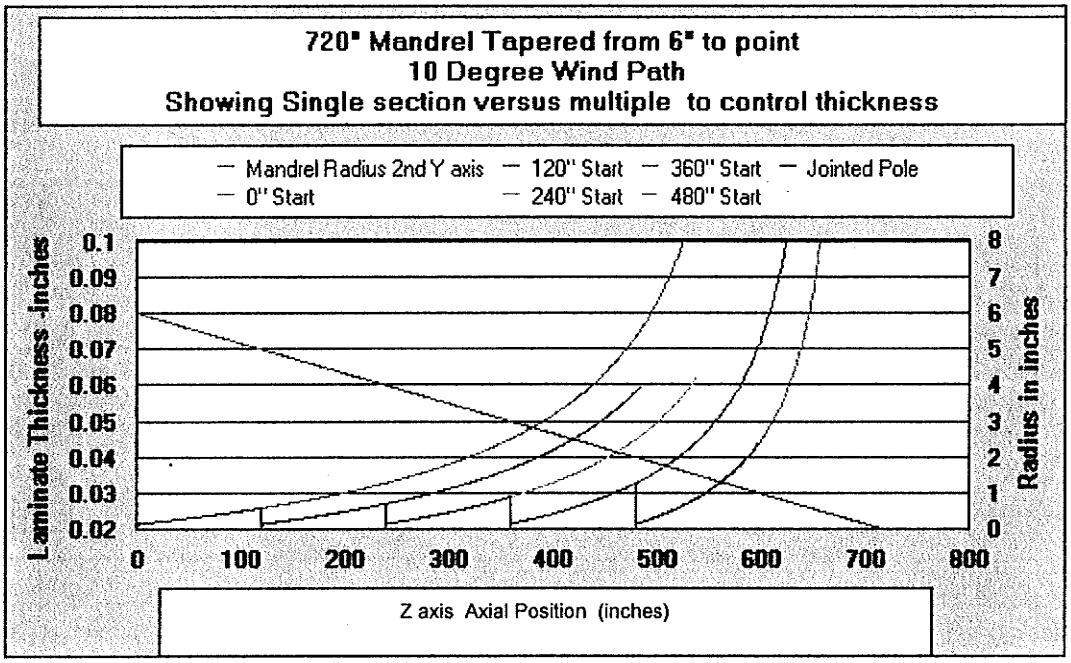

Figure 5.4: Jointed Pole compared to Single Segment Pole – Laminate Thickness

6 TOOLING

6.1 MANDREL DESIGN

The mandrel under consideration was very large and outside of the scope of local metal fabricators to produce at a reasonable cost. Due to the difficulty in obtaining a mandrel, its construction became a paramount issue. As a consequence some innovation in the approach was required.

The winding angles selected for the experimental poles were a combination of near zero longitudinal winding, for high stiffness during bending and circumferential winding for many other reasons, resistance to the ovalization phenomena during bending (Ibrahim, 2000). Two basic types of winding, geodesic and non-linear, were investigated (Figures 1.1 and 1.2).

Non-linear winding is where fiber is wound over a cylinder starting at 90^0 at a zero position and gradually increasing the angle to a desired value over some distance (Figure 1.2). The part is wound for a desired distance at that angle eventually transitioning to 90^0. Once at 90^0 the path can be reversed finishing a single cycle or circuit. Unfortunately such winding requires a large transition length to get from 90^0 down to the desired low wind angle. This results in additional length requirements for the mandrels. Also large amounts of resin and fiber must be removed and discarded to isolate the desired section of the part being fabricated.

The bed length of the winding machine can also impose restrictions on the solution to the problem. We felt that non linear winding would force a

reduction in the effective length being wound within the fixed bed capacity and result in high waste factors.

Non-linear winding was under consideration due largely to the simple requirement for a turn around method at the end of each fiber circuit, in spite of the handicaps. There was one other method available, and that being the use of pin rings shown in Fig.6.1. However, this solution did not solve the stripping force problem and added a large amount of complexity to preparation time and motion control programming. Pin rings also require substantial local mechanical support in order to cope with the tension in the roving lines, which can be very high at low winding angles. Furthermore there is a local distortion of the fiber path in the area adjacent to the pins due to the fact that several circuits are forced to share the same pin.

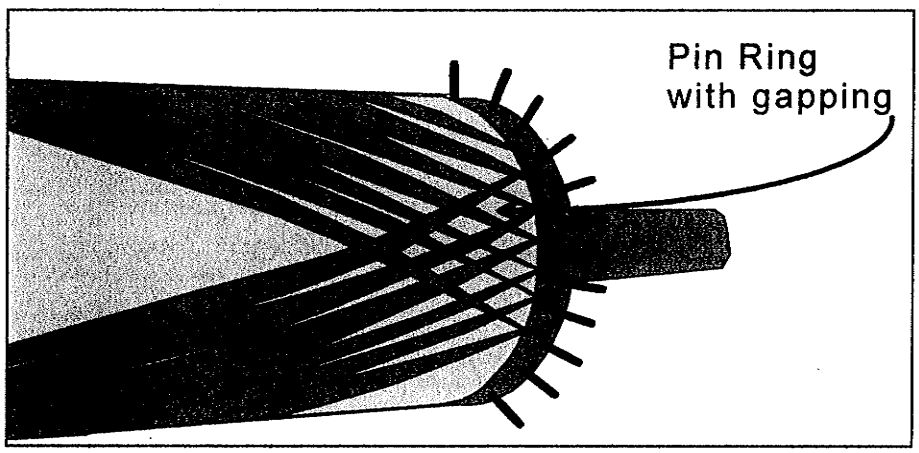

Figure 6.1: Pin Ring Turn around System

After reviewing the literature (Peters et. al. 1991) it became apparent that the pressure vessel industry and some pipe winders used dome ended mandrels to facilitate turn around. It was clear that both industries however were working with constant diameters as shown in Figure 6.2.

Review of the work of Hofeditz (1962) and Peters et. al. (1991) described a technique for generating geodesic dome contours to facilitate winding. Careful consideration revealed that while the dome apertures were necessarily confined to be equal at each end of the mandrel to avoid slippage, no such restriction actually applied to the geometry of the dome. Using the iterative geodesic path solver developed for the project as discussed previously and software developed by McClean Anderson as a reference guide, it was determined that unequal geodesic domes with non- equal apertures were indeed compatible with the geodesic wind path solver used by the McClean Anderson program. In fact the purpose built programs submitted the mandrel and dome designs to the McClean software to see if it could generate the same geodesic path over the proposed surface and generate the proper machine motion codes. Having established the mathematical validity of the concept, it was required to begin the design of such a mandrel.

It is worth noting at this point that the software shipped with our winding machine was not suitable for evaluating or designing tapered mandrels with domes. This left us with a need to understand the design details of the mandrels and geodesic space curves and thus began the process of developing in-house open architecture programs. However, the original McClean Anderson software was always required to convert the wind paths into functional machine motion files controlling the various motors associated with each axis.

In order to mount the mandrel, shafts are required and these were to enter the mandrel through the dome apertures, the size of which was controlled by Clairaut's Theorem (Eq.3.22). The maximum size of the shaft is

determined by the required wind angle, and also by the mass of the mandrel.

Now it was clear that the lower the wind angle, we wished to wind, the smaller the shaft diameters and therefore the mandrel would have to be ever lighter.

It was not clear at the time whether such large parts could actually be wound with such low wind angles, nor whether such light mandrels could survive the enormous forces required for removal of the finished parts, using conventional hydraulic mandrel strippers.

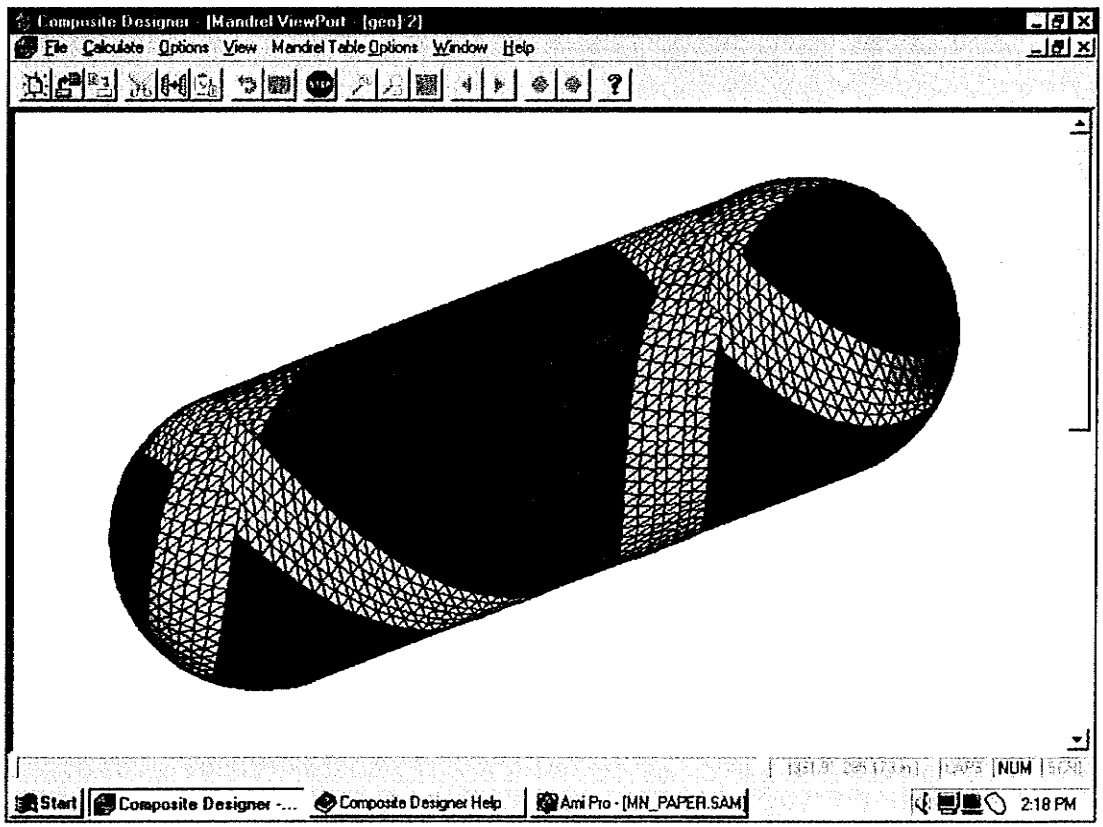

Figure 6.2: Dome-ended Mandrel

Unfortunately no examples of this technique being applied to tapered poles had been discovered during our searches. Also part removal solutions

for pressure vessels were not suitable. Geodesic winding on tapered dome ended mandrels appeared to promise precision control of low wind angle paths, reduced waste, better control of thickness, and fast winding times, but required new and independent solutions .

Using software provided by McClean-Anderson , Composite Designer, simulations of mandrels satisfying the geometry were designed and saved as .mdf and .mtf (mandrel definition files) files. Various wind paths were selected and examined for feasibility of encoding as .mmt (machine motion files) . This exercise would reveal any problems with machine motion and physical envelope limitations. Suitable wind paths were found with acceptable angles as low as from 20 to 10 degrees; it was decided to proceed with the fabrication of mandrels.

Three mandrels were required to produce 3, 20' sections totaling 60 ' with a base diameter of 24" and tip diameter of 12" (Figure 5.1). Step one was the construction of a 20' top section having diameter varying linearly from 16" to 12" with appropriate dome ends and extraction provisions. The taper rate was constant for all 3 poles at 1" of radius per 10" of length. Slope was determined to be (**-1/120**). The radius equation will remain the same for larger sections with only the B component adjusted.

6.2 COMPOSITE MANDREL DESIGN

A method was adopted which relies on a very light skeletal structure composed of high strength plywood stations aligned over a central spine

referred to as a Strong Back. The circular stations required a special tool to be fabricated, that would machine inner and outer circles precisely. In Figure 6.3 the basic arrangement is shown for the station cutting fixture.

The stations were sized such that construction details would assemble themselves to provide an ultimate outer surface matching the pole inner dimensions, Figure 6.4. Contrary to metal fabrication procedures where the starting material is reduced down to the desired dimension, this solution had to purposefully start at an inner position and build up to the target dimension. The circular stations were assembled and bonded to an aluminum spine. Bracing was deployed between stations to increase the shear resistance of the edge bonded structural rings.

The entire assembly was ultimately skinned over with thin wooden Strip-Planks. These strip planks were machined to a constant 3/8" thickness and tapered in width to permit meridian style planking. Each plank when applied over the top of the stations remains fixed in the same meridian path, eliminating the need for "Stealer Planking".

Once the planking was closed, the mandrel was cleaned of all fasteners and roughly machined to a concentric taper in the filament winder. The wooden surface was then laminated with epoxy and fiberglass fabric. This stage provides essential confinement for the very light and fragile core. Dome drive boots were installed just prior to the final closure and the shafts precisely aligned. See next section for dome details. Once the drive assemblies and the planking are closed in the preliminary laminate, the mandrel was mounted in the filament winder and the structural skin stage initiated.

The very first wind program implemented in our project was the coverage of the mandrel body. The mandrel was over wrapped with sufficient layers of fibreglass roving and epoxy resin to build the surfaces up beyond the minimum required pole inner dimensions. Up to this stage the mandrel weight was less than 200lbs. The winding process added almost 300 lbs of glass and resin. As was discussed earlier thickness problems were confirmed. The buildup rate on the smaller end was excessive.

The use of non-linear winding was found to be very problematic. As well as wasting large amounts of material and turn around zones, it was also noted that fibers oriented at near 90^0 were extremely difficult to machine properly. The problem appears to have been tearing out of very long strips of fiber as the cutter heads passed across the roving bundles. This discovery leads us to abandon the non-linear and circumferential winding and use only the geodesic winding patterns.

At the time another option was considered, to switch from cutter grinding heads to abrasive type belts, a process sometimes referred to as "linishing". The costs of conversion were found to be unacceptable and not pursued. These comments are made to qualify our experience and suggest to the reader, that our procedures are not to be considered ideal.

The surface was machined back down to the desired dimensions by substituting diamond bits for carbide bits in the router. The diamond abrasive cutters tended to reduce the fiber pull out problem, and provided a superior surface finish. The cutting debris was found to be so irritating to the machinists that production of the mandrel was stopped to adapt a power driven carriage with a dust extraction system.

The final machined surface was coated with a tooling resin and polished as would any fiberglass mould. The original mandrel design included a parallel system of internal air lines to provide air pressure assisted extraction of the completed parts. The air inlet ports were hidden beneath the dome face of the large end. The ports could be accessed only after the dome end was displaced by several inches. Since the large dome end is not used for extraction it is quite easy to release once a circumferential parting cut is made around the end of the big end of the barrel. Note that the barrel ends are covered with ¼" (6mm) steel plate specifically to assist the dome parting cuts.

The air release system was later abandoned when new tooling surfaces and release agents had reduced the required extraction force to less than 100 foot pounds of torque for a 20 foot (6 m) pole. The finished weight for the 20' long ,varying diameter of 16" to 12" tapered mandrel was approximately 390lbs (177 kgs). The drive boot assemblies made up approximately 40% of the total weight.

At the time of writing the prototype composite mandrel is still in service periodically and has exceeded 40 parts, some of which have weighed as much as the mandrel itself. The materials cost was less than $5,000 CDN, much of it spent on the tooling fixtures and router carriage system. The process has since proved to be well suited to the fabrication of low cost production quality tooling and has been adopted as the method of choice.

The process of building a low cost composite mandrel was driven primarily by economic considerations, but revealed a host of opportunities not

previously considered. In our situation the payout eye and its carriage were mounted on the reverse side of the mandrel to the router carriage. As such the router carriage did not obstruct the winder performance as long as the cutter heads were retracting from the surface. This relationship revealed that a filament winder could be adapted easily to become a combined manufacturing station.

By incorporating the machining heads into the robotics system, a complex series of machining processes could be performed on a part before it is removed from the winder and mandrel. The integration of the various processing technologies into the winding machine opens the possibilities for the technology not possible currently on any other type of composites fabrication process.

There is clearly a very accurate positioning system available for a number of drilling and cutting operations as well as testing procedures. Winding can be broken up into a number of stages interspersed with machining and material testing processes. The part that is ultimately removed from the machine may not require any further processing costs, since even the finishing process can be performed in the machine as was proved with our mandrel polishing procedures.

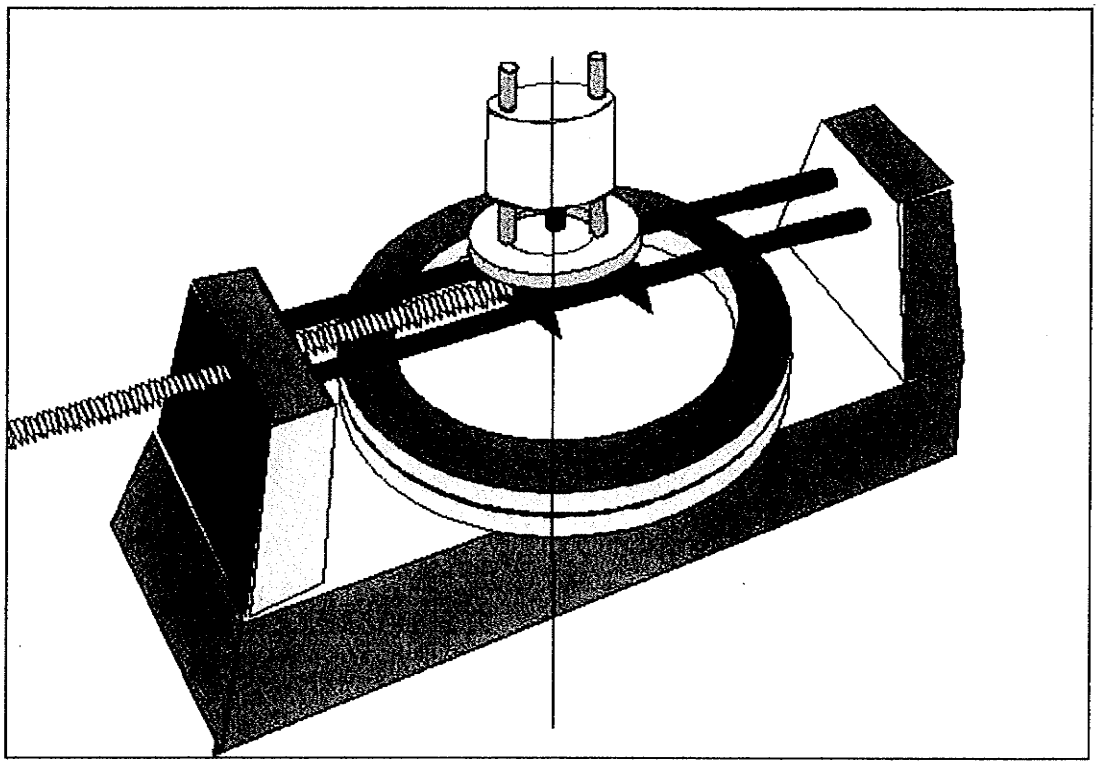

Figure 6.3 Tooling Fixture for Cutting Precision Cross-Sectional Mandrel Stations

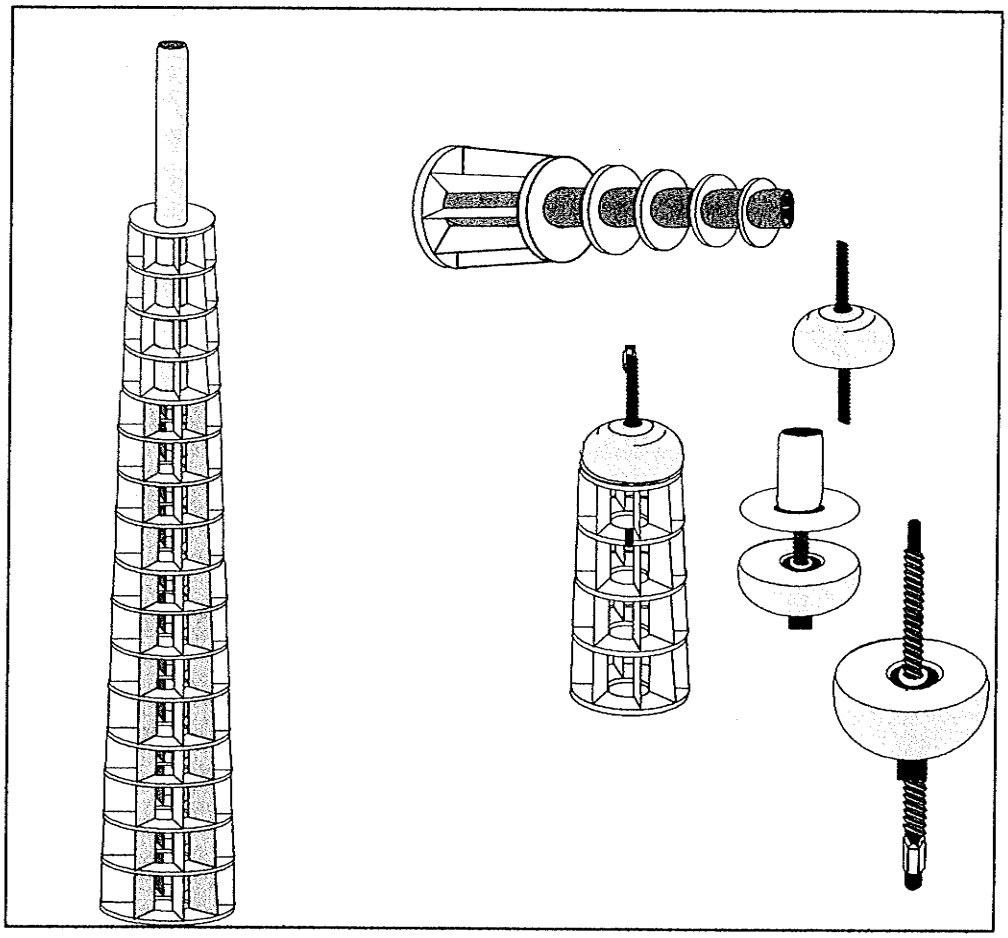

Figure 6.4: Composite Mandrel Skeleton

6.3 DOME-ENDED TURN AROUND: GEODESIC DOME MODELLING FOR SPECIFIC WIND ANGLES

The method of calculating ideal dome geometry for geodesic domes was adapted from the work of Hofeditz (1962) which was based on "Netting Analysis". The technique was commonly used by pressure vessel designers for its simplistic approach. Netting analysis permits the designer to neglect entirely the contributions from resin, as well as assuming stable geodesic wind paths. The geodesic stability permitted modeling of fibre forces per unit length

on a shell element to be in equilibrium with the internal pressure, p_i directed outwards and normal to a surface point. Cook and Young (1985) and Peters, et. al. (1991) describe the meridional and hoop membrane forces per unit length in terms of the hoop and meridional stresses as

$$N_M = \sigma_M t = \frac{p_i R_H}{2} \qquad \textbf{(Eq.6.1)}$$

$$N_H = \sigma_H t = p_i R_H \left(1 - \frac{R_H}{2R_M}\right) \qquad \textbf{(Eq.6.2)}$$

The two stress in the meridional and hoop directions are σ_M *and* σ_H respectively. The radii of curvatures in the meridional and hoop directions are respectively R_M and R_H . The term t denotes the thickness of the shell element.

Hofeditz (1962) and Peters, et. al. (1991) note that the membrane forces can also be resolved in terms of fiber forces acting on a unit length in the two principal directions. Figures 6.5 and 6.6 illustrate graphically how the meridional and hoop stress resultants are determined, respectively. The fundamental assumption being that the force per fiber is every where constant and equal. This assumption is principally due to the nature of geodesic filament winding where the fibers are stable under the influence of tension over a surface, having no slippage or shear forces to displace the fiber.

Hofeditz(1962) describes the two stress resultants in terms of fiber forces as

$$N_M = nT\cos^2\theta \qquad \textbf{(Eq.6.3)}$$

$$N_H = nT\sin^2\theta \qquad \text{(Eq.6.4)}$$

Please note that *n* is now defined as the number of fibers per unit length and T is now tension or Force per Fibre. The product of n and T is Force per unit length.

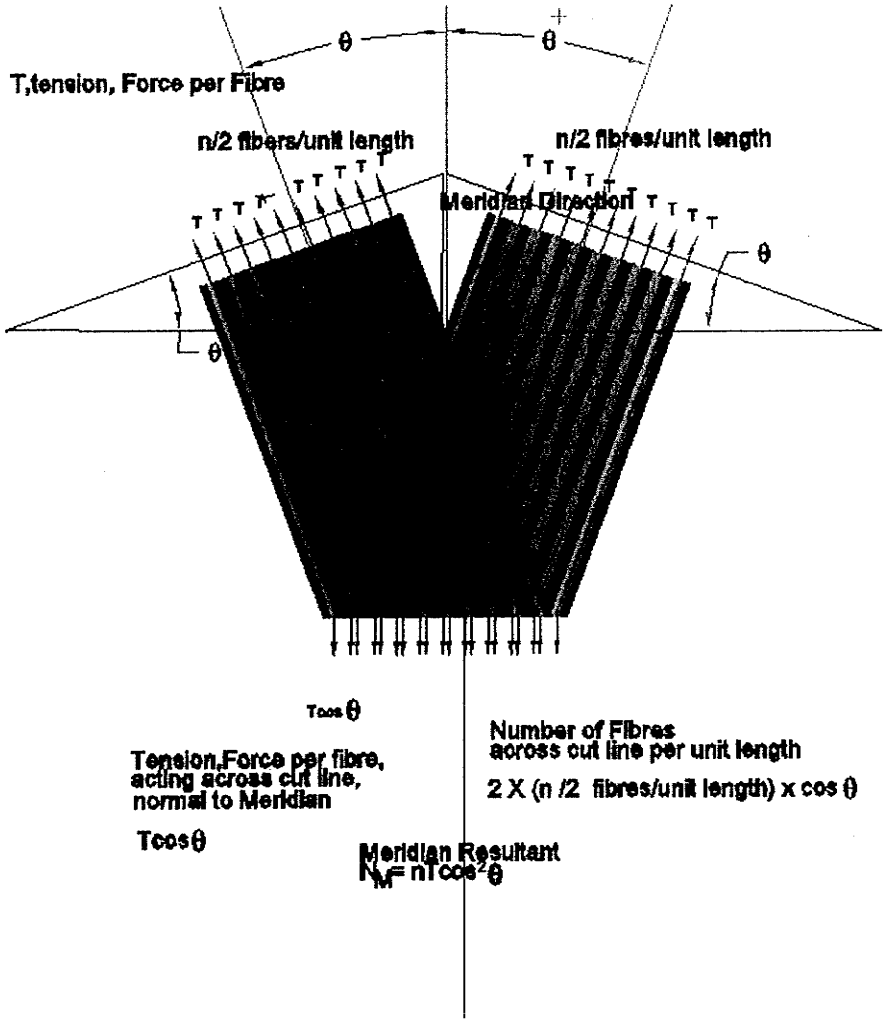

Figure 6.5 Meridional Resultants

Figures 6.5 and 6.6 show how to transform the Tension and number of fibres per unit length, oriented at an angle $\pm\theta$ with respect to the meridian, into forces acting across a cut line normal to either the meridian or the hoop axes.

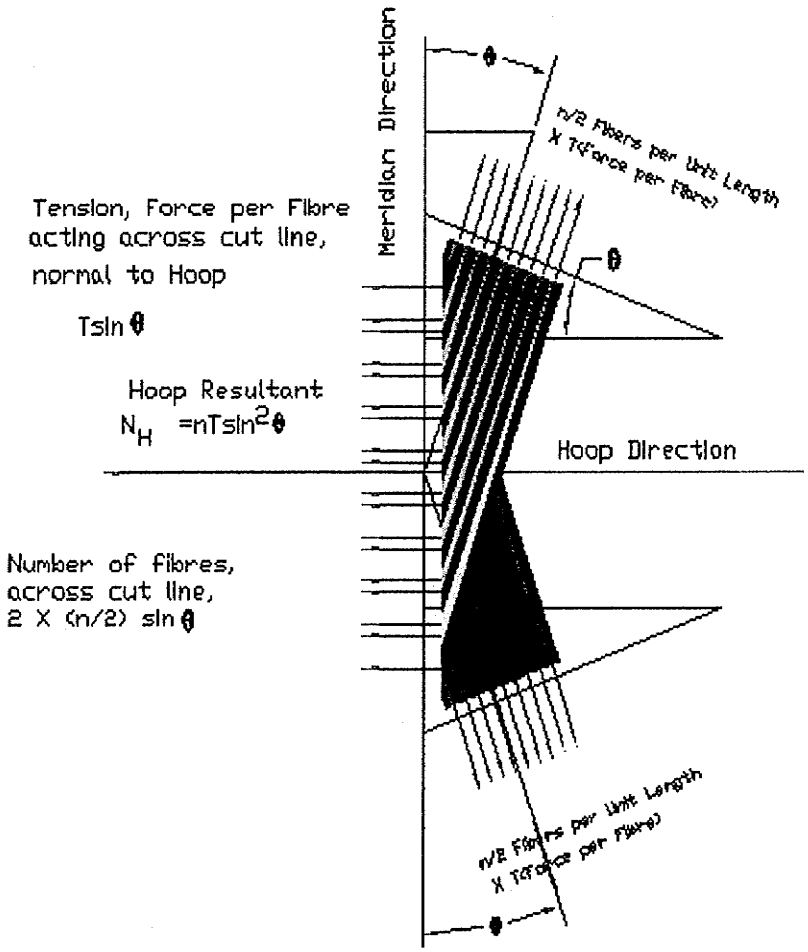

Figure 6.6 Hoop Resultants

Equilibrating the equations Eq.6.1 and 6.3 to eliminate the membrane resultant gives

$$\frac{p_i R_H}{2} = nT\cos^2\theta \qquad \textbf{(Eq.6.5)}$$

$$\frac{p_i R_H}{2}\left(2 - \frac{R_H}{R_M}\right) = nT\sin^2\theta \qquad \textbf{(Eq.6.6)}$$

To eliminate the θ terms, recall that

$$C = r\sin\theta \quad or \quad \sin\theta = \frac{C}{r} \qquad \textbf{(Eq.6.7)}$$

and using trigonometric relationships $\cos\theta = \frac{\sqrt{r^2 - C^2}}{r}$ **(Eq.6.8)**

Note that a new radius term r has been introduced by Eq.6.7 and refers specifically to the distance between the mandrel or dome surface and the axis of revolution at right angles to the axis. The two equations Eq.6.5 and 6.6 can now be written as

$$\frac{p_i R_H}{2} = nT\left(\frac{r^2 - C^2}{r^2}\right) \qquad \textbf{(Eq.6.9)}$$

$$\frac{p_i R_H}{2}\left(2 - \frac{R_H}{R_M}\right) = nT\left(\frac{C^2}{r^2}\right) \qquad \textbf{(Eq.6.10)}$$

Hofeditz(1962) points out that Eq.6.9 and 6.10 are not independent. Since if one divides Eq.6.4 by 6.3 the result is a relationship dependent on wind angle

$$\frac{N_H}{N_M} = \tan^2\theta \qquad \textbf{(Eq.6.11)}$$

Dividing Eq.6.10 by Eq.6.9 results in the following equation

$$\frac{R_H}{R_M} = \frac{2 - 3\left(\frac{C}{r}\right)^2}{1 - \left(\frac{C}{r}\right)^2} \qquad \textbf{(Eq.6.12)}$$

The method was also presented by Peters,et.al.(1991) in a slightly different format in order to resolve thickness of fibers to balance an internal pressure. Cook and Young (1985) present a discussion of a technique used to generate dome heads for pressure vessels based on the work of Biezeno in 1922. This technique appears strikingly familiar to the dome development discussed by Hofeditz (1962) and Peters et. al. (1991) and presented in the following discussion.

The geodesic dome contour profile can be generated in the 2 dimensions and given to the machinist for shaping each of the dome ends. The method presented in the following discussion was designed to permit graphical solutions to be generated by the Lotus 123 spreadsheet program. Fig.6.7 illustrates the construction of a generalized small end dome contour. Since a mandrel typically requires two domes, the large end dome contour can be solved by inverting the following procedure. The coordinates for the dome contours are self referential, so that they will still require transformation when coupled to a particular mandrel. This union of two domes with an intermediate barrel is required to solve for a complete wind path as was illustrated previously in Figs.3.11-3.15.

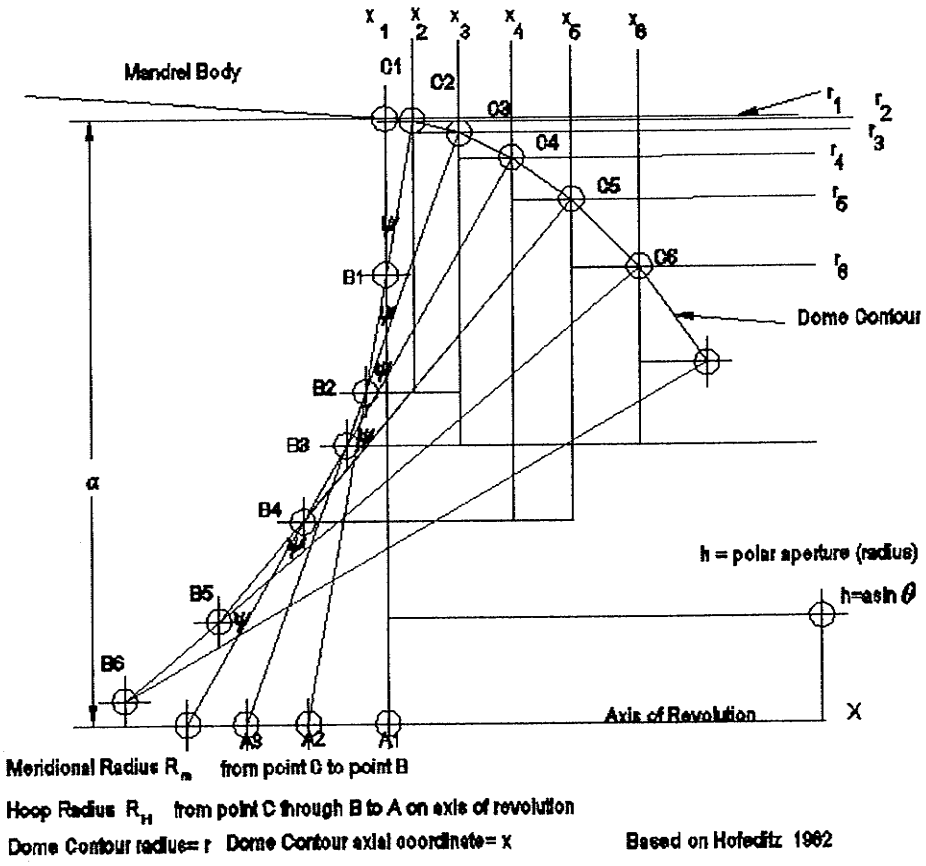

Figure 6.7: Geodesic Dome Contour Generation

For the first step or iteration the procedure requires that one start at the equator of the dome where x=0 ,r=a (the radius of the equator). The initial hoop radius, $R_H^1 = a$ (*the superscript denotes the iteration number*) is identical to the equator radius. The dome radius, $r_1 = a$ for the first iteration (*the subscript denotes the iteration number for this variable*). The winding angle with respect to the meridian is, $\pm\theta$, at the mandrel dome interface and must be established first in order to determine both the polar aperture radius, h and Clairaut's Constant, C since both are equal to the product $a\sin\theta$ discussed previously.

Substituting the parameters ***C, h***, and ***a*** into Eq.6.12 and gives a value for R_M^1, the meridional radius. Referring to Figure 6.7 the hoop radius, R_H^1 is laid out from point C1 to A1 and the meridional radius, R_M^1 from C1 to B1.

Now the procedure requires that the line from C1 to B1 be swung through an arbitrary angle, ψ, to point C2. The choice of angle, ψ should be limited to a very small value in order to avoid polygonalizing the contour. In this project the increment angle was set to 0.1 degrees. Having established point C2 it is possible to determine the Δx and Δr values to yield the x_2 and the r_2 values.

$\Delta r_1 = R_M^1 - R_M^1 \cos\psi$, (the change in radius) **(Eq.6.13)**

$\Delta x_1 = R_M^1 \sin\psi$, the meridional increment **(Eq.6.14)**

$r_2 = a - \Delta r_1$, solution required for next iteration **(Eq.6.15)**

$x_2 = x_1 + \Delta x_1$, solution required for next iteration **(Eq.6.16)**

$$R_H^2 = (R_H^1 - R_M^1)\frac{R_M^1}{R_M^1 \cos\psi} + R_M^1 \qquad \textbf{(Eq.6.17)}$$

$C2A2 = R_H^2$, is the new Hoop radius

Second Iteration,

$$\frac{R_H^2}{R_M^2} = \frac{2 - 3\left(\frac{C}{r_2}\right)^2}{1 - \left(\frac{C}{r_2}\right)^2} \qquad \textbf{(Eq.6.18)}$$

Note second angle increment by ψ for a total of 2ψ angular advance.

$\Delta x_2 = R_M^2 \cos(90 - 2\psi) - R_M^2 \cos(90 - \psi)$ **(Eq.6.19)**

$\Delta r_2 = R_M^2 \sin(90 - 2\psi) - R_M^2 \sin(90 - \psi)$ **(Eq.6.20)**

$r_3 = r_2 - \Delta r_2$ **(Eq.6.21)**

$$x_3 = x_2 - \Delta x_2 \qquad \text{(Eq.6.22)}$$

$R_H^3 = \dfrac{r_3}{\cos(2\psi)}$, new Hoop radius for next iteration,

(Eq.6.23)

The start of the third iteration which is now 3ψ degrees and the solution to the new meridional curvature radius, R_M^3 becomes

$$\frac{R_H^3}{R_M^3} = \frac{2 - 3\left(\dfrac{C}{r_3}\right)^2}{1 - \left(\dfrac{C}{r_3}\right)^2} \qquad \text{(Eq.6.24)}$$

The procedure is repeated until $r = C = polar\ \ aperture = h$

Note that the value of the polar aperture must be the same for left and right domes as it should be constant for compliance with the theorem of Clairaut, however the domes themselves will be quite different in geometry. To comply with the theorem we should modify one dome or the other to reflect the proper wind angle at the equators so that C is equal.

If the wind path were to deviate either through slip or some other method as it approaches a dome equator then establishing a new value of C, one can alter the dome aperture to some degree. Having non-equal dome apertures is the principal driving force behind the search for non-geodesic solvers. In effect the non-geodesic paths being sought are very small perturbations of a geodesic path and are not random in any way (Maheswaran (1998) and Denost (1982)).

In the following Figures 6.8 , 6.9 and 6.10 , the same mandrel barrel is used to show how the large and small dome ends must be changed to accommodate different wind angles. The mandrel is 120" (3048 mm) long with a slope of 1/120, base diameter 6" (152mm) and top diameter of 4" (101.6 mm). In Figure 6.6 the start wind angle at the base is 10^{o} drifting to 15.09 ^{o}. Since the barrel radius changes by 1" (25.4 mm) the two domes require different geometries accommodating the appropriate wind angles. Note that the dome apertures are significantly different. This situation can limit the size of the drive screw mechanism employed at the two ends. When the Figures 6.6 ,6.7 and 6.8 are compared, it is clear that low wind angles will require smaller drive shafts limiting the suspended weight of the mandrels. Higher winding angles permit greater latitude with drive shaft diameters at the expense of axial stiffness of the structure. The red plot is for the large end dome , the green line the small end dome and the blue line is the dome aperture required at the small end.

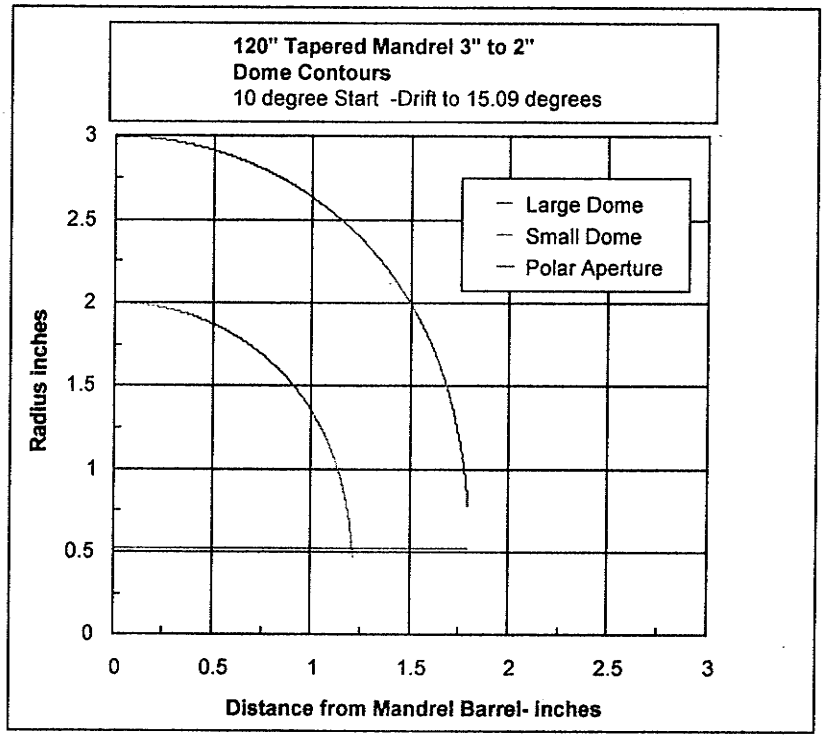

Figure 6.8 Dome Contours for Small and Large Domes with 10 deg. Start

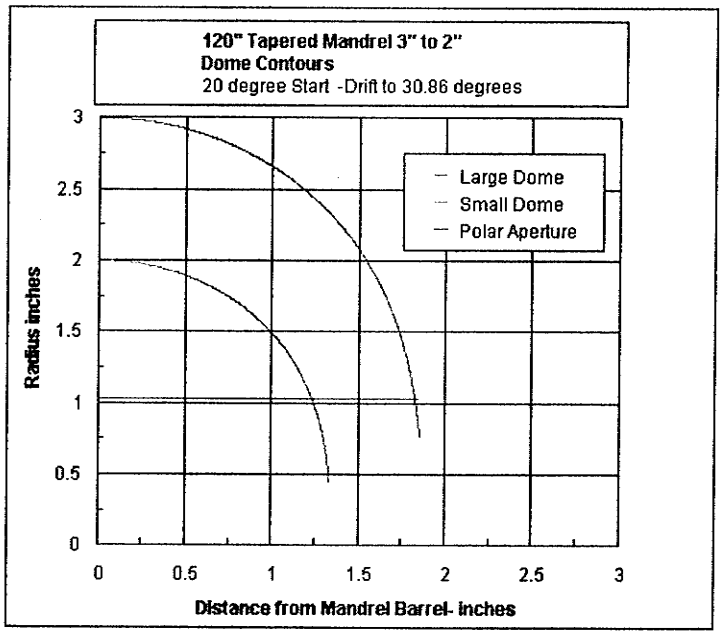

Figure 6.9 Dome Contours for Small and Large Domes at 20^0. Start on Large Dome.

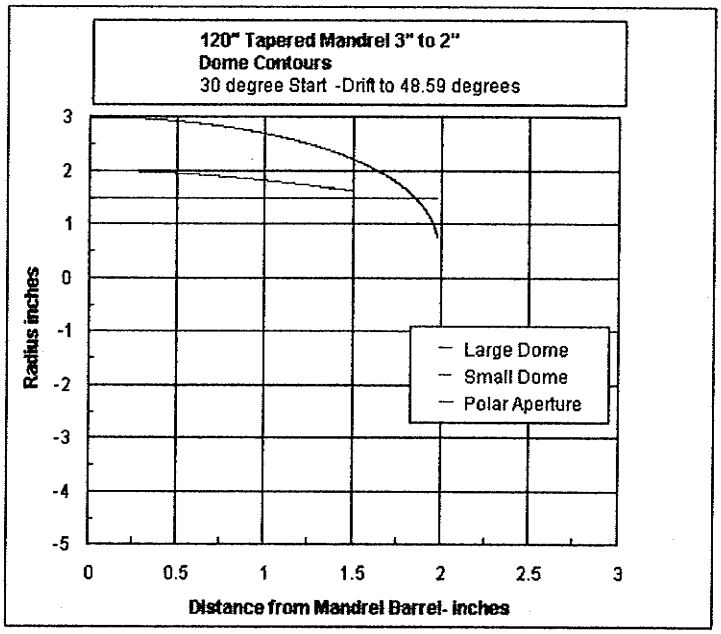

Figure 6.10: Dome Contour for Small and Large Domes at 30^0 Start on Large Dome

6.4 SELF-EXTRACTING DRIVE MECHANISM

The drive boots and thrust plates must be installed on their respective ends of the cylinder to permit fixturing of the assembled mandrel to the winding machine. Once the composite cylinder is completely closed and drive shafts and domes installed it can be mounted directly into a filament winding machine for final application of glass fiber.

Domes must be previously completed, covered with epoxy / glass and have the surface prepared. The mandrel cylinder must be wrapped with sufficient layers of fiber and resin to permit precise machining to the required dimensions. However dome geometry must remain fixed. This requires that the fiber bond to the mandrel cylinder and not to the domes. A release agent is applied to the dome surfaces.

Once the mandrel is completely surfaced the extra material is removed from the dome ends. The requirement of dome ends during mandrel fabrication illustrates the importance of providing a means for the filament path to reverse directions. While great effort was previously described in determining the ideal fiber path for poles, this effort is also fundamental to fabricating mandrels. Clearly the working surface of the mandrels must be wound with a controlled thickness of material. A typical non-linear wind path with dog-bone ends would have resulted in uncontrolled thickness build up at the ends where the path reverses direction. Furthermore, circumferential winding would have made no significant contribution to the axial stiffness of the composite mandrel. Due to the method of machining, problems were encountered with circumferential layers peeling in strips during the machining process.

The ends of the mandrel incorporated an innovative screw drive device to which the end domes were mounted. This mechanism permitted the application of torque to the drive screw to force the domes away from the cylindrical body of the mandrel without rotating the mandrel.

The drive screw assembly is analogous to a Bench Screw. The shaft is permitted to rotate freely within the drive boot by means of a large thrust bearing. The drive shaft itself is fitted through a steel sleeve to maintain proper centering of the shaft. When the dome is screwed down the shaft, it will friction lock with the end of the mandrel. Once the dome is locked to the mandrel it is possible to rotate the shaft and the entire mandrel within the filament winding machine mounting chucks.

The small dome end can be simply driven away from the mandrel small diameter, pulling the part (*The object being fabricated, filament wound tube*) with it Figure 6.11. However a parting cut is required at the junction of the large diameter and large dome before attempting to extract the part. Rotation of the drive shaft was converted to a linear displacement with no rotation in the dome through the use of a floating drive shaft restrained only in the axial direction. The self extracting dome end has now been utilized on six different filament winding mandrels.

In the case of very heavy mandrels with large counter rotating tension forces on the roving band, engagement pins may be installed on the inner faces of the mandrel ends that lock into the matching dome end faces.

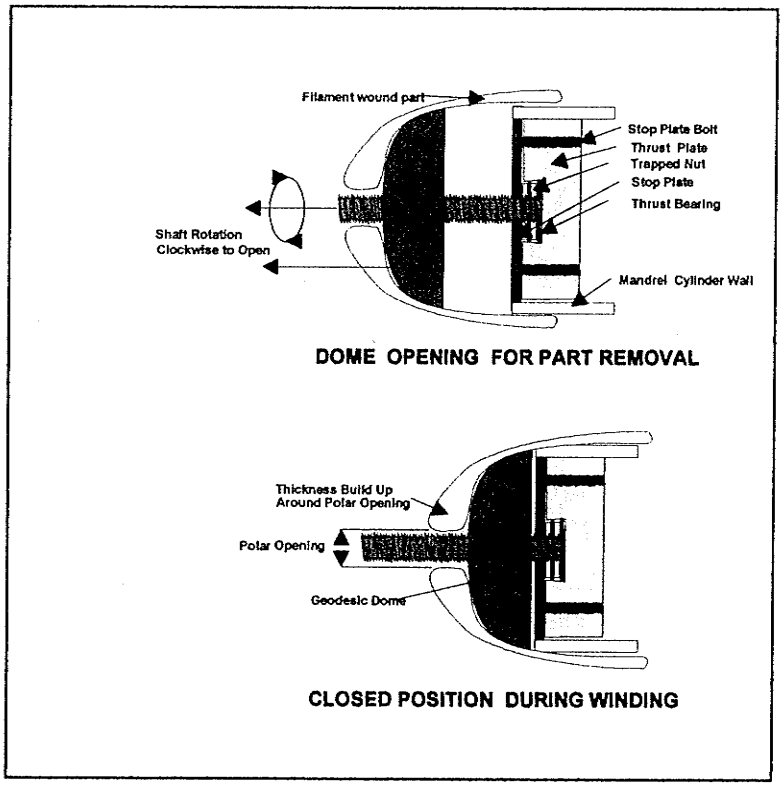

Figure 6.11: Self-Extracting Dome Drive Mechanism

From previous discussions, it becomes clear that the shaft and its sleeve must be limited to the maximum polar aperture diameter in order to maintain stable geodesic paths. Small increases in polar aperture, to accommodate larger shafts, have been shown to have serious effects on dome strength (Gramoll 1990). It may not be relevant to manufacturers of tubes where the domes are later discarded. However if small changes in the wind angle are also required to accommodate larger support shafts then as was discussed earlier, the entire structure will be altered as a consequence.

The limitations that geodesic wind paths impose on shaft dimensions are serious and conversely if mandrel weights require large diameter support shafts, these then impose a serious limit on the wind path. The use of light weight composite mandrels mitigates to some extend the severity of the problem.

The design engineer should also bear in mind during the design process that the mandrel shafts are also required to support the combined weights of the mandrel and finished part, as well as the frictional forces during the removal procedure. Clearly then the designer requires an accurate finished part weight before determining the shaft dimensions especially when using low angle helical winding.

7 ANALYSIS

The electrical power industry is currently considering replacement of wooden poles by new materials for a variety of environmental and economic reasons. To satisfy the electrical industry, tubular composite poles are now being produced, by a number of processes including pultrusion and filament winding. The composite tubes are to be used as distribution and transmission line poles. Currently wooden poles are classified according to ANSI 05.1 Pole Standards (1992).

Sherman(1984) found that composite poles, produced by filament winding, have been difficult to design to meet specific load classification parameters since they typically are designed with the focus on deflection limitations. Failure of poles was found to be due to excessive deflection rather than collapse. He described a method of overcoming some of the design obstacles that required considerable expertise in filament winding and experimental effort. He also noted some characteristics of filament wound tubes that lead to some difficulties in analysis. Since he was working with a limited number of pole designs, simple methods were sufficient to obtain satisfactory functional designs. It was clear that Sherman (1984) had acted in a unique pivotal capacity to integrate the filament winding process with the performance requirements of the electrical industry.

An extensive research program has been carried out at the University of Manitoba over the last 10 years aimed at developing performance criteria and design guidelines for composite poles. These guidelines are based on both strength and serviceability (deflection) criteria.

In this Chapter a new method for computing deflections of tapered composite tubes loaded as cantilevers, is presented. Sherman (1984) presented a paper using the simplified beam deflection model to predict deflections of fiberglass poles of various thicknesses. While Sherman (1984) limited his investigations to tip deflections, methods presented here determine the deflected shape of the entire pole. The theoretical model was designed so that, once satisfactory deflection performance is achieved for a pole, all input data is retrievable for manufacturing purposes. Such data includes, wind angles, number of layers, winding patterns and roving bandwidth .

The deflection model is based on the more sophisticated Bernoulli-Euler equation, capable of modeling large deflections, and is derived in part from the work of Bisshopp and Drucker (1945).

Traditional methods of analysis of composite structural members assume that the material properties are constant along their length. This, however, is not the case in tapered filament wound tubes. The fabrication method of tapered tubes is robotic controlled filament winding. This procedure uses both circumferential and geodesic winding patterns. Details on the filament winding procedures and fundamental mathematics are discussed in some detail by Peters, et.al. (1991).

One of the consequences of using the winding patterns based on geodesic space curve equations is the variation in material properties, along the length, due to the tapered mandrel surfaces. This phenomenon does not occur for circumferential winding patterns based on tapered helix equations. The winding of poles requiring both types of winding, results in complex variation of material properties.

This chapter addresses the deflection characteristics of filament wound poles that require special considerations due to the inherent variable material properties. Methods of determining the variation of the axial Young's modulus and the variable moment of inertia are presented. A brief description of a simple beam deflection model is presented and compared to an iterative solution, based on the Bernoulli-Euler (B-E) beam deflection equation. The deflection predictions for the new methods are compared to test data taken from experiments on single section poles.

The focus on theoretical issues is largely due to the frustration with expectations based on conventional materials. It was clear that filament winding was considerably different from traditional fabrication and would require new analysis methods. Chapter 7.0 is the search for analysis tools which will be employed in Chapters 8.0 through 10.0 and for discussion of the experimental results.

7.1 THE BEAM THEORY EQUATIONS

In the following discussion of deflections it is convenient to use the established nomenclature and as such the axial direction of tubes previously referred to as the Z axis is replaced by the X axis. The deflection of cantilever beams can be approximated by the following, "Simplified" Euler elastic curve equation

$$\frac{\partial^2}{\partial x^2} y = \frac{M}{EI} \qquad \text{(Eq. 7.1)}$$

Eq.7.1 however neglects the square of the first derivative in the fundamental Bernoulli-Euler curvature formula Eq.7.2 (Bisshopp and Drucker, 1945).

$$\frac{\frac{\partial^2 y}{\partial x^2}}{\left[1+\left(\frac{dy}{dx}\right)^2\right]^{\frac{3}{2}}} = \frac{M}{EI} \qquad \text{(Eq.7.2)}$$

In the case of cantilever beams, the shortening of the moment arm during the deflection is a major contribution to the error in the deflection value (Bisshopp and Drucker, 1945). This error increases with larger deflections.

Solutions to Eq.7.2 are problematic for the case of tapered cantilevers since the resulting differential equation contains variable coefficients. According to Parkinson, et. al.(2000), "The elliptic integral solutions for cantilever beams are cumbersome, time consuming and only usable for simple loading cases."

Many types of incremental or numerical methods have been developed. Bisshopp and Drucker (1945), prior to the computer era, used a combination of integral tables and numerical methods for a simple prismatic beam. Flodin (1957) developed a graphical method using the moments of inertia, calculated at various points along the beam to scale deflection values for tapered cantilever beams. A Runge-Kutta numerical approach was taken by Kemper (1968) with convergence problems that were solved with a trial and error approach. Other authors have foregone such numerical techniques and have relied on various finite element methods. Among them are Ohnishi and Matsuzaki (1985) who were analyzing a graphite composite fishing rod subject to large deflections.

The focus of previous work on large deflection of tapered tubes was typically applied to fishing rod designs. Among the international fly fishing community a number of deflection issues, as related to stress and rod

performance, have been debated and implemented by custom rod builders. Other complex procedures for designing high performance fishing equipment have also been developed (Spolek, G.A. and Jefferies, S. R., 1982). One such procedure includes the discretization of the composite rods into short sections which allows the computation of deflection using iterative procedures. The method described in this paper is derived from the method used by Falka Gregersen to design fly rod tapers (Personal Communication).

Previous work on large deflection problems has focused on simple isotropic problems or assumed that the study material could be described as such. In this paper, the material being analyzed is treated as having non-linearly variable thickness and material properties, with exact values calculated at any point along the length of the tube.

7.2 THE BERNOULLI-EULER BEAM DEFLECTION MODEL

According to Bisshop and Drucker (1945), the Bernoulli-Euler theorem states that the curvature of a flexible member is proportional to the bending moment and that the length of the member remains constant. The curvature, ***k***, is expressed in terms of arc length, ***s***, and slope angle ϕ as follows,

$$k = \frac{d\phi}{ds} = \frac{M}{EI} \qquad \text{(Eq.7.3)}$$

Using Eq.7.3, as the starting point, the curvature at any point can be calculated only if the moment function of the deflected shape is known. If the undeflected beam is discretized into short segments of uniform length, then

the flexural rigidity of the member at each point can be determined from the basic geometry of the beam in question.

The length of each segment is analogous to the arc length, ***s,*** of Bisshopp and Drucker (1945). If at first, the concentrated load is applied at the tip of the cantilever and curvature, ***k***, computed for each end of a segment, a first approximation of the radii of curvature ***(r=1/k)*** can be determined, as shown in Fig.7.1. The basal segment is fixed at the one end and has a slope equal to zero and a radius of curvature for the basal point, r_o , shown in Fig.7.2. The radius of curvature for the distal end of the first segment is also determined and is defined as r_1. Dividing the arc length of the segment, **s** by the average of the two radii, R_1, yields the arc angle θ_1, which is identical to the change in slope of the tangents over the length of the segment. In Fig.7.2, a single section is shown with the deformed configuration. In Fig.7.2 ***s*** is the arc length along the neutral axis. In order to determine the Cartesian coordinates of the end points of the neutral axis within the first segment, the chord length, C_1 between points is determined as follows for the first segment,

$$R_1 = (r_o + r_1)/2 \qquad \text{(Eq. 7.4)}$$

$$\theta_1 = \frac{S}{R_1} \qquad \text{(Eq. 7.5)}$$

$$C_1 = 2R_1 \sin\theta_1/2 \qquad \text{(Eq. 7.6)}$$

The mean value of the end slopes is the slope of the midpoint of the arc segment, which is coincidently the slope of the cord between the two end points. Using basic geometry the Cartesian coordinates of terminal ends of the first segment can be determined.

$$x_1 = 0 \quad \text{and} \quad y_1 = 0 \qquad \text{(Eq. 7.7)}$$

$$x_2 = x_1 + (C_1 \times \cos(\theta_1/2)) \qquad \text{(Eq. 7.8)}$$

$$y_2 = y_1 + (C_1 \times \sin(\theta_1/2)) \qquad \text{(Eq. 7.9)}$$

Summation of the preceding arc angles permits the determination of the subsequent coordinates. This produces a first approximation curve from which the iterative procedure begins. In this process, it is assumed that the flexural stiffness, ***EI***, in each segment remains unchanged. The load and segment lengths also remain constant. The moment M_i and the curvature, k_i , at the end of each segment are updated as follows,

$$M_{i_{(new)}} = P(x_n - x_i) \qquad \text{(Eq. 7.10)}$$

$$k_{i_{(new)}} = \frac{P(x_n - x_i)}{(EI)_i} \qquad \text{(Eq. 7.11)}$$

where, x_n is the x coordinate of the beam end, and x_i the point of interest

The degree of convergence is checked by back calculating the apparent load at the given point as follows,

$$P_{(new)} = \frac{(EI)_i k_{i(new)}}{(x_n - x_i)} \qquad \text{(Eq. 7.12)}$$

When the back calculated apparent load at every segment end is identical to the known applied load we assume convergence to the correct displacement curve.

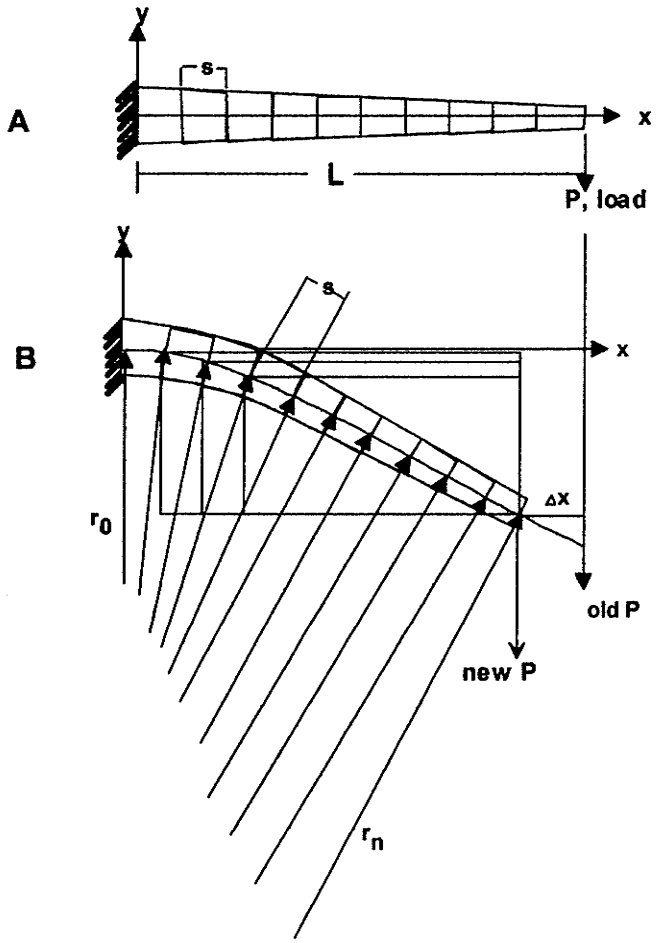

Figure 7.1: Discretization of cantilever and determination of curvature

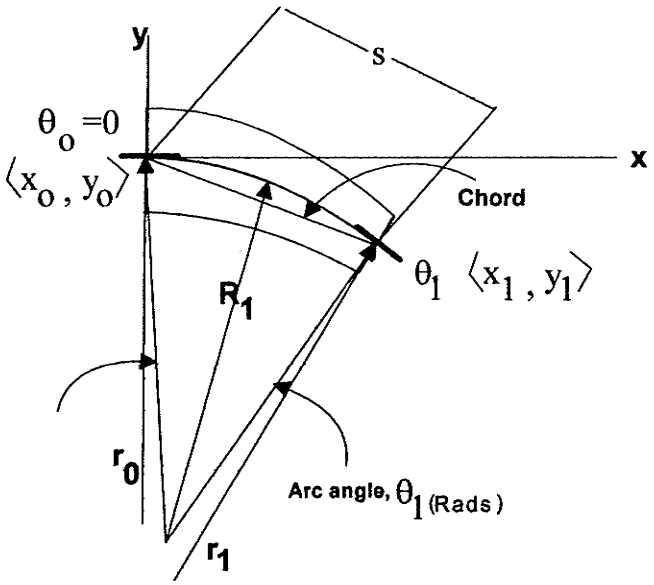

Figure 7.2: Details of first segment of discretized cantilever

7.3 DETERMINATION OF THE MOMENT OF INERTIA I AS A FUNCTION OF THICKNESS AND AXIAL POSITION

Each pole segment has variable thickness and modulus, which are functions of the wind angle, mandrel geometry and laminate structure. MapleV (1997), software was used to obtain the material constant, E, the moment of inertia, I, and curvature, k, for each segment end of the filament wound poles.

The thickness of tapered tubes is not constant and therefore *I* must become a function of position. The moment of Inertia for a hollow filament wound circular section is as follows,

$$I = \frac{\pi(r_o^4 - r_i^4)}{4} \qquad \text{(Eq. 7.13)}$$

The radius of the mandrel, r, or inner radius of the composite tube is now a linear function of x, since the mandrel is fixed at the time of fabrication, is defined as,

$$r = mx + B \qquad \text{(Eq. 7.14)}$$

Where r_i and r_o are respectively the inner and outer radii of the section. While the inner radius is defined by the radius of the mandrel, Equation 7.14, the outer radius is not and varies as a function of the wind angle and the number of layers.

A typical filament wound tube used in this study is composed of three layers over wrapping the mandrel. The fibre orientation of a layer is referenced with respect to the meridian of the mandrel. The first layer consists of fibers placed nearly 90° to the meridian and are called circumferential plies or hoop plies. Since there are some combination of + positive and –negative near 90° plies, these may be conveniently designated as $\pm 90^o$. A similar set of circumferential plies are used on the outer surface of the filament wound tubes. The term t_{ic} is used to define the total thickness of the inner set of circumferential layers and t_{oc} defines the thickness of the outer set of circumferential layers. Between these two sets of layers are the main structural layers of low angle winding. Since the fibres are oriented as close to the axis of rotation as possible they are referred to as the axial layer, with a thickness defined as t_a. Since these axial fibres are wound using a geodesic winding pattern, the angle with the meridian is variable. When an axial layer is named as having a particular winding angle, that value of angle is true only for the starting position, which is set to be the base position.

The thickness of the inner, and outer layers of circumferential winding are essentially constant over the length of the mandrels (see section 2.2). However, the axial layer thickness does change with the radius, and as such a function defining the change in axial layer thickness is required to complete the determination of both the moment of inertia and the effective axial modulus at any given point along the tube. Thus the moment of Inertia is expanded to include the various thickness terms as follows,

$$I = \frac{\pi}{4}\left[(r_i + t_{ic} + t_{oc} + t_a)^4 - r_i^4\right] \qquad \textbf{(Eq. 7.15)}$$

In Chapter 4.0, Eq.4.2 was shown to reflect thickness as a function of axial position and wind angleof a geodesically wound roving band. For this discussion of the axial thickness, t_a , is modified to have x as the axial variable and also includes the mandrel slope as follows,

$$t_a(x,\theta) = \left(2 \times \left(\frac{L^2}{4\pi} \times \frac{1}{BW_e}\right) \times \left(\frac{r_0}{r_x} \times \frac{\cos\theta_0}{\cos\theta_x}\right)\right) \qquad \textbf{(Eq. 7.16)}$$

Where L is the circumference of the roving tow to be used during winding, BW_e is the effective band width selected for the particular tow, and θ_o is the arbitrarily selected wind angle at the starting position. Taper is inherently a part of this function since r_x is the radius as determined by Equation 7.14. The physical aspects of these relationships are shown in Figure 7.3.

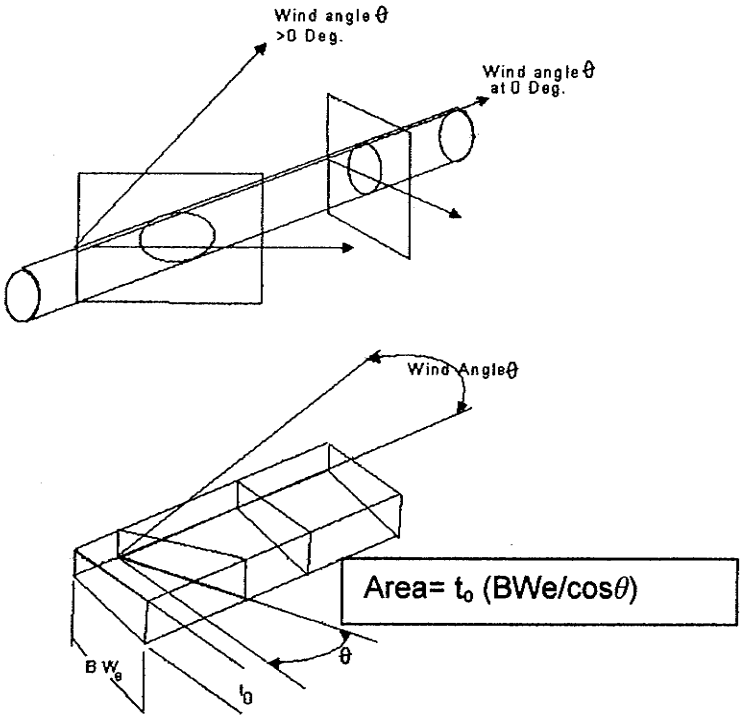

Figure 7.3: Fiber tow relationships to wind angle

Unfortunately Eq.7.16 requires that the radius, r_x and wind angle, θ_x at position, x be known. A method of determining the wind angle θ_x must be found. The wind angle is related to radius through the Constant of Clairaut, given in Eq 3.22.

All of the starting parameters are determined at the base of the mandrel which is the large end of the tapered pole. The roving band has a starting thickness t_0 and the bands are assumed to fit perfectly around the circumference of the mandrel at zero degrees, n times. Where n is also the circumference-to-bandwidth ratio. The factor 2 is used to account for the fact

that every geodesic wound pattern requires a positive and negative layer, as the fibres return to the base. The axial layer is composed of both positive and negative wind angles, but is treated as a single layer in the determination of thickness, t_a. Since the positive and negative layers are symmetric the values for each lamina can be easily calculated when determining the Young's modulus.

Since Eq.7.16 can not be used as is, a new formulation is required. Initially we ignore the problem of dealing with a variable wind angle and look only at what happens for the special case of 0^o winding. The thickness of the tube wall at any position, x can simply be determined by relating the cross sectional area at any position to the starting position. While the thickness of the tapered composite tube varies along the length, the total cross sectional area at any point remains constant for this special case. The resulting equation does not account for the changing wind angle and the only adjustment is for the changing radius, r_x, and is as follows,

$$\pi((r_x + t_a)^2 - r_x^2) = \pi\left((B + t_0)^2 - B^2\right) \qquad \textbf{(Eq. 7.17)}$$

where B is simply the base radius from Eq.7.14.

Knowing that the thickness of a filament band can be adjusted by dividing the original area, by the cosine of the wind angle at a position x, this procedure is applied to the base area

$$\pi\left((r_x + t_a)^2 - r_x^2\right) = \frac{\pi\left((B + t_0)^2 - B^2\right)}{\cos\left(\sin^{-1}\left(\frac{C}{r_x}\right)\right)} \qquad \textbf{(Eq. 7.18)}$$

The previous equation permits the wind path layer to vary its cross sectional area as the wind angle changes, without the explicit use of the θ term. In the case of a 0^0 wind angle Eq.7.18 will reduce to Eq.7.17.

Eq.7.18 is reduced to the quadratic form as follows to permit a solution,

$$t_a^2 + 2r_x t_a - \frac{A}{\pi \cos\left(\sin^{-1}\left(\frac{C}{r_x}\right)\right)} = 0 \qquad \textbf{(Eq. 7.19)}$$

C is the Constant of Clairaut, which is arbitrarily chosen as the starting wind angle. The cross sectional area , ***A***, of the axial layer at the starting position is then defined as follows,

$$A = \pi\left((B + t_0)^2 - B^2\right) \qquad \textbf{(Eq. 7.20)}$$

The solution to Eq.7.19, for the thickness of the axial geodesic layer is obtained using MapleV (1997) mathematical software.

Once the thickness of the axial layer is determined, it is then possible to evaluate the moment of inertia, ***I*** , at any position ***x***, by using Eq.7.15 . All the terms in the solution of Eq.7.19 are from the radius function Eq.7.14. Setting an arbitrary value for C at the start position is identical to setting a start winding angle. As the radius changes with respect to ***x***, the new wind angle is implicitly determined and the starting thickness t_o is modified to yield the thickness of the axial layer.

In Figure 7.4 a graphical representation of the variation in thickness is shown for a range of arbitrary start wind angles, note one can also see clearly that as the wind angle at the start is increased the distance covered is reduced through premature turn-around. Such graphical techniques provide the designer great insight into the role of taper rates and arbitrary choices

regarding the wind angles. The spikes at the turn-around point are an artefact of the number of interval points selected for the solution.

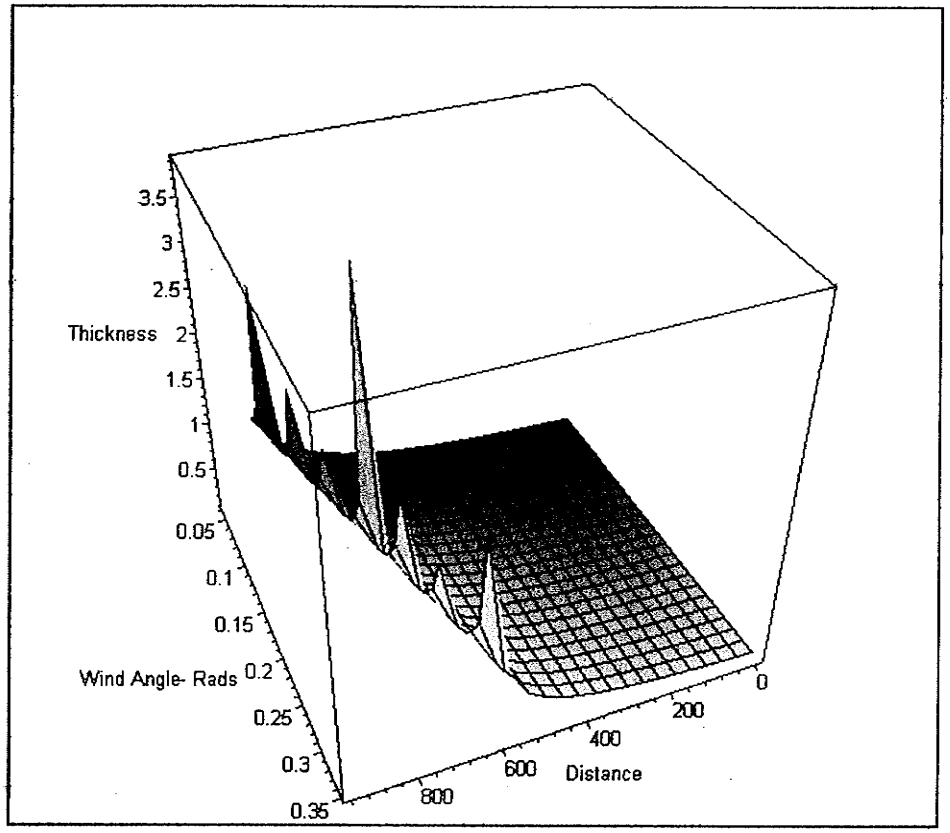

Figure 7.4 Plot of Thickness Variability due to Changes in the Constant of Clairaut (units=inches)

7.4 DETERMINATION OF THE EFFECTIVE YOUNG'S MODULUS OF A LAMINATE

The effective axial modulus, E_x, varies along the length of the tapered composite pole. Determination of E_x at any position, x, requires details of the laminate structure of the pole at that position. This includes the laminae thickness and the fibre angle with respect to the principal axis for every lamina within the laminate stack. A typical filament wound laminate stack is shown in

Fig. 7.5. This is a typical sequence used in filament winding of tapered tubes. The intermediate layer with longitudinal fibres is composed of both a positive and negative angle plies. This figure shows how the layer increases in thickness and wind angle toward the tip. It also shows a forward facing section from the base (left) through to the tip (right) of a pole.

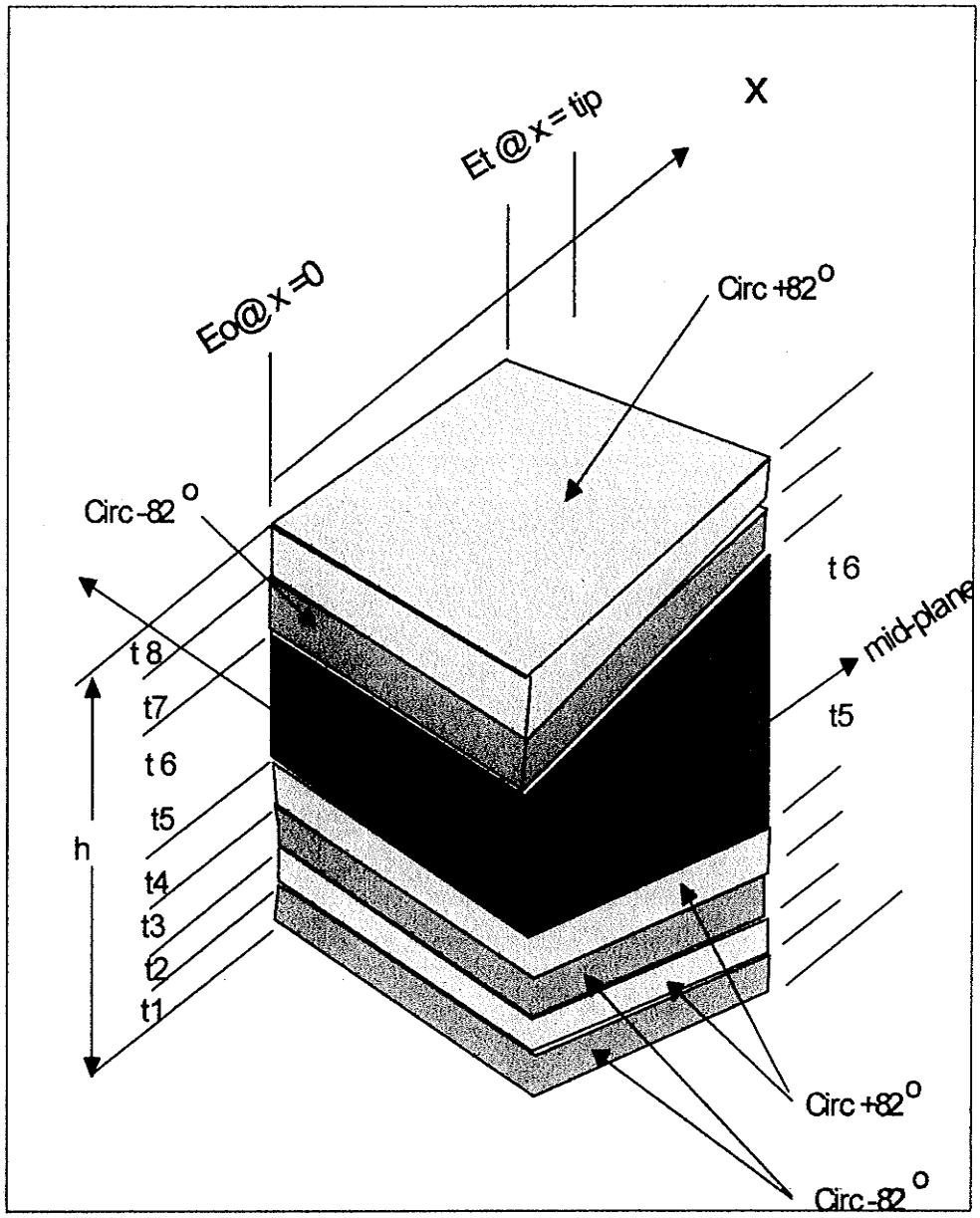

Figure 7.5 Laminate Stacking Sequence Nomenclature

The material properties for the isopthalic polyester resin and E-glass roving, used in this study to fabricate the experimental poles and test coupons, are presented in Appendix C. The various material properties were determined experimentally in accordance with he respective ASTM (2000,2000,1998) standards and standard test coupons and the techniques are detailed in the following chapter.

Having established the material properties, the engineering properties of the laminate can be determined by first evaluating the reduced form of the stiffness matrix for an orthotropic material in the plane stress state (Daniel and Ishai,1993 and Tsai,1988). The reduced stiffness matrix, ***Q,*** was presented in Eq.4.7 showing the basic stress strain relationships along the principal material axes. Here the stiffness matrix and its components is shown by itself

$$\boldsymbol{Q} = \begin{bmatrix} Q_{11} & Q_{12} & 0 \\ Q_{21} & Q_{22} & 0 \\ 0 & 0 & Q_{66} \end{bmatrix} \qquad \textbf{(Eq. 7.21)}$$

The matrix components in terms of the unidirectional material properties were previously given in Eq.4.8 through Eq.4.11. The Minor Poisson's ratiois given as follows

$$v_{21} = \frac{E_2}{E_1} v_{12} \qquad \textbf{(Eq. 7.22)}$$

The transformed, or rotated , stiffness matrix , ***Qt*** in terms of the principal direction of the laminate, is determined using a matrix rotation procedure presented in Equations 4.12 to 4.14.

Where θ is the wind angle of a filament wound tube which varies along the length of the tube. It is clear that when modeling a pole structure, a variable Young's modulus is required, since the effective axial modulus of the structure, at any discreet position, is dependent on the transformed lamina

stiffness matrices. This is accomplished using the classical lamination theory assumptions and methods described by Daniel and Ishai(1993)and Tsai(1988).

For a laminate, the fully populated matrix equations describing the force, N_i, and moment, M_i, as functions of the deformation strain, ε_i, and curvature, κ_i, and the laminate stiffnesses A_{ij}, B_{ij}, D_{ij}, are given by,

$$\begin{bmatrix} N_x \\ N_y \\ N_s \\ M_x \\ M_y \\ M_s \end{bmatrix} = \begin{bmatrix} A_{xx} & A_{xy} & A_{xs} & B_{xx} & B_{xy} & B_{xs} \\ A_{yx} & A_{yy} & A_{ys} & B_{yx} & B_{yy} & B_{ys} \\ A_{sx} & A_{sy} & A_{ss} & B_{sx} & B_{sy} & B_{ss} \\ B_{xx} & B_{xy} & B_{xs} & D_{xx} & D_{xy} & D_{xs} \\ B_{yx} & B_{yy} & B_{ys} & D_{yx} & D_{yy} & D_{ys} \\ B_{sx} & B_{sy} & B_{ss} & D_{sx} & D_{sy} & D_{ss} \end{bmatrix} \begin{bmatrix} \varepsilon_x^o \\ \varepsilon_y^o \\ \gamma_s^o \\ \kappa_x \\ \kappa_y \\ \kappa_s \end{bmatrix} \qquad \text{(Eq. 7.23)}$$

with ***i=x,y,s*** and ***j=x,y,s***

A typical balanced asymmetric angle ply laminate would appear as a stack designated by **[90, - θ, + θ, - θ, + θ, 90]** where plies on opposite sides of the midplane are mirrored. The balanced symmetric version would appear as **[90, + θ, - θ, - θ, +θ, 90]** where plies on opposite sides of the midplane have identical angles. Due to the fact that the filament winding process interweaves the positive and negative filaments of the forward and reverse patterns, neither description is absolutely true. A typical winding sequence used in this research program involving jointed poles, would be designated as **[-86, +86, (+/- 10)** $_n$ **, -86, +86]** , where the subscript **n**, is between 1 and 4, indicating one to four sets of +/-10° laminae. According to Daniel and Ishai (1993) this type of laminate stack might best be described as a Balanced Antisymmetric Angle-Ply laminate. The authors described in detail the difficulties associated with determining the engineering properties of laminates with various stacking sequences, and give some examples of simple approximations for E_x. These

approximation methods are well suited to balanced symmetric cross ply laminates $[0,90]_n$ but not so for more generalized laminate structures, as might be expected from filament winding procedures. In the following discussion a solution applicable to a wide range of advanced composite tubes is presented.

The components of the total laminate stiffness matrix are derived from the transformed stiffness matrices for each of the individual lamina, of thickness h_k, thus

$$A_{ij} = \sum_{k=1}^{n} Q_{ij}^{k}(h_k - h_{k-1})$$

$$B_{ij} = \frac{1}{2}\sum_{k=1}^{n} Q_{ij}^{k}(h_k^2 - h_{k-1}^2)$$

$$D_{ij} = \frac{1}{3}\sum_{k=1}^{n} Q_{ij}^{k}(h_k^3 - h_{k-1}^3) \qquad \text{(Eq. 7.24)}$$

with $i=x,y,s$ and $j=x,y,s$. Where A_{ij} , B_{ij} , and D_{ij} are respectively the extensional, coupling and bending stiffnesses.

The determination of the engineering constants of a general laminate is made easier by working with the compliance matrix, which is the inverse of the 6 x 6 , "total laminate stiffness matrix", $\begin{bmatrix} A & B \\ B & D \end{bmatrix}$, Eq.7.23, so that "the total laminate compliance matrix" $= \begin{bmatrix} A & B \\ B & D \end{bmatrix}^{-1}$.

According to Daniel and Ishai (1993), Eq. 7.23, the total laminate stiffness matrix, relating in-plane forces and moments to reference plane

strains and curvatures, can be rewritten after performing the matrix inversions as

$$\begin{bmatrix} \varepsilon_x^0 \\ \varepsilon_y^0 \\ \gamma_s^0 \\ \kappa_x \\ \kappa_y \\ \kappa_s \end{bmatrix} = \begin{bmatrix} a_{xx} & a_{xy} & a_{xs} & b_{xx} & b_{xy} & b_{xs} \\ a_{yx} & a_{yy} & a_{ys} & b_{yx} & b_{yy} & b_{ys} \\ a_{sx} & a_{sy} & a_{ss} & b_{sx} & b_{sy} & b_{ss} \\ c_{xx} & c_{xy} & c_{xs} & d_{xx} & d_{xy} & d_{xs} \\ c_{yx} & c_{yy} & c_{ys} & d_{yx} & d_{yy} & d_{ys} \\ c_{sx} & c_{sy} & c_{ss} & d_{sx} & d_{sy} & d_{ss} \end{bmatrix} \begin{bmatrix} N_x \\ N_y \\ N_s \\ M_x \\ M_y \\ M_s \end{bmatrix} \qquad \text{(Eq.7.25)}$$

and the submatrices [a], [b] , [c] and [d] are the compliance matrices derived from the stiffness matrices in the following manner

$$[a] = [A^{-1}] - \{[B^*][D^{*-1}]\}[C^*]$$

$$[b] = -[A^{-1}][B]$$

$$[c] = [D^{*-1}][C^*]$$

$$[d] = [D^{*-1}] \qquad \text{(Eq.7.26)}$$

where

$$[A^{-1}] = inverse\ of\ \ matrix[A]$$

$$[B^*] = -[A^{-1}][B]$$

$$[C^*] = [B][A^{-1}]$$

$$[D^*] = [D] - \{[B][A^{-1}]\}[B] \qquad \text{(Eq.7.27)}$$

The nine engineering constants in terms of the compliance matrix are given as follows,

$$\bar{E}_x = \frac{1}{h a_{xx}}, \quad \bar{E}_y = \frac{1}{h a_{yy}}, \quad \bar{G}_{xy} = \frac{1}{h a_{ss}},$$

$$\bar{\nu}_{xy} = -\frac{a_{yx}}{a_{xx}}, \quad \bar{\nu}_{yx} = -\frac{a_{xy}}{a_{xy}}, \quad \bar{\eta}_{sx} = \frac{a_{xs}}{a_{ss}},$$

$$\bar{\eta}_{xs} = \frac{a_{sx}}{a_{xx}} \quad , \quad \bar{\eta}_{ys} = \frac{a_{sy}}{a_{yy}} \quad , \quad \bar{\eta}_{sy} = \frac{a_{ys}}{a_{ss}} \qquad \text{(Eq. 7.28)}$$

$\bar{E}_x \bar{E}_y$ = *Laminate effective Young's Moduli in the x and y directions.*

$\bar{\upsilon}_{xy}, \bar{\upsilon}_{yx}$ = *Laminate effective Poisson's Ratio*

$\bar{\eta}_{xs}, \bar{\eta}_{ys} \bar{\eta}_{sx} \bar{\eta}_{sy}$ = *Laminate effective shear coupling coefficients*

The over bar in the terms of Eq.7.28, is a convention used by Daniel and Ishai (1993) to denote the average laminate values for the engineering constants.

The inversion of the total laminate stiffness matrix is facilitated by using the Maple program, and even so can be quite a lengthy procedure. It was also useful to carry out the inversion symbolically, once at the top of the program and filling in the variables of wind angles and thickness at each point along the length of a pole.

The effective axial modulus, E_x requires the basic input of the stiffness matrix **[Q]**,Eq.7.21, for the unidirectional material properties of the resin and matrix and the wind angle for the transformation matrix. It is possible to construct this matrix from material supplier data, but it is not recommended since the method of fabrication can result in serious discrepancies due to translation losses (Peters, et. al. 1991). The procedure used in this study was to fabricate coupons of the identical materials in unidirectional configurations using similar procedures including tension rollers and impregnation tanks.

7.5 BERNOULLI-EULER SIMULATION PROGRAMS

The previous sections described components required for the analysis of any single parameter such as effective axial modulus, thickness, moment of inertia and wind angle drift. Incorporating all simultaneously for arbitrary points along the length of the test poles required the development of a large program incorporating the code for each parameter in an iterative structure.

Originally the goal was to link the various programs simply to produce data files automatically for use in finite element modeling. Instead the structure and properties of the various points along the length of the pole were assembled into a single large matrix and the columns represented all the relevant information required to solve the Bernoulli-Euler equations for curvature, k and the displacement of the end points of each section. The determination of pole displacement was found to converge to the third decimal place typically after 5 iterations.

The program requires a number of user input parameters. These include pole length, inside diameters, taper rates or radius defining functions, laminate structure and thicknesses for the individual plies at the base of the pole as well as the winding type and angles. Also required are the material properties of the unidirectional lamina composed of the relevant materials and the position of the load and the interval distance. The interval distance was typically an integral distance between the base and applied load to avoid unequal length segments. However this was not absolutely required and non-uniform spacing could be used with suitable modification to the structure of the data matrix and the loop parameters.

The most computationally intensive aspect of the program is the determination of the inverse of the total laminate stiffness matrix known as the compliance matrix at each interval point.

Bernoulli- Euler equations take as input the data matrix columns and output a new matrix of curvatures and displacements for the mid-plane interval points using the applied load and the linear distance between the interval point and the load. At the end of each iteration the tip displacement is determined and the apparent moment arm is recalculated. Due to the shortening of the moment arm the next iteration calculates the curvature and displacements using the new moment arm length. By back calculating from the k value the apparent load at each interval point is identical with the applied load.

The program used to analyze the single segment poles was written using Maple8 (2002) mathematical software. Code written using MapleV (1997) is compatible with version 8. The program incorporates all the functions required, such as the geodesic winding thickness solution, moment determination, laminate structure and effective laminate axial modulus as well as the iterative Bernoulli-Euler deflection routines.

7.6 MODELING OF JOINTED POLES

The method used to model jointed poles is basically the same as that of single section poles. The most important consideration is the method of concatenating two sections each with its own distinctive geometry, lamination sequence and winding angles as well as thickness and material properties.

The jointed pole is composed of two sections each with its distinctive properties. Each pole section can be regarded as a string of points coincident with the long axis of the section. The points are spaced equidistant as was also the case with the single section poles. The last or upper most point of the basal segment is followed by the corresponding string of the upper pole segment. However, the zero point of the upper section is ignored for this analysis since it is adjacent to the last point of the lower section. In effect we step across the joint to the #1 point of the upper section which is beyond the joint.

At the time of creating the first working analysis program it was recognized that the joint area could be a source of concern. Unfortunately the classical lamination theory did not appear to apply to the joint structure in a straight forward manner. The decision to place the joint region between points is due in part to time constraints and a lack of information on the behaviour of the joint region, which is composed of dissimilar composite laminates with a variable thickness adhesive layer bonding the two together.

Prior to full implementation of the multiple segment pole deflection modelling a modified program was written to examine a number of hypothetical poles. The purpose was to assemble 3 distinct 2 piece poles with identical parameters but for the start winding angles and compare results simultaneously. These hypothetical poles are shown in Figure 7.6 illustrating the joint structure and the notation.

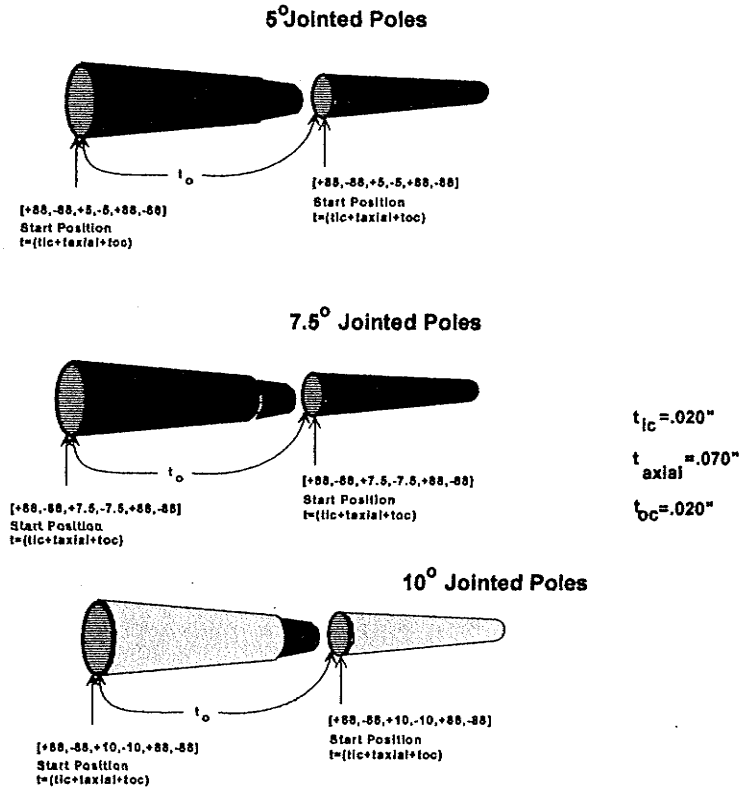

Figure 7.6: Hypothetical Jointed Poles Identical but for Wind Angle

In the Figure 7.7 the plot of effective axial modulus of the 5^0, 7.5^0 and 10^0 poles are superimposed. The 5^0 pole (*red top plot*) demonstrates an increasing stiffness with decreasing diameter. The 7.5^0 pole (*middle light blue*) appears to have a nearly constant stiffness, while the 10^0 (*bottom dark blue*) is clearly softening due to the wind angle drift. This example is presented to illustrate that the effective axial modulus for simple linear tapered tubes can behave in a non-intuitive manner. Further caution should be taken with tapers of different rates since the relative relationships shown in Figure 7.7 can not be expected to hold true for steeper tapers. The apparent increase in stiffness in the 5^0 pole is due to the thickness of the laminate increasing just fast

enough to cause this feature, if the pole were extended some distance the stiffness would begin to degrade due to accumulated drift. At 7.5^0 the tendency of thickness increasing the stiffness and drift degrading stiffness appear to be in nearly perfect balance. The 10^0 pole appears to be dominated by the wind angle drift problem much sooner than the two lower angle poles.

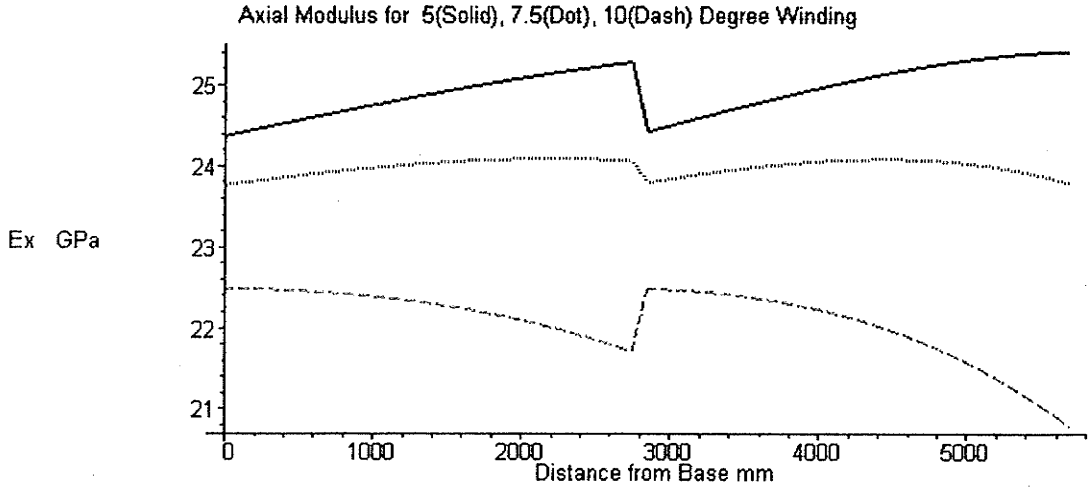

Figure 7.7: Variation in Effective axial stiffness due solely to wind angles

7.7 MAXIMUM NORMAL STRESS

The use of the Bernoulli-Euler equations for beam deflection appears to be viable for both single sections and multiple sections. It also appears viable as a method of modeling load deflection curves for tapered poles having variable wall thickness and axial moduli. In furtherance of the goal of understanding filament wound tapered tubes a suitable method of investigating the location and magnitude of maximum normal stress was required.

Using the simple formula for maximum stress in tubes,

$$\sigma = \frac{Mc}{I} \qquad \text{(Eq.7.29)}$$

where σ , the stress at an axial position, is equal to the product of the bending moment , M and the radial distance to the mid point of the tube wall, c, divided by the moment of inertia, I . The plot of the stress distribution in a constant diameter tube of constant thickness is a rather simple linear affair going from 0 to a maximum at the base. For tubes having a variable wall thickness and variable diameter somewhat more complex stress distribution is expected. Since the filament winding variables interact in a less than intuitively obvious manner, it was necessary to investigate the effects of such parameters on stress distribution.

MapleV software was utilized to illuminate stress distribution for a variety of hypothetical pole models. A set of three hypothetical poles was analyzed in Figure 7.8 for maximum stress distribution as a function of taper rates or the slope, and thickness variation regimes. The blue surface represents the pole with decreasing thickness toward the small end or tip. The red solution surface is for a pole with constant thickness. The green surface represents a pole with increasing thickness toward the tip, which is typical of filament winding. All three poles have a starting thickness , t_0 , equal to 0.125" thickness. The thickness variation schemes are arbitrarily chosen to examine possible modeling options. The actual thickness for each pole is shown in Figure 7.9, where it is obvious that we have a linear, constant and non-linear relationship between thickness and axial position.

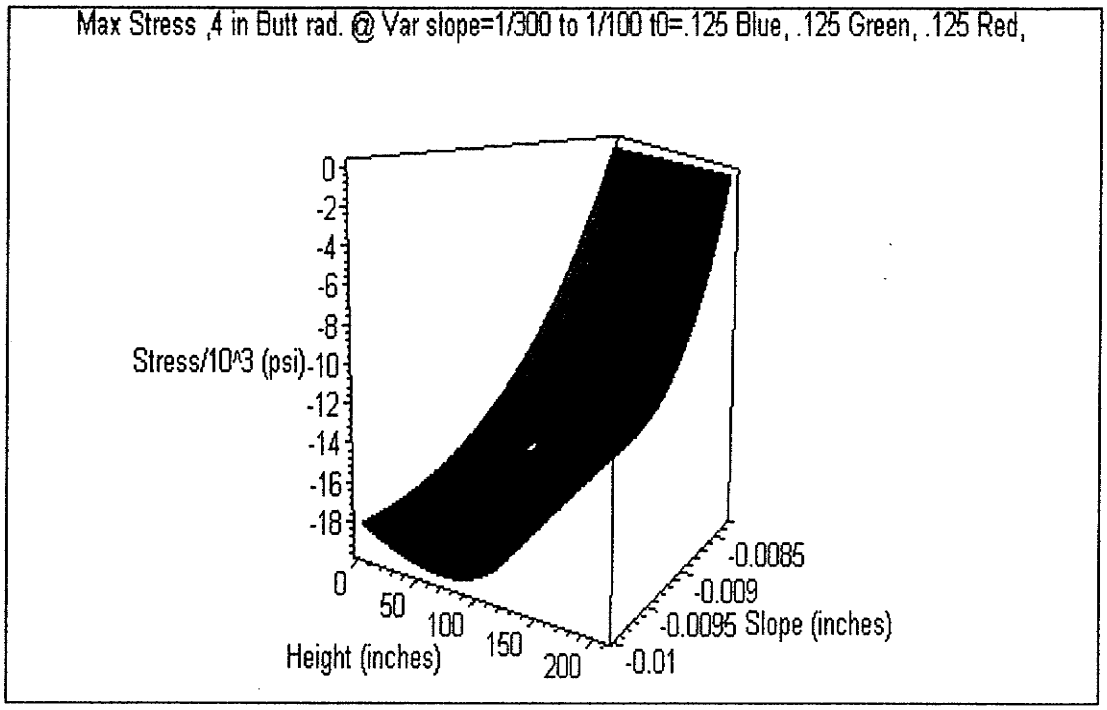

Figure 7.8: Multiple Variable Effects on Stress Distribution

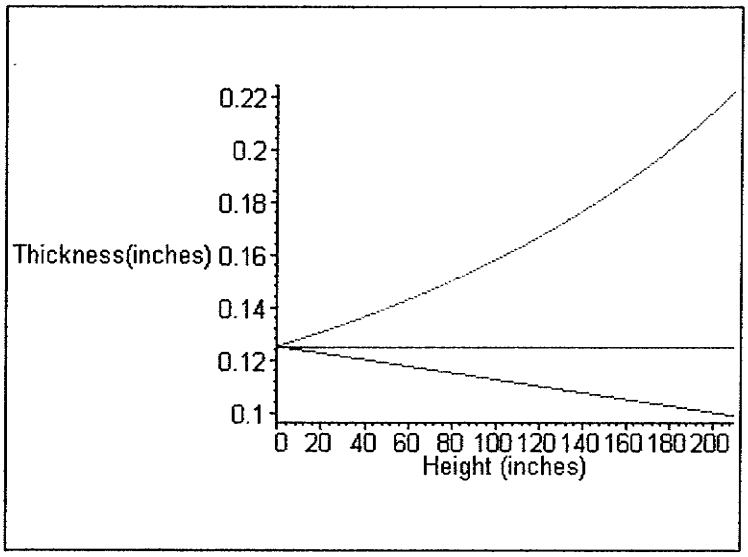

Figure 7.9 Thickness Variation for Poles in Figure 7.8

(Blue: Decreasing thickness, Red: Constant Thickness, Green: Increasing Thickness)

In order to satisfy one of the project mandates a simple method of evaluating a wide range of design options was required. In Figure 7.10 a series of different thickness regimes are displayed for a range of taper ratios. As such the stress distribution and intensity of the blue surface is markedly sensitive to taper rates. Whether or not the range of taper rates is open to consideration requires the knowledge of a critical stress parameter. Designs that exceed that value would be ruled out. A visual graphic tool was implemented using Maple V to assist in such a determination. In Figure 7.10 the decreasing thickness pole is plotted as an overlay on an arbitrarily chosen yellow failure surface. This surface is simply planar in this example and arbitrarily set at 19 ksi. However it appears that this hypothetical setup would imply that taper ratios greater than -0.009 exceed the critical stress value.

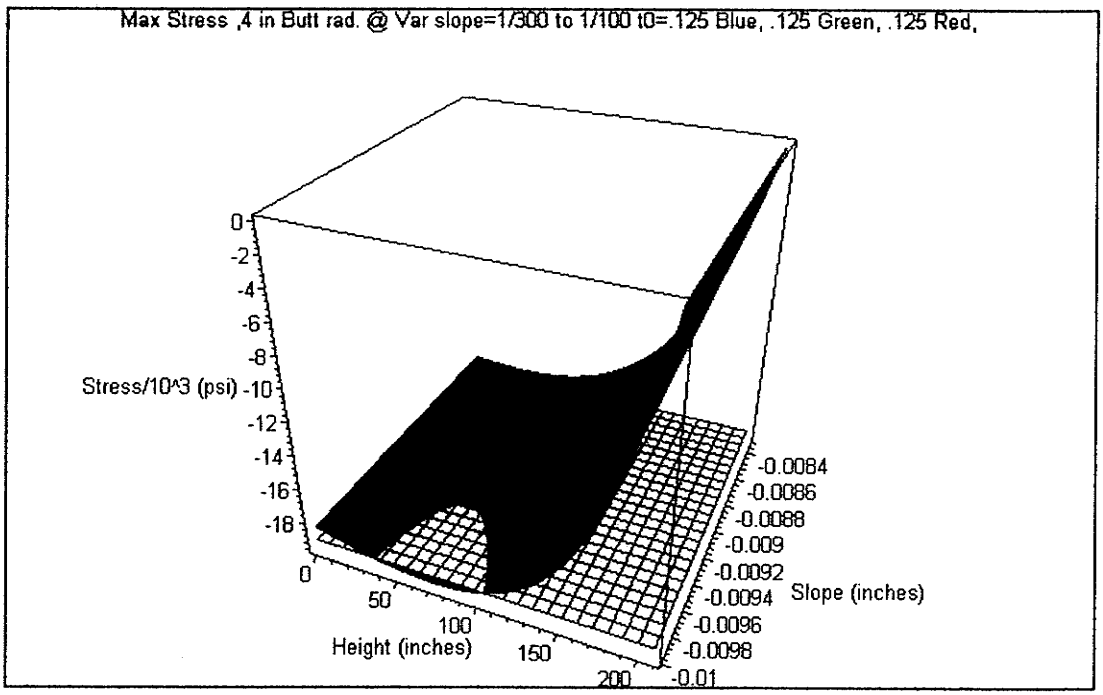

Figure 7.10: Critical Failure Stress Surface

Ultimately these analytic methods being presented will serve as the basis of design tools specifically suited to filament winding. In Chapters 8 and 9 these modeling tools will be compared with the experimental results from several different series of single segment and jointed poles.

7.8 FIBER VOLUME FRACTION COMPENSATION

When the material constants are used for analysis the values typically are based on a fixed volume fraction of fiber ***Vf*** relative to a fixed volume fraction of matrix resin ***Vm***. Unfortunately it was determined during the course of this study that poles were extremely difficult to manufacture with identical percentages of fiber and resin. A technique was employed to weigh the amount of glass incorporated into each layer and thus a total glass weight for each pole was possible to determine. The finished pole was weighed after curing and a calculated volume fraction was established for each specimen.

The variation in resin content was very difficult to control in spite of very consistent and predictable glass content. This situation created a problem for modeling. Clearly the same material properties E1, E2, and G12 were not universally applicable. The material properties can be adjusted to compensate for variations in fiber volume between specimens, if either the absolute volume of resin or fiber is known. This project kept track of the absolute weight of glass incorporated into each pole by weighing bales before and after the fabrication of each layer of each pole. Fluctuations in resin consumption are more difficult to measure absolutely since residual resin remains in the

tank, on control devices, and may even drip to the ground. The value for resin consumption is determined by subtracting the glass used from the total weight of a finished pole. For details see Chapter 8.

8 EXPERIMENTAL PROGRAM

8.1 INTRODUCTION

Filament winding exercises during the early part of the study were devised to develop sufficient expertise with the technology and analytical techniques such that experimental production of specimens could proceed. A series of 14 experimental poles were fabricated and tested by Ibrahim (2000). The performance of these poles is documented in that thesis. While Ibrahim's(2000) focused on the structural performance of these poles a more detailed and in depth discussion of the fabrication process and the material characterization is presented in this chapter.

Knowing the structure of a laminate stack for the poles permits the designer to model the load behaviour of a pole. However as was indicated in the previous chapter a number of user inputs are required. What may not have been as obvious is the importance of the material properties of the glass and resin system. It was found that supplier data, as is presented in the appendix, is of limited value for the purpose of analysis, for the following reasons:

1) Supplier data will represent testing standards for resin or for glass fiber. As such one will have limited information of the combined properties. As well, one will rarely get data on the specific resin /glass combination intended for production.

2) The materials used in our study were made available out of standard inventory for regular industrial production. Handling and storage issues are dominated by the need to minimize labour costs. As well, our raw materials required intensive contact with rollers , guides and tension equipment just to get through the resin impregnation tanks. Then the fiber was deployed through a payout eye onto a rotating mandrel.

3) Glass fiber was supplied in a format called "centre pull doffs". This type of bale permits the continuous removal of fiber without rotating the bale, unlike a spool which spins as fibre is deployed. (If one imagines that a roving is a belt of narrow width, which is coiled up neatly then if one applies tension to the outside end of the roving the coiled material spins. If, however, one applies tension to the inside end of the belt one can see that the coil remains stationary as the belt is extracted. However, the belt itself twists through 360 degrees for every loop extracted. This twist is referred to as " catenary twist"). Since in this project fibre containing catenary twist was employed and since product data represents perfectly parallel fibres, it was clear that the use of supplier data was not appropriate. Peters, et. al. (1993) mention translation losses as being a significant factor reducing expected performance of materials. In fact the primary material supplier data ideally represents the product quality as it exits the shipping department.

In this experimental program, the material properties of the unidirectional lamina making up the untransformed lamina stiffness matrix, **Q** were obtained experimentally. These values provided the basis for calculating the effective axial stiffness of the laminate. While it may be considered

possible to extract specimens from the actual poles to obtain laminate properties, this procedure would do little to resolve fundamental issues required for designing poles, nor increase the understanding of the filament winding process since such specimens are in compliance with standardized procedures.

The first part of the experimental program involved the determination of material properties for unidirectional samples of raw materials. These samples were required to conform to appropriate ASTM standards and reflect as closely as possible the losses due to the winding process.

Samples were removed from the base and top regions of the specimen poles. The samples were measured to determine the thickness as accurately as possible. The sample material was then burned using a low temperature propane torch to remove the organic polymer. The burning procedure permitted the sample material to be gently pryed apart to reveal the stacking sequence of the laminate. With careful handling the internal structure is maintained by the carbon residue. This fact makes it possible to measure the thickness of individual plies. Burning did not appear to change the measured thickness of sample materials.

The decomposition of the laminate was used to confirm the sequence of the geodesic winding and the circumferential layers. While the mathematical models for these wind patterns implied constant thickness for circumferential winding and variable thickness for geodesic winding, no such physical evidence could be collected prior to load deflection testing.

Knowing the experimental results of the load deflection studies for these poles (Ibrahim, 2000) it was decided to verify the Bernoulli-Euler deflection model presented in Chapter 7.

8.2 COUPON FABRICATION

Standard coupons were fabricated from the raw materials used to construct the poles. These coupons were specifically fabricated to meet recognized engineering standards for tensile, and compression testing. Shear testing coupons were the only exception for technical reasons and discussed later in this Chapter.

The requirement for unidirectional parallel fibers consolidated in the appropriate resin posed a curious problem. While the literature is replete with coupon testing, typically these coupons are fabricated from unidirectional plies of pre-impregnated material. Often the sample material is supplied to the researcher awaiting only the attachment of grip stock and final dimensioning to fit the specific test. In our study no such pre-consolidated material was available nor would any such material reflect the true fabrication process used by the pole fabricator.

A simple filament winder was constructed in our facility (Fig. 8.1) to fabricate flat coupons using glass and resin identical to those used in the poles. The apparatus used a circumferential wind pattern over a flat-sided mandrel to wind parallel fibers in a manner equivalent to that used to make poles. The drive system was a device used by spool winders called a Uhing rolling ring drive. As the mandrel rotates the drive unit transporting the resin tank and payout eye advances a fixed distance relative to shaft rotation. The fixed advance distance is set equal to one band width of the fiber tow.

Our system used a 0.75" (19.05 mm) wide, 8 line, 1,100 Tex Glass roving. The angle of winding was therefore 0.75" per revolution of the mandrel. The mandrel was 48" (1229.36 mm) long, with a 14" (355.6 mm) square cross section. The corners were rounded with a 1" (25.4 mm) radius. The cross section was chosen to provide slightly better than 12" (304.8 mm) of flat material x 48" (1229.36 mm) per side. The actual wind angle relative to the circumference was determined to be 0.76^0 on the forward stroke and -0.76^0 on the reverse stroke. While relative to the meridian of the mandrel this would be a wind angle of $\pm 89.24^0$.This small angular deviation was considered acceptable when weighed against the potential advantages for the technique.

The specimen material, when completely wound, was vacuum bagged for full compaction and removal of excess resin in the case of series C. The series B material was covered with release film and swept with squeegees to remove excess resin. The film remained in place during curing.

A cured test slab, of a rectangular box shape, was removed from the mandrel and sawn into four flat panels 12" (304.8mm) wide by approximately 36"(914 mm)(Fig. 8.2). This resulted in 12 square feet (0.278 m^2) of sample material. The test sample materials require grips of test specific sizes to be mounted to their ends before testing can commence. The grip stock was fabricated in various thicknesses, from biaxial glass fabric and epoxy laminating resin. The glass fabric for our tests was 5.6 oz. per square yard, style 144, finish 139 manufactured by Bayex of Midland, Ontario, Canada.

The wet out grip stock slab was prepared by covering the wet surface with a polymer release film and then squeegee the surface flat pushing

excess resin to the margins. The cured grip stock was cut to correct dimensions using diamond saw blades to prevent fracturing of the edges.

The slabs were assembled with the grip stock regions prepared by a solvent cleaning and light surface sanding. A single slab had all four grip stock strips, aligned precisely with tape hinges to prevent the contamination of the gauge zones. The adhesive was applied between the grip stock and the specimen stock and clamped or vacuum bagged until cured. The adhesive was the same as used to fabricate the grip stock with the addition of colloidal silica to increase the viscosity and thereby prevent loss of bonding material. Both contact surfaces which have been surface prepared must have completely wet surfaces prior to closing the bond area.

Slabs are cleaned of tape and excess resin , then trimmed to exact width in the diamond saw as shown in Fig.8.2. Finally they were at the correct width for the particular test. Typically the shear and tensile coupons were 9.0" (228 mm) long with a 6.0" (152 mm) gauge length and they were 1.0" (25.4 mm) wide for shear and transverse coupons while only 0.5" (12.7 mm) wide for the longitudinal tensile tests. The compression test specimens are 4.5" (114 mm) long by 0.250" (6.35 mm) wide and 0.200" (5.08 mm) thick with a gauge length of 0.5" (12.7 mm).

The longitudinal and transverse test coupons were made according to the ASTM specification, D3039-76 (Daniel and Ishai,1989) and later updated as ASTM D3039 (2000) .

The shear coupon as was used in this study is not a recognized standard. The configuration was selected in order to utilize our existing test equipment and test slabs with minimum retooling and uses basic dimensions

taken from ASTM D3039-76. As such the coupon does have some limitations as discussed later in the shear test results section. However, it requires no additional tooling or specialized grips or fixtures.

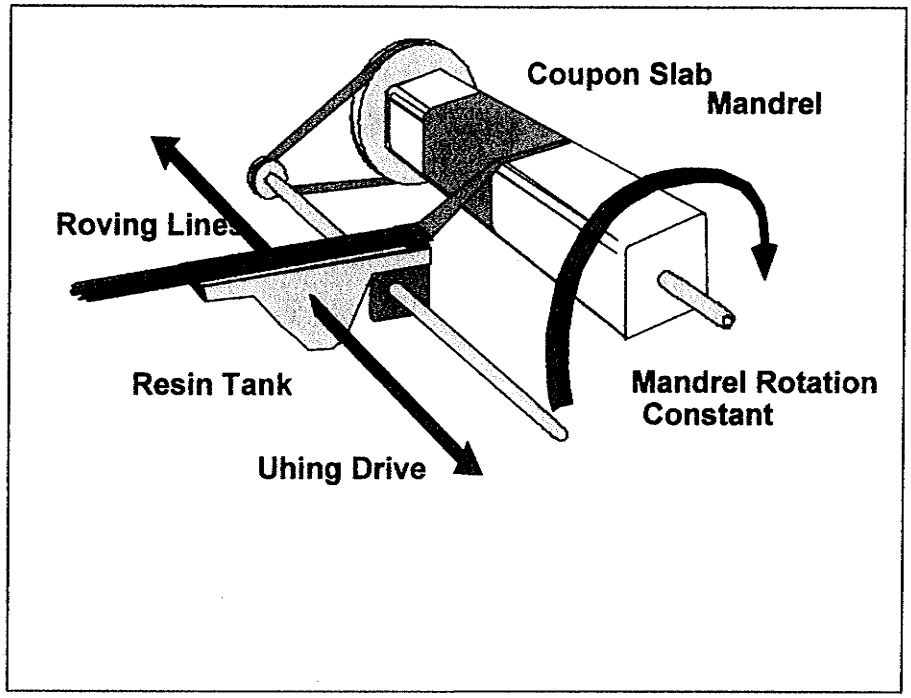

Figure 8.1: Slab Winding Machine

The compression coupon is called the "Modified Wyoming Compression Coupon". It is a modification of the I.I.T.R.I. and Celanesse Coupons. The current version is designed to eliminate the limitations of the previous styles covered under ASTM Standard D3410-95 (Adams and Odom,1991). This system improves on previous standards for which tooling was difficult to obtain. The Modified Wyoming Compression Coupons were tested using a fixture supplied by the Wyoming Test Fixture Co. The dimensions of all test coupons are shown in Figure 8.3. This fixture fit easily into the existing loading machine with no modifications. In Fig. 8.4 the various physical measurements are related to the final calculated material properties .

The advantages of this set of procedures and the equipment used are the uniformity of the samples and the ease with which hundreds of specimens can be produced using a variety of raw fiber and resin variations. Coupons can now be fabricated to detect critical differences in any of the factors involved in the manufacturing processes. This may simply be as part of a quality assurance program or an actual design tool.

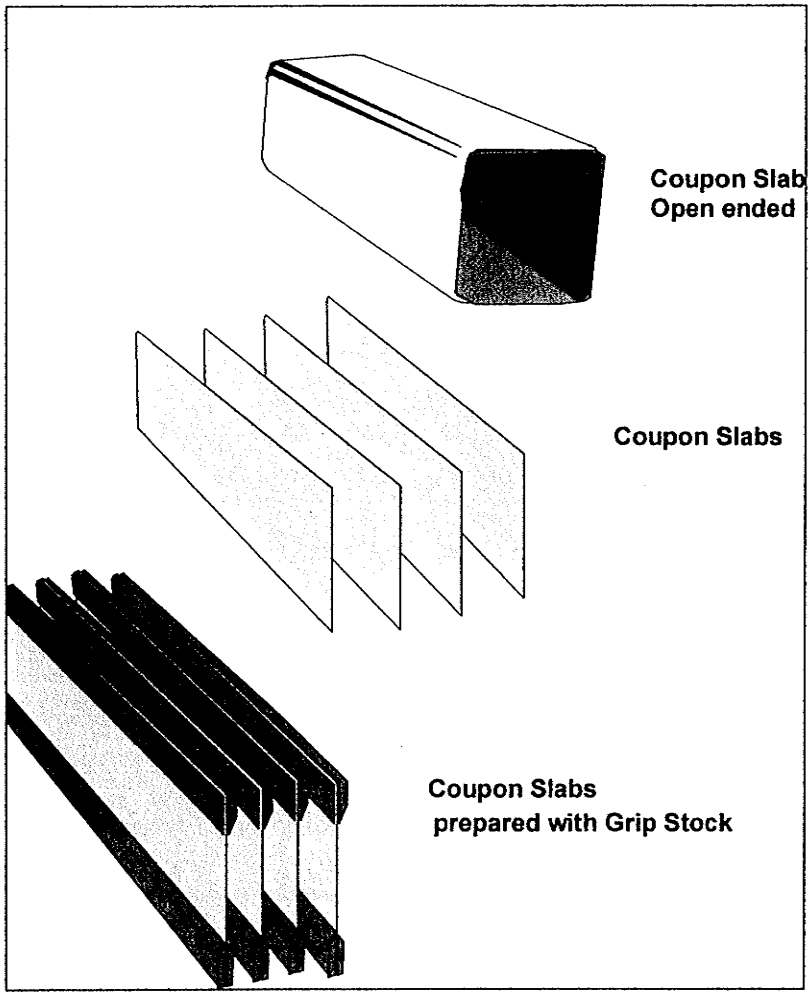

Figure 8.2: Slab Processing

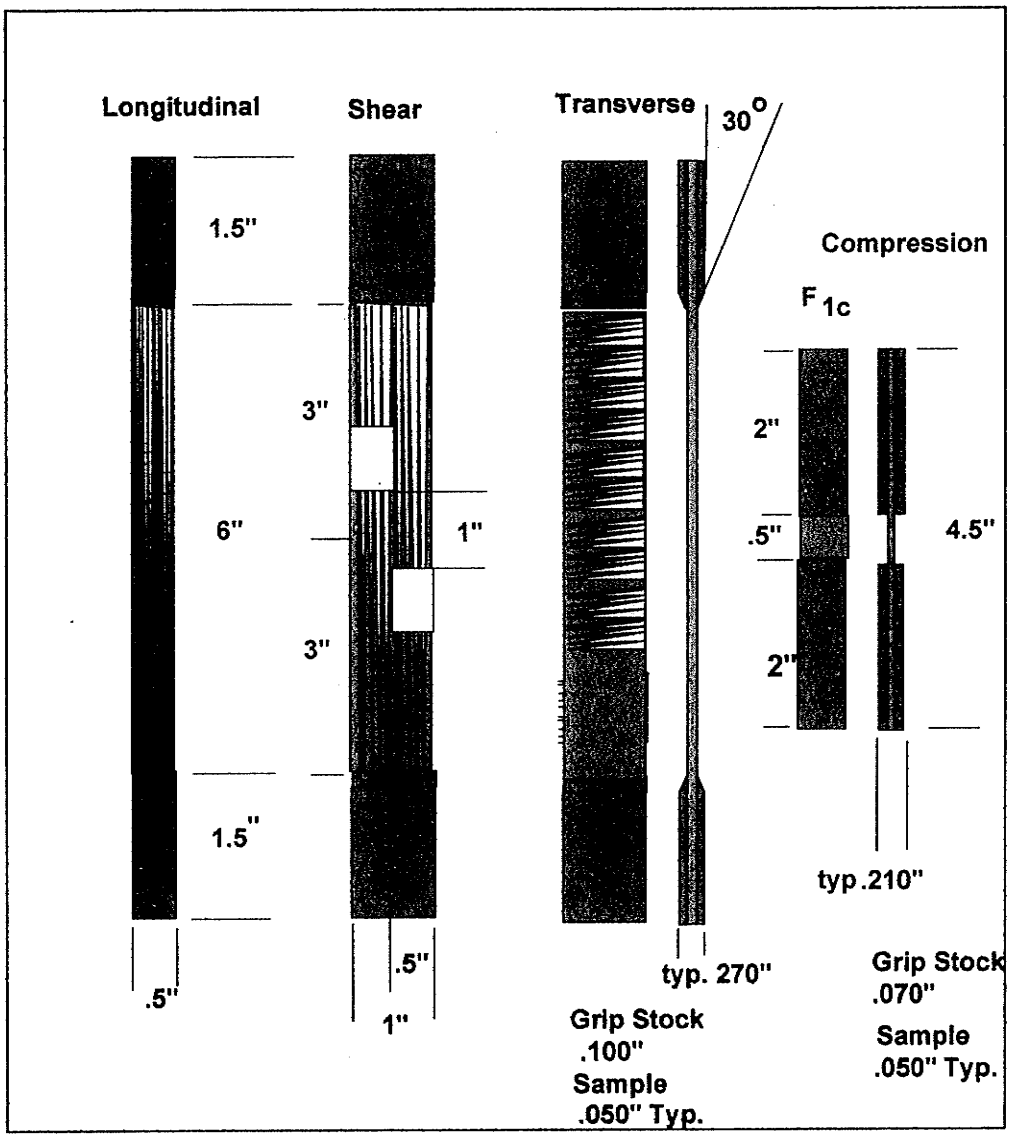

Figure 8.3: Coupon Configuration

Type of Coupon	Measured Parameters		Calculated Properties	
Longitudinal	Load to Failure	**P**	Ultimate Stress Longitudinal tensile	σ_{1t}^{u}
	Area	**A**	Longitudinal tensile Strength	F_{1t}
	Longitudinal Tensile Strain	ε_{1t}	Ultimate Longitudinal Tensile Strain	ε_{1t}^{u}
	Transverse Tensile Strain	ε_{2t}	Major Poisson's Ratio	υ_{12}
			Modulus of Elasticity Longitudinal	E_1
Transverse	Load to Failure	**P**	Ultimate transverse Tensile Stress	σ_{2t}^{u}
	Area	**A**	Transverse Tensile Strength	F_{2t}
	Transverse Tensile Strain	ε_{2t}	Ultimate Transverse Tensile Strength	ε_{2t}^{u}
	Longitudinal Tensile Strain	ε_{1t}	Transverse Modulus	E_2
Shear	Load to Failure	**P**	Shear Stress	τ_6
	Strain (Longitudinal @ 45^0) x axis of strain gauge at 45^0	ε_x	In-Plane Shear Strength	F_6
	Gauge Length	**L**	Shear Strain	γ_6
	Gauge Thickness	**t**	Shear Modulus	G_{12}
Compression	Load to Failure	P	Longitudinal Compressive Strength	F_{1C}
	Area	A		
	Longitudinal Compressive Strain	ε_{1C}		
	Transverse Compressive Strain	ε_{2C}		

Figure 8.4: Nomenclature for Material Properties

8.3 DERIVATION OF MATERIAL PROPERTIES FROM MEASURED PARAMETERS

The following is a list of the formulas used to convert the measured physical parameters to the calculated material properties.

$$\sigma_{1t}^{u} = \frac{P}{A} \quad \text{(Eq. 8.1)}$$

$$\sigma_{2t}^{u} = \frac{P}{A} \quad \text{(Eq. 8.2)}$$

with P being the load applied to the coupon and the area, A is simply the width times the thickness of the cross section of the coupon. Note that P and A are specific to the particular type of coupon. The use of the superscript ***u*** denotes the ultimate value of a parameter determined at the failure limit over the range of an experiment. The alphabetic subscripts c and t denote the direction of the load applied relative to a principal direction. The principal longitudinal direction of laminate in the direction of the fibre is denoted by the numeral subscript 1. While the transverse direction is denoted by the subscript 2.

$$E_1 = \frac{\sigma_{1t}^{u}}{\varepsilon_{1t}^{u}} \quad \text{(Eq. 8.3)}$$

$$E_2 = \frac{\sigma_{2t}^{u}}{\varepsilon_{2t}^{u}} \quad \text{(Eq. 8.4)}$$

$$\tau_6 = \frac{P}{L \times t} \quad \text{(Eq. 8.5)}$$

$$\gamma_6 = 2 \times E_x \quad \text{(Eq. 8.6)}$$

(Ex is determined by having the long axis of strain gauge mounted at 45^0 at the centre of notched section (Daniel and Ishai, 1994)

$$G_{12} = \frac{\tau_6}{\gamma_6} \qquad \textbf{(Eq.8.7)}$$

$$\upsilon_{12} = \frac{E_1 \times \varepsilon_{2t} \times A}{P} \qquad \textbf{(Eq. 8.7)}$$

$$\upsilon_{21} = \frac{E_2}{E_1}\upsilon_{12} \qquad \textbf{(Eq.8.9)}$$

$$F_{1t} = \sigma_{1t}^u \qquad \textbf{(Eq.8.81)}$$

$$F_{2t} = \sigma_{2t}^u \qquad \textbf{(Eq.8.92)}$$

8.4 TEST COUPON DESCRIPTIONS

The series of test coupons, designated as Series B, was made using Type 30, 1100 Tex Roving E-Glass supplied by Faroex Ltd. of Gimli, Manitoba, Canada and manufactured by Owens Corning . The roving is supplied on centre pull doffs. The resin system used for this series, was a modified polyester resin system formulated by Faroex and designated as ***CX132***. Particular modifications included the use of a light activated curative agent , a defoaming agent and a viscosity reduction additive. The system was promoted with cobalt naphtalate and cured using Methyl Ethyl Ketone Peroxide (MEKP), CADOX 50. Since the additives are not considered to affect the structural properties in any direct way, the resin system can still be regarded as a typical polyester winding resin.

The viscosity of the resin was very low at 200-300 cps. and was found to be well suited for filament winding the full scale pole specimens. Due to the

long working times required for the winding of the poles, a retarder was used and this required the addition of the light curative to insure full cure of the exposed surfaces which tended to remain sticky at lower curing temperatures due to oxygen inhibition. The exact details of this resin system were not made available.

The coupon slab was enclosed in a vacuum bag and excess resin absorbed by a bleeder/ breather system when the vacuum was applied at approximately 14" Hg. The slab was permitted to cure completely under this condition before removal. The coupon slab was made using the identical glass and resin used in the production of the large scale test poles.

In the second series, **Series C**, a new resin system based on Vinyl-ester Resin, was introduced. The resin was supplied by DOW Chemicals. The system is designated as Derakane 411-350 . Technical details of this resin system are listed in the **Appendix** . The resin was promoted using a combination of DMA (Dimethyl aniline) and Cobalt Napthalate. The catalyst was MEKP (CADOX 50).

Series C used 1000 Tex E-Glass roving on centre pull doffs supplied by Fiberex Corporation of Edmonton, Alberta, Canada.

The fully wound series C slab was also enclosed in a vacuum bag and the excess resin absorbed by a bleeder/breather system when the vacuum was applied at approximately 14"Hg. The slab was also permitted to cure completely under this condition before removal. The series C slab was produced using the identical resin and glass system used by the CANZEAL Ltd. of Yellowknife, N.W.T., Canada, which produced a set of three 30 foot

prototype poles, using their new winding technology. These prototype poles were tested to failure in a cantilever bending setup during the course of this project . The results of these tests are discussed later.

8.5 COUPON TEST RESULTS

8.5.1 Series B , Longitudinal Coupon Test Results

The results of series B, longitudinal testing are shown in Figure 8.8.

The 10 longitudinal coupons for this set of tests were equipped with a pair of Pi gauges mounted on a quick change bracket, designed to fit the coupons. This device significantly reduced alignment problems, as well as deviations between the Pi gauges, see Fig.8.5. Each coupon was equipped with two Pi gauges and a single foil type strain gauge, as shown in Fig.8.6. This arrangement was used in both series.

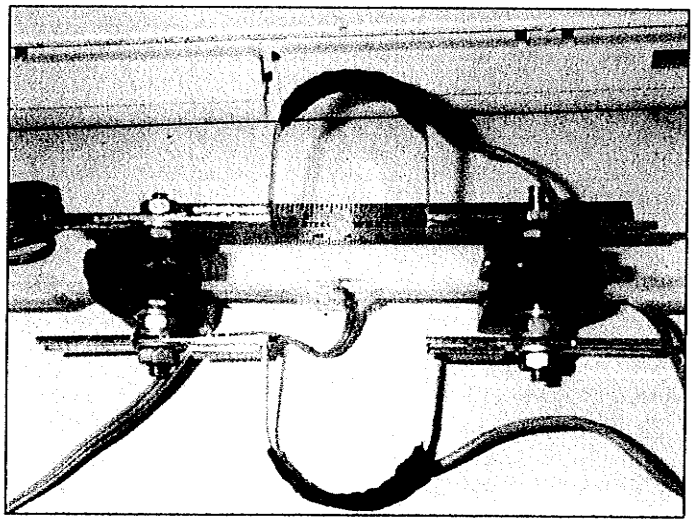

Figure 8.5: Tension Test Setup with PI Gauges

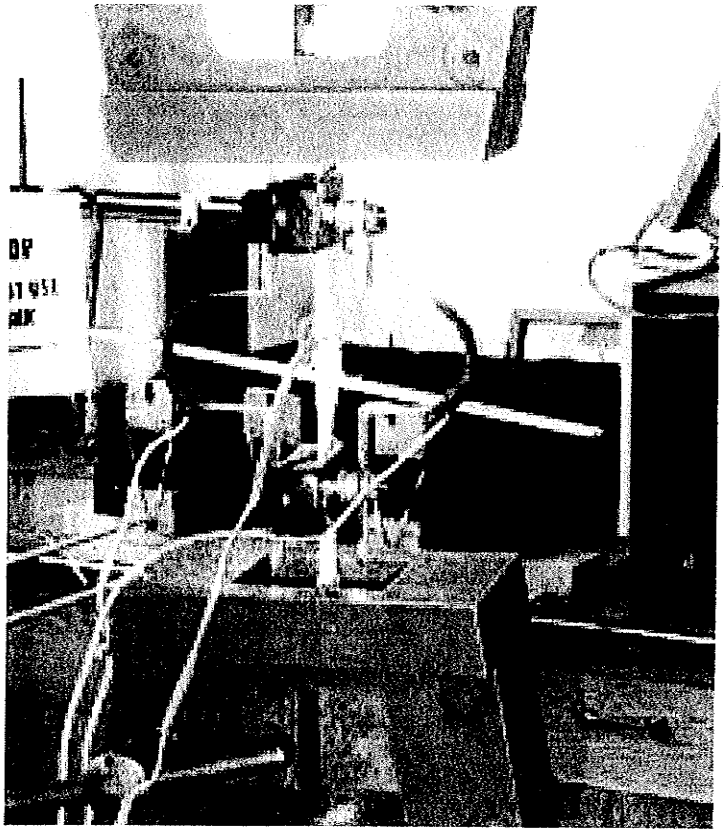

Figure 8.6 Tension Test Fixture

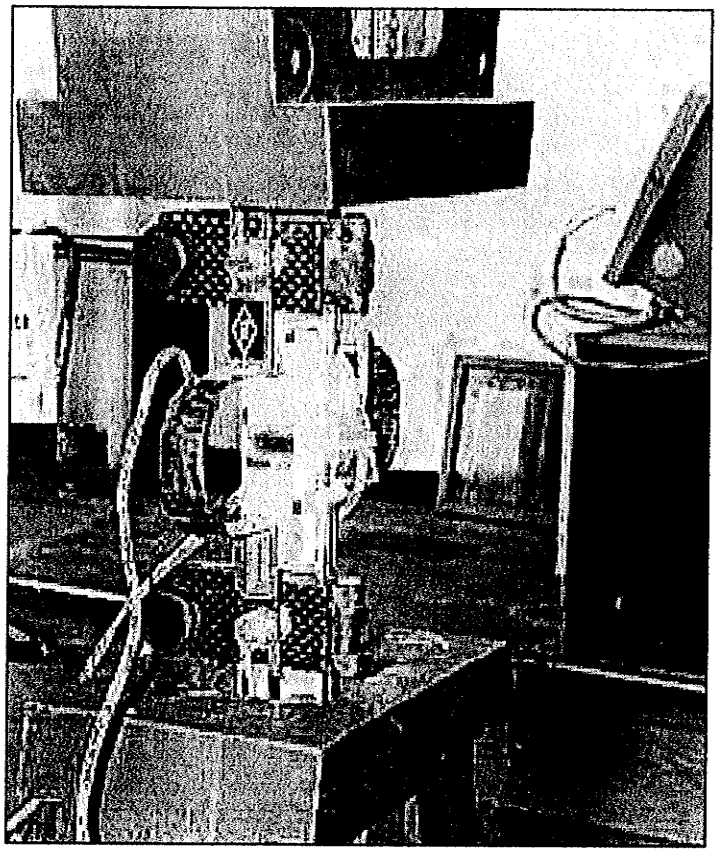

Figure 8.7 Coupon Testing Transverse Setup

The average thickness of each specimen was determined, to be .0555" (1.4mm). The average load to failure, P, was **2457 lbs**. The typical strain at failure was **.024**.

The material properties for series B longitudinal coupons are as follows;

$$\sigma_{1t}^{u} = \frac{P}{A} = \frac{2457}{.5 \times 0.5549} = 88546 \ psi$$

$$F_{1t} = \sigma_{1t}^{u} = 88546 \ psi$$

$$\varepsilon_{1t}^{u} = .024$$

$$E_1 = \frac{\sigma_{1t}^{u}}{\varepsilon_{1t}^{u}} = \frac{88546}{.024} = 3.69 \ Msi \ (Msi = 1{,}000{,}000 psi)$$

$\upsilon_{12} = \frac{-\varepsilon_{2t}^{u}}{\varepsilon_{1t}^{u}} = .35$ ***(Average of Plot of Instantaneous values see Fig.8.9)***

$-\varepsilon_{2C}^{u} = .00969$

The longitudinal modulus of 3.69 Msi (10^6psi), is lower than one would expect when compared to values typically present in the general literature (Daniel and Ishai,1994). The longitudinal specimens behaved quite linearly and except for a slight slippage in the grips due to some coupons being slightly thinner than others (Fig. 8.8).

The value of the Major Poisson's ratio was interpolated from Fig.8.9, and based on an average of end point values was determined to be .35. The υ_{12} value of 0.35 is slightly higher than typical book values which are approximately 0.3 (Daniel and Ishai,1994).

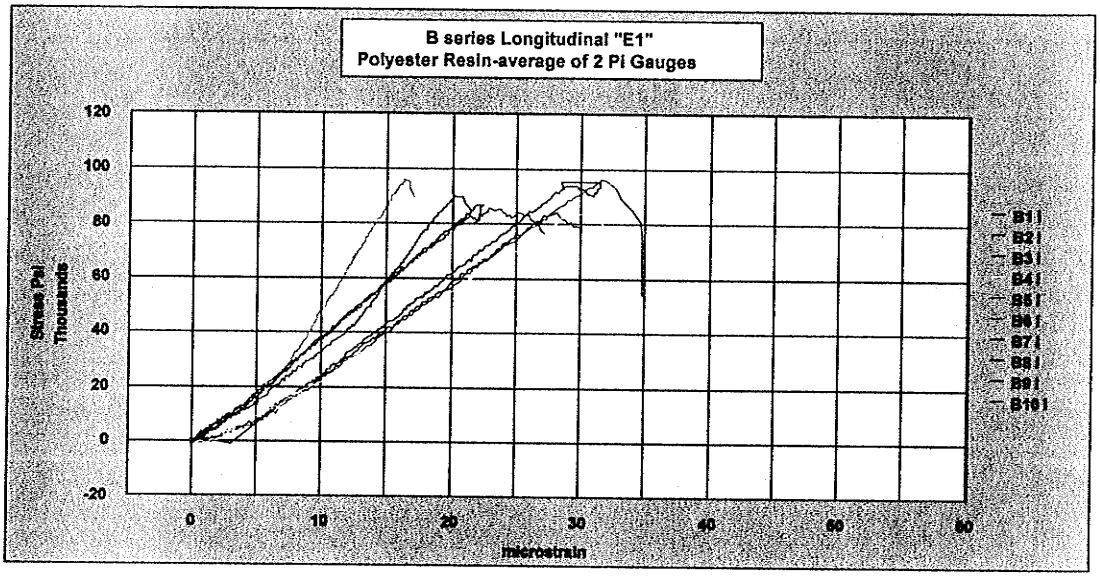

Figure 8.8 Series B, Longitudinal Stress-Strain Plots

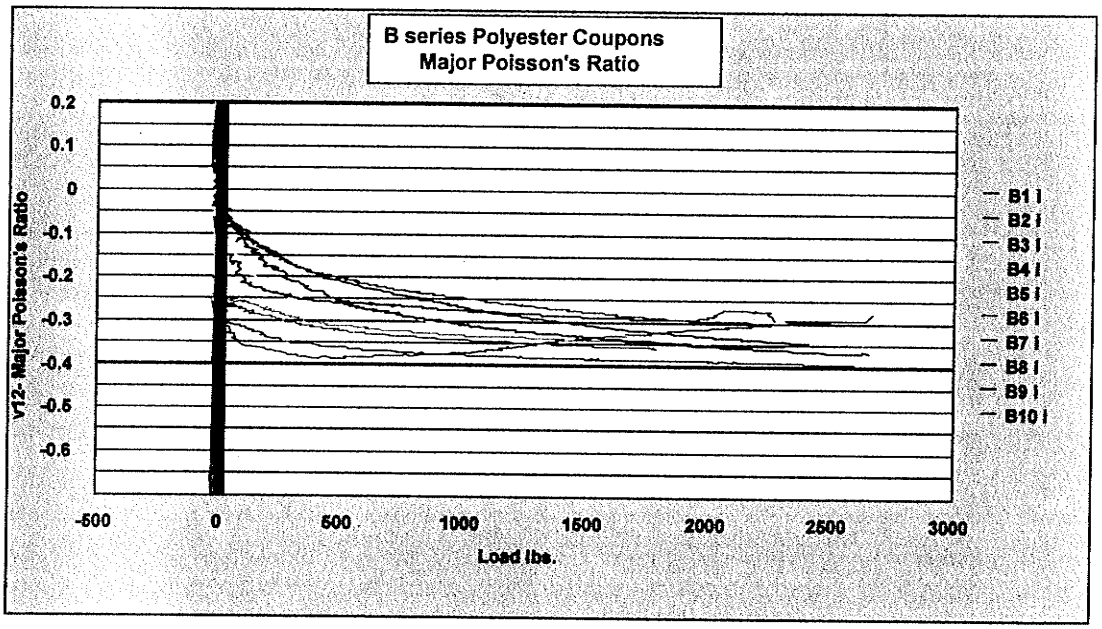

Figure 8.9: Series B, Instantaneous Major Poissoin's Ratio Plots

8.5.2 Series B , Transverse Coupon Test Results

The results of the series B Transverse tests are plotted in Fig.8.10. Seven of the ten original coupons survived handling and the results are plotted. Some slippage of the Pi gauges has resulted in shifted plots. The wide range in failure strengths is due in part to a slightly ribbed texture in specimens resulting from the "ropey" texture of the twisted roving with the fiber bands. The material properties of the series B transverse coupon tests are listed as follows;

$$\sigma_{2t}^{u} = \frac{P}{A} = \frac{89.3}{.052} = 1783 \ psi$$

$$F_{2t} = \sigma_{1t}^{u} = 1783 \ psi$$

$$\varepsilon_{2t}^{u} = 0.0029 \ (Average \ of \ 8 \ specimens)$$

$$E_2 = \frac{\sigma_{2t}^{u}}{\varepsilon_{2t}^{u}} = 0.615 \ Msi$$

$$\upsilon_{21} = \frac{E_2}{E_1} \times \upsilon_{12} = .058 \ (Betti's \ \text{Re}ciprocal \ Law)$$

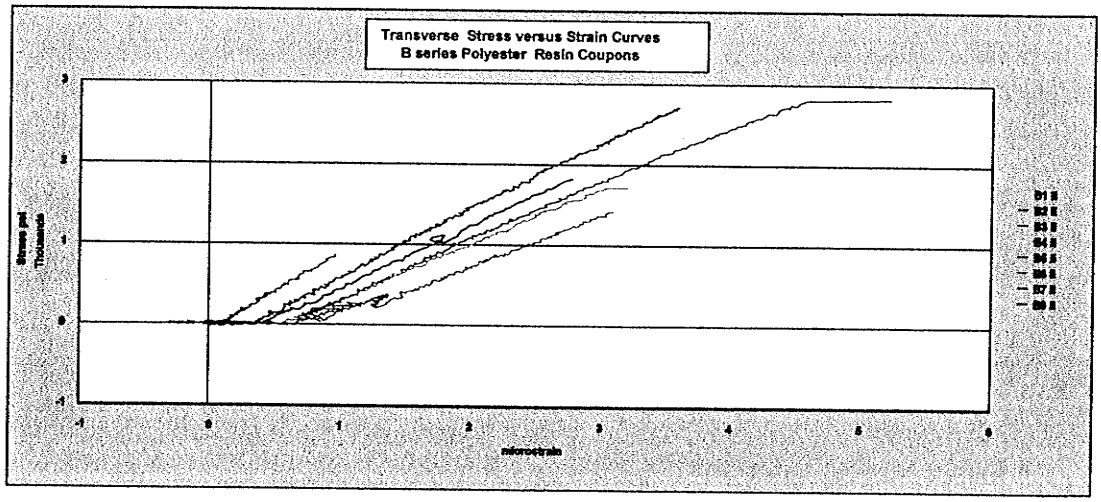

Figure 8.10: Series B, Transverse Stress Strain Plots

8.5.3 Series B: In-plane Shear Modulus Coupon Test Results

The results of the shear tests for series B are shown in Figures 8.11 and 8.12. There is evidence that three modes of failure are captured in these plots. The plots in Figure 8.12, indicate widely variable initial slope of 2.5 Msi which suggests that the principal mode of failure is tensile for samples B3iii, B6iii and B7iii. The lower curves, for samples B1iii, B2iii and B4iii , have an initial slope of approximately 0.4 Msi , which suggests a shearing mode of failure. All curves appear to progress toward another much lower strength state, which turns out to be fibre pullout. This tearing pull-out failure mode was visually observed during the testing of the coupons. Many coupons simply failed to completely break into two distinct pieces and were still partially connected by small numbers of fibers.

Since the failure process was so complex, the ultimate shear stress to failure was arbitrarily set to coincide with the inflection point of the lower set of coupons, B1iii, B2iii and B4iii. In the following Fig. 8.12 the same coupons can be distinguished as having the lower instantaneous shear moduli. The material properties for the series B, shear tests are as follows:

$\tau_6 = F_6 = 2500\ psi$

$\gamma_6 = 2 \times (E_x) = .005$ *(where E_x was placed at 45^0)*

$G_{12} = \frac{\tau_6}{\gamma_6} = .50\ Msi$ *(Slope of $\tau 6$ versus $\gamma 6$, curve.)*

The values of the τ_6, are arbitrarily set to coincide with the point of inflection at 2500 psi with a shear deflection γ_6 of .005%. The In-plane Shear strength, F_6 is as a consequence set to be **2.5** ksi (1 ksi=1,000 psi)

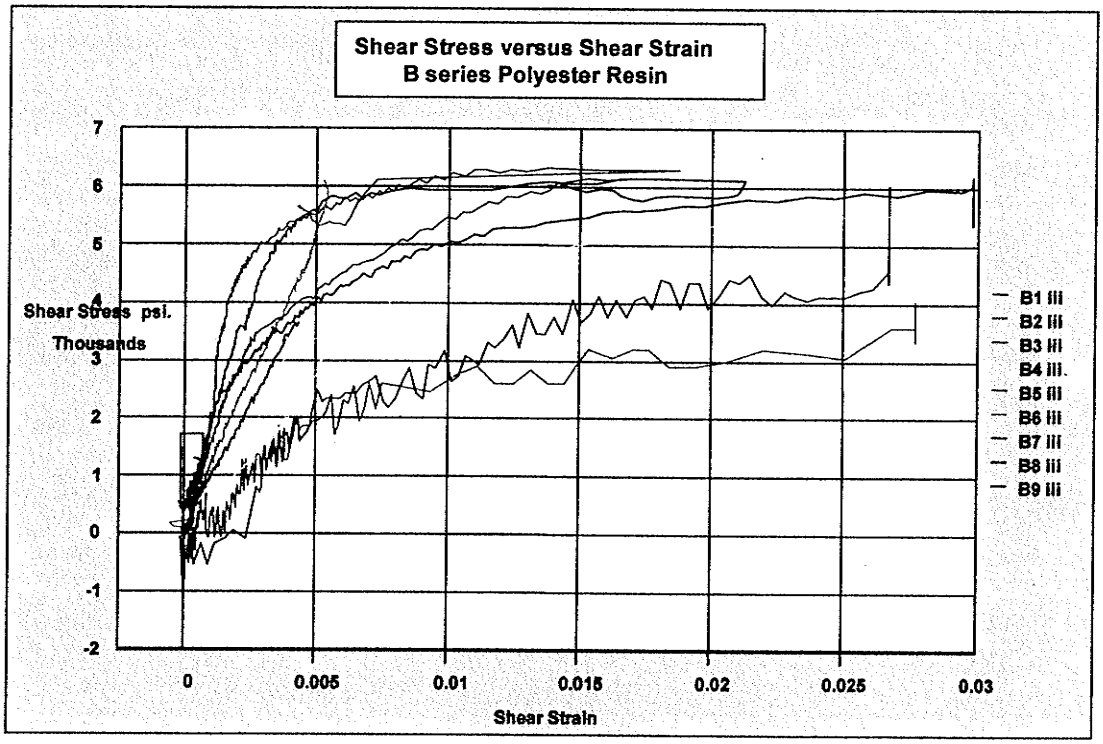

Figure 8.11: Series B, Shear Stress versus Shear Strain Plots

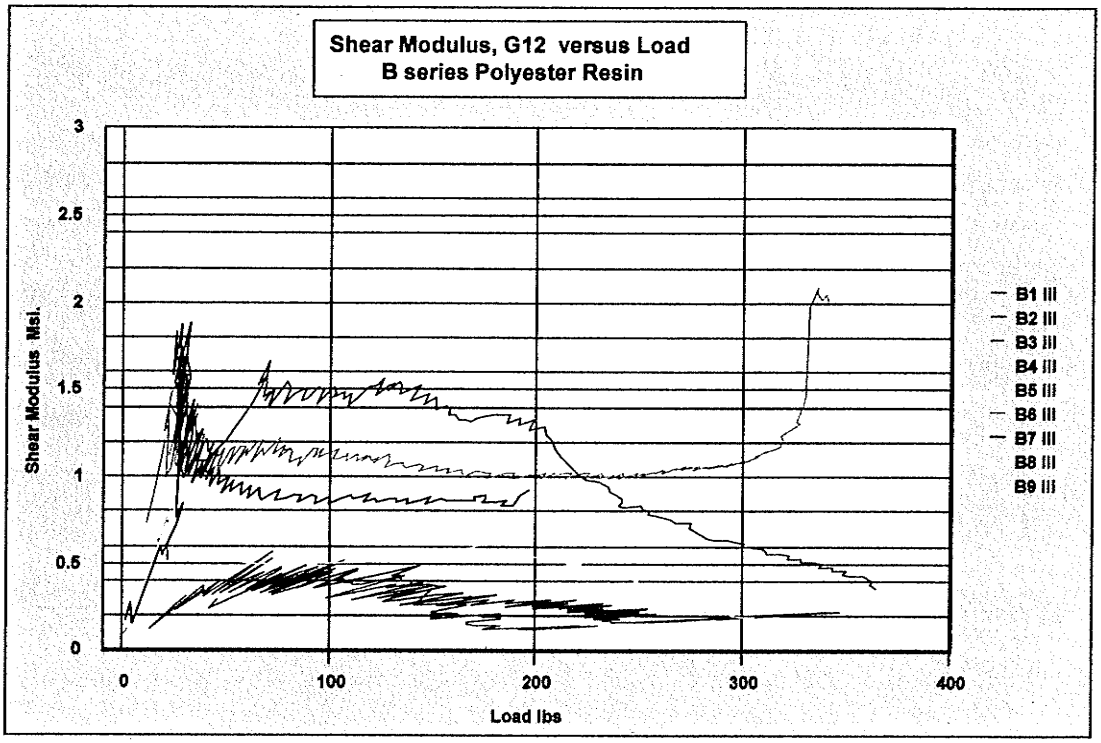

Figure 8.12: Series B, Instantaneous Shear Modulus

8.5.4 Series B , Compression Coupon Test Results

A total of nine specimens were tested for this series of tests . The plots of compressive stress versus strain are illustrated in Fig.8.14. In general the coupons demonstrated a very homogeneous set of results. The average load to failure was 1,323 lbs. The average strength at compressive failure designated as, **F1c**, was determined to be 49,741 psi

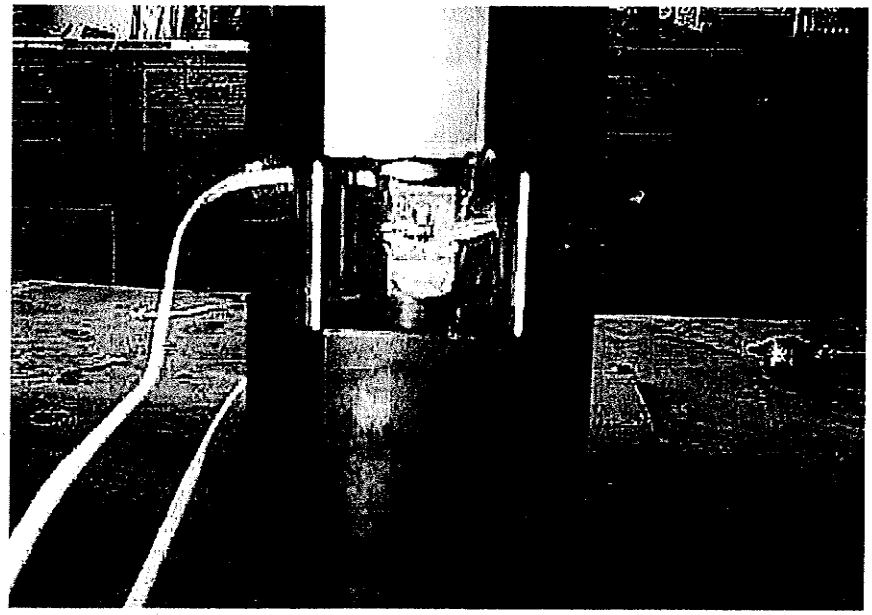

Figure 8.13 Compression Test Fixture

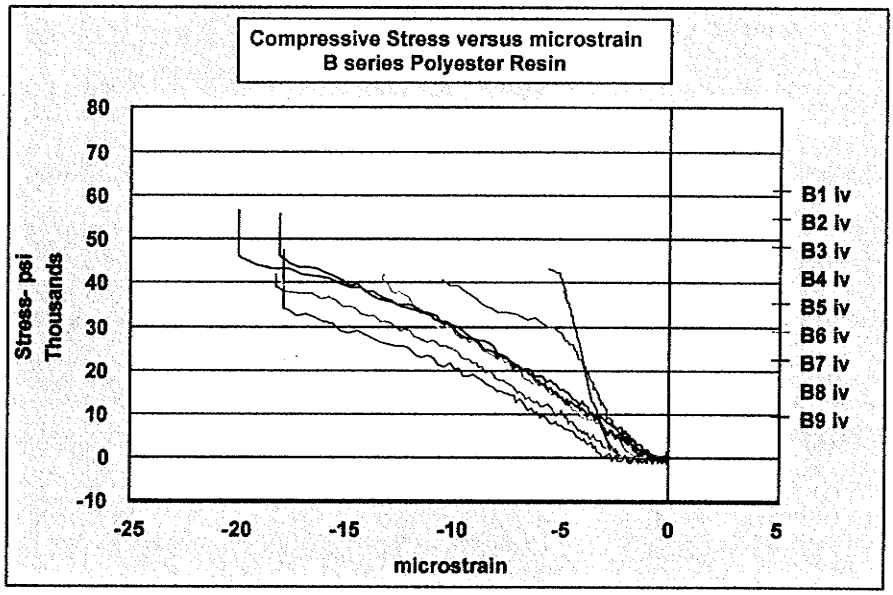

Figure 8.14: Series B Compressive Stresses versus Strain

8.5.5 Series B:

8.5.6 Determination of Classical Lamination Theory Stiffness Matrix

The unidirectional lamina stiffness matrix, ***Q***, (Eq.7.21) parameters were defined previously by Eqs. 4.8, 4.9, 4.10, 4.11 and 7.22, so that the untransformed ***Q*** matrix, for use in classical lamination theory procedures, for the B- series material becomes,

$$Q_{B-series} = \begin{vmatrix} .3767\times10^{7} & 219700 & 0 \\ 219700 & 627800 & 0 \\ 0 & 0 & 400000 \end{vmatrix} psi$$

The stiffness matrix as determined above for polyester/glass was used to model all of full sized and jointed poles produced during the project at the Faroex facility.

To model any particular pole the above stiffness matrix is transformed by the the appropriate ± wind angle for each and every lamina composing the laminate stack. To obtain the effective axial stiffness at each and every point along the length of the pole, the computer model assembles the transformed stiffness matrices using the appropriate wind angle and thickness to determine the Total laminate stiffness matrix, A_{ij}. The compliance matrix a_{ij} is then determined and subsequently the basic engineering properties as described in Chapter 7 by Eqs. 7.25 to 7.28. Circumferential layers with $\pm 86^0$ wind angles are treated exactly the same as the geodesic lamina.

8.5.7 Series C, Longitudinal Coupon Test Results

The results of the series C longitudinal coupons are shown in Figs. 8.14 and 8.15. This series was fabricated using Fiberex E-glass roving 1000 TEX, from centre pull doffs. The resin was the Dow Derakane 411 series with a viscosity of 350 cps, see Appendix for resin details. The wet wound slabs were covered with a release fabric and bleeder breather fabric and closed up with a vacuum bag. The vacuum pump was set to a maximum rate and the vacuum gauge read 28+ inches (14"Hg) which is approximately 1 atmosphere of pressure.

Three prototype poles 30' long tapered from 20" to 12" were manufactured by CANZEAL Ltd. and submitted for load deflection experiments. The resin system and glass used in the fabrication of the poles is identical with this series of coupons. The material properties for this series are used in the modeling of the poles and the results of the deflection model are compared to experimental values in the following section of this chapter.

A total of 8 coupons were analyzed. To determine E_1 value for the test slab coupons the average thicknesses were determined to be 0.073" with values ranging from a low of 0.068" to a high of 0.081". The average load to failure, P, was taken as 2706 lbs. The typical strain at failure was recorded as, **0.0176**. The other properties were computed as follows;

$$\sigma_{1t}^{u} = 69{,}416\ psi$$

$$F_{1t} = \sigma_{1t}^{u} = 69{,}416\ psi$$

$$\varepsilon_{1t}^{u} = .0176$$

$$E_1 = \frac{\sigma_{1t}^{u}}{\varepsilon_{1t}^{u}} = \frac{69416}{.0176} = 3.94\,Msi$$

$\upsilon_{12} = \frac{-\varepsilon_2}{\varepsilon_1} = 0.43$ (*Interpreted from Plot of Instantaneous values, hence no ultimate values*)

$-\varepsilon_{2c}^{u} = .0084$

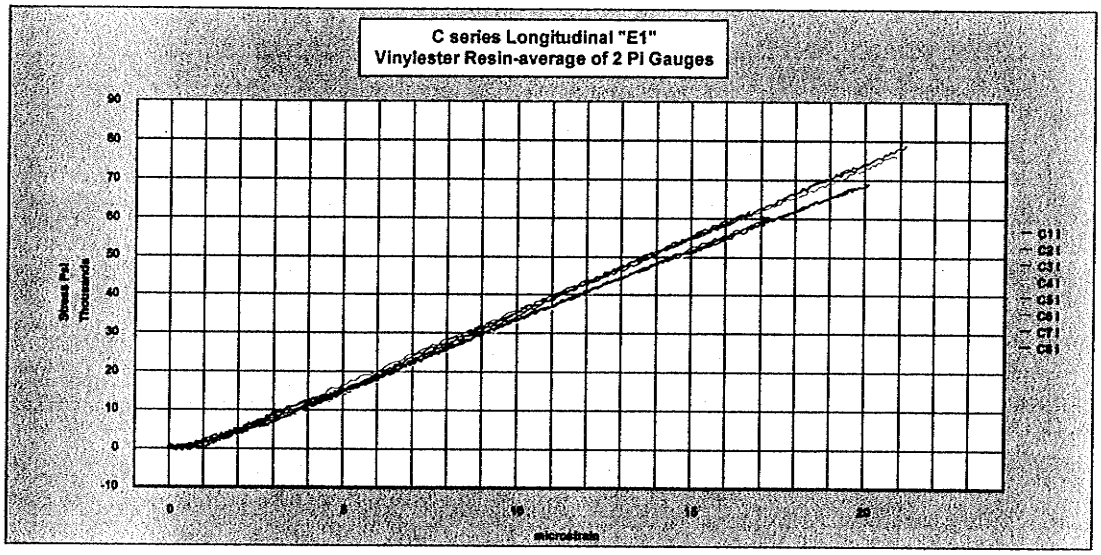

Figure 8.14: Series C, Longitudinal stress Strain Plots

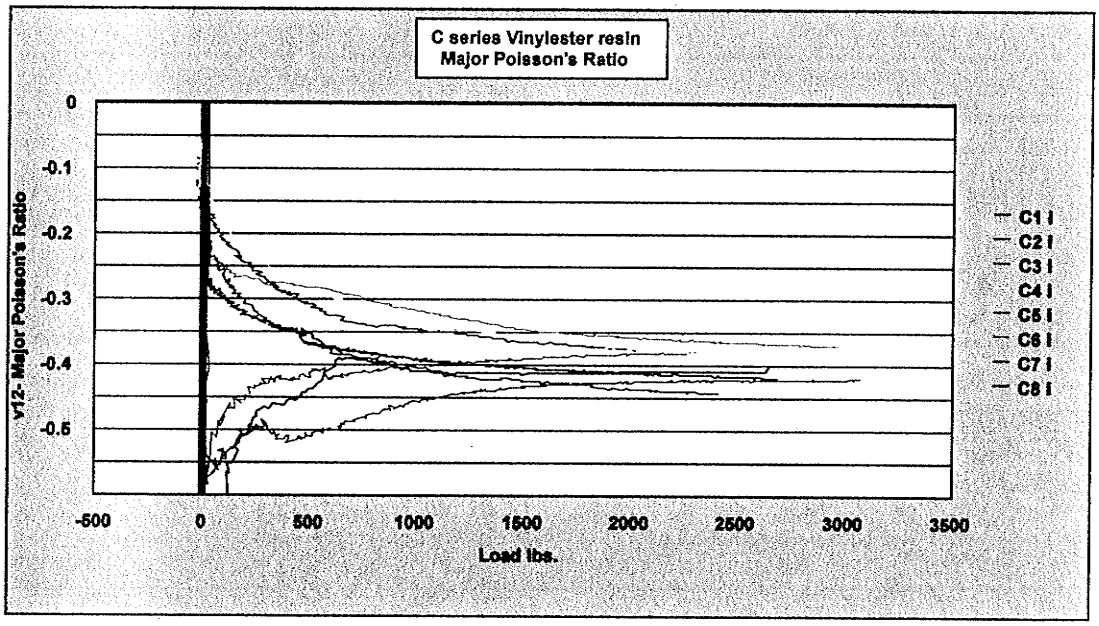

Figure 8.15 Series C, Longitudinal Instantaneous Major Poisson's Ratio Plots

The value of the Major Poisson's ratio was interpolated, and determined to be 0.43. The υ_{12} value of 0.43 is higher than typical book values which are approximately 0.3.

8.5.8 Series C,Transverse Coupon Test Results

The results of the series C, transverse tests are presented in Figure 8.16. Some slippage of the Pi gauges has resulted in shifted plots. The problem with variable results is demonstrated with this series as with all previous transverse tests. The process parameters and the delicate nature of these specimens suggest that in future, thicker specimens should be used. However, if the same slab manufacturing process is to be employed then the other test samples would also be increased complicating the fixturing procedures.

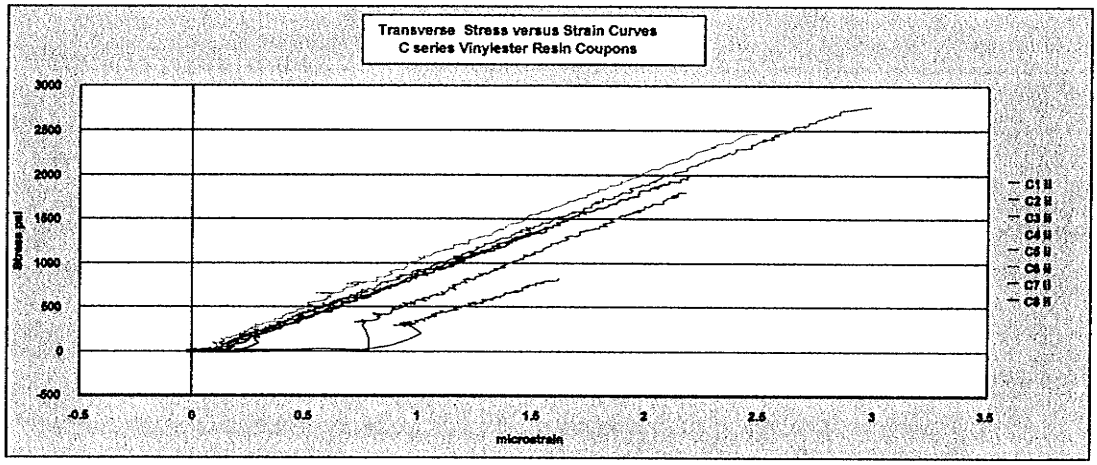

Figure 8.16 Series C, Transverse Stress-Strain Plots

Eight coupons survived handling and the results are as follow:

$\sigma_{2t}^{u} = 1556$ psi.

$F_{2t} = \sigma_{2t}^{u} = 1556$ psi

$\varepsilon_{2t}^{u} = .002$ Average of 8 specimens

$$E_2 = \frac{\sigma_2^u}{\varepsilon_{2t}^u} = .77 \text{ Msi}$$

$$\upsilon_{21} = \frac{E_2}{E_1} \times \upsilon_{12} = .095 \text{ (Betti's Reciprocal Law)}$$

8.5.9 Series C , Shear Coupon Test Results

Eight coupons were tested , and found to vary considerably, with only six plotted in the Figs. 8.17 and 8.18. The average shear load at failure was determined to be 315 lbs. The in-plane shear strength F_6 was therefore found to be 5764 psi.

The determination of the shear modulus G_{12} appears to be more difficult than with any previous specimens as can be seen in Figure 8.18. It was noted that when instantaneous shear moduli versus load are plotted there is a low modulus state near the end of the loading regime characterized by fiber pull out. Since the results were unsatisfactory it was decided to apply a value based on information from our supplier and set G_{12} to have a value of .34Msi(10^6 *x psi*). Typical values for E-glass composites with polyester , vinyl ester and epoxy resins range from .3 Msi (10^6 *x psi*) to .54 Msi (10^6 *x psi*). The lower end of the range is represented by polyesters and the upper end of the range by epoxy resins (Daniel and Ishai, 1993). The sensitivity of Q_{11} term to G_{12} variations in the transformed lamina stiffness matrix was checked and found to be relatively insensitive for a wide range of values of shear modulus. Material properties for the series C shear tests are as follows:

$\tau_6^u = F_6 = 5764 \ psi$ (***using Ultimate value***)

$\gamma_6 = 2 \times (E_x) = 0.0207$ (***Strain gauge mounted at 45^0***)

$$G_{12} = \frac{\tau_6^u}{\gamma_6} \ results \ unreliable \therefore Arbitrary \ setting \ used \Rightarrow .34 \ Msi$$

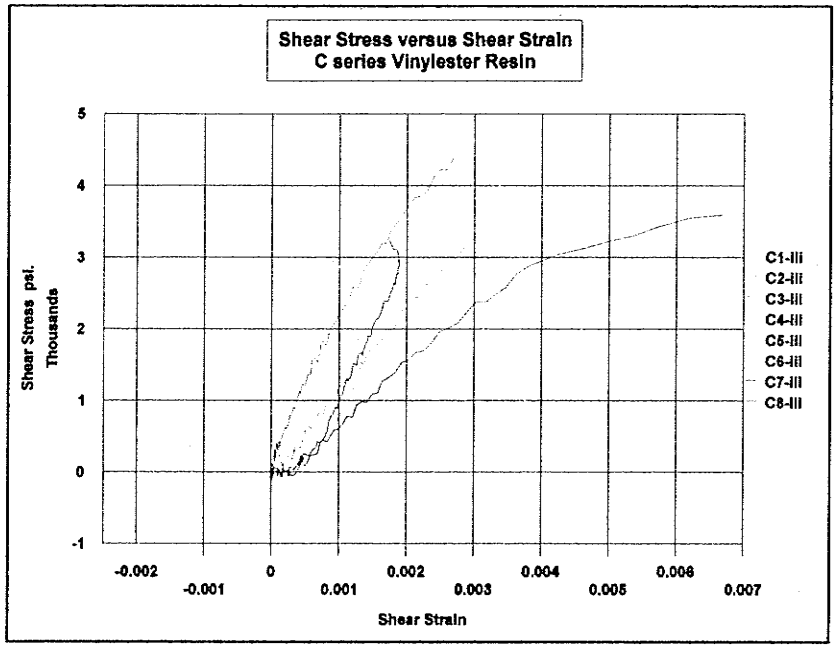

Figure 8.17: Series C, Shear Stress versus Shear Strain Plots

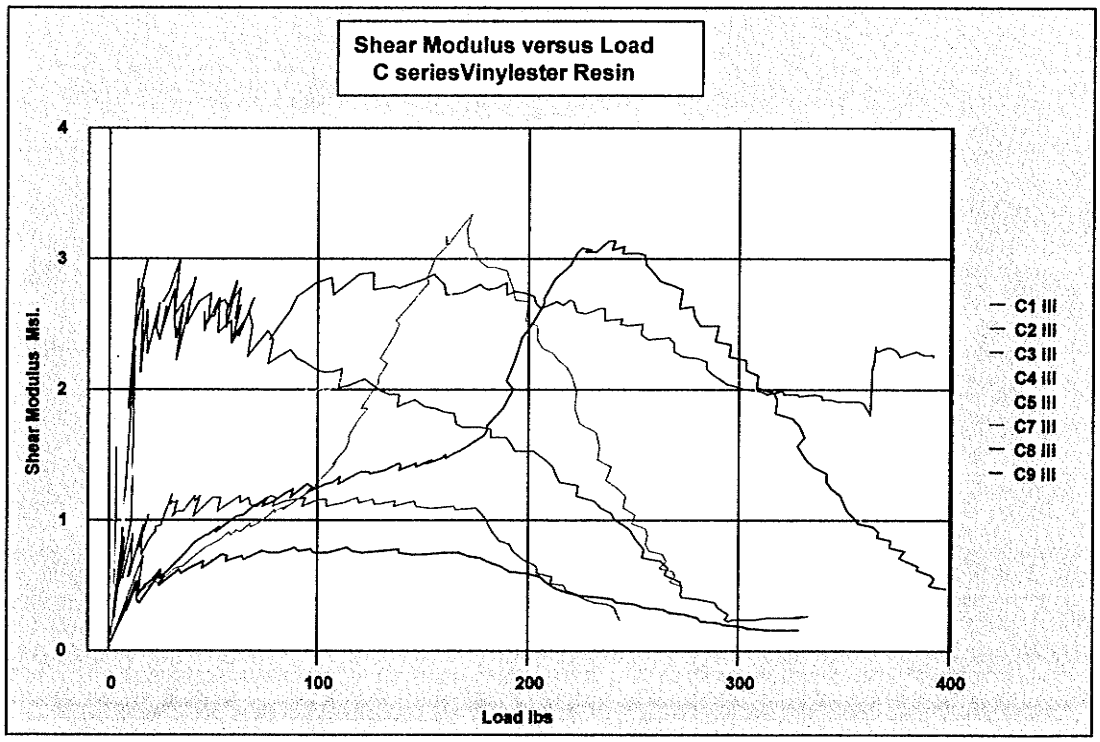

Figure 8.18: Series C, Insantaneous Shear Modulus Plots

8.5.10 Series C, Compression Coupon Test Results

Eight coupons were tested with seven curves plotted in the Fig. 8.19. The limit of the foil gauges was exceeded and some grip slippage was apparent for coupon C9, but this did not appear to be of any relative significance due to the linearity of the curve. The average load at failure was determined to be 2290 lbs. The average compressive stress was determined to be 64,297 psi. The compressive strength, F_{1c} , is therefore **64 ksi**

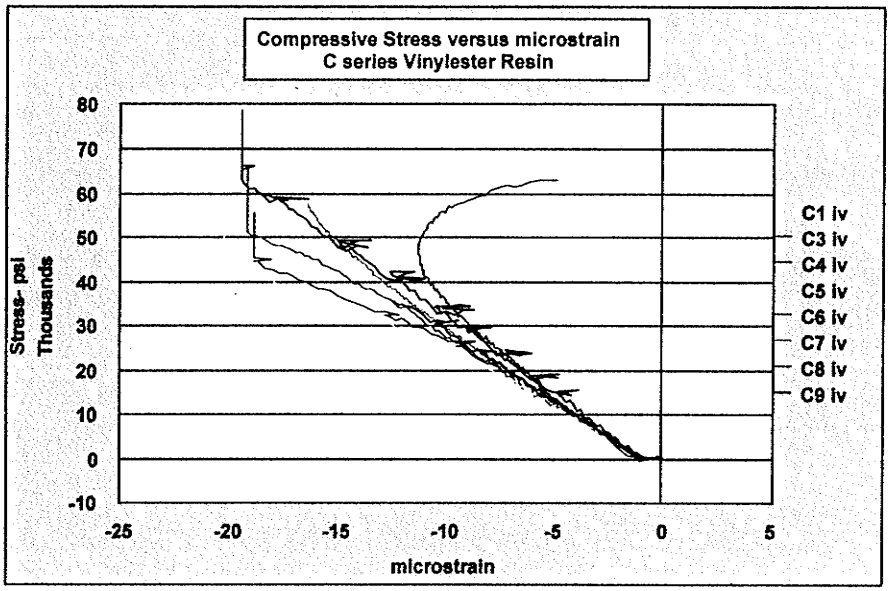

Figure 8.19: Series C, Compression Test Plots

8.5.11 Series C, Determination of Classical Lamination Theory Stiffness Matrix

The stiffness matrix, Q parameters are defined previously by Eqs.4.8 to 4.11 and Eqs. 7.21 to 7.22 .

So that the untransformed ***Q*** matrix, for use in classical lamination theory procedures for the C series, becomes,

$$Q_{C-Series} = \begin{vmatrix} 0.3761\times10^{7} & 348200 & 0 \\ 348200 & 802200 & 0 \\ 0 & 0 & 340000 \end{vmatrix} \; psi$$

This stiffness matrix will now form the basis for the determination of the laminate properties for modelling of the deflection of the three Canzeal poles which will then be compared to the experimental results in a following section. Peculiar to the Canzeal poles is that the axial layers are wound at a true 0^0 angle and no rotation transformation will be required. However the circumferential winding must still be appropriately transformed.

8.5.12 Series B,C : Fibre volume ,Vf , Burn tests

Samples of the coupon slabs were held back until the end of the procedures to evaluate material properties for the various coupons. The burn data is presented in Table 8.1. Surprisingly the volume percentage is much lower than expected. The series B coupons were overlaid with release film and squeegeed flat. Only Series C was actually vacuum bagged at approximately a full atmosphere of pressure. In spite of a pressure of nearly 15 psi the volume fraction, v_f for series C is only 4.2% higher than B series .

There is one significant complication to the low fiber volume of coupons manufactured in this manner. If the material properties are based on these low values then there is a risk that we underestimate the actual performance of a manufactured pole if it should have a higher volume fraction of fiber. In fact, the poles as manufactured have significantly higher fiber volume fractions and will be further discussed later in this chapter. The poles are typically over

wrapped with circumferential fiber as the last stage of the process. Surface normal forces are very high for this last layer and typically the forces drive large amounts of resin out of the underlying laminae.

Table 8.1 Test coupon burn test results

		Series B Polyester /E-glass	Series C Vinylester /E-glass
Sample Weight (grams)		44.91	52.16
After Burn Glass Weight (grams)		26.10	32.54
Fiber Weight Percent W_f		58.1%	62%
Resin Weight Percent W_m		41.9%	37%
Glass S.G.		2.6	2.6
Resin S.G.		1.1	1.1
Volume Percent V_f		36.8%	41%

8.5.13 Summary

The results of the coupon testing program are summarized in the following Table 8.2.

Table 8.2 Material properties of test coupons

Property	E-Glass/ Polyester (B Series)	E-Glass Vinylester (C Series)
Resin Type	Faroex CX 132 Isopthalic Polyester	Dow Derakane Vinylester 411-350
Glass Type Bale type	Owens-Corning 1100 TEX Center-Pull Doff	Fiberex 1000 TEX Center-Pull Doff
Fiber Volume Percent V_f	36.8%	41%
Longitudinal Modulus (E_1 Msi)	3.69 Msi*	3.61 Msi*
Transverse Modulus (E_2 Msi)	0.615 Msi	0.77 Msi
In-Plane Shear Modulus (G_{12} Msi)	0.4 Msi*	0.34 Msi*
Major Poisson's Ratio ν_{12}	0.35	0.43
Minor Poisson's Ratio ν_{21}	0.06	0.0925
Longitudinal Tensile Strength (F_{1t} Ksi)	88.5 ksi	69.4 ksi
Transverse Tensile Strength (F_{2t} psi)	1783 psi	1556 psi
In-Plane Shear Strength (F_6 psi)	5404 psi	5764 psi
Ultimate Longitudinal Strain (ε_{1t}^u F_{2t} Msi)	0.02	0.0176
Ultimate Transverse Strain (ε_{2t}^u)	0.0029	0.002
Longitudinal Compressive Strength (F_{1c})	49.7 ksi	64.3 ksi
	*(Msi $= 10^6 \times psi$)	

8.6 DETERMINATION OF EFFECTIVE AXIAL MODULUS OF LARGE SCALE POLES USING CLASSICAL LAMINATION THEORY

Eleven poles were modeled; all had the same internal dimensions determined by the mandrel dimensions. The poles were all fabricated using the Owens-Corning 1,110 TEX E-glass roving. The resin used was that developed by Faroex and designated CX132. The series B coupon tests determined the material properties of that particular resin/glass system. In order to confirm that each pole is described correctly in the model, samples from the base and top of each pole were extracted and analyzed after completion of the load deflection experiments conducted by Ibrahim(2000). The samples were all cut out parallel to the meridian.

The first step is to establish the wind angle at the base of the pole and the initial thickness of the axial geodesic and circumferential layers. The term layer is not a reference to lamina or laminate rather a layer is a programming concept derived from the filament winding process. In this case a layer is a completely closed surface of filaments all of the same winding pattern whether it be circumferential or geodesic. A circumferential layer is typically near 90 degrees with respect to the meridian and is composed of a forward and reverse direction i.e. $+88^{0}$ and -88^{0}. The circumferential layers therefore are composed of pairs of unidirectional laminae of opposite sign. The fact that the two laminae have only a small total difference in angles makes the pairs very difficult to separate after the burn out. So the pair is measured and given a thickness value. A single lamina is assumed to have half the thickness of the

pair. In practice the winding of a single circumferential lamina is problematic and must be forced with manual interference of the winding program.

Individual lamina of axial geodesic wind patterns can be easily teased apart after burning out the resin. There are two ways to vary the thickness of a geodesic wind pattern. One method is to set the starting number of circuits to a higher value than is the minimum required for complete coverage. The second method is to wind multiple layers above each other of the same pattern. The first method results in some difficulties when attempting uniform compaction and reduced resin content. So for this study multiple layers are employed. Since each layer is a pair of laminae of opposite angles then a stack of n layers is simply ±(n/2) laminae.

In the case of multiple layer axial winding, a difficulty is encountered at the dome ends. As the number of layers is increased the subsequent layers no longer contact the geodesic dome surface but rather the previous layers. The geometry of the dome is changed with each layer applied. In this study it was found that 4 consecutive layers was the maximum practical limit before the filaments would begin to slide off the dome ends. This problem did not appear to apply to circumferential winding since this type of winding does not extend beyond the mandrel barrel. The problem limiting total axial thickness was easily resolved.

For the purpose of modeling of the laminate, the inner circumferential layer is assumed to be composed of 1 positive and 1 negative lamina. The outer circumferential layer is also treated the same way. However the n number axial layers of positive and negative wind angles are summed to a total thickness t_a and the reduced to 1 positive lamina of $t_a/2$ thickness and 1

negative lamina of the same thickness. This procedure was used to simplify the input of data and to avoid having to treat each of the poles as a special case.

The laminate structures and total number of laminae at the base of each pole used in this study are detailed in the Table 8.3. The number outside of a bracket in the last three columns details the number of times the particular winding pattern was run. The term in brackets is referred to as a winding layer since winding requires both positive and negative paths for closure of a surface. A winding layer is therefore composed of 2 laminae. The specific winding layer is measured for thickness and knowing the number of laminae within permits calculation of individual lamina thickness. The thickness of the individual laminae within the laminate as measured by the burn tests are given in the following Table 8.4. The data as presented refers only to conditions at the base or start position of each pole.

Table 8.3 Laminate Structure at Base of Test Poles

Pole ID	Laminate stack generalized designation at BASE Position	Inner Circ. Layer 1 Circ layer thickness composed of 1 forward and 1 reverse direction	1 Axial layer is composed of 1 positive and 1 negative lamina	Outer Circ Layer
		circ	axial	circ
s11v14	[(+88,-88),(+5,-5),(+88,-88)]	[+88,-88]x2	(5/-5)x2	[+88,-88]x2
s12v12	[(+88,-88),(+5,-5),(+88,-88)]	[+88,-88]x1	(5/-5)x1	[+88,-88]x1
s1v1	[(+10,-10)]		(10/-10)x4	
s3v4	[(+88,-88),(+10,-10),(+88,-88)]	[+88,-88]x2	(10/-10) x2	[+88,-88]x2
s4v3	[(+88,-88),(+10,-10),(+88,-88)]	[+88,-88]x1	(10/-10) x2	[+88,-88]x1
s5v13	[(+88,-88),(+10,-10),(+88,-88)]	[+88,-88]x1	(10/-10)x1	[+88,-88]x1
s6v8	[(+20,-20)]		(20/-20)x4	
s7v7	[(+88,-88),(+20,-20),(+88,-88)]	[+88,-88]x1	(20/-20)x3	[+88,-88]x1
s8v6	[(+88,-88),(+20,-20),(+88,-88)]	[+88,-88]x2	(20/-20)x2	[+88,-88]x2
s9v5	[(+88,-88),(+20,-20),(+88,-88)]	[+88,-88]x1	(20/-20)x2	[+88,-88]x1
s10v11	[(+88,-88),(+20,-20),(+88,-88)]	[+88,-88]x1	(20/-20)x1	[+88,-88]x1

The second step is to establish the drift in wind angle and the resultant increase in thickness of the axial component of the laminate. The burning and

decomposition of the top sample yields the change in wind angle of the various layers and is given in Tables 8.5 and 8.6. The measurement of the various winding layers permits determination of which type of winding pattern is responsible for the thickness variation.

Table 8.4 Laminate Structure and Thickness at Base for Test Poles

Pole ID	Laminate stack generalized designation at BASE Position	Inner Circumferential layer thickness		Axial (Geodesic) layer thickness at BASE		Outer Circumferential layer thickness	
		(inches)	mm	(inches)	mm	(inches)	mm
s11v14	[+86,-86,+5,-5,+86,-86]	0.04	1.02	0.108	2.74	0.043	1.09
s12v12	[+86,-86,+5,-5,+86,-86]	0.021	0.53	0.056	1.42	0.021	0.53
s1v1	[+10,-10]			0.235	5.97		
s3v4	[+86,-86,+10,-10,+86,-86]	0.042	1.07	0.107	2.72	0.042	1.07
s4v3	[+86,-86,+10,-10,+86,-86]	0.021	0.53	0.118	3.00	0.021	0.53
s5v13	[+86,-86,+10,-10,+86,-86]	0.021	0.53	0.056	1.42	0.021	0.53
s6v8	[+20,-20]			0.231	5.87		
s7v7	[+86,-86,+20,-20,+86,-86]	0.024	0.61	0.138	3.51	0.025	0.64
s8v6	[+86,-86,+20,-20,+86,-86]	0.037	0.94	0.186	4.72	0.038	0.97
s9v5	[+86,-86,+20,-20,+86,-86]	0.02	0.51	0.115	2.92	0.021	0.53
s10v11	[+86,-86,+20,-20,+86,-86]	0.02	0.51	0.069	1.75	0.02	0.51

Table 8.5 is identical to Table 8.3 except for the column describing the axial layer wind angle. The change in wind angle from the base to top position is due to the wind angle drift.

Table 8.5 Laminate Structure at TOP of Test Poles

Pole ID	Laminate stack generalized designation at TOP Position	Inner Circ. Layer 1 Circ layer thickness composed of 1 forward and 1 reverse direction	1 Axial layer is composed of 1 positive and 1 negative lamina	Outer Circ Layer
		circ	axial	circ
s11v14	[(+88,-88),(+6.7,-6.7),(+88,-88)]	[+88,-88]x2	(+6.7/-6.7)x2	[+88,-88]x2
s12v12	[(+88,-88),(+6.7,-6.7),(+88,-88)]	[+88,-88]x1	(+6.7/-6.7)x1	[+88,-88]x1
s1v1	[(+13.5,-13.5)]		(+13.5/-13.5)x4	
s3v4	[(+88,-88),(+13.5,-13.5),(+88,-88)]	[+88,-88]x2	(+13.5/-13.5) x2	[+88,-88]x2
s4v3	[(+88,-88),(+13.5,-13.5),(+88,-88)]	[+88,-88]x1	(+13.5/-13.5) x2	[+88,-88]x1
s5v13	[(+88,-88),(+13.5,-13.5),(+88,-88)]	[+88,-88]x1	(+13.5/-13.5)x1	[+88,-88]x1
s6v8	[(+27,-27)]		(+27/-27)x4	
s7v7	[(+88,-88),(+27,-27),(+88,-88)]	[+88,-88]x1	(+27/-27)x3	[+88,-88]x1
s8v6	[(+88,-88),(+27,-27),(+88,-88)]	[+88,-88]x2	(+27/-27)x2	[+88,-88]x2
s9v5	[(+88,-88),(+27,-27),(+88,-88)]	[+88,-88]x1	(+27/-27)x2	[+88,-88]x1
s10v11	[(+88,-88),(+27,-27),(+88,-88)]	[+88,-88]x1	(+27/-27)x1	[+88,-88]x1

The thickness of the various lamina at the top position are given in Table 8.6. The small thickness changes to the circumferential winding laminae are thought to be due to variation in measurement technique.

Table 8.6 Laminate Structure and Thickness at TOP of Test Poles

Pole ID	Laminate stack generalized designation at TOP Position	Inner Circumferential layer thickness		Axial (Geodesic) layer thickness at TOP		Outer Circumferential layer thickness	
		(inches)	mm	(inches)	mm	(inches)	mm
s11v14	[(+88,-88),(+6.7,-6.7),(+88,-88)]	0.043	1.092	0.144	3.6576	0.043	1.0922
s12v12	[(+88,-88),(+6.7,-6.7),(+88,-88)]	0.021	0.533	0.07	1.778	0.021	0.5334
			0.000				
s1v1	[(+13.5,-13.5)]		0.000	0.31	7.874		
s3v4	[(+88,-88),(+13.5,-13.5),(+88,-88)]	0.042	1.067	0.138	3.5052	0.042	1.0668
s4v3	[(+88,-88),(+13.5,-13.5),(+88,-88)]	0.021	0.533	0.143	3.6322	0.021	0.5334
s5v13	[(+88,-88),(+13.5,-13.5),(+88,-88)]	0.020	0.508	0.065	1.651	0.02	0.508
s6v8	,(+27,-27)]			0.296	7.5184		
s7v7	[(+88,-88),(+27,-27),(+88,-88)]	0.024	0.610	0.186	4.7244	0.024	0.6096
s8v6	[(+88,-88),(+27,-27),(+88,-88)]	0.038	0.965	0.13	3.302	0.038	0.9652
s9v5	[(+88,-88),(+27,-27),(+88,-88)]	0.021	0.533	0.138	3.5052	0.021	0.5334
s10v11	[(+88,-88),(+27,-27),(+88,-88)]	0.021	0.533	0.076	1.9304	0.02	0.508

The third major step is to assemble a detailed graphic containing the raw data collected from the burn tests for each individual pole. The following

Figure 8.20 shows the graphic details of how the structure changes over the length of the pole. For brevity sake the graphics for the remaining poles are not presented. However the information contained in those graphics is given in Tables 8.3 through 8.6. In all examples it is quite clear that the axial or geodesically wound layer (Green) is increasing in thickness and the circumferential layers are unchanged.

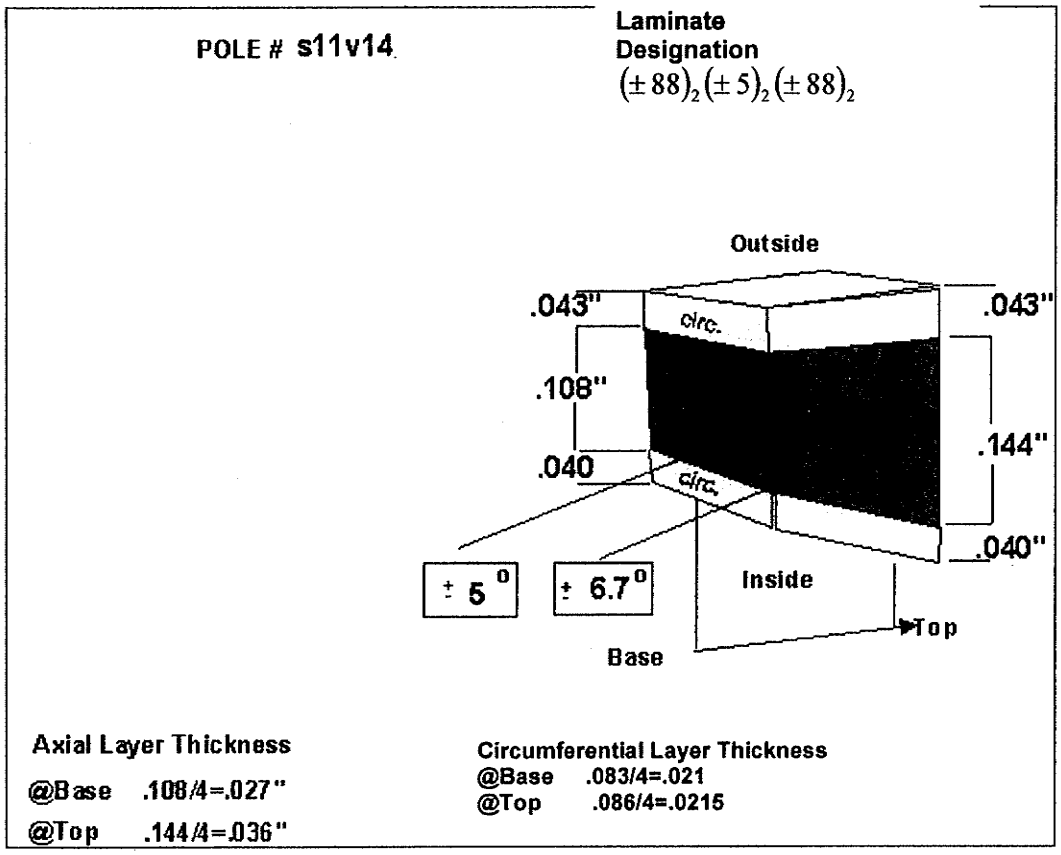

Figure 8.20 Test Pole s11v14

Knowing all the conditions at the base of the pole it is the goal to describe mathematically all the conditions at any other position in order to ultimately conduct the load deflection model. Recall that the base conditions

can be easily determined by the designer since these are the basic winding machine input parameters.

The first critical step is to be able to model the changes in thickness due to wind angle drift. Using the Eq.7.19 and 7.20 the top thickness can be predicted since only the axial layer is affected by drift. To determine a top thickness for a given test pole it is required that t_0 of Eq.7.20 be set equal to the total base axial layer thickness. In addition the inner and outer circumferential layer thickness must be provided as well as the correct equation for radius, length and the B parameter. Faroex large scale test poles were all constructed on a 240" (6096 mm) long mandrel with a B value=8"(203.2 mm) and having r=mx+B where m =-1/120 (Base radius=8"(203.2 mm) Top radius=6"(152.4 mm)) .

The predicted top thicknesses, derived only from the base data, for the experimental test poles are given in the following Table 8.7 and compared with the actual values determined by burn out and direct measurements. The results in some cases are extremely encouraging. It was evident at the time of winding test poles that some variation in resin content between poles and within poles themselves was occurring for unidentified reasons. Some discrepancies were to be expected since the entire thickness modeling procedure is based on the assumption that the cross-sectional area of a resin impregnated roving band does not vary. The variation of the cross-sectional area of impregnated roving is expected to involve factors such as resin viscosity, temperature, and forces due fibre tension in the case of both the circumferential and geodesic winding patterns. At the time of fabrication no knowledge of the significance of these issues was possible.

Table 8.7 Comparison of Predicted Top Thickness with Experimental Values

Pole ID	Top measured thickness		TOP Axial Lamina Thickness From Burn Analysis (inches)		total of top axial plies		TOP total of axial and circ plies		Model Top Thickness prediction (from thickness equation)		Exper./Pred.
	(inches)	(mm)	(inches)	(mm)	(inches)	(mm)	(inches)	(mm)	(inches)	(mm)	
s11v14	0.220	5.59	0.035	0.89	0.144	3.66	0.228	5.79	0.226	5.74	1.01
s12v12	0.112	2.84	0.036	0.91	0.07	1.78	0.112	2.84	0.116	2.95	0.97
s1v1	0.31	7.87	0.0387	0.98	0.3096	7.86	0.31	7.87	0.312	7.92	0.99
s3v4	0.222	5.64	0.0345	0.88	0.138	3.51	0.222	5.64	0.227	5.77	0.98
s4v3	0.185	4.70	0.035	0.89	0.14	3.56	0.182	4.62	0.196	4.98	0.93
s5v13	0.105	2.67	0.0325	0.83	0.065	1.65	0.107	2.72	0.116	2.95	0.92
s6v8	0.296	7.52	0.037	0.94	0.296	7.52	0.296	7.52	0.319	8.10	0.93
s7v7	0.23	5.84	0.031	0.79	0.186	4.72	0.234	5.94	0.239	6.07	0.98
s8v6	0.206	5.23	0.0325	0.83	0.13	3.30	0.194	4.93	0.239	6.07	0.81
s9v5	0.18	4.57	0.0345	0.88	0.138	3.51	0.18	4.57	0.201	5.11	0.90
s10v11	0.117	2.97	0.038	0.97	0.076	1.93	0.116	2.95	0.136	3.45	0.85

The last column of Table 8.7 lists the experimentally measured thickness divided by the mathematically predicted value of thickness for each pole. This value is a measure of how close the predicted values are to the measured values. The predictions range from 81% of measured to 101% of measured thickness. Overall the thickness predictions average 93% of the actual experimentally determined values and it was felt that further elaboration of the modeling was justified.

Knowing the thickness and wind angle of the axial layers at any point within the length of the pole permitted the determination of the effective laminate stiffness at the same points. In the following Table 8.8 the values of the effective laminate stiffness are given for Base and Top of each of the experimental poles. In Table 8.8 only the base

configuration of the laminate is given, for the top configuration refer back to Table 8.6.

The values for the stiffness at the Base (x=0 mm) and Top (x=6096 mm) in Table 8.8 are entirely derived from the Base data presented in Tables 8.3 and 8.5 and were determined using the classical lamination theory solver program written with the aid of MapleV. The term Msi in Table 8.8 is 10^6 psi.

Table 8.8 Effective Laminate Stiffness of Test Poles: at Base and Top

Large Scale Poles		Calculated effective axial Young's modulus		Calculated effective axial Young's modulus	
	Generalized Base Laminate Structure	@ Base		@ Top	
Specimen #		Msi	Gpa	Msi	Gpa
s11v14	[+86,-86,+5,-5,+86,-86]	2.309	15.92	2.44	16.82
s12v12	[+86,-86,+5,-5,+86,-86]	2.34	16.13	2.47	17.03
s1v1	[+10,-10]	2.74	18.89	2.34	16.13
s3v4	[+86,-86,+10,-10,+86,-86]	2.158	14.88	2.134	14.71
s4v3	[+86,-86,+10,-10,+86,-86]	2.493	17.19	2.306	15.90
s5v13	[+86,-86,+10,-10,+86,-86]	2.178	15.02	2.147	14.80
s6v8	[+20,-20]	1.693	11.67	1.23	8.48
s7v7	[+86,-86,+20,-20,+86,-86]	1.798	12.40	1.38	13.08
s8v6	[+86,-86,+20,-20,+86,-86]	1.745	12.03	1.405	9.69
s9v5	[+86,-86,+20,-20,+86,-86]	1.797	12.39	1.383	9.54
s10v11	[+86,-86,+20,-20,+86,-86]	1.761	12.14	1.4	9.65

Table 8.8 is a summary of the results obtained by running the modeling program for each test pole, only the base and top values of stiffness are presented. The program actually plots the data regarding stiffness graphically with respect to axial position. The following Figures 8.21 to 8.23 are taken from the output of the modeling program and show that the variation in stiffness is clearly not necessarily linear. The stiffness variation of the two 5^0 poles are shown superimposed in Figure 8.21. The fact that the stiffness is increasing is the result of increasing thickness offsetting the losses due to

wind angle drift.

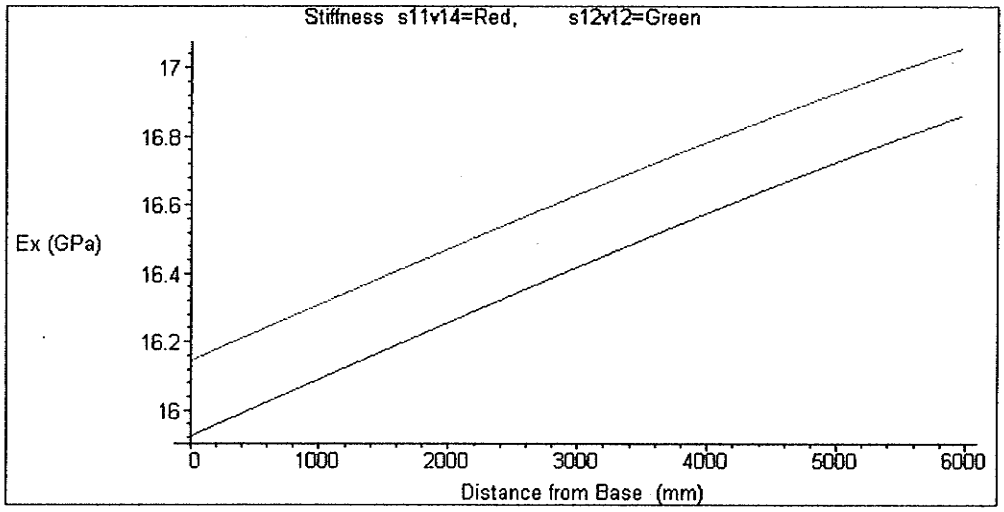

Figure 8.21 Stiffness Variation of Poles s11v14 and s12v12

The effective axial stiffness of the four 10^0 poles are shown in Figure 8.22. Two poles, s4v3 blue, and s1v1 red, demonstrate degrading stiffness toward the tip.

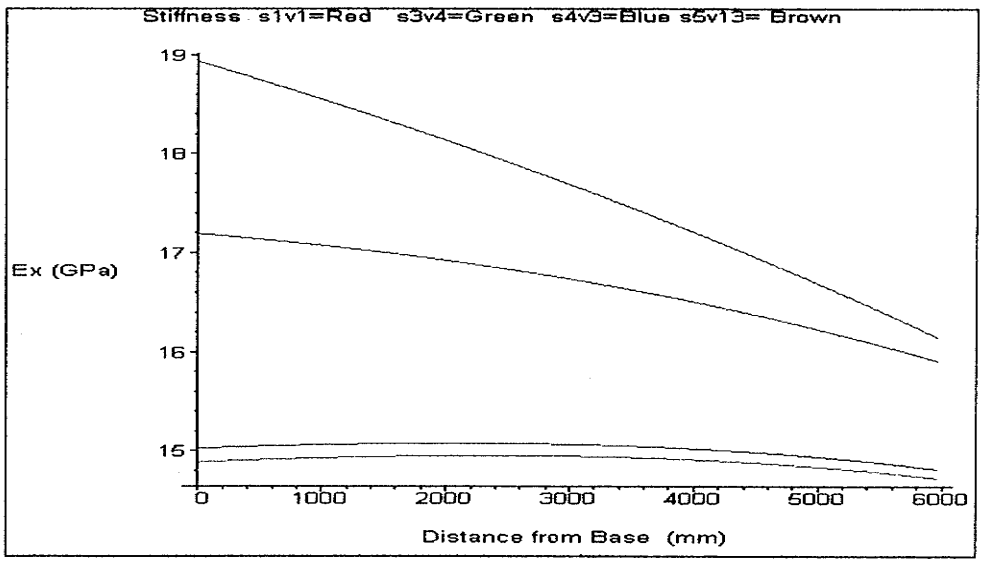

Figure 8.22 Stiffness of Poles s1v1, s3v4, s4v3, s5v13

The two other poles (green *s3v4* and brown *s5v13* curves) show a relatively stable modulus from base to top.

In Figure 8.23 the axial stiffness of the five 20^0 wind angle poles are plotted. Characteristic of these poles is the low initial stiffness and the rapid degrading of the initial values.

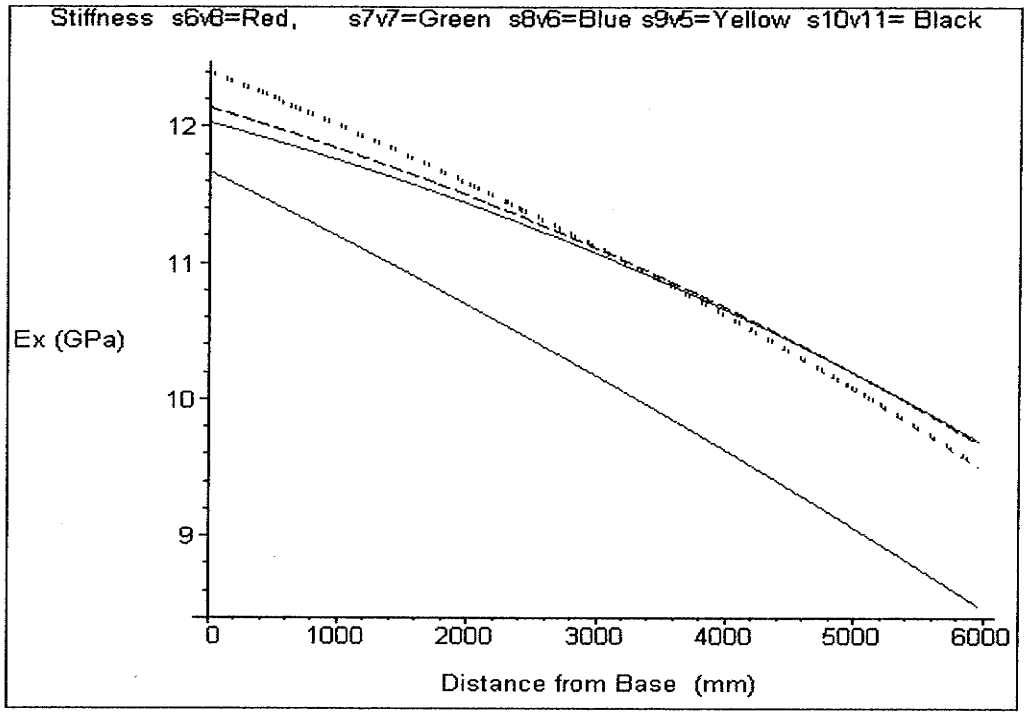

Figure 8.23 Stiffness of Poles s6v6, s7v7, s8v6, s9v5, s10v11

8.7 EXPERIMENTAL DATA ON LARGE SCALE POLES (*FAROEX POLES*)

The main goal of this project was to be able to model test poles and the curious interaction between winding types, thickness, and general laminate structures with regards to ANSI 05.1 load classes

The Faroex poles were large scale single section poles, shown in detail in Fig.8.24. The setup complies with the ASTM (1999) standard for testing wooden poles and is intended to represent a typical 1 meter deep burial with a load applied to the cross arms approximately 26" (660 mm) below the top of the pole, this provides a 175" (4445 mm) gauge length.

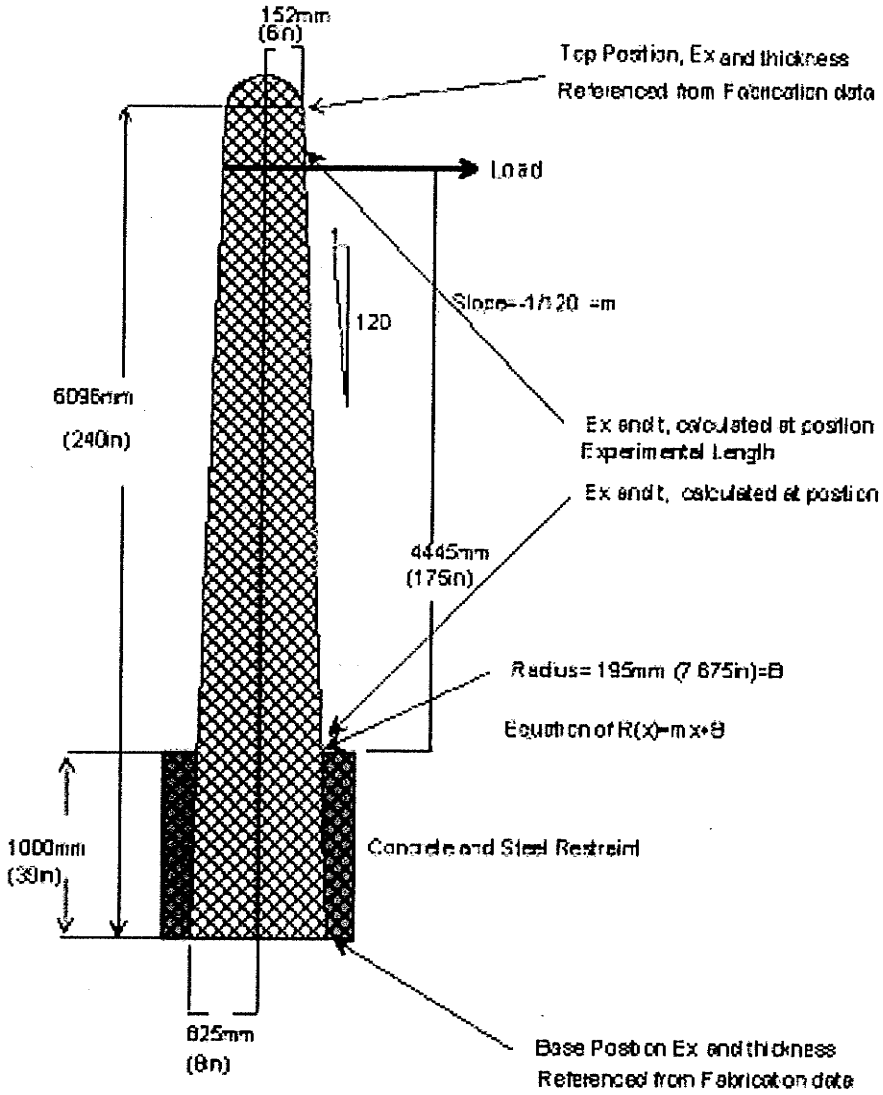

Figure 8.24 ASTM (1999) Standard Pole Testing set up

The experimental testing program for the Faroex poles previously discussed was conducted as part of a Ph.D. thesis (Ibrahim 2000). In that work the poles were incrementally loaded to ultimate failure and the results tabulated and fitted to the equivalent ANSI 05.1 Pole class.

The testing data is summarized in Table 8.9:.

Table 8.9: Faroex Full-scale Pole Experimental Performance Data

Large Scale Poles	Ultimate Load		Experimental Deflection		ANSI 05.1 Equivalent Pole Class	Weight	
Specimen #	kN	(lbs)	mm	(inches)		kgs	(lbs)
s11v14	20	4496	403	15.87	1	63	138.6
s12v12	8.8	1978	278	10.94	5	38	83.6
s1v1	34.2	7688	490	19.30	H3	100	220
s3v4	30.1	6767	608	23.94	H2	68	149.6
s4v3	20.8	4676	430	16.93	1	61	134.2
s5v13	7.55	1697	240	9.45	6	39	85.8
s6v8	30.4	6834	431	16.97	H2	95	209
s7v7	36.4	8183	634	24.96	H3	81	178.2
s8v6	28.1	6317	593	23.35	H2	72	158.4
s9v5	18.9	4249	416	16.38	2	60	132
s10v11	6.9	1551	252	9.92	6	38	83.6

The load ranges and classes of the ANSI 05.1 system are presented in the following Table 8.10.

Table 8.10 Wooden Pole classification system based on load capacity

ANSI 05.1(1992)

Class	Transverse Load (lbs.)	Transverse Load (kN)
H6	11400	50.7
H5	10000	44.5
H4	8700	38.7
H3	7500	33.4
H2	6400	28.5
H1	5400	24.0
1	4500	20.0
2	3700	16.5
3	3000	13.3
4	2400	10.7
5	1900	8.5
6	1500	6.7
7	1200	5.3

8.8 DEFLECTION AND THICKNESS MODELING OF LARGE SCALE POLES

8.8.1 Faroex Types

The following Figs.8.25 to 8.27 are Maple V output from the Bernoulli-Euler Iterative Beam deflection model, presented in Chapter 7.0, and was used to compare ultimate deflections. The test pole models are reduced from 240"(6096mm) down to 175" (4445mm) long according to the ASTM testing procedure as shown in Fig.8.24. The test pole properties used in the model were set up to reflect that portion of the pole undergoing loading. The zero point for the following graphs is the top of the 1 meter deep concrete restraint and the tip is actually the loading point where displacement measurements were taken during the actual experiments (Ibrahim, 2000). Knowing the properties at the true base of the pole, the intermediate zone, under going loading, can be determined with some degree of accuracy since the winding angle changes and thickness variation can be determined mathematically.

In Figure 8.25 the ultimate load is quite different and is expected since these two poles are quite different in overall weight and thickness. From Table 8.9 the weight of s11v14 is 62 kgs and that of s12v12 is nearly half at 38kgs. Much of the weight difference is known to have come from the increased number of laminae in s11v14(see Table 8.3). Both poles were wound using the same patterns only the number of them was altered as can be seen in Tables 8.3 through to 8.7. These two poles represented the culmination of our efforts to control the problems associated with very low wind angle fabrication.

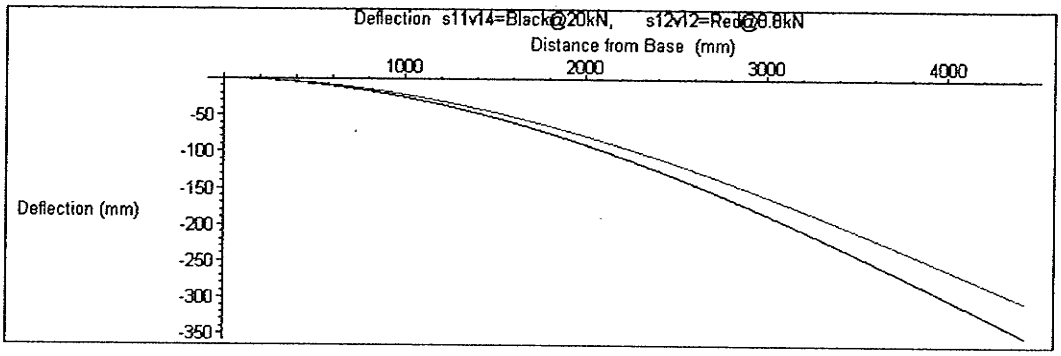

Figure 8.25 Deflection at Failure 5^0 Poles : s11v14 and s12v12

In Figure 8.26 the four 10^0 poles are shown super imposed, with poles s1v1 and s4v3 virtually identical in displacement at failure. However, these two poles are quite different in thickness and load capacity as can be seen in Table 8.4.

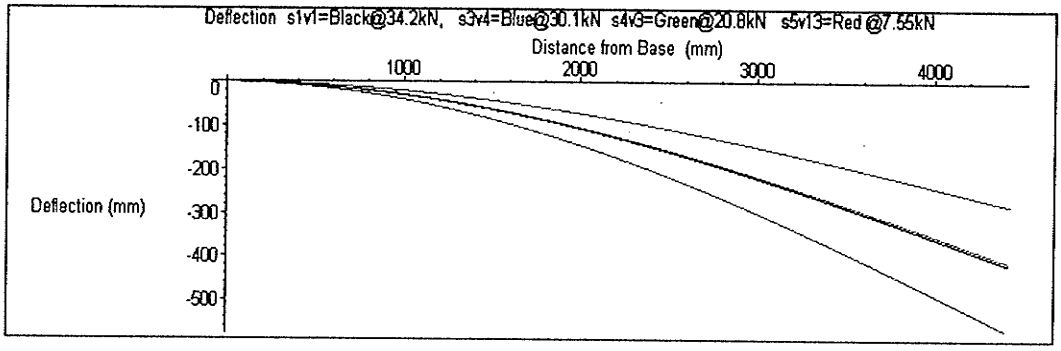

Figure 8.26 Deflection at Failure 10^0 Poles: s1v1, s3v4, s4v3, s5v13

The 20^0 poles are shown in the following Figure 8.27.This group of poles represents a very wide range of load classes, from Class 6 to H3.

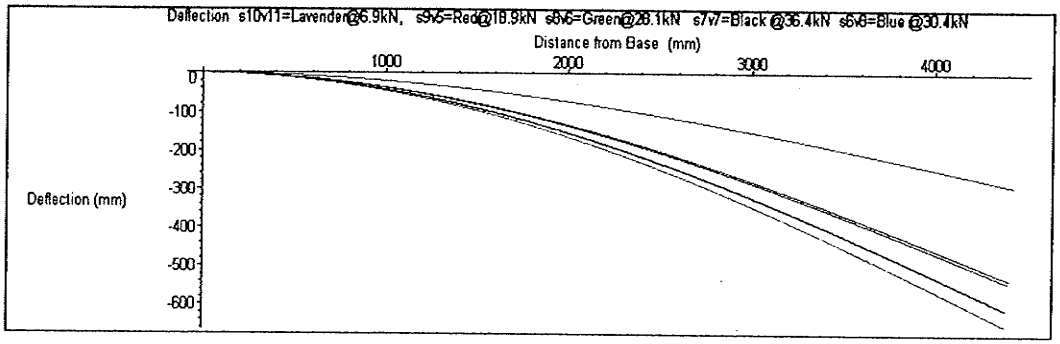

Figure 8.27 Deflection at Failure 20 Poles: s6v8, s7v7, s8v6, s9v5, s10v11

The 20^0 axial wind angle group of poles represented a range of thickness in order to determine the limits of winding stability over our geodesic domes. Test pole ***s6v8*** is one of the thickest wound during this phase and was in fact completed with great difficulty. Filament tows had to be manually positioned during the last winding pattern as all stability was lost due to fibre build up on the smaller geodesic dome. The rest of the 20^0 group used circumferential winding to compact the axial geodesic filaments.

The results of the deflection modeling are presented in Table 8.11.

Table 8.11 Faroex full-scale poles, Model Deflection versus Experimental

Large Scale Poles	Ultimate Load		Experimental Deflection		Predictions based on Bernoulli-Euler Iterative Model		accuracy
Specimen #	kN	(lbs)	mm	(inches)	mm	(inches)	Pred/Exp.
s11v14	20	4496	403	15.87	352	13.87	0.87
s12v12	8.8	1978	278	10.94	306	12.06	1.10
s1v1	34.2	7688	490	19.30	418	16.46	0.85
s3v4	30.1	6767	608	23.94	567	22.34	0.93
s4v3	20.8	4676	430	16.93	412	16.22	0.96
s5v13	7.55	1697	240	9.45	283	11.15	1.18
s6v8	30.4	6834	431	16.97	543	21.36	1.26
s7v7	36.4	8183	634	24.96	611	24.04	0.96
s8v6	28.1	6317	593	23.35	659	25.96	1.11
s9v5	18.9	4249	416	16.38	532	20.96	1.28
s10v11	6.9	1551	252	9.92	291	11.46	1.16

In general the model appears capable of modeling the deflection of poles quite well. The accuracy of deflection predictions (predicted value/ experimental value) ranges from 87% to 128% with the overall average being 117%. The wide range of prediction accuracy is somewhat discouraging. Since the model is totally dependent on accurate measurement of the

laminate thickness at the base of a pole, unidentified manufacturing irregularities can drastically undermine predictions. The problem is compounded by another factor namely that of resin content.

The data used to model the laminate effective stiffness E_x is taken from the Series B coupon data which is composed of identical materials to the test poles but fabricated under slightly different circumstances. The actual resin content of the test poles fluctuates, as was to be expected due to lack of experience. The coupons were known to have a lower glass content (v_f = 0.38) than the typical test poles, see Table 8.12, but some of our poles were behaving in an unexpected manner. Some poles were much stiffer than expected based on coupon material properties.

The 20^0 winding pattern encircles the mandrel with substantially more force than was evident with either 10 or 5 degree patterns. At the time of winding the 20^0 pattern resin squeeze out was occurring at an alarming rate and had the appearance of circumferential winding. The pressure on the laminate stack was clearly higher than for any other pole sets.

This change in pressure was evidenced through comparison between Pole s1v1 a 10^0 wind otherwise very similar to Pole s6v8 a 20^0 pole. In Table 8.11 the deflection prediction of the Bernoulli-Euler Model of Poles s6v8 and s7v7 represents a deviation from all other poles. The effective axial stiffness for these two poles is increased by a multiplication factor of 1.4. This adjustment factor to the coupon data is the resin volume compensation factor.

8.9 Balancing Resin Content

The material properties of the poles were calculated based on the properties determined experimentally from test coupons, but the poles were found to differ in resin content from the coupons in spite of using the identical constituents. Since these resin volumes were not identical, a procedure based on the Rule of Mixtures was used to adjust the E_x value determined from coupons at one resin volume to poles with a different resin volume.

It was assumed that the difference in the derived E_x values is entirely due to the difference in the volume of resin. Filament winding circumferential fibers over top of low angle axial fibers results in very high compression and squeeze out of resin not possible to duplicate with manual coupon fabrication. For this study it was determined that the average filament wound tube had a glass volume of between 52 and 55 %. The coupon burn tests indicated that the glass volume was 38% for the isopthalic polyester samples.

Burn tests of large pieces from scrap test poles indicated that the new winding protocols adopted had significantly reduced the resin content. The jointed pole production technique resulted in glass content average of 53% by volume. The clear impact of such a mismatch between coupons and machine made filament wound test samples resulted in a serious underestimate of pole stiffness.

According to the basic Rule of Mixtures,

$$E_C = E_f v_f + E_m v_m \qquad \text{(Eq.8.12)}$$

Where the Young's modulus of the composite is the sum of the products of moduli and the volume fractions for fiber and matrix respectively. Substituting into this equation the known values determined experimentally from coupon

testing an adjustment factor was required to correlate coupons with samples of identical material but different volume fractions.

The following are typical material properties values from supplier information, however the value for resin is so much less than that of the fiber that in effect it is almost negligible.

$E_c = 3.6 \times 10^6 \, psi$

$v_f = 0.38$

$E_m = 9{,}000 \, psi$

$v_m = (1 - v_f)$

Substituting these known values into the Eq. 8.12, the value of E_f is solved for and found to be 9.46 Msi. This is very close agreement with general literature (Flinn, R. A. and P.K. Trojan, 1990) which lists a value for E_f at 10 Msi. Substituting the calculated value of E_f back into the Eq. 8.12 and replacing the coupon matrix volume fraction, v_m with that for the filament wound poles, 0.531, the new E_c value is determined to be 5.0 Msi. This value is then divided by the original 3.6 Msi to derive a multiplication factor of. 1.396 The factor of 1.4 is applied to the E_f longitudinal moduli value determined by the Classical Lamination theory prior to the modeling process. It appears that the compensation factor can be applied directly to the values of E_1 and E_2 of the 3 x3 Q, lamina stiffness matrix, derived from coupon tests, since E_2 is possible to derive from E_1 using Betti's Reciprocal Law. The effective axial modulus can then be calculated as described earlier, using Classical Lamination theory. As a check, the compensation factor was applied to both the original calculated laminate effective axial stiffness and the Q stiffness

matrix and found to be in close agreement . It appears the differences in the two methods of application of the compensation factor are equivalent for these specific cases.

Our coupon testing work revealed a conceptual problem with the axial modulus E_1. If a pair of identical longitudinal coupons are fabricated and one is tested, one could assume the sister would exhibit the same failure properties. If however we take the untested sister coupon and apply pure resin to both faces should we expect a change in failure strength? This possibility was tested in our program and it was noted that the failure of such coupons was nearly always identical to the original coupon. The contradiction occurs inadvertently when the thickness is measured to calculate the stress applied to a cross-sectional area to calculate the Young's modulus.

While fabricating our test poles, occasionally the operator would squeegee the surface of the mandrel to remove free running resin and recycle it into the impregnation tanks. This was done for economy and cleanliness, as was required. On some days this operation was performed more regularly than on other days. Small changes in the ambient temperature would affect resin viscosity. At higher temperatures the resin would drip noticeably and required more squeegee work to control the drips.

The burn out data on sample sections clearly showed variation in resin content but the actual cause was never clearly determined at the time since the tension on the filament tows and the resin mixture were assumed to be constant.

At the time of fabrication a record of the total amount of glass fibre consumed was made by weighing the glass fibre bales before and after each

pole was fabricated. Resin weight was more difficult to account for due to spillage. The total weight of the pole less the weight of glass consumed was used to determine the weight of resin consumed by the particular pole. The formula for determining the volume percentages from weight percentages is as follows,

$$\left(\frac{Glass\ wt.}{Sp.G.of\ Glass}\right)/\left(\frac{Glass\ wt.}{Sp.G.of\ Glass}+\frac{\text{Resin}\ wt.}{Sp.G.of\ \text{Resin}}\right) \qquad \textbf{(Eq.8.13)}$$

The Specific gravity, *Sp.G.*, of Glass, was set to 2.55 grams/cm^3 and resin was set to 1.1 grams/cm^3 . The data obtained is presented in Table 8.12.

A small number of extra samples were taken from the top and base of certain poles, weighed, burned out and weighed again. These few burn specimens are recorded under the Fiber Volume columns of Table 8.12 on either side of the values determined from production data in green.

Table 8.12 Fibre Volume Percent Data

Pole #	Base Sample measured thickness mm	Base sample weight grams	After Burn weight grams	Fiber volume		Top Sample measured thickness mm	Top Sample weight grams	After Burn Weight grams	Fiber Volume
s11v14	4.674	72.110	56.870	0.62		5.588	68.760	49.950	0.53
s12v12	2.489	N/A	N/A	N/A		2.845	N/A	N/A	N/A
s1v1	5.969	60.04	43.72	0.54		7.874	90.21	72.25	0.63
s2v2	5.3848	67.85	51.45	0.58		7.112	92.06	70.93	0.59
s3v4	4.8514	N/A	N/A	N/A		5.6388	N/A	N/A	N/A
s4v8	4.064	N/A	N/A	N/A		4.699	N/A	N/A	N/A
s5v13	2.4892	N/A	N/A	N/A		2.667	N/A	N/A	N/A
s6v8	5.8674	59.02	42.65	0.53		7.5184	101.35	74.61	0.55
s7v7	4.7752	66.950	52.090	0.60		5.842	98.700	81.400	0.67
s8v6	4.7244	98.320	65.180	0.46		5.2324	114.350	88.980	0.60
s9v5	3.9624	N/A	N/A	N/A		4.572	N/A	N/A	N/A
s10v11	2.7686	N/A	N/A	N/A		2.9718	N/A	N/A	N/A
				0.55	0.55				0.60

The most important conclusion drawn from the deflection modeling is that the designer of poles must have some assurance that the fabricator of poles is consistently producing poles with the intended properties. The performance of the deflection model presented in Chapter 7.0 is very

encouraging and it appears to have a potential for use during the design stage. A typical pole design requires only minutes to input and run, thus allowing the designer to make multiple modifications to a design and quickly see the effect on performance.

8.10 Canzeal Poles

Canzeal Inc. of Yellowknife N.W.T, Canada, submitted three filament wound poles to the University of Manitoba for load deflection and ultimate load tests. The poles represented a set of prototypes that were being manufactured with a new type of winder being designed and built by Canzeal shown in Figure 8.28.

The sample poles were the produced with this new machine, as such, no expectations of suitability were ever in their plans. Rather these poles served as design aids in the machinery building stage and verification of the technology. The prototype machine is shown placing axial fiber tow along the length of a 30 foot (10 m) mandrel.

In Figure 8.28 the axial tow is shown working one side of the mandrel, in fact the machine simultaneously applies fibre to the opposite side of the mandrel just out of view of the camera. The same heads can be redirected to apply circumferential fibres during the over wrapping stages. The inner circumferential fibres can be just seen in a gap below the axial tow.

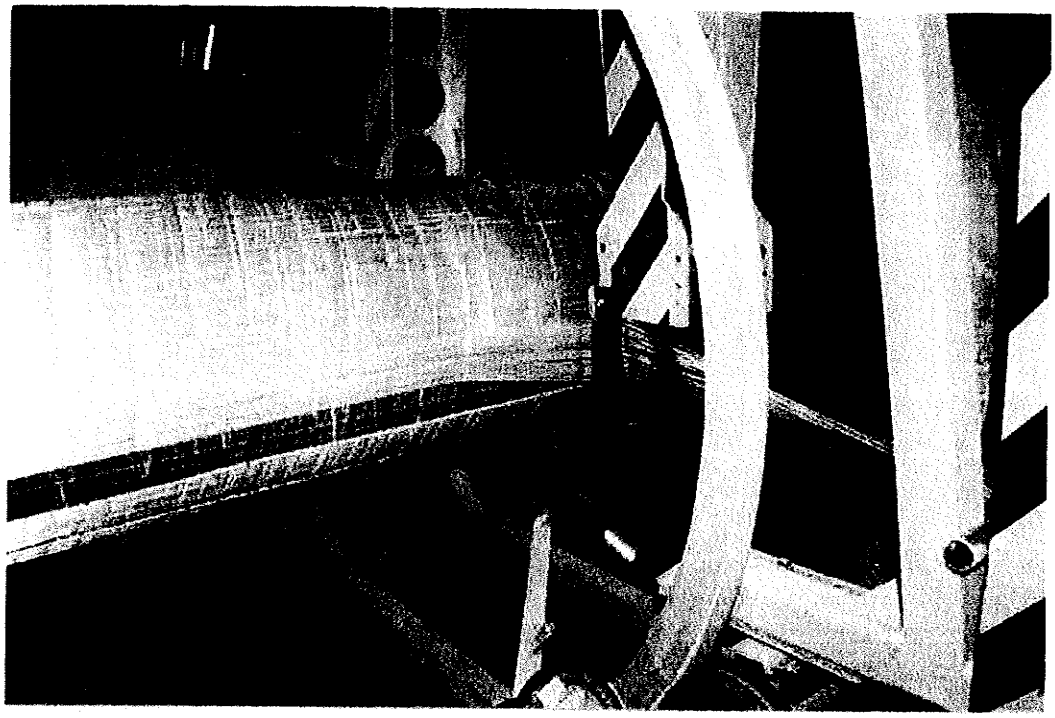

Figure 8.28 Canzeal Prototype Winding Machine Placing Zero Degree Roving

8.10.1 TEST APPARATUS AND SET UP

Three specimens fabricated by Canzeal were delivered to the University of Manitoba for full scale static load deflection tests. The test set up is shown in Figure 8.29. Included in the shipment was a specially constructed flange base for the support of the test specimens. The flange was fabricated with a heavy steel I-Beam core and Steel Base Plate. The entire surface was finished smooth with an FRP barrel. (Figure 8.30)

The first step in the testing program was to mount the flange to the vertical strong wall of the structures laboratory. This required the use of a pair of steel box beams to mount to the base of the Flange and also to accomodate the 0.5 m spacing for fixtures on the strong wall. Eight 3/4" (19

mm) dia. steel bolts secured the flange to the box beams. Four, 1" (25.4 mm) dia. , bolts held the box beams to the strong wall (Figure 8.29)

. The test poles required modification in order to mount the pole properly to the flange. Four wooden strap anchors were bonded to each pole base , shown in Figure 8.29 in order to pull the test poles tight over the flange. The wooden anchors were 24" long , 1.5" thick and 5.5" wide. Mounting at the diagonal positions allowed for unobstructed top and bottom surfaces of the poles. The wooden strap anchors were trimmed so as not to project beyond the flange barrel into the free volume of the poles being tested.

Poles were securely drawn tight onto the tapered flange by tensioning four ratchet straps looped over the wooden strap anchors and through four individual ring bolts mounted to the flange . The slight gap, found at the base of each pole with the flange, was filled with thickened epoxy pumped into the void. This prevented any slight shifting of the pole during loading. Straps remained in place during the test as a precaution, to prevent pieces of broken poles from falling unexpectedly.

Poles were instrumented with triplet rosette strain gauges, 45^0, 0^0 and -45^0 at 2.5 cm , 25 cm, 50 cm, 75 cm and 100 cm from the flange tip, along the top and bottom meridians. This making for five locations in the expected tension zone (bottom) and five locations in the expected compression zone (top) . The pole load was applied in an upward direction at 24" (0.610m) from the tip. The loading point was 28' (8.534 m) from the base. A cable type extensometer LVDT was mounted directly below the loading point, this determined tip deflection. For Pole #3, a rigid rod type extensometer, LMT,

was mounted directly beneath the flange tip to measure vertical flange displacement.

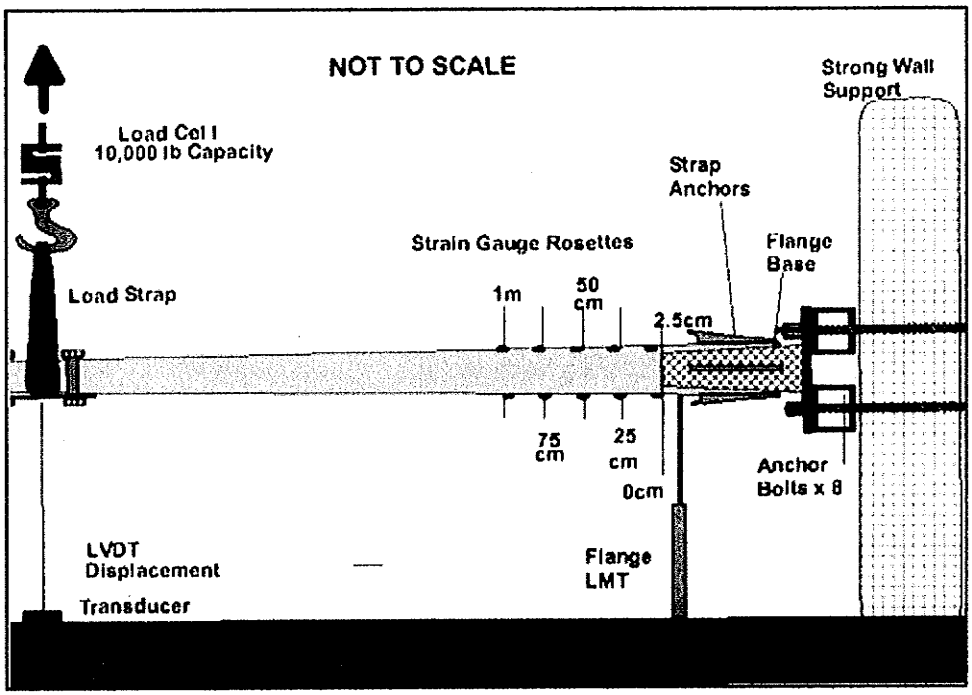

Figure 8.29 Horizontal Testing Configuration

In total each pole was equipped with 30 strain gauges and one or two extensometers. Loads were measured with a 10,000 lb load cell mounted between the pole and the loading crane. Data was collected with a Digital Data Acquisition System, sampling every 1/100 second intervals each of the 33-34 channels .

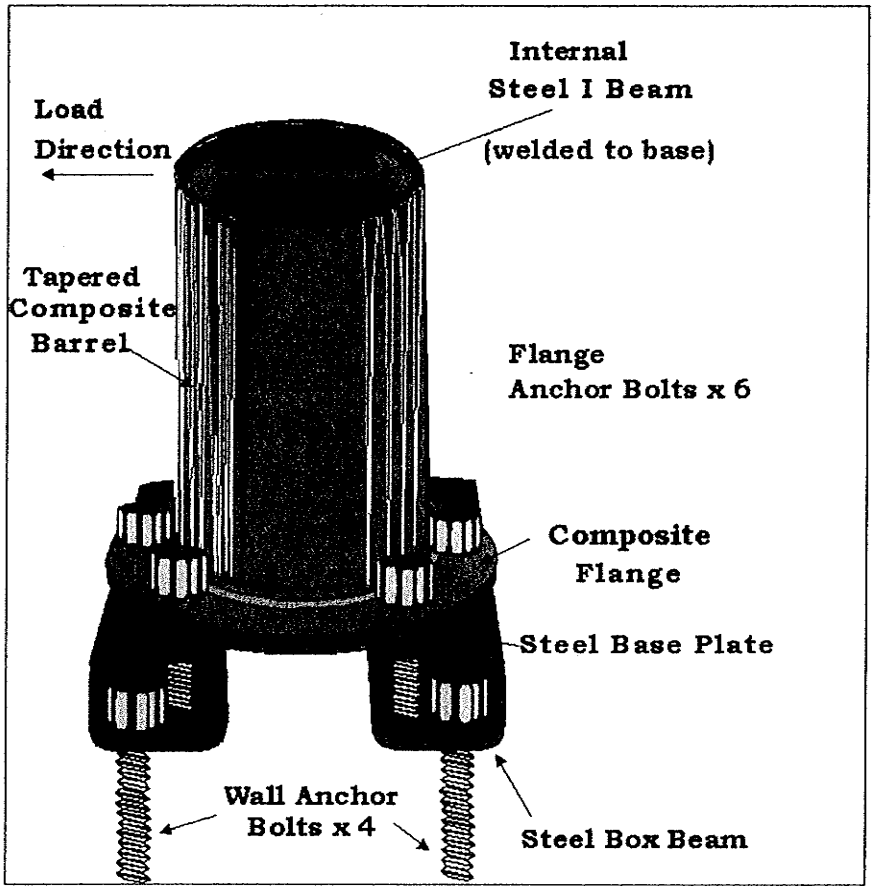

Figure 8.30 Canzeal Flange Assembly

These poles were 30' long with a base diameter of 19.5" , and top diameter of 12". Basic data is presented in Table 8.13-8.16. The graphical data for the laminate structures of the three poles is presented in Figures 8.31-8.33. The experimental loading conditions are presented in Tables 8.13-8.16 and the experimental load deflection curves for the three poles are given in Figs. 8.34 and 8.35. Note that in Figure 8.34 that five displacement curves are plotted. Poles 1 to 3 are plotted as raw data for tip deflection and repaired pole 3 plot represents the results of repairing pole 3 and retesting, pole 3 is also plotted in red with flange displacements removed. In Figure 8.35 Pole#3 is plotted as raw data in yellow and also with the flange effects removed from

the total deflection in blue. The correct displacement curve is determined by measuring the flange deflection at the top edge with a linear measuring device. The Corrected tip deflection is then calculated using the following formula,

$$C.T.D = M.T.D - (L\sin(\tan^{-1}(\frac{F.D.}{F.L.}))) \quad \textbf{(Eq.8.14)}$$

Where, C.T.D. is the Corrected Tip Deflection; M.T.D. is the Measured Tip Deflection; L the constant gauge length (length of the test pole); F.D. is the measured Flange Displacement; and the final term F.L. is the constant length of the flange barrel.

This technique was not used with the Faroex test poles since the poles were fixed within a concrete block which was strong enough not undergo any rotation.

The test Pole #3 was the only pole that had a working flange LMT. Raw displacements of the Canzeal Poles are plotted in Fig.8.34. The corrected tip displacement for poles #1, #2, and #3R. were determined by using the slope of the corrected deflection plot for Pole#3 which is shown in Fig.8.35. In Tables 8.13 through 8.16, the original tip deflections are given beside the corrected tip deflections. In Figure 8.36 the four test poles are shown with maximum load and the locations of the failure zone relative to the base of the flange. The repair method used on the broken Pole#3 is shown in Fig.8.37. After the repair, Pole#3 is designated as Pole#3R in the Table 8.16.

Canzeal Pole #1

based on Burn Tests

Laminate Designation [±82, 0, ±82]

Axial Layer Constant 0° Green

Circ. Layer Constant 82° Yellow

Dimensions in Inches (±25.4=mm)

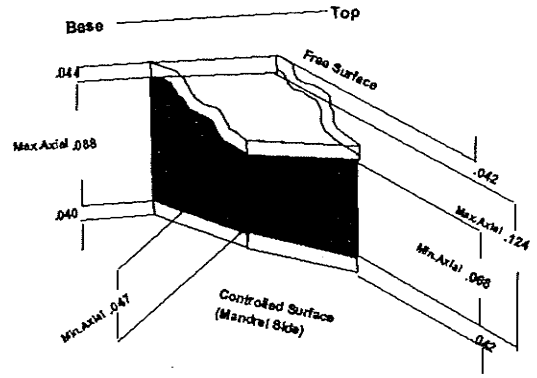

Figure 8.31: Canzeal Pole#1 Description

Canzeal Pole #2

based on Burn Tests

Laminate Designation [±82, 0, ±82]

Axial Layer Constant 0° Green

Circ. Layer Constant 82° Yellow

Dimensions in Inches (±25.4=mm)

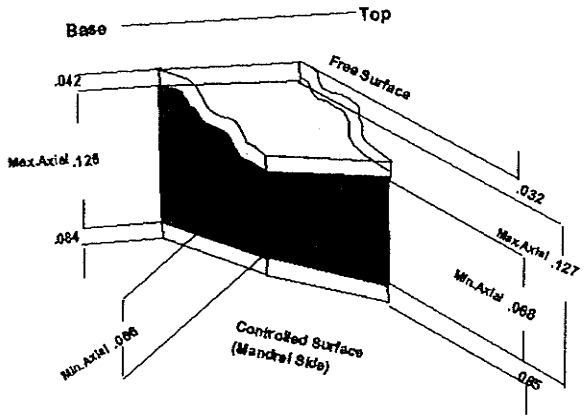

Figure 8.32: Canzeal Pole#2 Description

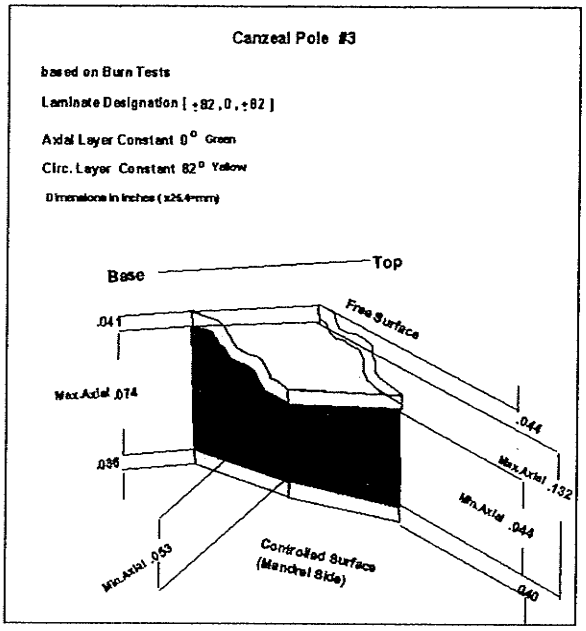

Figure 8.33: Canzeal Pole#3 Description

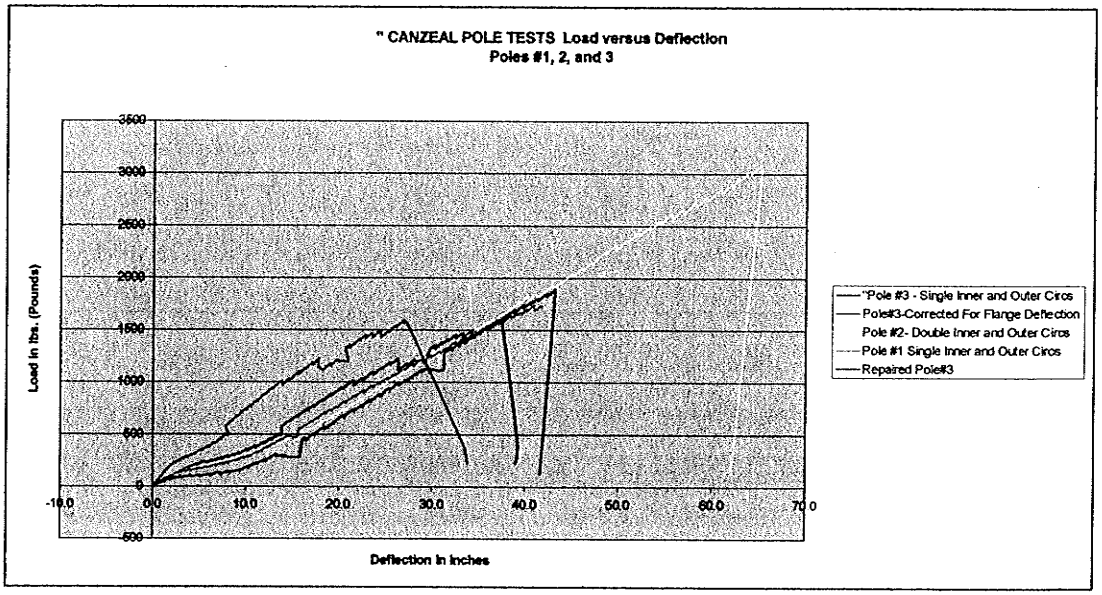

Figure 8.34 Canzeal Test Poles Deflection Curves

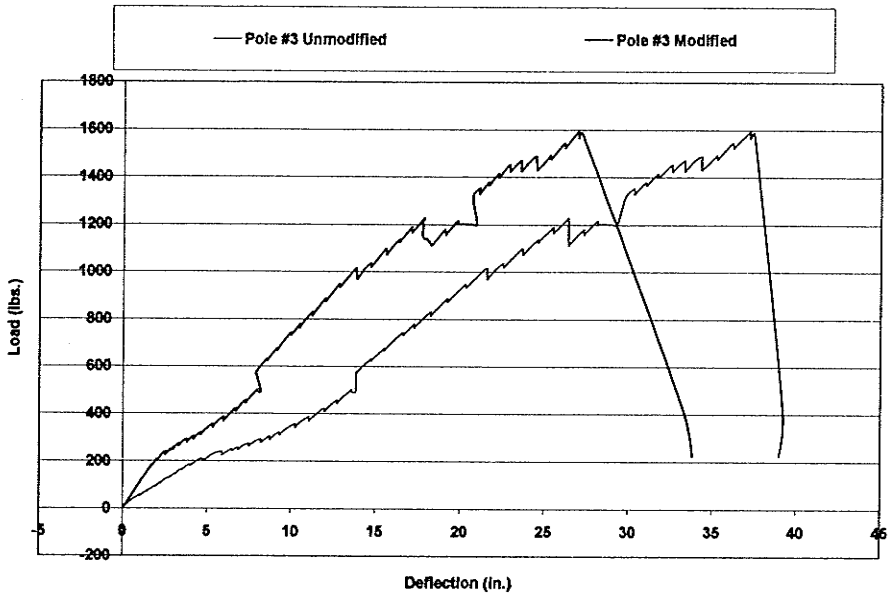

Figure 8.35 Corrected Tip Deflection Curve Pole #3

Burn out tests were conducted on samples taken from the Canzeal poles tested.The results revealed discrepancies in the expected and actual laminate structure of the poles. Unlike the previously discussed Faroex Poles, the new Canzeal poles had significantly different geometry and laminate structures. Since the axial component of the laminate was 0°, the Constant of Clairaut, $C = r\sin\theta$ was undefined. The Bernoulli-Euler deflection model developed in this study was modified to permit a solution by replacing the 0° wind angle with the infinitesimally small $\pi x10^{-6}$ to avoid a substantial rewriting of the MapleV code.

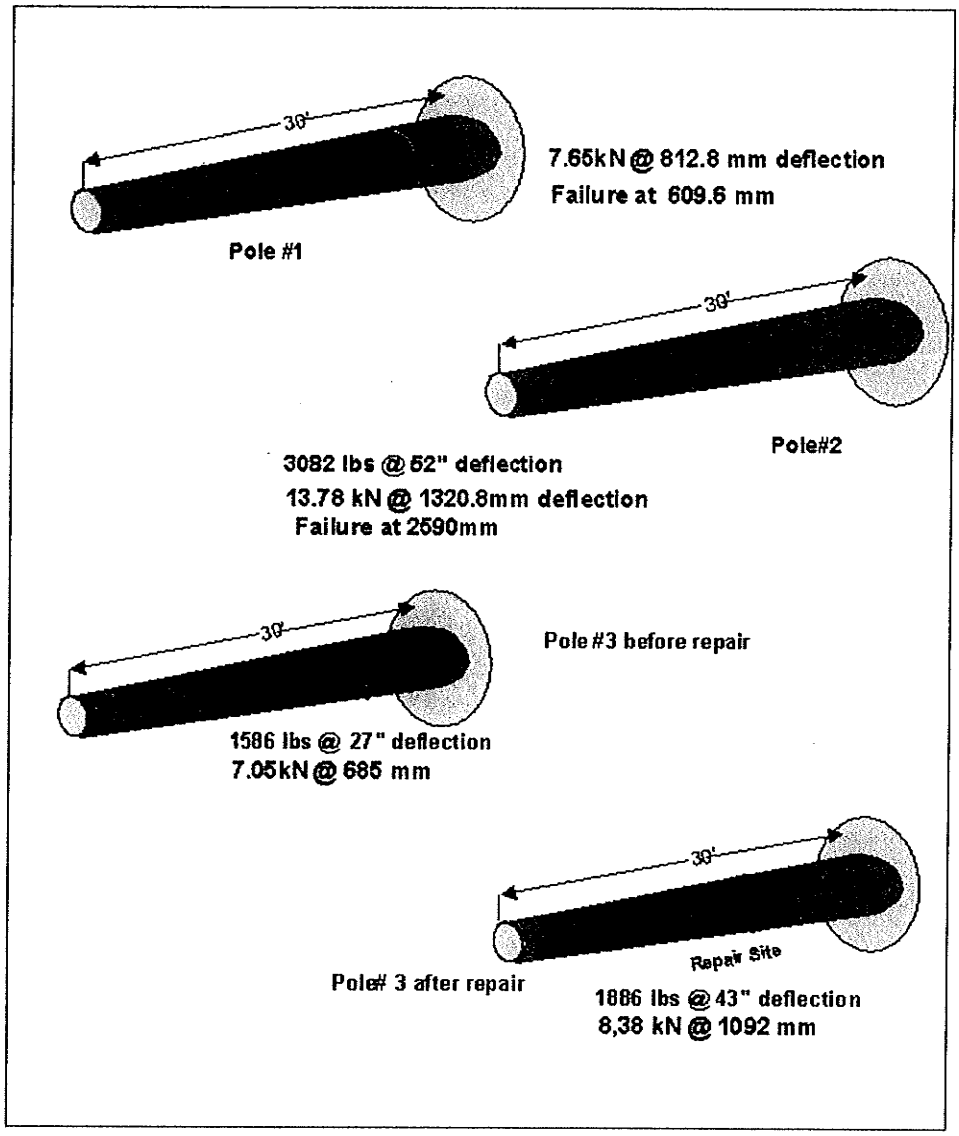

Figure 8.36 Failure Locations for Canzeal Test Poles

The thickness equation, Eq.7.19 for geodesic winding on tapered mandrels is capable of handling the special case of 0^0 winding since the Cosine term goes to Unity and Eq.7.20 maintains a constant cross sectional area over the length of the mandrel. This implies that the axial layer will maintain a constant stiffness, but the interaction with the circumferential fibers over wrapping the axial fibers was not clear.

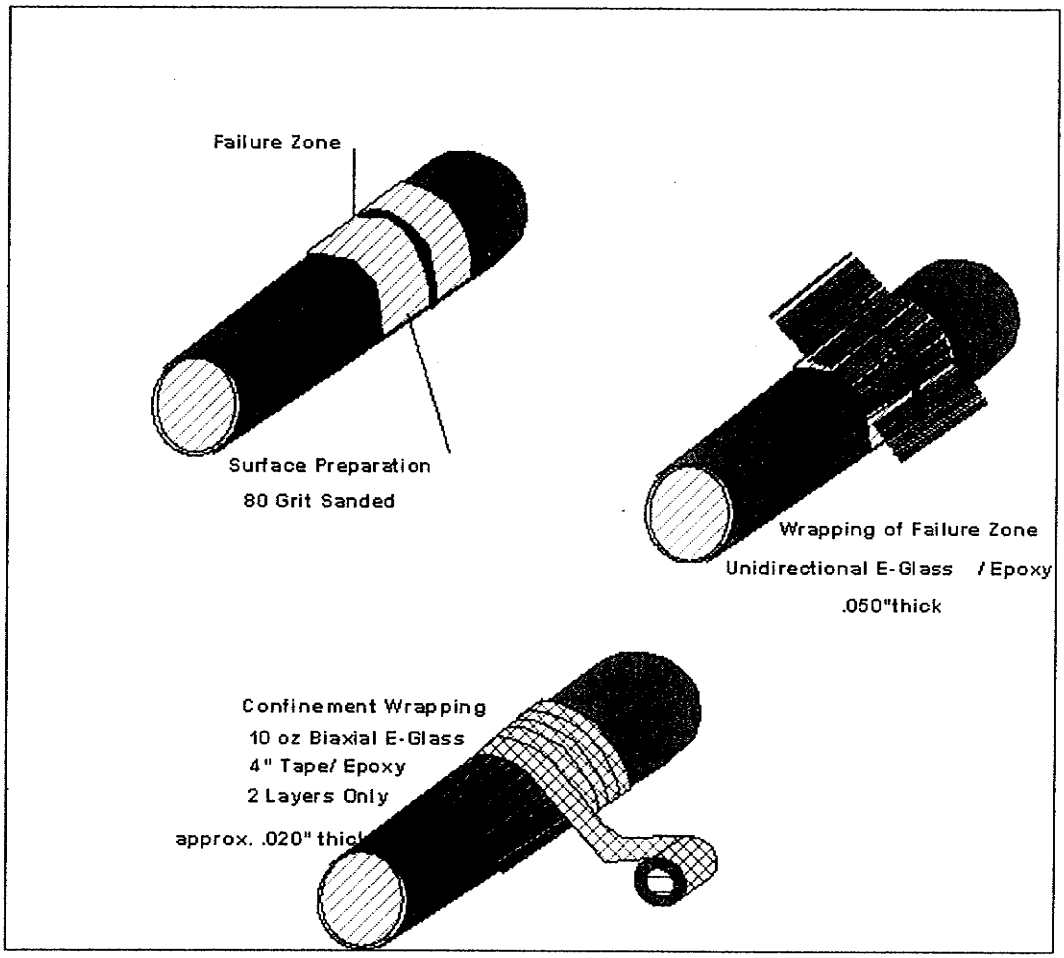

Figure 8.37 Pole #3 Repair Procedure

The Canzeal poles were analyzed using the Bernoulli-Euler Iterative deflection model. These poles were also used to uncover some technical weaknesses in the robotic control systems. The primary consequence of these resolution errors was the inconsistent application of axial fibers. The fiber paths were irregular and resulted in some overlap and some gapping. The determination of laminate thickness posed some difficulty as can be seen in the Figs. 8.31-8.33. To resolve the discrepancies, average thickness and the minimum thicknesses were used. Each pole was modeled using the two thickness

values and deflections calculated for the given load. The results are presented in Tables 8.13-8.16 for Poles #1, #2, #3, and Pole #3R respectively. The determination of the effective axial modulus of the pole laminates was made using the **Series C** vinylester material properties, described previously (see Appendix for resin details).

The deflection model was reconfigured for the different geometries and loading conditions as well as the different thicknesses at the base for the circumferential and axial layers.

As a consequence of 0^0 winding there is no geodesic drift and the modulus of the axial layer does not vary. However, the unusual nature of the winding results in the effective stiffness of the total laminate actually increasing toward the tip, as seen in Fig. 8.39, since the thickness of the axial layer increases due to the pole taper .

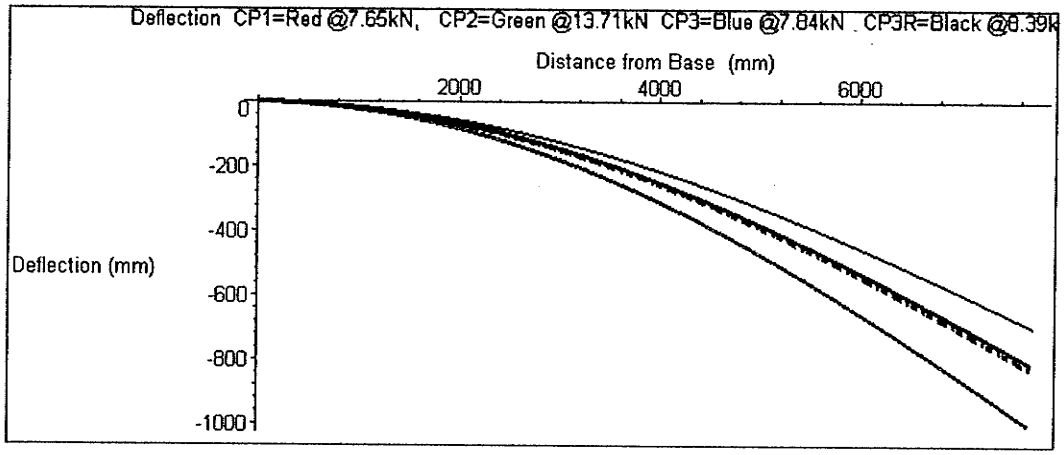

Figure 8.38: Canzeal poles: Ultimate Load Deflection Curves Using Minimum Axial Thickness

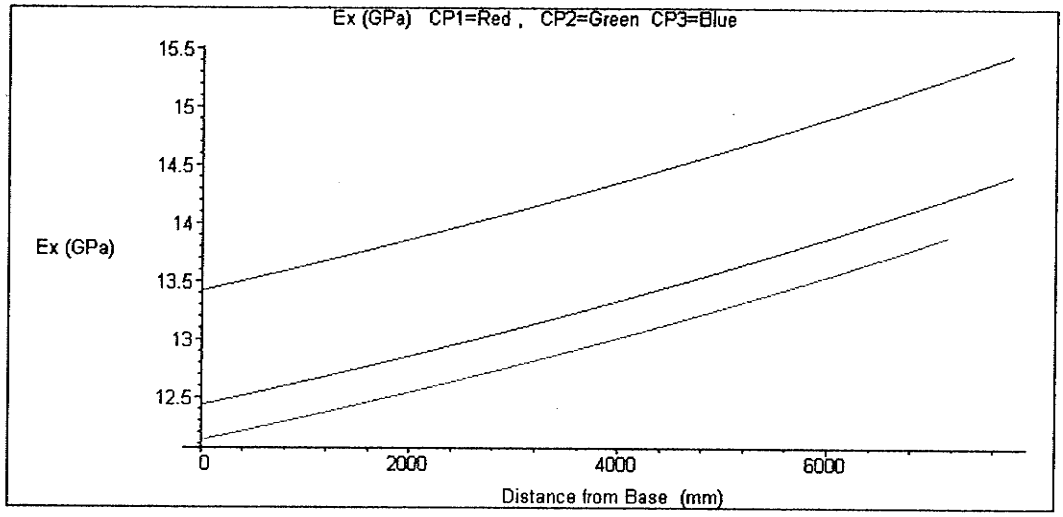

Figure 8.39: Axial Modulus of Canzeal Poles

Table 8.13 Canzeal Pole #1 Deflection Model Predictions

Canzeal Pole #1	Laminate Schedule				Ultimate Capacity (lbs)	Ultimate Capacity (kN)		Measured Tip Deflection (inches)	Measured Tip Deflection (mm)	Experimental Deflection Corrected (inches)	Experimental Deflection Corrected (mm)
	circ	axial	circ								
	82	0	82.00		1720.00	7.65		41.69	1058.93	30.27	768.76
Layer thickness (1 Layer= 1+ &1- Lamina)	Layer thickness (inches)		Layer thickness (mm)	Average axial thick. (inches)	(mm)	Minimum axial thick. (inches)	(mm)				
tic	0.04		1.02								
taxial (range)	0.088	0.047	2.24	0.068	1.71	0.05	1.19				
toc	0.044		1.12								
Bernoulli-Euler Model Deflection	using average axial thickness and minimum thickness										
				24.39	619.51	32.12	815.85			30.27	768.76
	Accuracy (Pred./Exper.)			0.81		1.06					

Table 8.14 Canzeal Pole #2 Deflection Model Predictions

Canzeal Pole #2	Laminate Schedule				Ultimate Capacity (lbs)	Ultimate Capacity (kN)		Measured Tip Deflection (inches)	Measured Tip Deflection (mm)	Experimental Deflection Corrected (inches)	Experimental Deflection Corrected (mm)
	circ	axial	circ								
	82	0	82.00		3082.00	13.71		65.20	1656.00	47.33	1202.23
Layer thickness (1 Layer= 1+ &1- Lamina)	Layer thickness (inches)		Layer thickness (mm)	Average axial thick. (inches)	(mm)	Minimum axial thick. (inches)	(mm)				
tic	0.084		2.13								
taxial (range)	0.125	0.066	3.18	0.096	2.43	0.07	1.68				
toc	0.042		1.07								
Bernoulli-Euler Model Deflection	using average axial thickness and minimum thickness										
				30	762.00	39.60	1005.8			47.33	1202.23
	Accuracy (Pred./Exper.)			0.63		0.64					

Table 8.15 Canzeal Pole #3 Deflection Model Predictions

Canzeal Pole #3	Laminate Schedule				Ultimate Capacity (lbs)	Ultimate Capacity (kN)		Measured Tip Deflection (inches)	Measured Tip Deflection (mm)	Experimental Deflection Corrected (inches)	Experimental Deflection Corrected (mm)
	circ	axial	circ								
	82	0	82.00		1582.00	7.04		37.42	950.37	27.16	689.95
Layer thickness (1 Layer= 1+ & 1- Lamina)	Layer thickness (inches)		Layer thickness (mm)	Average axial thick. (inches)	(mm)	Minimum axial thick. (inches)	(mm)				
tic	0.036		0.91								
taxial (range)	0.074	0.053	1.88	0.064	1.61	0.05	1.35				
toc	0.041		1.04								
Bernoulli-Euler Model Deflection	using average axial thickness and minimum thickness										
				24.03	610.36	27.58	700.53			27.16	689.95
	Accuracy (Pred./Exper.)			0.88		1.02					

Table 8.16 Canzeal Pole #3R Post Repair Deflection Model Predictions

Canzeal Pole #3R post Repair	Laminate Schedule				Ultimate Capacity (lbs)	Ultimate Capacity (kN)		Measured Tip Deflection (inches)	Measured Tip Deflection (mm)	Experimental Deflection Corrected (inches)	Experimental Deflection Corrected (mm)
	circ	axial	circ								
	82	0	82.00		1886.00	8.39		43.09	1094.49	31.28	794.58
Layer thickness (1 Layer= 1+ &1- Lamina)	Layer thickness (inches)		Layer thickness (mm)	Average axial thick. (inches)	(mm)	Minimum axial thick. (inches)	(mm)				
tic	0.036		0.91								
taxial (range)	0.074	0.053	1.88	0.064	1.61	0.05	1.35				
toc	0.041		1.04								
Bernoulli-Euler Model Deflection	using average axial thickness and minimum thickness										
				24.03	610.36	32.76	832.10			31.28	794.58
	Accuracy (Pred./Exper.)			0.77		1.05					

The experimental load deflection data was plotted in Fig 8.38. A small component of rigid body deflection due to deformation of the mounting base was detected . The last pole #3 had a specific LVDT attached to track flange deflection. When this rotation was subtracted from total deflection the component of the deflection due to load on the pole alone was plotted in Figure 8.38.

The Bernoulli-Euler deflection model predicted deflections, for a given load quite well, when using the minimum thickness value obtained from the base samples. The analysis of the Canzeal poles demonstrated the sensitivity of the model to thickness values in determining the effective moduli of poles and the deflection behavior.

8.11 SUMMARY OF POLE LOAD DEFLECTION PERFORMANCE ANALYSIS

From the preceding discussion it is clear that the total thickness of the pole and the relative thickness of the axial and circumferential layers determine the eventual deflection behavior of the pole as a structure. In early chapters, it was shown that circumferential winding essentially results in constant thickness and almost constant wind angle. As such this type of winding produces nearly constant stiffness along the length of the pole.

Geodesic axial winding on the other hand is characterized by wind angle drift and thickness increase on tapered mandrels toward the small ends. The effective axial stiffness may increase, decrease or remain nearly constant depending on the initial starting wind angle and taper rate of the mandrel. This variation in stiffness requires special attention since it clearly affects thestructural performance of the pole.

Zero Degree winding is a special class of geodesic winding and should be treated separately. The Canzeal Test poles demonstrated near linear increase in stiffness over the length of the pole. While subject to the similar thickness increase toward the small end of the pole as did the Faroex poles, the increase is due purely to the taper since there is no drift effect involved. The Zero degree winding may also be somewhat simpler to model with reference to the Test Coupon data since the rate of compaction is not as severe as with the Geodesic winding. Therefore there appeared to be no need to employ a resin volume compensation factor as was done occasionally with the Faroex poles.

In general the Faroex poles appeared to have consistently higher effective axial stiffness values than the Canzeal poles but this is simply due to production decisions to limit the amount of axial material applied. There is no evidence with which to compare the two technologies.

8.12 COMPARISON OF DEFLECTION MODEL WITH FINITE ELEMENT MODEL

Ibrahim (2000) attempted to model deflection of the Faroex full scale poles using the finite element method, and presented a very limited graph comparing experimental results to finite element predictions. Out of the eleven poles fabricated, the only finite element deflection results presented were for three of the 10° poles identified in the text as poles #1,#4 and #5 which correspond to S1V1, S4V3 and S5V13 respectively in this study.(See Table 8.11). The finite element predictions are plotted but not tabulated so with the aid of geometry tools direct measurements were taken from the plots knowing that the data for the lines representing the experimental deflections is the same as presented in Table 8.11.

The finite element deflection prediction for pole#1 (s1v1) at the ultimate experimental load of 34.2 kN appears to be approximately 421 mm which is 86% of the actual experimental value. The Bernoulli-Euler model prediction is 418 mm or 85% of the experimental value of 490 mm.

The finite element deflection prediction for pole#4 (s4v3) at the ultimate load of 20.8 kN appears to be 358 mm or 83% of the experimental deflection which was determined to be 430 mm. The Bernoulli-Euler model predicted a deflection at the same load of 412 mm or 96% of the experimental deflection.

The pole #5 (S5V13) when modeled with finite element methods showed perfect alignment on the Ibrahim (2000) plots. Bernoulli-Euler modeling predicted a deflection of 283 mm at a load of 7.55 kN while the experimental deflection was only 240 mm or 1.18% of experimental deflection.

Unfortunately comparisons of the finite element method with the Bernoulli-Euler method are not meaningful with only three specimens to look at. It should be stated clearly that the development of the Bernoulli-Euler model was prompted because of unsatisfactory performance of the finite element methods employed for predicting deflections. It was not clear at the time why this was so. In order to resolve some of the assumptions being made about the geometry and fiber orientations it was necessary to step back from the finite element method and begin with the development of basic descriptive analytical mathematics. Using the Maple mathematics program as the main device it was found to be easier to describe the pole accurately rather than using assumptions to utilize specific element classes within ANSYS.

Eventually the classical lamination theory solver was incorporated directly into the Maple code describing the pole structure. At some point it was decided to validate the model using the simple linear deflection equation used by Sherman (1984) and presented in Chapter 10. When this was eventually replaced by the Bernoulli-Euler method adapted from Bisshopp and Drucker (1945) it seemed to have evolved into a complete stand alone analysis procedure. At no time was this effort thought to replace finite element methods but was thought only to illuminate the flaws in the assumptions made using ANSYS. In truth the Maple code was expected to clean up the weaknesses within the input data for finite element methods.

9 JOINTED POLE STUDY

9.1 GENERAL

Two key issues, previously discussed, were considered problematic for the design of large diameter tapered tubes: the increasing thickness of filament wound geodesic layers as the radius decreases and the upward drift in wind angle as a consequence of decreased radius. These two variables affect the stiffness of the poles. Careful selection of winding angles and taper rates can mitigate these effects. The most significant concept developed during the course of this study was to break up the pole length into segments whose lengths are chosen to reduce the effects of variable stiffness.

The basic issues of variable thickness and wind angle drift were discussed in Chapter 5.0. An analytical model based on the Bernoulli-Euler fundamental beam deflection equations described by Bisshopp and Drucker (1945) was presented in Chapter 7.0. To test the veracity of the modeling program, and to gain new insights about the production process, a number of small poles were fabricated. These poles were to be assembled with a ferrule type joint to permit assembly of a lower and upper pole segment with the same taper and matching radii at the joint interface to permit a smooth external surface.

9.2 MANDREL GEOMETRY

Two mandrels were designed using the techniques previously discussed in Chapter 6.0. The lower mandrel was modified to provide an extension, which

would result in a stepped down region of 12" length over which the upper segment would slip into place. The lower mandrel had a base radius of 4" (101.6 mm) and at the top had a 3" (76.2 mm) radius (120" from the base). At 120" (3048 mm) position the radius is stepped back by .375" (9.525 mm) and continues to the 132" (3352.8 mm) position with the same slope of -1/120.

At the 132" (3352.8 mm) position a self-extracting dome end drive is placed to permit mandrel extraction from the part and provide a smooth stable turn around surface for the geodesic winding. The .375" (9.525 mm) set back provides for the thickness of the upper pole segment and the thickness of the lower pole segment. Since the thickness of the lower pole segment increases toward the small end and the step down region further decreases the radius, a significant increase in the thickness of the joint substrate was expected. The set back was made larger than actually required as an insurance precaution. Any need to enlarge the ferrule diameter was accomplished by over wrapping the 12" (304.8 mm) extension with circumferential windings. This permitted the underlying axial fibers to remain undisturbed. Having a region of high modulus axial fibers incorporated directly into the joint was considered advantageous and was intended to control any local deformation at the joint. The various mandrel geometric relationships are shown in Figure 9.1.

The greatest difficulty during the design stage was that filament winding surface control is typically possible only through contact with the mandrel surface. The joint requires a precise outer surface geometry to permit a locking taper system to be fabricated. The upper pole segment is not an issue since the inner surface of the upper segment is under direct control of that

mandrel surface. The lower segment outer surface is uncontrolled but inferred through the control of thickness. It was found to be impractical to achieve the tolerances required for a locking taper surface on the outer surface of the lower segment if they were not under complete control.

A split clam shell mould was made from the upper segment base region and used to compress the ferrule after winding so it would have the exact surface geometry of the analogous region of the upper segment. This introduced a new issue. The ferrule surface was now possible to fabricate with the exact surface required but the alignment was not under complete control. To resolve this issue the clam shell mould was extended to include a short section that would engage the dome drive shaft and insure proper alignment. An additional feature of the clamshell mould was that it provided a means of including additional surface treatment for the joint bearing surface. By applying tooling resin to the inside of the clamshells we could add a resin rich surface only in the joint area, which was not feasible during winding.

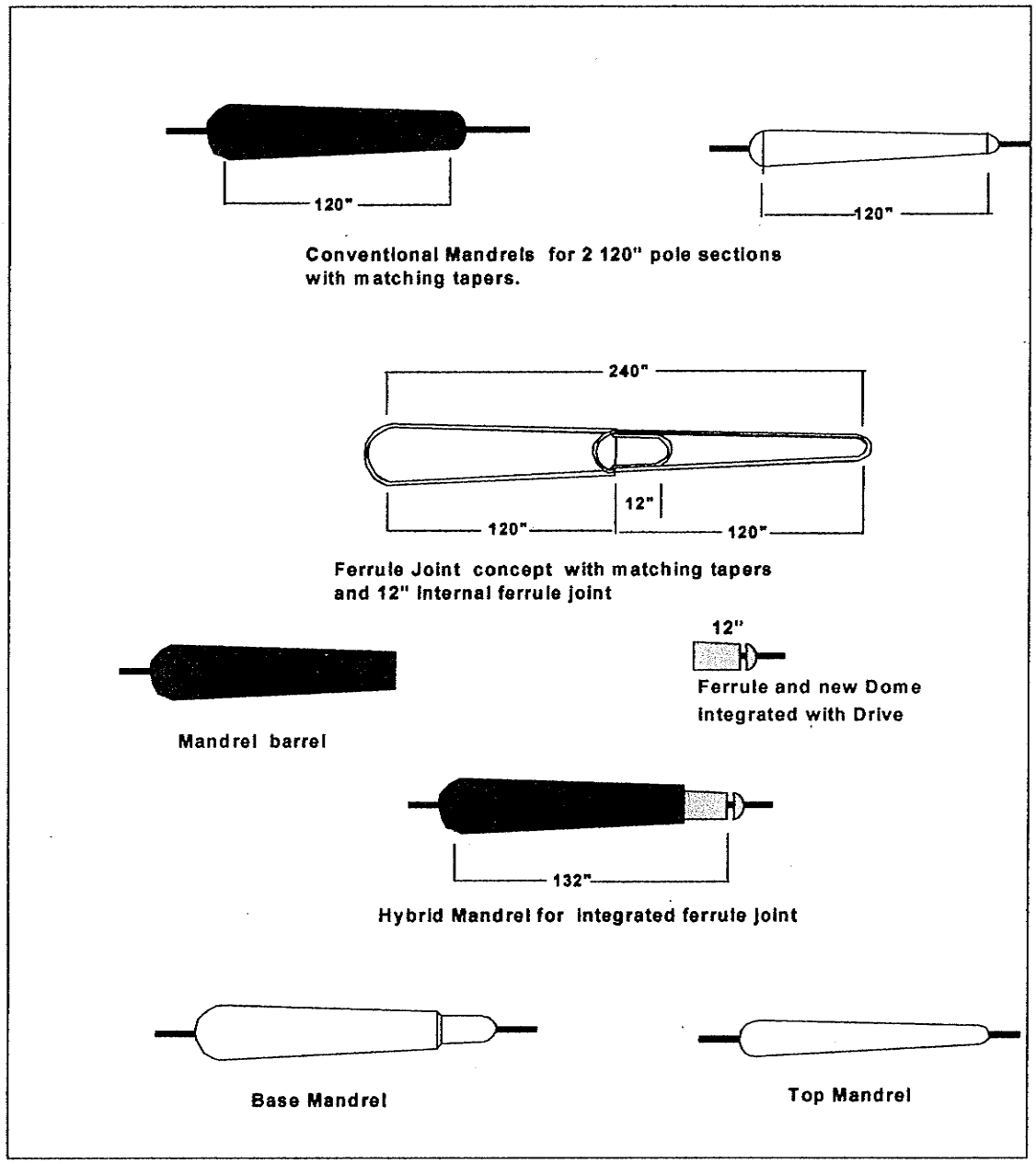

Figure 9.1:Mandrel for integrated joints

9.3 FIBER OPTIC INSTALLATION

At the time of manufacturing a procedure was developed to embed fibre optics into the laminates of pole sections. To provide a maximum embedded length of fiber within the laminate it was found to be necessary to

pass over and around the dome ends. Access to free fiber ends was made possible by having the ends exit the laminate near the base. The filament winding process is interrupted during optic embedment and subsequently resumed with final circumferential winding layers. This project was initiated to evaluate the commercial feasibility of installing optic fibers, with a filament winding machine, directly within the principal structural lamina. Fiber optic lines were evaluated after part removal from the mandrel by exposing one of the terminal ends of a filament to 690 nm HeNe Laser beam. A second witness would confirm visually if the red light was observed on the output end.

Two installation patterns were evaluated for feasibility. In the first case fiber optic filament was pulled through the machine payout eye with structural glass roving. The fiber tow placement algorithm determines the circuits used for laminate winding, one of which is used to install the fiber optic filament. The machine is manually stopped in mid-pattern (after the completion of some number of normal circuits) and the controller reduces all relevant velocities. During the hold stage a fiber optic filament is inserted into the roving band and slowly pulled through the payout eye. The fiber optic filament is inserted with a brightly colored tracer thread to aid in the tracking of the filament. The winding circuit is slowly completed and halted. When the fiber reaches the desired exit point, the fiber optic filament is then cut, secured and the normal winding resumed. In this case the filament is integral to a specific ply of the structure, and traverses a geodesic helical path a arbitrary distance along the fiber. Any position L along the fiber does not correlate directly with a z-axis position along the tube. To calculate the exact position in space of any point L along

the fiber, one is required to employ the parametric equations for the Geodesic Space Curve previously discussed.

The geodesic installation method is shown in Figure 9.2. The most significant feature being the manner in which the fiber optic filament passes through the payout eye concurrent with the structural glass roving but does not pass through the impregnation tank.

In the second case, the machine is again halted at a specific location. However the operator after inserting the fiber through the payout eye does not resume a normal circuit. Instead the operator manually jogs the machine to the end of the mandrel and the fiber is applied along the mandrel meridian in a linear fashion. This linear technique is shown in Figure 9.3. The filament is manually looped over the dome end and then the machine is jogged back through the same path on the opposite side of the part.

Serious difficulties were encountered with this procedure but ultimately resolved. This technique permits a distance L, along the filament to be correlated with a specific z location along the part. However, the fiber is in fact no longer located in a specific lamina nor aligned with the structural fibers.

The large diameter of optical fibers compared to the structural fibers creates a bridging effect when the optic filament is overwrapped. Bridging of the optical fiber results in some cases to produce an induced air void parallel to the fiber. This is especially true when using low viscosity resin. The filaments so implanted proved to be continuous but suspect since they did not have a well resolved interface with the surrounding laminae.

This project established the physical feasibility of single and multiple filament embedment with optical continuity. The project established procedures for two distinctly different fiber optic path types. Finally the accessibility of terminal ends of filaments was established.

The telecommunications grade fiber optics used in this experiment were relatively easy to incorporate into cylindrical structures. Many of the techniques using fiber optic strain sensors are still in the research phase. Since this technology is still being developed it is not possible to anticipate the full requirements at this time for commercialization.

A number of sensor types are presently being considered. Some systems require access to a single fiber end and others to two ends. Jointed poles can be implanted as single units. The most suitable method of getting data across the joint discontinuity has yet to be determined.

The main insight gained from this work was that the simple linear installation was slower and more problematic than the geodesic installation. From a fabricators point of view the geodesic installation technique is preferred while the optical technicians will be required to use complex calculations to relate a distance L, along the filament to a global Cartesian coordinate system. In part, this problem is partially resolved with the equations presented in Chapter 3.0.

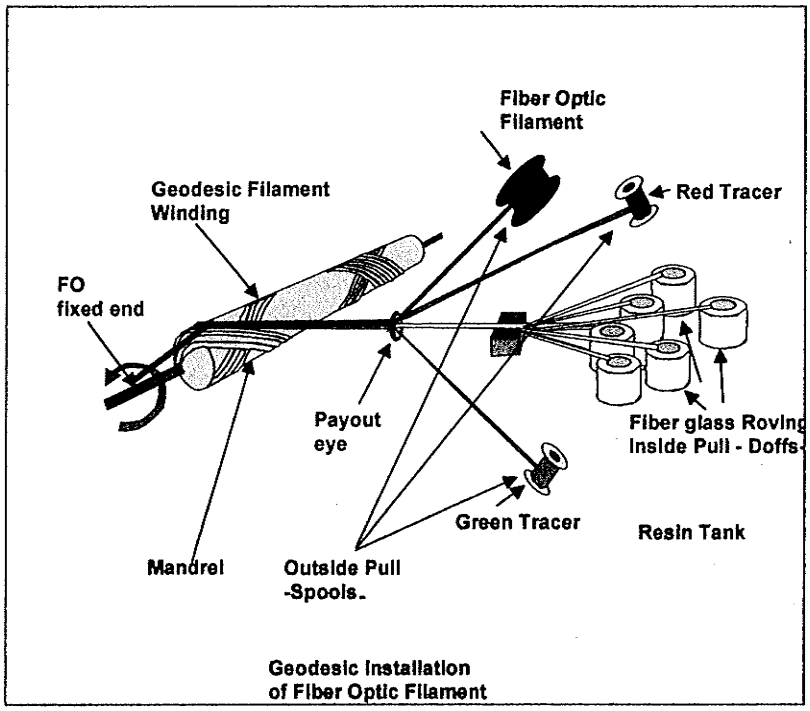

Figure 9.2: Geodesic Installation of Fibre Optic Filament

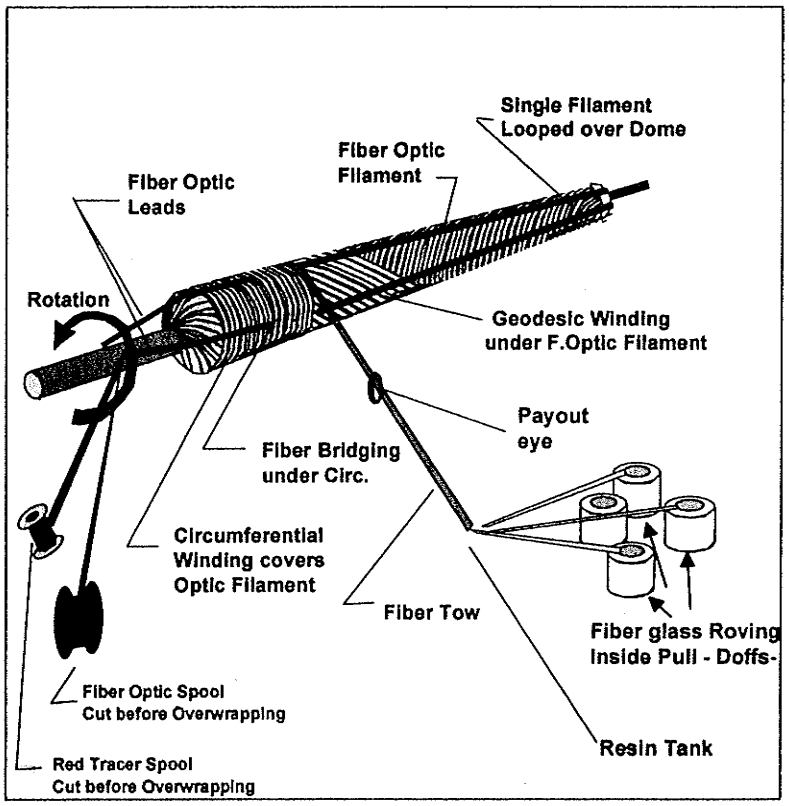

Figure 9.3: Linear Fibre Optic Installation

9.4 COMPOSITE FLANGE POLE ANCHOR

Previous experimental tests with larger poles used steel reinforced concrete base supports. These supports were found to be difficult and time consuming to assemble and dismantle. For testing of jointed poles, a new flange base was designed and fabricated using composite materials. The flange system would restrain the pole base during testing and permit rapid removal and installation. A mould, shown in Fig. 9.4 was fabricated from the base section of a pole to capture the exact geometry of the taper and provide a high quality surface. The height of the flange barrel was 12" (304.8 mm) and a perpendicular flange base was incorporated with the barrel mould. The barrel to flange outer surfaces were the control surfaces. The union of the two surfaces was accomplished by filleting the interface region. Having the outer surfaces under control, it was required to establish internal dimensions to cope with the anticipated bending stresses.

The top of the flange required a small radius to avoid damaging the tubes internally yet required substantial stiffness to avoid ovalization. The base area required additional support to avoid interlaminar delamination during bending.

A plug mandrel was designed to fit inside the flange barrel mould to provide surface control of the inner surfaces of the flange. In short, since the outer surface was controlled by the need to match fit the inside of the test tubes, the only direction available for dimension control was the internal area.

The internal plug, shown in Fig. 9.4 allowed the local reinforcement of the flange top and the massive reinforcement of the base.

In Figure 9.5, the general shape of the flange is shown. To accommodate the small working space, a complex composite laminate structure was employed. Since this is a female mold the first materials laid down represent the outer surface of the flange. An epoxy tooling resin was applied initially to provide a smooth wear resistant surface. The next material to be applied was bi-directional fiber glass fabric 5.6 oz. per square yard and epoxy laminating resin. The fabric was laid up with the zero axis parallel to the natural axis of the flange barrel and 90 degree in the hoop direction.

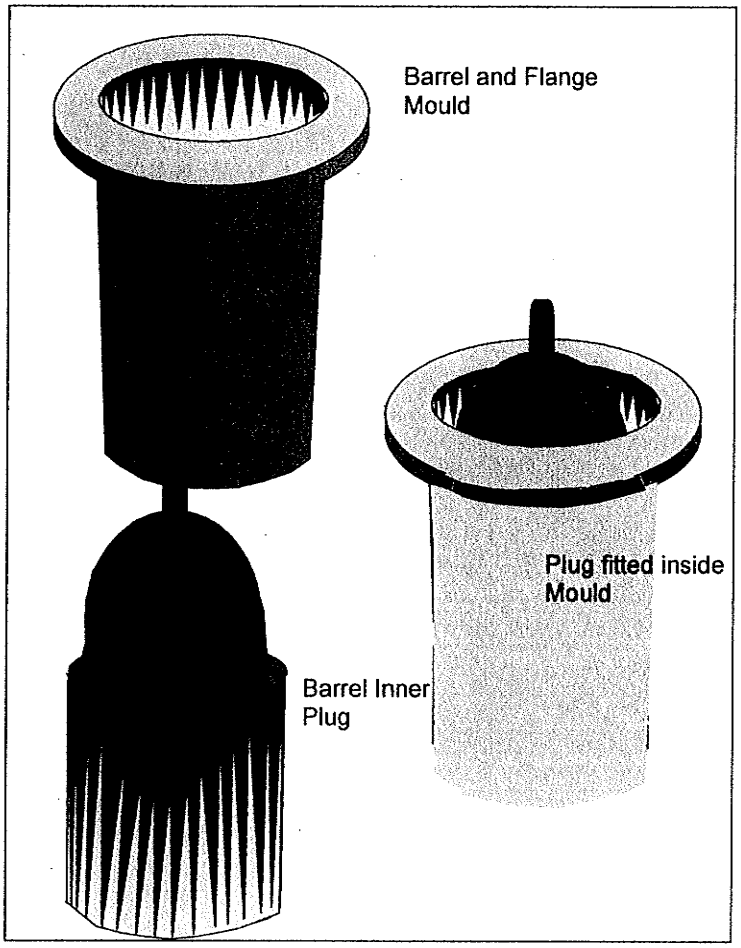

Figure 9.4: Moulding of Composite Flange

The flange-barrel interface was laid up using a 0^0-90^0 stack rotated by 45^0 degrees to provide a ± 45^0 stack to pass from the outer rim over the fillet and then to overlap the barrel stack by several inches. A loop of unidirectional glass roving impregnated with epoxy was dropped into the mould to bond with the barrel stack and fill the area up with a massive unidirectional rim hoop. A second massive internal hoop was placed inside the flange coincident with the overlap region effectively beginning the development of a second internal flange supporting and restraining the external flange.

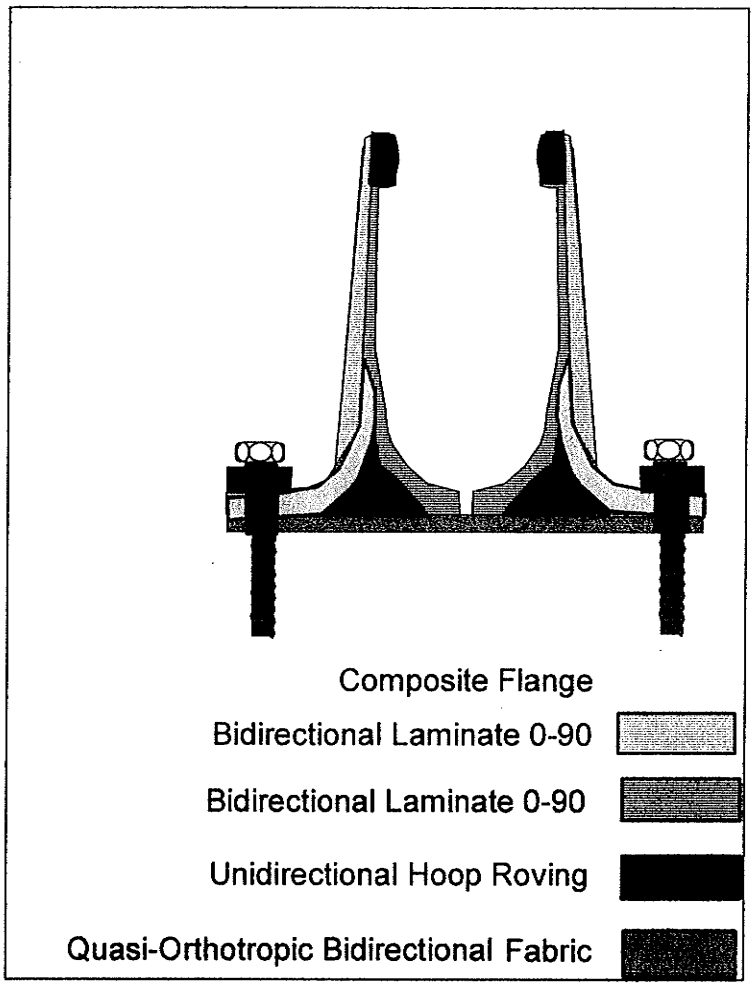

Figure 9.5: Composite Flange fabrication details

The material was allowed to cure and the part then cleaned up of rough edges. The flange base was machined flat and then bonded to a stack of bi-directional glass with a quasi-isotropic stacking sequence. This lower stack was a continuous plate. After curing, the flange was ready for the final internal reinforcement of more massive internal circumferential hoops. These last hoop fibers were used to develop a smoothly contoured internal circular buttress with a much larger radius of curvature. The Flange was drilled in several places to permit installation of mounting bolts. The mounting bolts were dropped through a steel ring plate through the composite and through a

steel base plate system. The entire system was anchored to the structural floor of the test laboratory.

Unfortunately, as robust as the flange design was, it still had some deflection. A series of single pole segment tests were conducted to determine the load deflection characteristics of the flange base. The set up procedure is shown in Fig 9.6.

A plot of flange deflection was made to establish the deflection characteristics for use in subsequent pole tests. In Figure 9.7, a load deflection plot shows a linear response of the flange top to loads over 230.00 in. lbs. The flange system was tested three times with base pole segments loaded 96" above the flange top. The maximum load ever applied during the testing of poles was 2462 lbs. The poles all failed catastrophically and no damage was discerned for the flange. At the moment of failure, flange rebound was very large and the shock wave was found to damage the LMT sensors. For all future tests the LMT was removed and pole deflection due to the rigid body contribution imparted by flange deflection was subtracted from the measured tip deflections.

Poles were installed on the flange by tapping them into place. No adhesive was used for any testing and no slippage was ever detected. Poles proved to be easily removed and suffered no damage in the areas supported by the flange barrel.

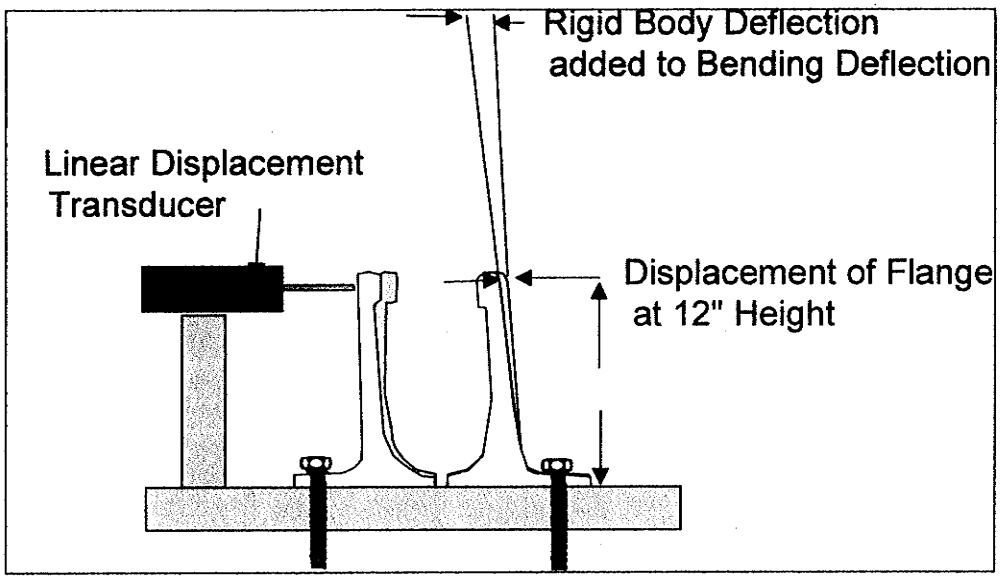

Figure 9.6: Correction of rigid body motion due to Flange deflection

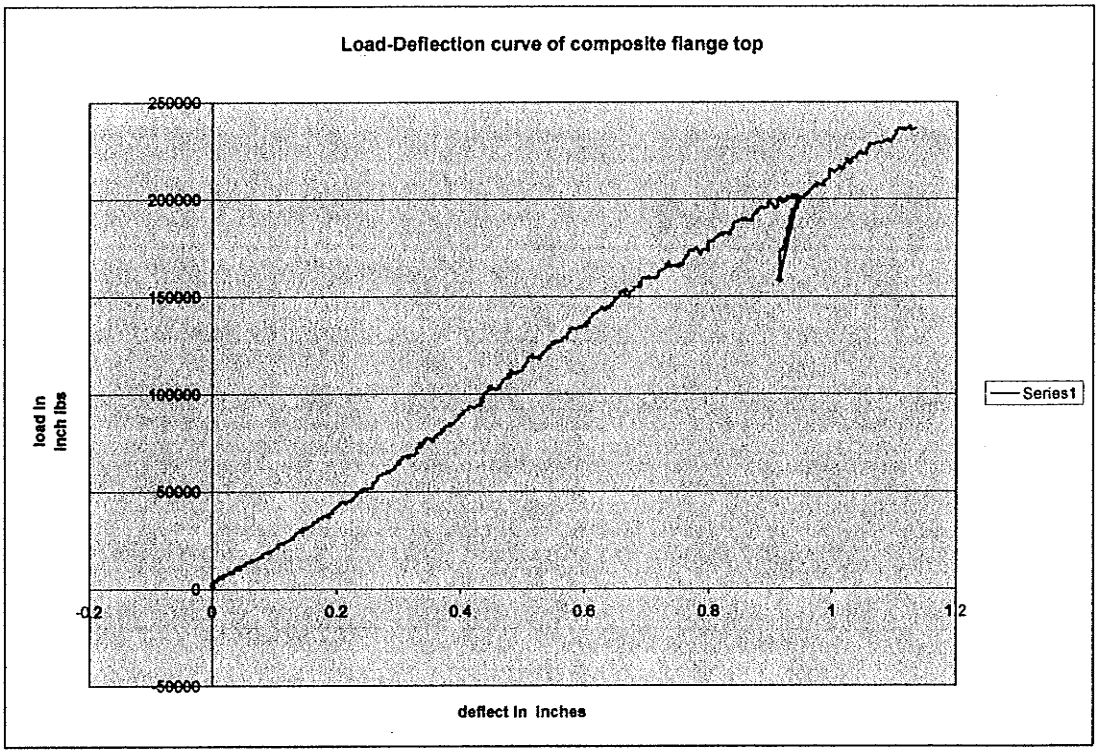

Figure 9.7: Load deflection curve for composite flange

9.5 JOINTED POLE FABRICATION

Test poles were fabricated with the assistance of the Faroex staff using the same machinery as previously used for the large diameter 20 foot poles. The materials used were discussed in chapter 8.0 and were the same polyester glass composite as used for the Faroex poles (Series B).

Several procedures were however altered for the smaller specimens. Firstly, a smaller tow was pulled and wider bandwidth settings were used to reduce thickness. It was clear after the fabrication of the large poles, that the control of laminate thickness was very important. Roving and bandwidth settings were set to investigate the degree of control, which could be exercised to minimize laminate thickness. Pole winding programs were designed to verify whether or not we could predict a laminate thickness for the base and tip of each pole segment. Differences in the behavior of circumferential and axial layers were also examined.

Greater insight into filament winding permitted a higher quality of production than ever before. Significantly the poles appeared to have consistently high glass content.

9.6 EXPERIMENTAL SET UP

The research on jointed poles was divided up simultaneously between three investigators. The work of Dr. Ninguan Xu focused on stress distribution and finite element modeling of jointed poles while Mr. Dino Philopulos focused on the failure mechanism and critical joint length (Philopulos, 2002). Some of the following sections may seem to be overlapping that of my colleagues,

since the focus of this thesis is performance modeling of filament wound tapered tubes. By necessity the discussion will be brief when the topic is covered in other publications. Some overlap is however required to provide coherency to the deflection analysis.

The foil type strain gauges, SG and linear measurement transducers, LMT sensors are arranged in specific locations as outlined in Table 9.1. The location of transducers was selected to model jointed pole performance using finite element methods (Philopulos, 2002). The generalized pole dimensions are shown in Figure 9.8. These figures were taken from the work of Philopulos (2002).

Table 9.1: X-Coordinates of Instrumentation Elements (inches)

	Specimen A 12" joint+Dome	Specimen B 12" joint	Specimen C 8" joint	Specimen D 4" joint
Load Position (inches)	218	218	218	210
SG1	0	0	0	0
SG2	6	10	10	10
SG3	12	20	20	20
SG4	18	30	30	30
SG5	120	40	40	40
SG6	132	50	50	50
SG7	138	115	115	115
SG8	144	120	120	120
SG9	-	132	128	124
SG10	-	138	134	130
SG11	-	144	140	136
LMT1	54	54	54	54
LMT2	102	102	102	102
LMT3	114	114	114	114
LMT4	170	170	170	164
LMT5	224	224	224	214

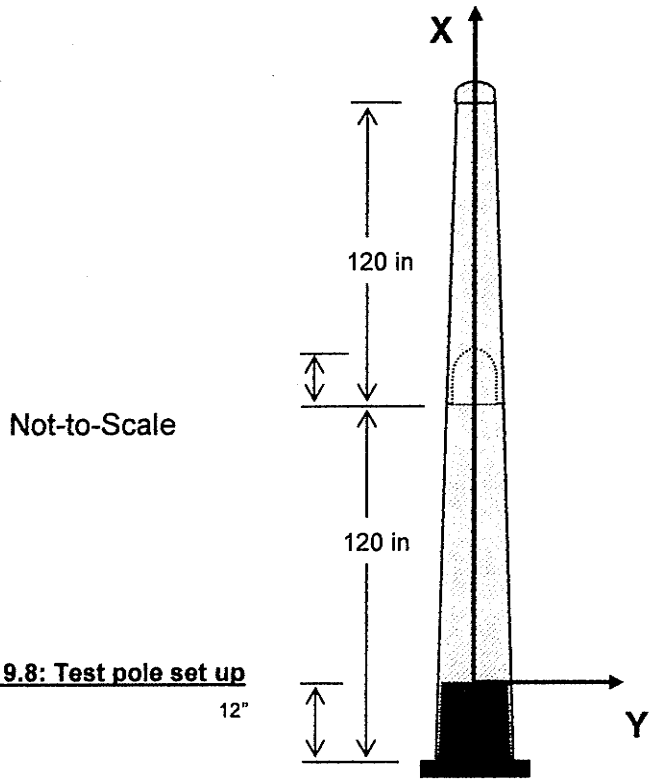

Figure 9.8: Test pole set up

9.7 EXPERIMENTAL RESULTS

Data for the four pole tests is presented in Table 9.2. The four specimens are recorded as Poles A through D. Pole A has a ferrule length of 12" and includes a complete residual dome section. It is composed of an upper and lower section. Pole B has the same dimensions as Pole A, with a ferrule length of 12" but this specimen has had the dome removed. Pole C has a ferrule of 8" in length and pole D has the shortest ferrule with a length of only 4".

All surfaces were sanded to remove all traces of surface contaminants and bonded together with a general-purpose epoxy adhesive thickened with colloidal silica to prevent the joints from draining. Both surfaces were fully wet with adhesive before assembly. All joints were hammered close then splinted to insure proper alignment and left to cure for a day or more. The poles were

mounted on the flange and tapped into place with a large hammer and wooden block serving as a pad to prevent local impact damage.

The Pole D was found to have a slightly undersized diameter for the ferrule and required that the upper segment be shortened 12" to provide a tight fit. The data reflects this modification.

Strain Gauges of the foil type were installed at various locations, (see Table 9.1) to monitor stresses in the immediate joint areas. LMT displacement instruments were mounted at several locations along the length. These measurements were used to determine ultimate deflections and curvature of the poles under load to isolate joint effects on bending. Free body deflection of the pole was not measured due to the violent nature of failure but was determined from previous tests and applied during analysis.

A detailed analysis of bending stresses and strains was published separately (Philopulos, 2002). This paper shows that experimental stresses at the joint edges were not significantly different than predicted with finite element analysis. Failure location was determined using the ANSYS finite element software and proved to accurately predict failure stress and location. A buckling wave was detected visually just prior to failure and the period of the wave and amplitude tended to shift failure locations slightly up or down from predicted locations. No damage to joints was detected in Poles A, B and C.

Failure locations are shown in Figure 9.9. Pole D, not shown, failed at the joint through the adhesive. It was determined that bonding imperfections initiated the adhesive failure. However this specimen failed at a load value nearly identical to the previous specimens.

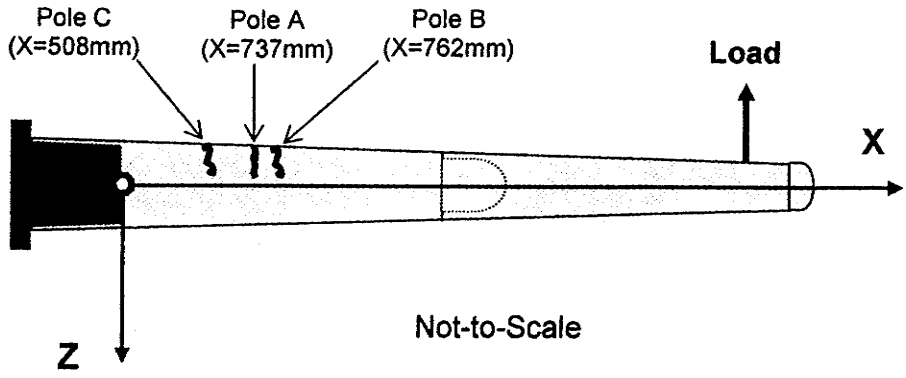

Figure 9.9: Test pole failure locations

Typical local bucking failure is shown in Fig.9.10. The joint collapse failure is shown in Fig.9.11. In Figure 9.12, failure occurred directly beneath a strain gauge and shows the extremely local area of delamination typical of all failure seen during this project. The delamination zone is attributed to the post failure effects of edges grinding past each other.

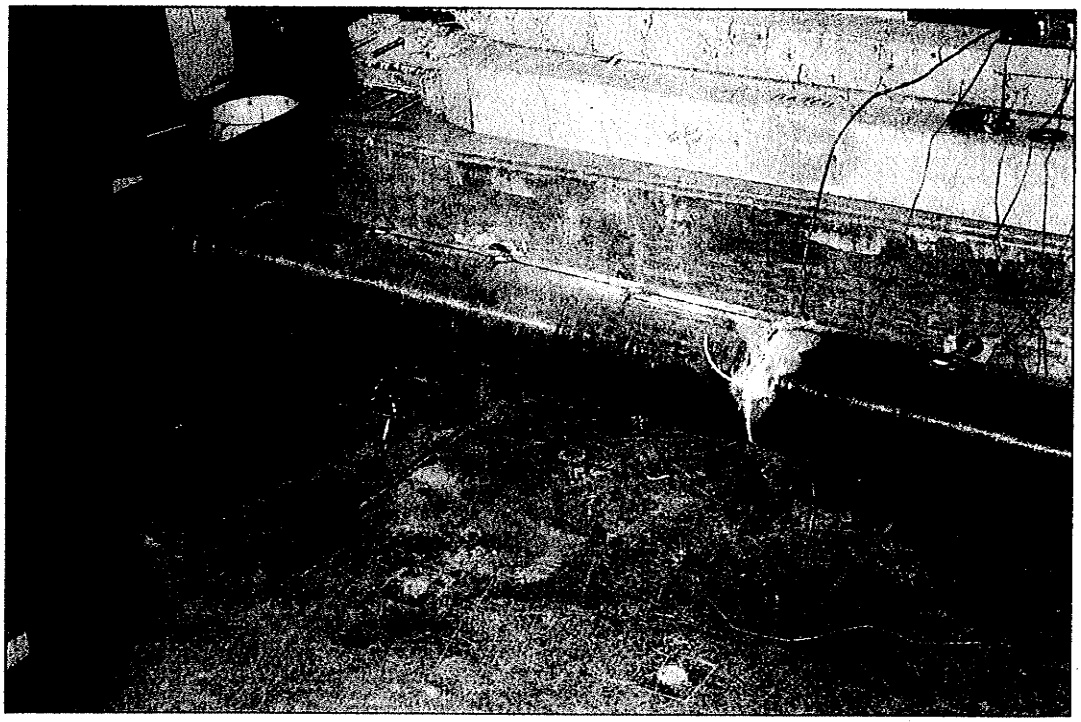

Figure 9.10: Test pole showing typical local buckling failure

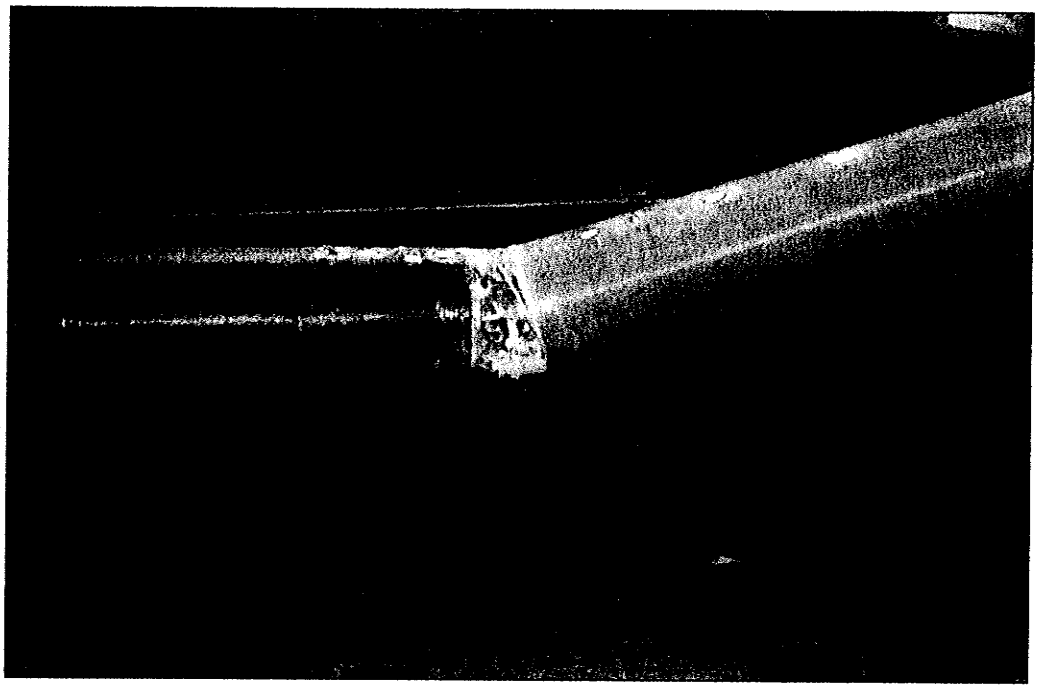

Figure 9.11: Test pole showing failure of 4" joint due to adhesive failure

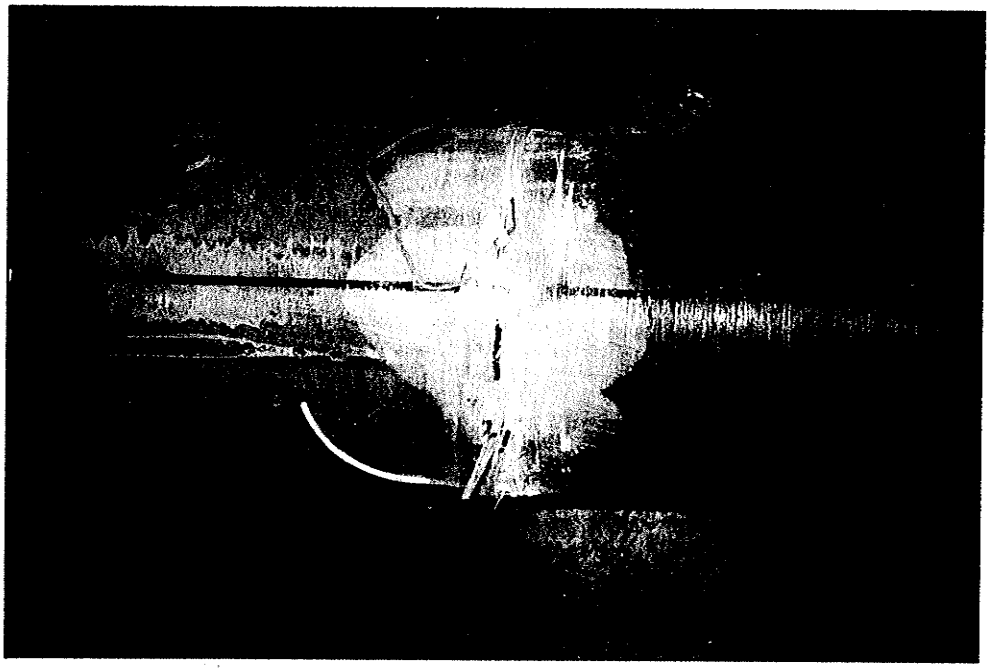

Figure 9.12: Test pole showing failure zone delamination

The Load deflection curves for Poles A-D are shown in Figs.9.13-9.16. The curves of all the LMTs are shown in each Plot. The right most curve of each figure is the ultimate displacement, subsequently used for comparison with the Bernoulli-Euler deflection model of the same pole. The most significant interpretation of these plots is the remarkable linearity of the load response up to the ultimate load. This strongly suggests that the joints do not visibly affect the curvature of loaded poles.

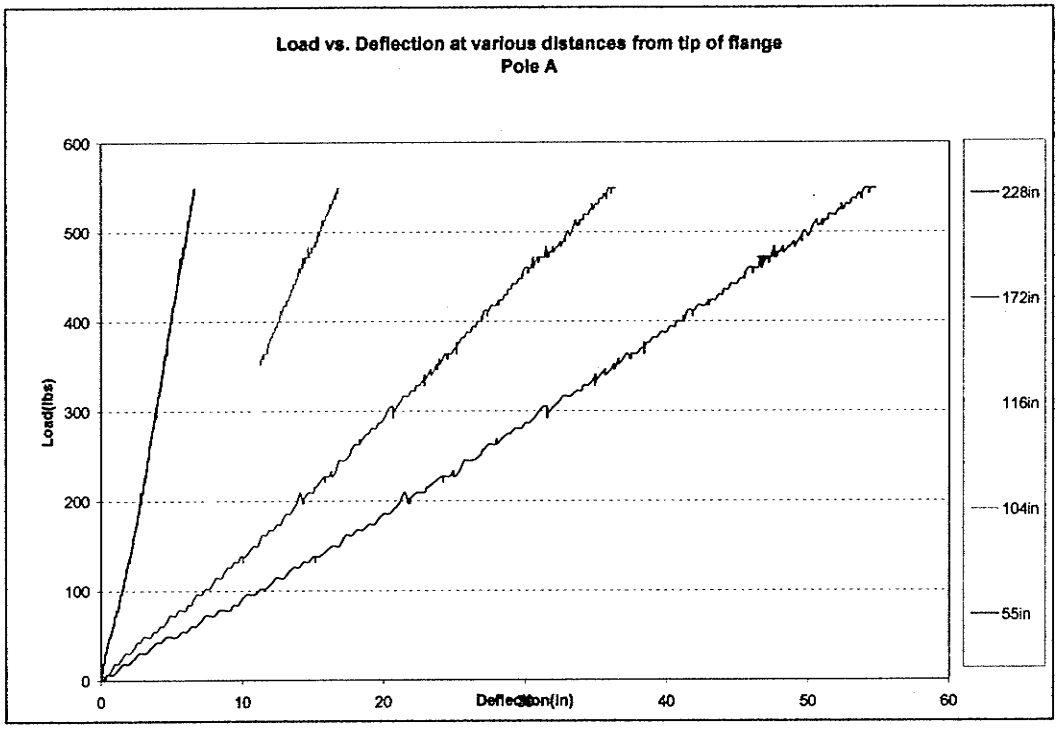

Figure 9.13: Pole A Load –Deflection curves

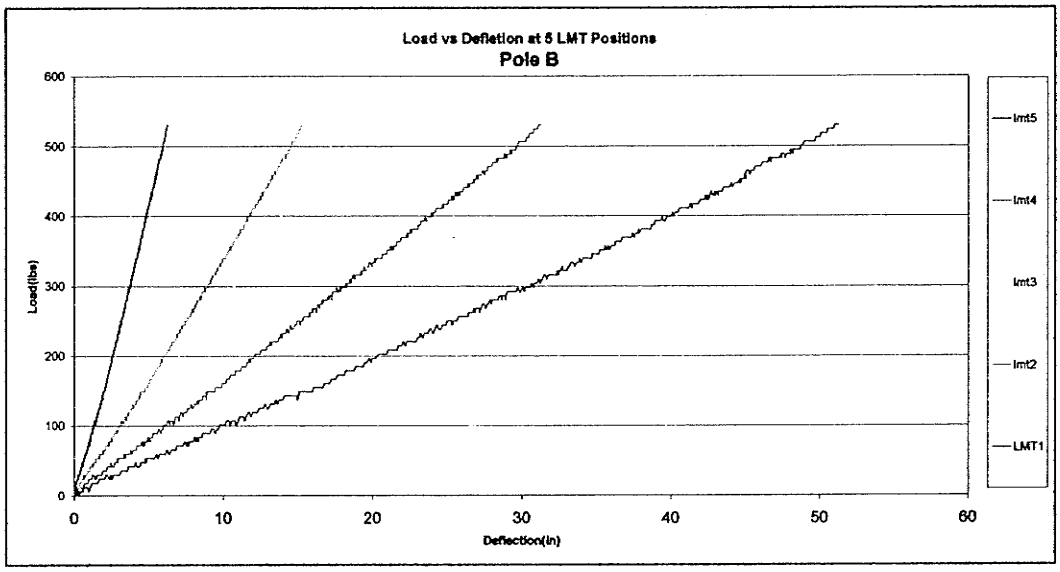

Figure 9.14: Pole B Load –Deflection curves

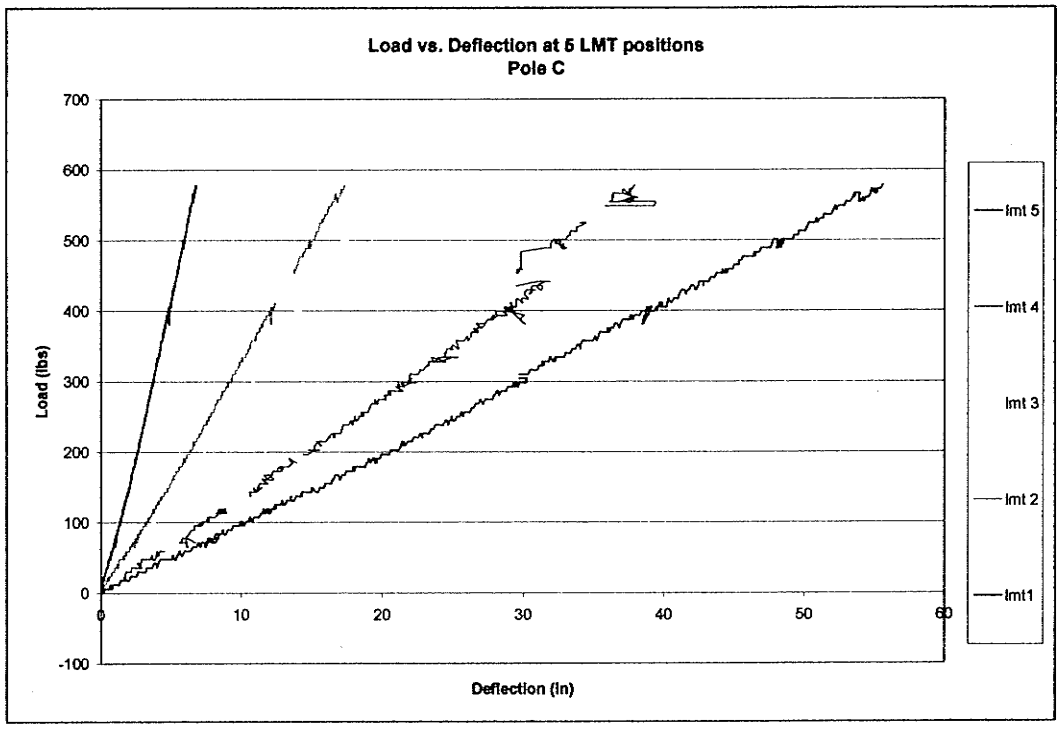

Figure 9.15: Pole C Load –Deflection curves

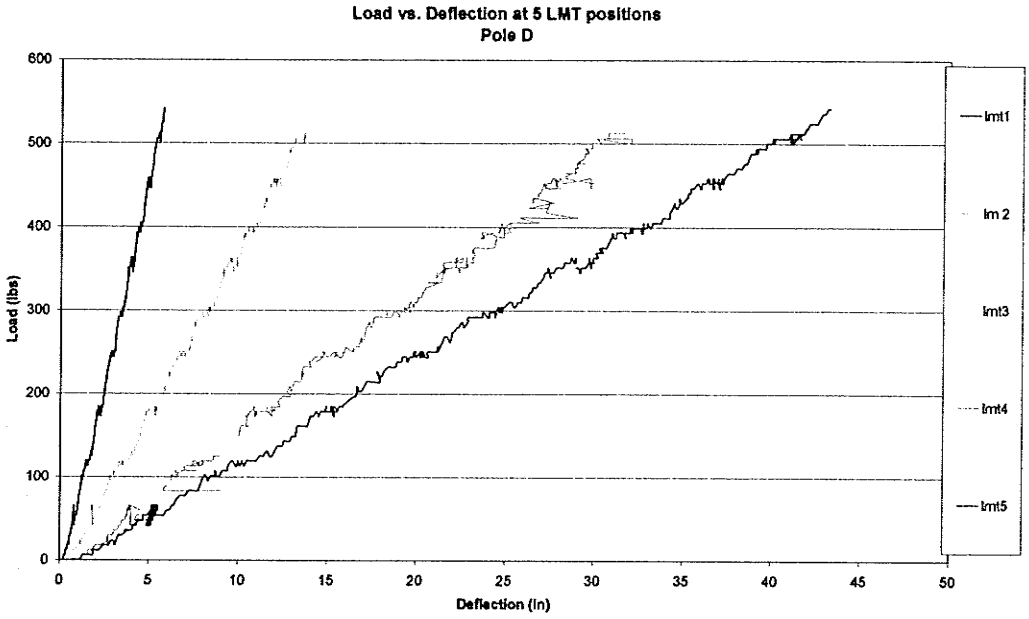

Figure 9.16: Pole D Load –Deflection curves

9.8 JOINTED POLE DEFLECTION MODELING

9.8.1 Jointed Pole Deflection Modeling

The general geometry and laminate structure for the four test poles are given in Fig.9.17. Specific geometries for the analysis set up are shown in Figs. 9.19 9.23, 9.27, and 9.31. The modeled deflection curves from the MapleV programs are shown in Figs. 9.21, 9.25, 9.29, and 9.33 for poles A-D, respectively. The MapleV program modeled thickness of the tube wall with respect to axial position for the four poles in Figs. 9.20, 9.24, 9.28 and 9.32 respectively.

Additional inputs include the slope and dimensions for each segment and the starting thickness of each segment for both the axial and circumferential layers. The model as used completely ignores the joint. This assumption is required to keep the exercise manageable. The main thrust of this work is to begin a process where by deflection control can be achieved through appropriate manipulations of individual segment laminate properties.

The laminate structures and geometries are summarized in the Fig. 9.21. A generalized pole is shown composed of the two sections mounted on a flange. Beneath the drawing are rows of laminate structures. The left most represents the structure of a lower section while the right most represents the structure of the upper section. Below each pair of winding laminae is given the thickness for the pair. While the poles appear very similar there are important differences.

Each of the Poles A through D are processed by the Bernoulli-Euler Deflection Program. The output for each of the poles shows plots for effective axial modulus versus position, axial and total thickness versus position and a fifth iteration deflection curve.

Pole A processing yields Figures 9.18-9.21, Pole B Figures 9.22-9.25, Pole C Figures 9.26-9.29 and Pole D processing results in Figures 9.30-9.33. The pole information is shown in this order to give the reader some perspective for interpretation of the plots.

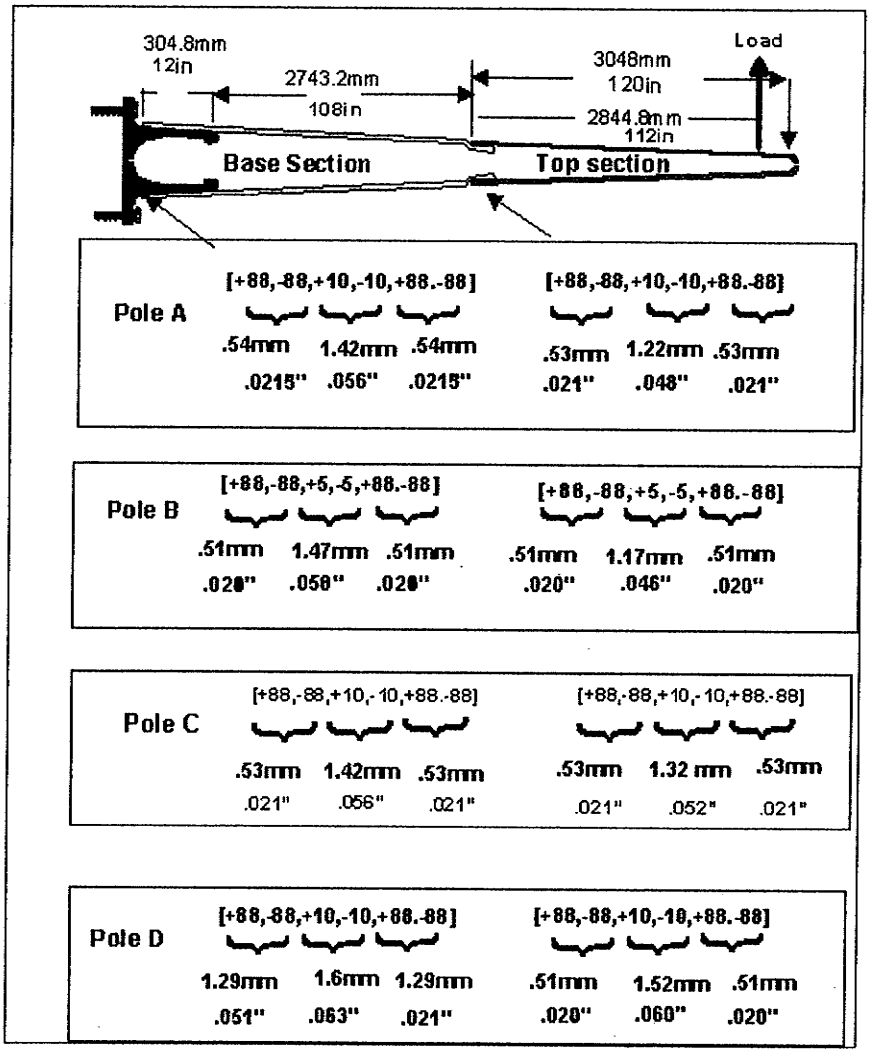

Figure 9.17 Laminate Structures of Jointed Poles

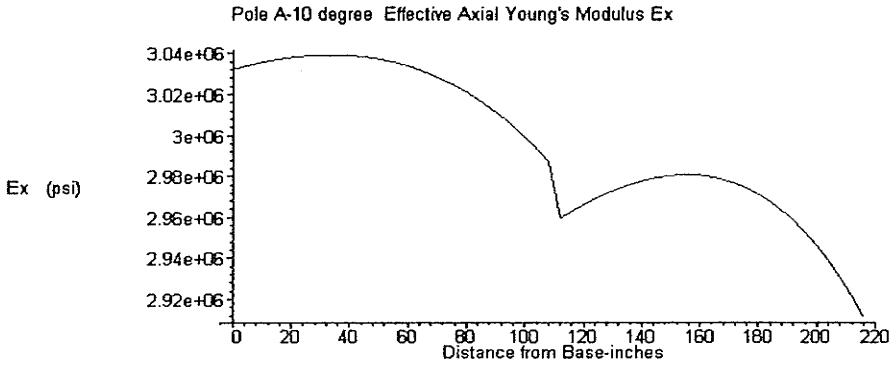

Figure 9.18 Pole A Axial Modulus Variation

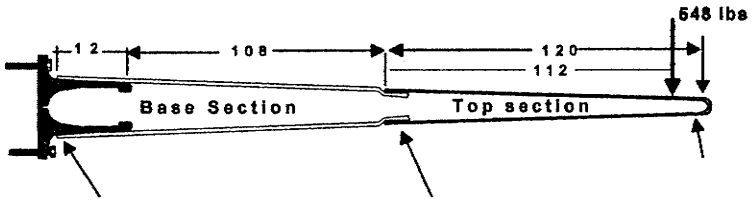

Figure 9.19 Pole A Geometry and Load

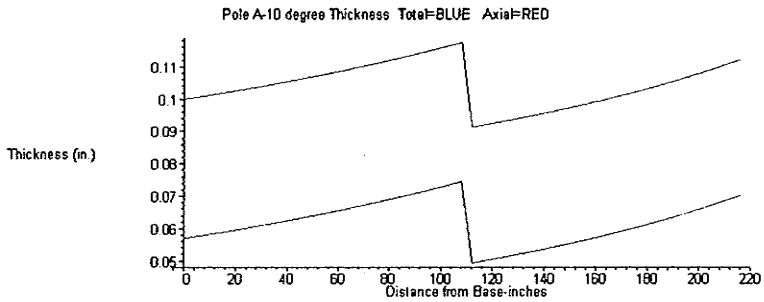

Figure 9.20 Pole A Variation in Thickness

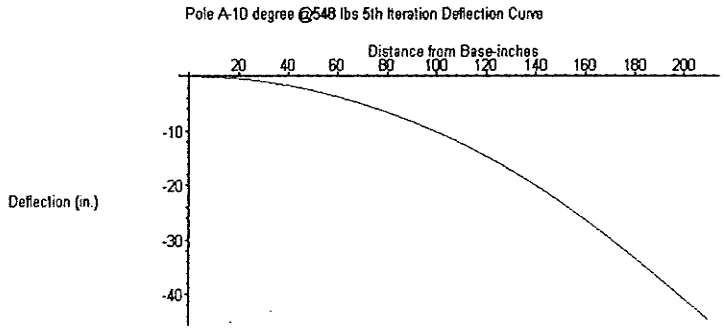

Figure 9.21 Pole A Deflection Curve 5th Iteration

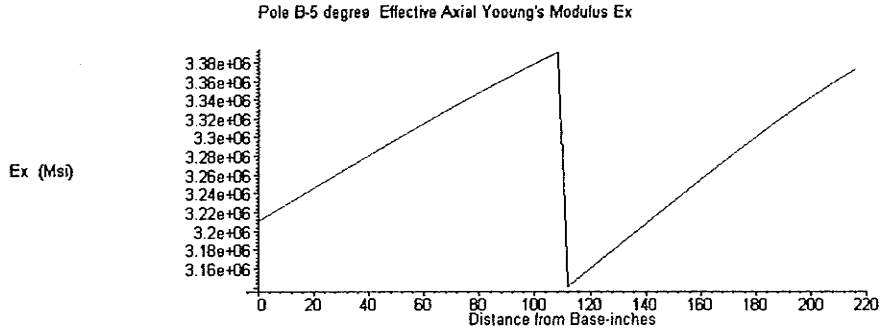

Figure 9.22 Pole B Axial Modulus Variation

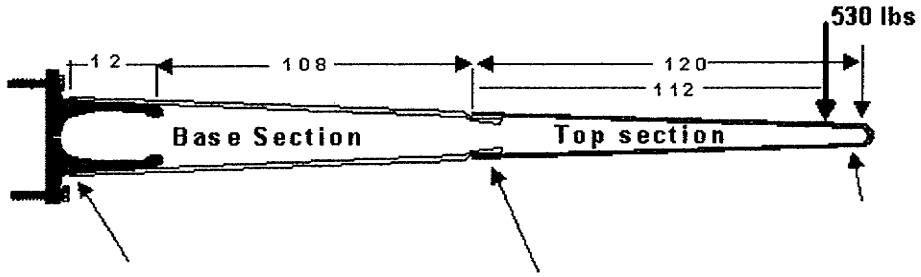

Figure 9.23 Pole B geometries and Load

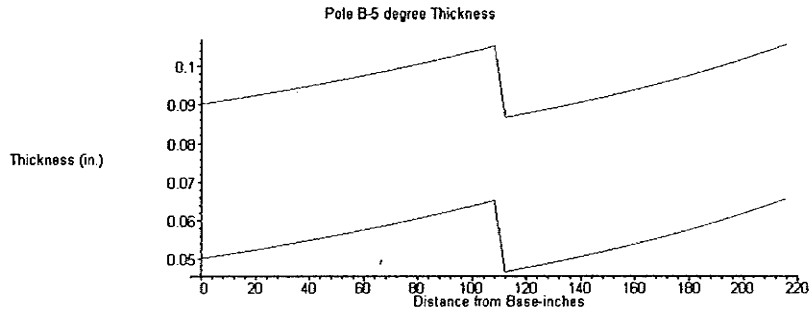

Figure 9.24 Pole B Variation in Thickness

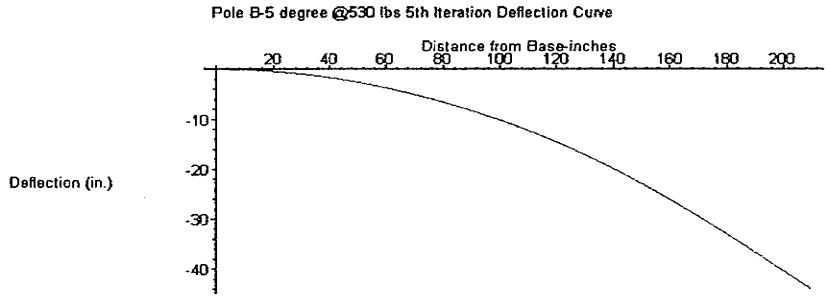

Figure 9.25 Pole B Deflection Curve 5th Iteration

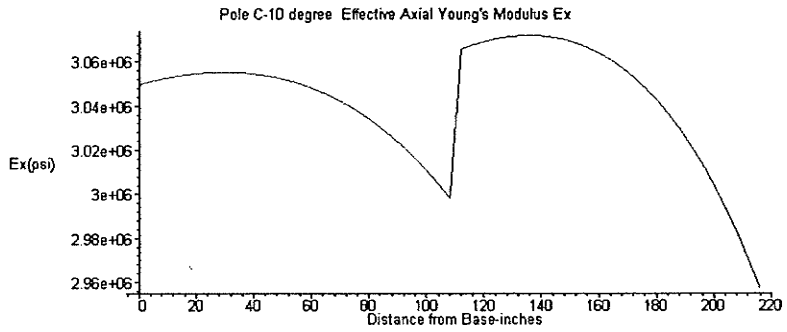

Figure 9.26 Pole C Axial Modulus Variation

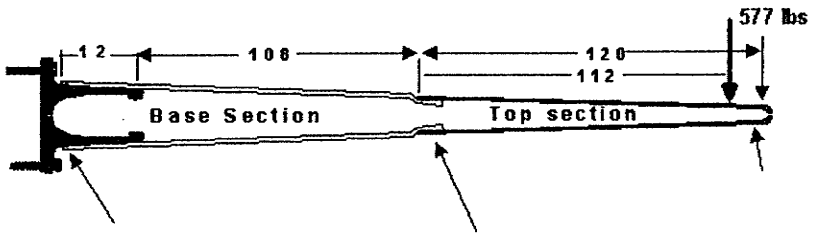

Figure 9.27 Pole C Geometries and Load

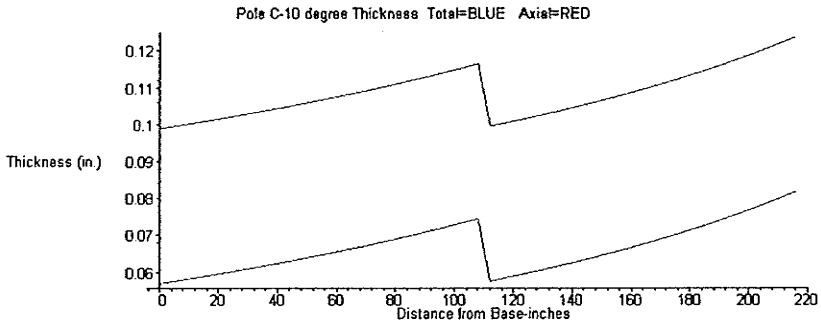

Figure 9.28 Pole C Variation in Thickness

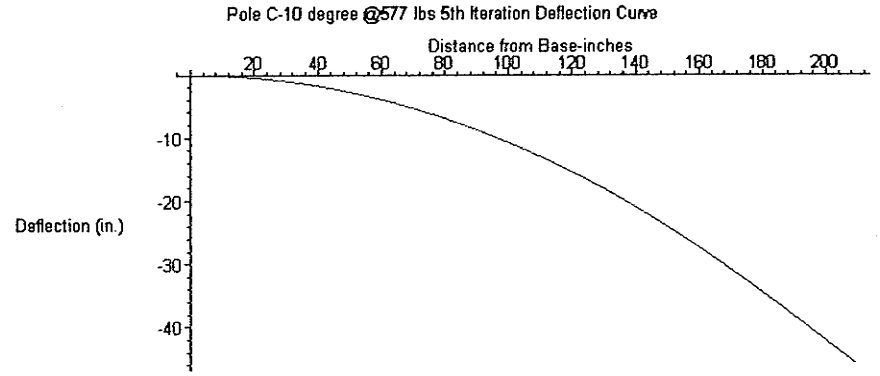

Figure 9.29 Pole C Deflection Curve 5th Iteration

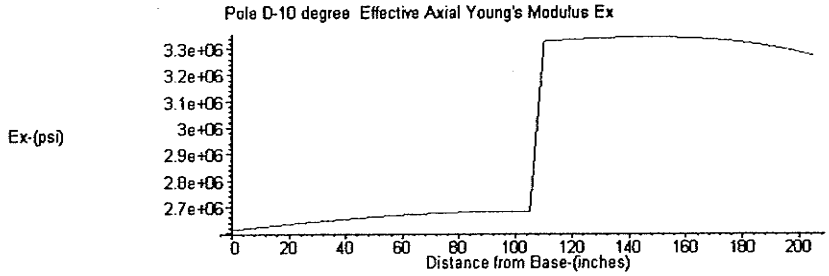

Figure 9.30 Pole D Axial Modulus Variation

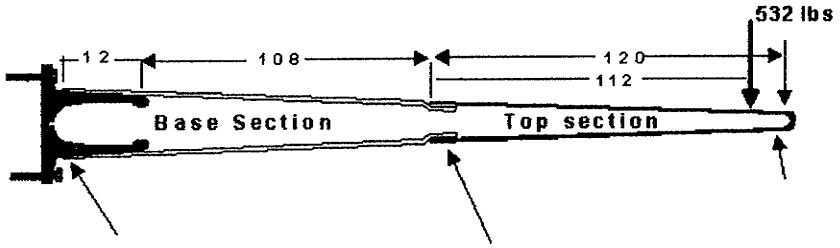

Figure 9.31 Pole D Geometry and Load

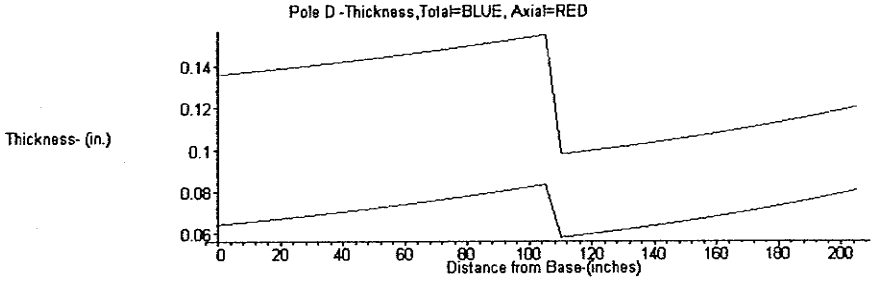

Figure 9.32 Pole D Variation in Thickness

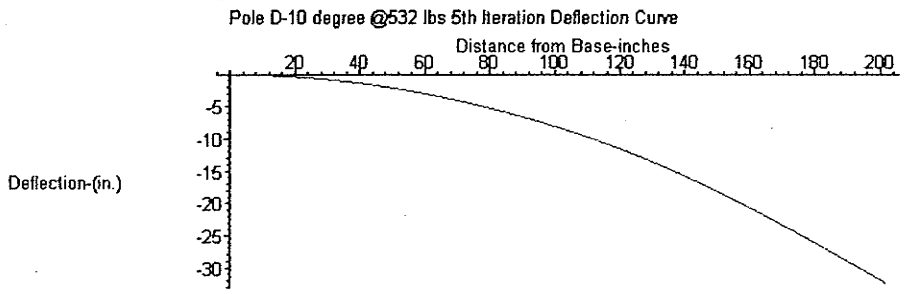

Figure 9.33 Pole D Deflection Curve 5th Iteration

The results of jointed pole modeling are summarized in the following Table 9.2 and predictions are compared to experimental values. The model predictions are in good agreement with the corrected experimental results for deflection, when the effective moduli of poles are adjusted for the difference in fiber volume fractions as compared to test coupon values.

Table 9.2 Summary of Pole Deflection Model Predictions versus Experimental

	Pole A	Pole B	Pole C	Pole D
Experimental Measured Deflection includes Flange Deflection (inches)	54.71	51.26	55.55	43.7
(mm)	1389.63	1302.00	1410.97	1109.98
Flange Deflection Compensation Corrected Pole Deflection (inches)	44.32	41.23	44.6	34.17
(mm)	1125.73	1047.24	1132.84	867.92
Model Inputs				
Load (lbs.)	548.64	530.17	577.83	532
(kN)	2.44	2.36	2.57	2.37
Bernoulli-Euler Iterative Model Deflection Prediction Based on Series B material properties and Resin Comp Factor =1.52 (inches)	44.79	44.06	45.97	32.17
(mm)	1137.67	1119.12	1167.64	817.12
Accuracy Pred/Corrected	1.01	1.07	1.03	0.94

9.8.2 Volume Fraction Compensation

As previously demonstrated in Chapter 8.0, the determination of material properties of the pole is based on coupon test results and the application of the classical lamination theory. Test coupons were shown to have a modulus in the longitudinal direction of 3.6 Msi. When these values are used in the determination of the effective axial modulus of a laminate composed of axial and circumferential fibers, they were found to result in modeling overestimates of deflection. In effect the model was expecting the poles to be much softer than the experimental results would indicate was true.

Substituting the calculated value of E_f into the Eq.8.12 and replacing the coupon fiber volume fraction with, that for the filament wound poles, 0.58. The new Ec value is determined to be 5.49Msi. This value is then divided by the original 3.6 Msi to derive a multiplication factor of 1.52 . The factor of 1.52 is applied to the $\overline{E}_x$, effective axial Young's modulus determined by the classical lamination theory during the modeling process.

9.8.3 Deflection Model Sensitivity to Shear Modulus Variation

The difficulties in determining a value for the shear modulus, G_{12} , were discussed in sections 8.5.3 and 8.5.9. Due to these difficulties encountered from the twisting of roving during the unwinding process, it was decided to use a typical shear modulus based on recommendations of the Faroex staff and the resin suppliers. That value as previously discussed was determined to be 0.4×10^6 psi (0.4 Msi). However, it was decided to verify the significance of deviations in the shear modulus to determine the risk to calculating tip deflection.

The method chosen to illuminate the sensitivity of the Bernoullli-Euler beam model to variations in the shear modulus is not experimental but rather mathematical in nature. Since we have experimental data for both the full scale single section and the two section jointed poles it was an arbitrary decision to choose Pole A from the jointed series as the reference. The decision to avoid the use of the Faroex poles as reference material was due in part to our regarding these poles as having been superseded by the jointed poles as a consequence of the improved production procedures.

Knowing the original material properties of Pole A used for the Bernoulli-Euler Model which included the arbitrarily chosen value of the shear modulus, the total tip deflection for the experimental load was calculated to be 44.79 inches (1137 mm) (see Table 9.2).

The Bernoulli-Euler model incorporated a major subroutine to calculate the laminate effective axial moduli as previously described in chapter 7.0. Inputs for the Pole A material properties are described in section 8.5.13 and are derived from Series B coupon testing.

In order to determine the sensitivity of Bernoulli-Euler deflection model to variations in the value of the shear modulus, the analysis program is run multiple times with different values of G_{12} under and over the original value to inspect effects on deflection. The data for the multiple runs of the program are presented in Table 9.3. The original values for the analysis of Pole A are highlighted in yellow.

In chapter 9.0, deflection is given as a value in the direction normal to the principal axis of the pole. It is unconventional but somewhat more accurate to describe the deflection in terms of both X and Y directions especially in the case of large deflections. The experimental setup for testing pole deflection did not afford a means of calculating the X axis displacement of the tip, so only the Y component of displacement is presented for experimental tests. In the case of Pole A the actual experimental tip displacement, after excluding

rigid body motion of the flange mount, was calculated to be -44.32" in the –Y direction at a load of 548.64 lbs.

Examination of the results presented in Table 9.3 suggests that the value of the shear modulus has a very minor influence on the calculated deflections of the Bernoulli-Euler Model. This is not surprising since the only influence that the shear modulus has is during the calculation of the material properties of the individual laminae, prior to the assembly of the laminate compliance matrix.

In general the higher the shear modulus the stiffer the pole appears to be but the effect is very small. At a deviation of +10% of the shear modulus, the displacement is reduced in the Y direction by 0.30". At a deviation of -10%, the displacement in the Y direction is increased by 0.35". A ± 0.30" deviation is only 0.00669% of the displacement originally calculated using a shear modulus of 0.40 x 10^6 psi. In short, an error of 10% for the shear modulus results in a displacement error of less than 1%. In fact an error of $\pm 20\%$ for the shear modulus value, results in a displacement error of only 0.012%. Focus on the shear modulus as a potential source of deflection error is not considered to be significant for this study.

Table 9.3 Deflection Model Sensitivity to Shear Modulus Variation

G_{12} (Msi)	X-position (at zero Load X=220")	Y-position (at zero Load Y=0 inches)

0.5	210.02"	-44.11"
0.48	209.99"	-44.23"
0.46	209.96"	-44.35"
0.44	209.92"	-44.49"
0.42	209.88"	-44.635"
0.40	209.84"	-44.79"
0.38	209.79"	-44.959"
0.36	209.74"	-45.14"
0.34	209.68"	-45.34"
0.32	209.619"	-45.56"
0.30	209.55"	-45.81"
0.20	209.02"	-47.60"

9.8.4 Comparison of FEM and Bernoulli-Euler Models

The numerical modeling program, ANSYS, using the finite element method was employed to analyze the behaviour of the four jointed poles. Philopulos (2002) describes the method in detail and summarized the work in an undergraduate thesis. At the time Philopulos was using a copy of an earlier version of Maple Code that predated the fully integrated Bernoulli-Euler

model previously discussed. This older version had very similar results for deflection predictions to those presented earlier in this chapter.

Philopulos (2002) states that the ANSYS model of the jointed poles incorporated eight-node layered solid elements in contrast Ibrahim (2000) used eight node layered shell elements to model the Faroex poles. The key difference being that the solid elements had corner nodes while the shell elements had mid-plane nodes and therefore the thickness of a shell element is expressed as a "Real Constant". The Philopulos (2002) analysis method was considerably more complex than that of Ibrahim (2000) since he was trying to model the geometries of the joint region where the lower pole section acts as a ferrule inside the end of the top section. The requirement for and intermediate contact layer to model the adhesive interface was also incorporated in the Philopulos (2002) model.

Philopulos (2002) was able to accurately model stresses and strains through the joint region as well as the rest of the pole lengths. He noted that there is an abrupt local decrease in strain and stress along the length of the joints. This fact is due to the increased thickness of material in the overlap region of the joint.

Philopulos (2002) states that," The FEM results for deflection were about 50% higher than the test (*experimental*) results". He goes on to state that the FEM model "...did not account for the fact that the effective modulus of elasticity was variable along the length of the pole, as a result of the change in fiber

angle...". Since pole design is necessarily a deflection issue, the use of FEM analysis was appropriate when limited to stress, strain and failure issues and only when combined with the Bernoulli-Euler deflection model it became possible to get a good overall picture of jointed pole behaviour.

10 DESIGN OF FILAMENT WOUND POLES

10.1 LOAD CAPACITY CLASSIFICATION OF POLES

The previous chapters were devoted to the development of a filament winding process for tapered tubes and to methods for controlling the material properties of a given pole structure. Algorithms were developed to calculate the variation of geodesic winding thickness over a length of the pole and the subsequent changes in wind angle and axial stiffness. A method of computing the deflection of a given pole design was also developed using the Bernoulli-Euler Iterative procedure which typically predicts deflections slightly greater than the experimentally derived results.

The model as presented is however less than ideal for designing a pole to meet a particular service load requirement. Wooden poles used by the electric power utilities are classified according to ANSI

Standard 05.1 (1992). This classification system is based on the ability of a given pole to carry a specified transverse load. No matter what the length of a pole, in order to meet a particular Load Class, it must support the required transverse load. The shorter the pole then the lower the moment capacity, and the longer the pole then the moment capacity must be increased.

For example, a 30' wooden pole of Class 1 is required to support a minimum transverse load of 4500 lbs. A 60' Class 1 pole has the same requirement. Thus it is not possible to extend a 30' Class 1 pole to 60' since the moment capacity required is double. In practice the longer poles have significantly greater diameters at the base. There are 13 classes described by the ANSI standard 0.5.1(1992) and these are presented in Table 10.1.

This is by no means the only set of standards being employed for the industry with regards to wooden poles (CAN/CSA-015-90, 1990) while other standards exist for steel poles, (Design of Steel Transmission Pole Structures (1990)).

It was always apparent that filament wound utility poles were going to be evaluated by direct comparison to the wooden pole classes, which had been widely adopted by the utilities. One of the objectives of the research project was to design filament wound poles to meet a wooden pole classification system.

Table 10.1: Wooden Pole classification system based on load capacity

ANSI 05.1

Class	Transverse Load (lbs.)	Transverse Load (kN)
H6	11400	50.7
H5	10000	44.5
H4	8700	38.7
H3	7500	33.4
H2	6400	28.5
H1	5400	24.0
1	4500	20.0
2	3700	16.5
3	3000	13.3
4	2400	10.7
5	1900	8.5
6	1500	6.7
7	1200	5.3

10.2 THE DESIGN PROBLEM

Since wooden poles are not geometrically or materially similar to composite poles, a common design parameter was required. One such parameter was load capacity. For filament wound poles, the load capacity is a value derived from the laminate structure, overall geometry and material properties. There was no way to inform the fabricator how to design a mandrel or to set his machine and program parameters to fabricate a pole to meet a given load capacity. The problem becomes more difficult if one must find an optimal solution based on some external parameter such as economics.

The solution to this problem requires an additional input parameter, i.e. deflection. In conversations with Mr. Ben Yu of Manitoba Hydro (Yu, 2002) it was made clear that many power line designers preferred to limit pole deflection to 10% of the free length. The standards did not specify a maximum acceptable deflection at load capacity but clearly deflection was of some concern to the distribution and transmission line designers.

The 10% maximum deflection parameter proved to be the missing parameter required to link filament wound poles to wooden pole classes.

If the deflection is preset at 10%, then it is possible to solve the closed form solution to the differential equation in reverse for the load required to produce such deflection knowing of course the material

properties and geometries. Sherman (1984) made some basic assumptions for the variation in thickness by using a linear interpretation to get values for moment of inertia. The same procedure could be used to linearize the variation in axial stiffness without too much loss of detail since the actual values can easily be determined using the Classical Lamination Theory programs. However, it is now clear that the stiffness in filament wound tapered tubes can be increasing, decreasing or stable towards the tip. The linearization of thickness is a much simpler issue than the linearization of the axial stiffness.

According to the simple beam theory,

$$\frac{d^2y}{dx^2} = \frac{M}{EI} \qquad \text{(Eq.10.1)}$$

the modeling of pole deflection using Eq. 10.1 represents an expectation of reducing the complexity of the problem to a single solution equation. Traditionally Eq. 10.1 is solved explicitly by assuming that the Young's modulus, E, is constant as is the second moment of inertia, I. These assumptions can not be used in the case of composite tubes, so the ***E*** and ***I*** values are made to be simple linear functions of ***x.*** Thus,

$$\frac{\partial^2}{\partial x^2} y(x) = \frac{M_x}{E_x I_x} = \frac{P(L-x)}{E_x \left(\pi\, t_x\, r_x^{\,3}\right)} \qquad \text{(Eq.10.2)}$$

Recall that from previous discussion that the thickness of filament wound tubes, t_x, requires a constant value for circumferential winding, t_c, and a

second to reflect the geodesic winding which increases as radius decreases, t_a. Thus thickness of the tube can be expressed as

$$t_x = t_a + t_c \qquad \text{(Eq.10.3)}$$

The solution for t_a , from the quadratic form of Eq.7.19 is inconvenient when integrating the deflection equation. A simple expression accurately reflecting Eq.7.19, was required. In our project the winding angles were kept below 20^0 and wind angle drift occurred relatively slowly. As a consequence it was found that a simple expression could model the variation in axial thickness,

$$t_a \approx \frac{t_0 + B}{r_x} \qquad \text{(Eq.10.4)}$$

So that the combined thickness term becomes

$$t_x = \frac{t_0\ B}{r_x} + t_c \qquad \text{(Eq.10.5)}$$

The bending moment, M is described as a function of x,

$$M_x = P(L - x) \qquad \text{(Eq.10.6)}$$

The moment of inertia, I, is conveniently represented as follows.

$$I_x = \pi t_x r_x^3 \qquad \text{(Eq.10.7)}$$

And finally the simple linear radius defining function, m being the slope and B the starting radius of the mandrel gives

$$r_x = mx + B \qquad \text{(Eq.10.8)}$$

In order to simplify the solution of Eq.10.2, direct incorporation of the wind angle relationships and the classical lamination theory used in the Bernoulli-Euler deflection model were avoided. Keeping in mind that the solution of Eq. 10.2 will require the simultaneous solution of each of the

Equations 10.3 through 10.8 at each and every point along the length of the pole.

Clearly, we cannot find a simple general function to describe the manner of variation for different wind angles and tapers, but we can adequately determine the E_x values at the start and end positions using the Classical Lamination Theory. Knowing the two values of E at the base and top it is possible to assume a linear variation between those points. Thus E_x at any point between is simply

$$E_x = E_0 + (S\,x) \qquad \textbf{(Eq.10.9)}$$

Assuming that we know the moduli at the top and base the slope, S is as follows

$$S = (E_t - E_0)/L \qquad \textbf{(Eq.10.10)}$$

and E_0 and E_t are the moduli at the base and the top respectively. L is the length of the pole.

The terms of Eq.10.2 are now expanded to represent functions of x , but only indirectly linked to wind angle drift,

$$\frac{\partial^2}{\partial x^2} y(x) = \frac{M(x)}{E(x) \times I(x)}$$

$$= \frac{P(L-x)}{\left(E_0 + \left(\frac{(E_t - E_0)}{L}\right)x\right) \times \left(\pi\left(\frac{t_0 \times B}{mx+B} + t_c\right)(mx+B)^3\right)} \qquad \textbf{(Eq.10.11)}$$

It is possible to solve the second order linear differential equations, Eq.10.2 and 10.11 symbolically, with MapleV, using the appropriate boundary conditions, ***(@x=0, slope=0, y=0).*** The symbolic solution can then be set up

to be equal to the 10% value of deflection. This solution can be resolved symbolically for the unknown value of load, P. This is basically a rearrangement of the equation to get the load over to the left side of the equation. To derive a solution for a particular set of geometric and material properties specific to a pole all the symbolic quantities will have to be assigned values.

One of the most significant aspects of MapleV is the ability to place a number of equations within a single execution group to be solved simultaneously. By placing the symbolic solution of Eq.10.2 in terms of the unknown load P into the execution group followed by Eqs.10.5 ,10.6, 10.7, 10.8, 10.9 and 10.10 they can be solved simultaneously for values of x over a range that is user specified. Naturally our interest is limited to the values of x between 0 and the top of the pole. Since the Eqs. 10.5 to 10.10 are also symbolic, they must have a means of being assigned floating point values. It is possible to have a list of assignments either within the execution group or outside and ahead of it. The other input parameters required to permit the solution of the equations using MapleV and are as follow,

$L = Total\ Length\ to\ Load$

$P = Load$

$m = slope\ of\ taper$

$B = radius\ at\ Base\ of\ mandrel$

$t_0 = starting\ thickness\ of\ Geodesic\ Layer\ at\ base\ of\ mandrel$

$t_C = Thickness\ of\ Circumferential\ Plies\ (Total\ of\ all\ plies)$

When Eq.10.10 is set up in MapleV it is quite simple to manipulate the thickness of various plies since everything is referenced to the start position. It is a simple matter to input the new starting position parameters, as well as the known values of axial stiffness at the base and top of the pole.

The procedure was set up in MapleV as a complex program. The first set of parameters required for the solution is the geometries of the pole such as length, taper, and butt radius. The basic axial fiber wind angle is input. The thickness variations over the length of the mandrel are calculated using either the exact thickness equations Eq.7.19 and Eq.7.20, presented earlier or an approximation such as Eq.10.5. As long as the exact thickness equation is kept out of the execution group that solves the differential equation Eq.10.11 there seems to be little trouble finding a solution In general, an effort is made to keep complexity within an execution group to a minimum.

This procedure uses an approximation of the effective axial stiffness to eliminate the need for the construction the fully populated laminate stiffness matrix, $\begin{bmatrix} A_{i,j} & B_{i,j} \\ B_{i,j} & D_{ij} \end{bmatrix}$ and the subsequent inversion to determine the laminate compliance matrix.

This contracted procedure is strictly speaking valid only for symmetric balanced laminates, **[90,+ θ,- θ,- θ,+θ,90]**, the inherent assumption justifying the use of the contracted method is that circumferential plies of 88^0 are close enough to 90^0 and the axial laminae are so interwoven that they can appear equally as symmetric or antisymmetric. The basic contracted formula for E_x is taken from Daniel and Ishai (1994), where

$$E_x = \frac{1}{h}\left[A_{xx} - \frac{A_{xy}^2}{A_{yy}}\right] \qquad \textbf{(Eq.10. 12)}$$

With h being the total laminate thickness and the stiffness matrix , A_{ij} is given as

$$A_{xx} = \sum_{k=1}^{n}(Q_{xx})^k t_k = t_a Q_{xx}^{axial} + t_c Q_{xx}^{circ} = hQ_{xx}$$

$$A_{xy} = \sum_{k=1}^{n}(Q_{xy})^k t_k = t_a Q_{xy}^{axial} + t_c Q_{xy}^{circ} = hQ_{xy} \qquad \textbf{(Eq.10. 13)}$$

$$A_{yy} = \sum_{k=1}^{n}(Q_{yy})^k t_k = t_a Q_{yy}^{axial} + t_c Q_{yy}^{circ} = hQ_{yy}$$

The right hand expressions in Eq.10.13 include the total geodesic axial thickness, t_a and the total circumferential layer thickness, t_c , which is the sum of the inner and outer circumferential laminae, t_{ic} and t_{oc} . The transformed lamina stiffnesses, Q, for the circumferential and axial layers are denoted with the superscript terms *circ* and *axial.*

Expanding Eq.10.12 by incorporating Eq.10.13 gives the following

$$E_x = \frac{1}{h}\left(\left(t_a Q_{xx}^{axial} + t_c Q_{xx}^{circ}\right) - \frac{\left(t_a Q_{xy}^{axial} + t_c Q_{xy}^{circ}\right)^2}{\left(t_a Q_{yy}^{axial} + t_c Q_{yy}^{circ}\right)}\right) \qquad \textbf{(Eq.10. 14)}$$

The formula for $\boldsymbol{E_x}$ is now constructed so that the actual thickness of the axial layer is normalized to 1 unit and the thickness of the circumferential layer is some fraction of the axial layer. Recognizing that the actual thickness of a laminate, h in Eq.10.14 does not affect the $\boldsymbol{E_x}$ value, since it will always cancel out by the total thickness terms seen in Eq.10. 13. The laminate axial modulus can now be expressed in terms of a thickness ratio of the axial to circumferential layers, so that, the thicknesses of the circumferential and axial layers are defined by the ratio,

$$F = \frac{t_a}{t_c} \qquad \text{(Eq.10.15)}$$

And the normalized formula for stiffness in the axial direction becomes

$$E_x = \frac{F}{(F+1)}\left(\left(\frac{Qt_{xx}^{circ}}{F} + Qt_{xx}^{axial}\right) - \left(\frac{\left(\frac{Qt_{xy}^{circ}}{F} + Qt_{xy}^{axial}\right)^2}{\left(\frac{Qt_{yy}^{circ}}{F} + Qt_{yy}^{axial}\right)}\right)\right) \qquad \text{(Eq.10.16)}$$

where the Qt_{nn}^{circ} and Qt_{nn}^{axial} terms are the xx xy and yy terms from the respective transformed lamina stiffness matrices for the circumferential and axial layers. Note that when an effective laminate stiffness value is required for the base and top of the pole the respective wind angles and F ratios must be accounted for as separate operations.

The E_x value increases non linearly as the thickness of the circumferential layer decreases with respect to the axial layer. As the amount of circumferential fibre decreases the effective modulus converges with the theoretical unidirectional modulus of the axial plies. Ibrahim (2000) presented a correlation between load performance and ultimate load capacity of the Faroex poles using the ratio of circumferential to axial fibre thickness. This approach is now regarded as suitable only for comparison of very similar poles with nearly identical geometries.

Having Eq.10.16 constructed in MapleV as a symbolic expression requires further the construction of the laminae stiffness matrices and transformation by the appropriate wind angle. The basic material properties for the resin/fiber system are input in order to fill out the matrices. Since the project only used the two basic fibre / resin systems, B and C, series the

properties could be handled quite simply as a data block with the transformation matrices adapted based on the user input specified wind angles. The effective axial stiffness of the laminate, E_x can then be solved explicitly once the transformed laminae stiffness matrices are constructed. In order to handle base and top stiffnesses they are denoted as E_0 and E_t. Note that the term $\overline{E}_x$ is used to refer to Eq.10.16 which is the approximation of the term within the differential equation Eq.10.11. This second $\overline{E}_x$ is an approximation based on the assumption of linear variation between E_0 and E_t

The solution to the unknown value of the load, P, is carried out using the MapleV solve function.

Knowing the anticipated load for the particular laminate structure, it is quite simple to determine the maximum stress value for a particular pole. Cross checking the load with the ANSI 05.1 standard, the composite pole can be classified accordingly. By checking the maximum stress value with the known failure criteria, it is now possible to establish the suitability of the laminate design. If the stress state is found to be unacceptably high, the designer can modify the starting thickness of the pole, by increasing the value of either the circumferential or axial layers. Safety factors can also be incorporated into the analysis as required. Clearly varying the thickness of the axial or the circumferential layers will affect the ultimate pole performance in different ways.

The Faroex pole, ***s7v7*** was used to illustrate the effectiveness of the simplified approach given in this chapter. The deflection modeled under the

experimental failure load of 8183lbs (36.4kN) was calculated to be 26.4 inches. The experimental value was measured to be 24.96 inches. The load capacity of this pole was re-calculated at 10% deflection limit using 175"(4445mm) as the free length and the deflection limit of 17.5" (444.5 mm).

Based solely on the ANSI 05.1 standards, the pole could be designed as H3 class, that is with no consideration for deflection. At a limit of 10% deflection however, this pole was calculated to support a load of 6000 lbs.(26.7kN). If deflection was a criteria for classification this would drop pole s7v7 down to H1 class. If then the pole were to be re-designed to fit back into the H3 classification, using a 10% deflection limit, it is found that the axial layer must be increased from .138" at the base to a thickness of .178". The existing circumferential thickness of .048" remains unchanged, as do the wind angles.

The maximum stress, σ_{max} can be simply determined from

$$\sigma_{max} = \frac{Mc}{I} \qquad \textbf{(Eq.10.17)}$$

where M is the moment with ***I*** and ***c*** being the moment of inertia and the radius to the centre of the tube wall, respectively. The ultimate failure stress of the original pole design, with 24.96" deflection at 8183 lbs of load was found to be 42,720 psi. If however the pole design was modified by the addition of .040" thickness to the total circumferential layer thickness load performance is changed slightly. Increasing the circumferential layer results in a 10% pole deflection at just under 6428 lbs of transverse load. This modification is just sufficient to raise the pole to H2 classification. However, the maximum stress at the base drops to 26620 psi.

In order to demonstrate the complexity of making modifications to a pole design a demonstration is provided in Table 10.2. The example pole, s7v7, is placed in the middle row with its original description laid out from left to right. The consequences of additional thickness to the circumferential layers are tabulated above the middle row, in increments of 0.010". For each increment of thickness the F parameter and moduli are recalculated in order to determine the new load capacity at 10% deflection. At the end of each row the new load class is presented. Below the central row, 0.010" increments are added to the axial layer and the results tabulated.

The consequence of the two alternatives is to either degrade or improve the effective axial modulus of the pole. It is evident that the addition of thickness will improve the load capacity but in more or less efficient manner depending where the additional material is placed.

Table 10.2: Pole s7v7 at 20 deg. Thickness modifications and the effects on Load capacity and Classification.

Pole# s7v7	Thickness t axial @ Base (to) mm (inches)	Thickness t-circ+tic+toc mm (inches)	F-Ratio Base	F-Ratio Top	Young's Modulus Base GPa (Msi)	Young's Modulus Top GPa (Msi)	Maximum Load Capacity @ 10% deflection kN (lbs)	Maxi.Stress @ Base MPa (psi)	ANSI 05.1 Equiv.Pole Class
Increasing Circ. Thick.	3.51 (0.138")	2.24 (0.088")	1.57	2.33	13.96 (2.024)	12.31 (1.785)	-1.45 (-6428 lbs)	-183.54 (-26620psi)	H2
	3.51 (0.138")	1.98 (0.078")	1.77	2.63	14.38 (2.085)	12.51 (1.814)	-1.42 (-6330 lbs)	-188.72 (-27370psi)	H1
	3.51 (0.138")	1.75 (0.068")	2.03	3.01	14.82 (2.149)	12.71 (1.843)	-1.40 (-6224 lbs)	-194.16 (-28160psi)	H1
	3.51 (0.138")	1.47 (0.058")	2.38	3.53	15.30 (2.219)	12.90 (1.871)	-1.37 (-6115 lbs)	-200.16 (-29030psi)	H1
Original Configuration Pole # s7v7	3.51 (0.138")	1.22 (0.048")	2.88	3.875	15.82 (2.294 Msi)	13.10 (1.897 Msi)	-1.35 (-6000 lbs)	-206.44 (-29940psi)	H1
	3.76 (0.148")	1.22 (0.048")	3.08	4.58	16.00 (2.32)	13.13 (1.904)	-1.44 (-6393)	-208.78 (-30280psi)	H1
	4.01 (0.158")	1.22 (0.048")	3.29	4.88	16.14 (2.341)	13.16 (1.909)	-1.52 (-6780)	-210.71 (-30560psi)	H2
	4.27 (0.168")	1.22 (0.048")	3.5	5.19	16.29 (2.362)	13.20 (1.915)	-1.61 (-7172)	-212.64 (-30840psi)	H2
Increasing Axial Thick.	4.52 (0.178")	1.22 (0.048")	3.71	5.5	16.41 (2.38)	13.23 (1.919)	-1.70 (-7562)	-214.37 (-31090psi)	H3

Gpa/6.895=Msi
mm/25.4=inches Msi=10^6 psi MPa/6.895=ksi 1lb=4.448N

Knowing that changes to thickness of either the circumferential or axial layer thickness can alter the pole designation, the designer will wish to alter wind angles. The effects of changing winding angles are presented in Table 10.3. Again using the pole s7v7 as reference, a simple change of wind angle from $+20^0/-20^0$ to $+10^0/-10^0$ results in a 10% deflection under 7476 lbs of transverse load. This is only 24 lbs short of the 7476 lb minimum for H3 class. There was no change to either the circumferential or axial layers. However the maximum stress value is much higher at 37,300psi. Further improvement is demonstrated by changing the wind angle to $(+5^0/-5^0)$. With this winding angle

the load required to get a 10% deflection has further increased to 7862 lbs, and maximum stress is further increased to 39370 psi

Table 10.3: Pole s7v7, with fixed laminate thickness, Wind angle effects examined.

Wind Angle Start position to End position degrees	t axial inches (mm)	t circ inches (mm)	F @ Base	F @ Top	Ex @ Base psi Mpa	Ex @ Top psi Mpa	Load Capacity @ 10% Deflection pounds (kN)	Max. Stress psi (MPa)	ANSI Pole Class
5 drift to 6.7	0.138 3.5052	0.048 1.2192	2.88	3.83	2.88 13.95	2.998 12.31	-7862 -34.97	-39250 -270.63	H3
10 drift to 13.3	0.138 3.5052	0.048 1.2192	2.88	3.91	2.757 14.38	2.7775 12.51	-7476 -33.25	-37300 -257.18	H2
20 drift to 27.3	0.138 3.5052	0.048 1.2192	2.88	4.27	2.294 14.82	1.897 12.71	-5999.6 -26.69	-29940 -206.44	H1

The failure stress in the compressive mode F_{1c} was determined to be 49.7 ksi for the unidirectional, E-glass/polyester material (see Table 8.2, Section 8). The designer may choose to reduce the maximum stress by a combination of lower winding angles and slight increase in axial layer thickness.

In Figure 10.1, the pole class limits are not shown, however one can extrapolate easily the required axial layer thickness required to meet a specific class designation with a fixed circumferential layer total thickness of 0.040".

In Figure 10.2 the maximum stress at the 10% limit is plotted versus axial layer thickness for poles wound with 5^0,10^0 and 20^0 patterns. The circumferential layer is again fixed at .040" in thickness. This plot is again based on the 240" (175" free length), 8" to 6" radius tapered mandrel.

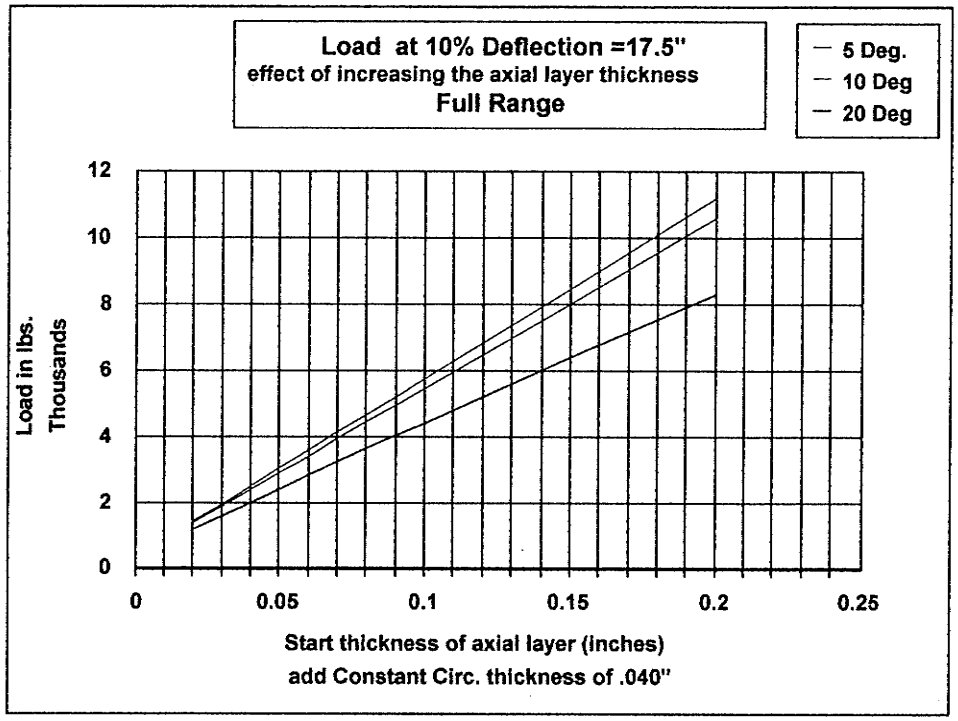

Figure 10.1: Plot of Load capacity versus axial layer thickness

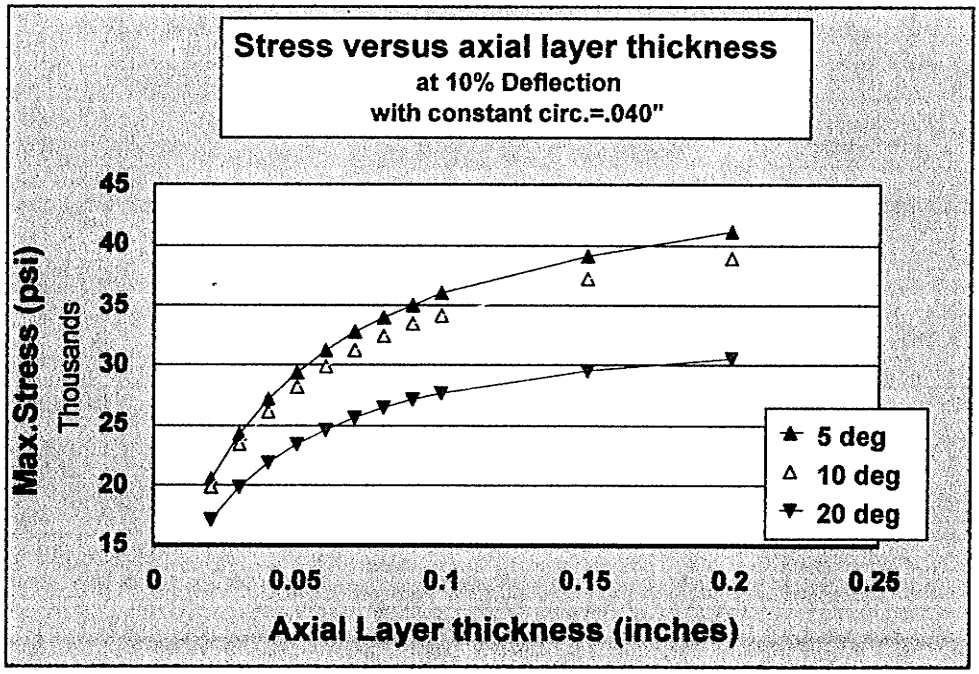

Figure 10.2: Plot of Maximum stress versus Axial layer Thickness for 5, 10 and 20 Deg. Winding angles

11 SUMMARY AND CONCLUSIONS

The original goal of this thesis was to provide industry with a technology that would replace wooden electric utility poles with advanced composite poles, bearing in mind that these new poles would be judged by standards originally developed for the wooden poles. Previous to this thesis there was no comprehensive set of procedures to aid the manufacturer to determine, in advance, the design of a pole meeting a specific load class. This thesis not only describes such procedures but also provides the manufacturer with guide lines to fabricate the specialized mandrels for single and multiple section poles.

The mathematical tools developed here in are suitable for use with a variety of filament winding technologies. Also these tools can easily be employed to determine material costs of pole structures as well as providing the basis for robotics programming.

The concept of replacing wooden utility poles with filament wound poles is no longer a theoretical discussion as is proved by the number of examples fabricated in a variety of geometries. The analysis of jointed and single segment pole structures using the Bernoulli-Euler Iterative procedures has demonstrated consistently accurate results.

11.1 MAJOR PROJECT INNOVATIONS

a) The development of light weight composite mandrel construction procedures.

b) The use of filament winding machines as machining stations to produce their own mandrels.

c) The development of Geodesic Dome Ends of unequal size for tapered mandrels eliminating the need for pin-ring turn around structures.

d) The development of self-extracting mandrels and the elimination of costly stripping equipment.

e) Integration of ferrule joint fabrication during the winding process.

f) Development of simple solutions to estimate laminate thickness and material properties variation in tapered tubes.

g) The derivation of a parametric closed form solution to geodesic wind paths on tapered mandrels, with both first and second derivative solutions.

h) The development of wind path solvers for both circumferential and geodesic wind paths.

i) The integration of laminate properties analysis routines with wind path solvers.

j) Development of wind path software capable of integrating mixed mandrel geometry problems.

k) Development of composite coupon manufacturing process for the evaluation of process translation losses and determination of material constants.

11.2 COMMERCIAL ACCEPTANCE

This research project has proved that the concept of the designer setting machine parameters is feasible. In order that the product meets quality assurance protocols, basic design parameters must be met. Currently, advanced composites are largely employed in low demand situations, largely due to the complexity of the design phase and weak understanding of performance.

Such a situation is not lost on the utility and regulatory agencies. In order to satisfy the tradition of scepticism it is necessary that rigid protocols be adopted. The premise of this work was that composites while complex were not the problem. Rather the process of design and fabrication were flawed as long as designers thought of the material as another version of traditional materials. By giving the designer the tools to manipulate ideas with a link to the manufacturing technology, the fabricator would never mistake or take liberties with the designer's intentions.

12 References

Adams,D.F. and E.M.Odom "Influences of Test Fixture Configuration on the Measured Compressive Strength of a Composite Material" *Journal of Composite Technology and Research, Vol. 13, No.1 pp 36-40 , Spring 1991*

American Society of Testing and Materials, "D 1036-99, Standard Test Methods of Static Tests of Wooden Poles", Subcommittee D07.04, 1999.

American Society of Testing and Materials, "D3039, Standard Test Methods for Tensile Properties for Polymer Matrix Composite Materials", Subcommittee D30.04, 2000.

American Society of Testing and Materials, "D3410, Standard Test Method for Compressive Properties for Polymer Matrix Composite Materials with Unsupported Gauge Section by Shear Loading", Subcommittee D30.04, 2000.

American Society of Testing and Materials, "D5379, Standard Test Method for Shear Properties of Composite Materials by the V-Notched Beam Method", Subcommittee D5379M, 1998

Anderson, R. McClean Anderson Ltd Wassau, Wisconsin *personal communications, 1999*

ANSI 05.1 (1992) *American National Standard for Wood Poles-Specifications and Dimension,* American National Standard Institute, New York, U.S.A.

ANSYS, "ANSYS User Manual, Revision 5.2", ANSYS Inc., 1995.

Bisshopp, K. E. and Drucker, D.C. "Large deflections of Cantilever Beams" Q. Applied Mathematics, Vol.3:272-275, 1945.

CAN/CSA-015-90 (1990). *Wood Utility Poles and Reinforcing Stubs Forest Products,* Canadian Standards Association, Ontario Canada.

Cook, Robert D., and Young W. C. "Advanced Mechanics of Materials" Published by Prentice-Hall , Upper Saddle River, New Jersey, 1985

Denost, J. P. "New Design Concepts for Filament-Wound Pressure Vessel with Unequal Polar Openings" S.N.I.A.S. Societe Nationale Industrielle Aerospatiale Division Systemes Balistiques et Spatiaux, Etabilissement d'Aquitaine, 1982

Daniel, I. M. and Ishai, O. " Engineering Mechanics of Composite Materials" *Oxford University Press, New York, N.Y.* , 1994

De Carvalho, J., Lossie, M. and Van Brussel, H. "Computer integrated optimization of filament wound parts." *CADCOMP 96 Conference , Computer Aided Design in Composite Material Technology* pp203-212 *1996*

Design of Steel Transmission Pole Structures ASCE Manual and Reports on Engineering Practice No.72, American Society of Civil Engineering, New York, U.S.A., 1990

Flinn, R.A. and Trojan, P.K. "Engineering Materials and Their Applications" Fourth Edition, Houghton Mifflin Company Boston, 1990

Flodin, J. 'Deflections of beams with varying moments of inertia' *J. of American Society of Nautical Engineers*, Vol.69, pp.511-514, 1957

Gramoll, K. "Stress analysis of filament wound open-ended composite shells"(Conf.Proc. Of the 34th Structural Dynamics, and Materials Conf.(SDM), La Jolla,CA, pp1-9,1993

Gramoll, K., and Ramaprasad, S. "Effects of band weaving on fiber strength in filament-wound composite structures" Composites Engineering Vol 5 No.4 pp 363-373, 1995

Gramoll, K., Namiki, F., and Onoda, J. "Dome thickness of filament wound pressure vessels." Transactions of the Japan Society for Aeronautical and Space Sciences, Vol. 33, No. 100, pp65-79, 1990

Gramoll, K. Namiki, F., and Onoda, J. "General structural analysis of an upper stage composite rocket motor case." 17th International Symposium of Space Technology and Science 21-25 May, Tokyo, Japan 8 pages, 1990

Hartung, R.F., "Planar-Wound Filamentary Pressure Vessels" AIAA Journal, Vol. 1, Dec, pp 2842-2844, 1963.

Hofeditz, J.T. "Structural Design Considerations for Fiber Glass Pressure Vessels" *Preliminary copy of a Report to be presented at 18th Annual Meeting of the Reinforced Plastics Division*)Section 7-C pp1-10, 1962

Ibrahim, S. M. "Performance Evaluation of Finer-Reinforced Polymer Poles for Transmission Lines" PhD Thesis, University of Manitoba, Winnipeg Manitoba, Canada, 2000

Kemper, J. D. 'Large deflections of tapered cantilever beams', *International Journal of Mechanical Science*,Vol.10, pp. 469-478, 1968

Kokan, D., and Gramoll, K., "Analysis of orthotropic composite cylinders" Composites Engineering Vol. 4, No.10, pp.979-993, 1994

Kreyszig, Erwin, (1991), Dover Publications, Inc. Mineola, N.Y. Reprint of original published by University of Toronto Press, Toronto 1959.

Lossie, M and Vandepitte, D. "Extending filament winding capabilities towards obstacle integration.", *CADCOMP 96 Conference , Computer Aided Design in Composite Material Technology V.*,Udine,pp 263-272,*1996*

Lossie, M, Vandepitte, D., and K. Olofsson. "Experimental design approach to off-line quality control in filament winding" *personal communications publication status unknown*, 2000

Maheswaran, M. Department of Mathematics ,University of Wisconsin-Marathon County ***"Non-geodesic Filament Winding on Mandrel Surfaces-A Differential Equations Approach to generating Trajectories"*** A paper on research work carried out for McClean-Anderson Division of ISAMI, 300 Ross Avenue Schofield Wisconsin Made available by R.Anderson of McClean-Anderson. Later formally presented as ***" Non-geodesic Paths with Specified Boundary Conditions on Surfaces of Revolution"*** at Mathematical Association of America -- Wisconsin Section, Spring 1998.

McClure, G., Boire, L., and Carriere, J.C. "Applications of Advanced Composite Materials in Overhead Power Lines and Telecommunications Structures" Advanced Composites in Bridges and Structures, K.W. Neale and P. Labossiere, Canadian Society of Civil Engineering. pp543-549, 1992.

Murphy, J. *"Reinforced Plastics Handbook"*, Second Edition, Elsevier Advanced Technology, 1998

Ohnishi, H. and Matsuzaki, A, "The large deformation analysis of a graphite fishing rod", *Computers and Structures*, Vol. 21, No. ½, pp. 265-271, 1985

Parkinson, M.B., Roach, G.M., and Howell, L.L. "Predicting the large-deflection path of tapered cantilever beams" , *Proceedings of the ASME IMECE,* 2000

Peters, S. T., Humphrey, W.D. And Floral, R.F., "Filament Winding - Composite Structure Fabrication", *(SAMPE , Covina, CA.), 1991*

Philopulos, S. D. "An Investigation on the Structural Performance of Jointed Filament Wound GFRP Poles for Light Utility Applications", Undergraduate Thesis, University of Manitoba, Winnipeg Manitoba, Canada, 2002

Scholliers, J. and Van Brussel, H. "Computer -integrated filament winding: computer-integrated design, robotic filament winding and robotic quality control", *Composites Manufacturing* Vol 5 No 1, pp15-23, 1994

Sherman, B.W. "Analysis of Fiberglass Poles for Electric Power Distribution", IEEE Transactions on Power Apparatus and Systems, Vol. PAS-103, No.5, May, pp1116-1119, 1984

Spolek, G.A. and Jefferies, S. R., 'Analysis of Large Deflections of Fishing Rods' Proceedings of the International Conference on Computational Methods and Experimental Measurements, Washington D.C. pp637-648, 1982

Struik, Dirk, J., "Lectures on Classical Differential Geometry" 1988 Reprint by Dover Publications, Mineola, N.Y. of Originally published : Addison-Wesley Pub. Co. 1961.

Swokowski, Earl, W., "Alternate Edition Calculus with Analytic Geometry" Prindle, Weber and Schmidt Boston, Mass., 1983

Tsai, S.W. " Composites Design ", Think Composites, Dayton, OH., 1988

Yu, B., P.Eng ,*Personal communications,2002*

APPENDIX : Resin Technical Details

(from http:www.westsystem.com)

Typical Physical Properties of WEST SYSTEM Epoxy Resin/Hardener systems. (from http:www.westsystem.com)

Test specimens cured at room temperature for two weeks, unless otherwise noted. Typical values; not to be construed as specifications. Neat epoxy specimens (i.e., containing no fillers or fiber reinforcements) were used for testing.

Property	105/205	105/206		105/207
105/209				
Mix Ratio by weight*	5.07:1	5.0:1	3.4:1	3.56:1
Mix Viscosity @ 72°F (cPs)	975	725	775	725
Pot Life of 100 g @ 72°F (min.)	12	21.5	26.4	51
Specific Gravity of Cured Resin	1.180	1.180	1.163	1.163
Hardness @ 1 day (Shore D)	80	80	78	70
Hardness @ 2 weeks (Shore D)	83	83	82	82
Compression Yield @ 1 day (PSI)	10,120	7,990	6,014	1,226
Compression Yield @ 2 weeks(PSI)	11,418	11,500	10,838	10,027
Tensile Strength (PSI)	7,846	7,320	7,509	7,338
Tensile Elongation (%)	3.4	4.5	3.4	3.5
Tensile Modulus (PSI)	4.08E+05	4.60E+05	4.10E+05	
4.30E+05				
Flexural Strength (PSI)	14,112	11,810	13,016	12,600
Flexural Modulus (PSI)	4.61E+05	4.50E+05	5.14E+05	4.28E+05

Heat Deflection Temperature (°F)	**118**	**123**	**118**	**116**
Onset of Tg by DSC (°F)	**129**	**126**	**123**	**121**
Ultimate Tg by DSC (°F)	**142**	**139**	**137**	**134**
Izod Impact, notched (ft-lbs/in)	**0.93**	**0.54**	**1.27**	**1.10**

Typical values; not to be construed as specifications. Neat epoxy specimens, i.e.,containing no fillers or fiber reinforcements, were used for testing.* Actual Ratio Dispensed by Calibrated WEST SYSTEM® Minipumps.

This page is maintained by Gougeon Brothers, Inc. Last Modified on Tuesday, December 05, 2000.

DOW - DERAKANE MOMENTUM 411-350 EPOXY VINYL ESTER RESIN

DERAKANE* MOMENTUM* 411-350 epoxy vinyl ester resin is a bisphenol-A epoxy resin designed to provide resistance to a wide range of acids, alkalis, bleaches and solvents for use in many chemical processing industry applications.

Typical Physical Properties of DERAKANE MOMENTUM 411-350 resin[1]

Viscosity, mPa.s at 25°C/cps at 77°F	350
Specific Gravity	1.045

Uncatalyzed Stability, dark, months at 77°F/25° C[2]	12

[1] TYPICAL PROPERTIES; NOT TO BE INTERPRETED AS SPECIFICATIONS.

[2] NO ADDITIVES, PROMOTERS, ACCELERATORS, ETC

Typical Room-Temperature Properties of Clear Castings made with DERAKANE MOMENTUM 411-350 resin1

Tensile Strength, MPa/psi	86/12,100
Tensile Modulus, GPa/ unit 10^5 psi	3.2/4.6
Tensile Elongation, %	5.0-6.0
Flexural Strength, MPa/psi	21,400
Flexural Modulus, GPa/ unit 105 psi	3.4/5.0
Heat Distortion Temperature, (°C)F° at 1.82 MPa applied stress (at 264 psi applied stress)	105/220
Barcol Hardness	35

[1]TYPICAL PROPERTIES; NOT TO BE INTERPRETED AS SPECIFICATIONS.

Recommended gel time promotion information:

Gel Time Data Using MEKP (Norox 925H)

Gel Time Data Using MEKP Alternatives

Gel Time Data Using BPO

European Gel Time Data Using MEKP (Butonox LPT)

*Trademark of The Dow Chemical Company

DERAKANEHome: Specification Center: Product Information Table: MNTM 411-350